

# Nucleon and hadron structure changes in the nuclear medium and impact on observables

K. Saito,<sup>1</sup> K. Tsushima,<sup>2</sup> A.W. Thomas<sup>3</sup>

<sup>1</sup>Department of Physics, Faculty of Science and Technology,  
Tokyo University of Science, Noda 278-8510, Japan

<sup>2</sup>Physics Division, National Center for Theoretical Sciences, Taipei 10617, Taiwan

<sup>3</sup>Thomas Jefferson National Accelerator Facility,  
12000 Jefferson Ave., Newport News VA 23606 USA

February 2, 2008

---

## Abstract

We study the effect of hadron structure changes in a nuclear medium using the quark-meson coupling (QMC) model. The QMC model is based on a mean field description of non-overlapping nucleon (or baryon) bags bound by the self-consistent exchange of scalar and vector mesons in the isoscalar and isovector channels. The model is extended to investigate the properties of finite nuclei, in which, using the Born-Oppenheimer approximation to describe the interacting quark-meson system, one can derive the effective equation of motion for the nucleon (or baryon), as well as the self-consistent equations for the meson mean fields.

In conventional nuclear physics, the Skyrme effective forces are very popular, but, there is no satisfactory interpretation of the parameters appearing in the Skyrme forces. Comparing a many-body Hamiltonian generated by the QMC model in the zero-range limit with that of the Skyrme effective forces, it is possible to obtain a remarkable agreement between the Skyrme force and the QMC effective interaction. One can also investigate the relationship between the QMC model and Quantum Hadrodynamics, by carrying out a re-definition of the scalar field in matter. Furthermore, by using *naive dimensional analysis*, it is possible to see that the QMC model can provide remarkably *natural* coupling constants and hence the model itself is regarded as a *natural* effective field theory for nuclei.

The model is first applied to nuclear matter, where the coupling constants are determined so as to produce the saturation condition at normal nuclear matter density. We find a new, simple scaling relation for the changes of hadron masses in a nuclear medium, which can be described in terms of the number of light quarks in a hadron and the value of the scalar mean-field in matter. Once the coupling constants are fixed, the model can be applied to various finite nuclei, including strange and exotic hypernuclei. In this article, we discuss in detail the properties of hypernuclei and meson-nucleus deeply bound states.

It is also of great interest that the QMC model predicts a variation of the nucleon form factors in nuclear matter, which will affect certainly the analysis of electron scattering off nuclei, including polarization-transfer experiments. Recent experimental analysis of data taken at Jefferson Laboratory (JLab) and MAMI indeed seems to support such a variation of nucleon form factors in nuclei. The change of nucleon structure in a nuclear medium is also expected to modify nuclear structure functions (the nuclear EMC effect), which

are measured by scattering with high-energy charged-leptons and/or neutrinos. We study such possibilities, including consideration of the empirically observed, Bloom-Gilman (quark-hadron) duality.

We also study hadronic reactions in nuclear medium, namely, subthreshold kaon production in heavy ion collisions,  $D$  and  $\bar{D}$  meson production in antiproton-nucleus collisions, and  $J/\Psi$  suppression. In particular, the modification of the  $D$  and  $\bar{D}$  meson properties in nuclear medium derived by the QMC model, can lead a large  $J/\Psi$  absorption cross section, which is required to explain the observed  $J/\Psi$  suppression in microscopic hadronic comover dissociation scenario, without assuming the formation of a QGP phase.

The present investigation indicates that the traditional nuclear/hadronic physics approach may have its limitations. It further suggests the need for the study of alternate approaches which include subhadronic degrees of freedom, even at normal nuclear matter density.

*Keywords:* Quarks in nuclei, Quark-meson coupling model, Relativistic nuclear model, Properties of finite nuclei, A new scaling formula for hadron masses in matter, Nucleon form factors, Hyper and exotic nuclei, Meson-nucleus bound states, Nuclear structure functions, Hadron reactions in matter

---

## Contents

1. Introduction .....	
2. Foundation of the QMC Model.....	
2.1. Non-relativistic treatment.....	
2.1.1. Classical consideration.....	
2.1.2. Quantization at the quark level.....	
2.1.3. Correction due to the center of mass motion.....	
2.1.4. Correction due to $H_1$ and Thomas precession.....	
2.1.5. Total Hamiltonian in the mean fields.....	
2.1.6. Equations for the meson fields.....	
2.1.7. Self-consistency procedure.....	
2.2. Relativistic treatment.....	
2.2.1. Relativistic model.....	
2.2.2. Properties of the in-medium nucleon mass.....	
2.2.3. Effect of meson structure.....	
2.2.4. Naturalness.....	
2.3. Relationship between the QMC model and conventional nuclear models.....	
2.4. Relationship between the QMC model and Quantum Hadrodynamics.....	
2.5. Modified quark-meson coupling model.....	
2.6. Variants of the QMC model.....	
3. Properties of nuclei.....	
3.1. Nuclear matter properties - saturation properties and incompressibility.....	
3.1.1. A new scaling formula for hadron masses in matter.....	
3.1.2. Variations of quark and gluon condensates in nuclear matter.....	
3.1.3. Nuclear matter at finite temperature and neutron stars.....	
3.2. Finite nuclei - $^{16}\text{O}$ , $^{40}\text{Ca}$ , $^{48}\text{Ca}$ , $^{90}\text{Zr}$ , $^{208}\text{Pb}$ .....	
3.3. Strange, charm and bottom hadrons in nucleus.....	
3.3.1. Strange, charm and bottom hadron properties in nuclear matter.....	
3.3.2. Mean-field equations of motion for strange, charm and bottom hypernuclei.....	
3.3.3. Spin-orbit potential in the QMC model - strange hypernuclei.....	

3.3.4.	Pauli blocking and channel coupling effects.....	
3.3.5.	Results for strange hypernuclei.....	
3.3.6.	Results for charm and bottom hypernuclei .....	
3.4.	Meson-nucleus bound states.....	
4.	Effects of nucleon substructure on lepton-nucleus scatterings .....	
4.1.	Nucleon form factors.....	
4.1.1.	Electromagnetic form factors.....	
4.1.2.	The QMC predictions and experimental results (EM interactions).....	
4.1.3.	Nucleon substructure effect on the longitudinal response functions.....	
4.1.4.	Axial form factors - neutrino-nucleus scattering .....	
4.2.	Quark-hadron duality, the nuclear EMC effect and nuclear structure functions.....	
4.2.1.	The nuclear EMC effect.....	
4.2.2.	Bloom-Gilman duality and the nuclear EMC effect .....	
4.2.3.	Bloom-Gilman duality and the nuclear structure functions .....	
5.	Hadronic reactions in nuclear medium.....	
5.1.	Subthreshold kaon production and in-medium effects .....	
5.2.	$D$ and $\overline{D}$ meson production in nuclei.....	
5.3.	$J/\Psi$ suppression .....	
6.	Summary and outlook .....	

# 1 Introduction

It is very well recognized that the dynamics of electrons in a molecular system can be completely separated from the dynamics of the nucleons in the nuclear core, because the ratio of the typical energy scales of a molecular system ( $\sim 10$  eV) to a nucleus ( $\sim 10$  MeV) is as much as  $10^{-6}$ . One is naturally led to ask whether the dynamics of nucleons in a nucleus can also be described independent of the underlying degrees of freedom, namely the quarks and gluons. However, in this case the ratio of these energy scales is at most of order  $10^{-1}$ .

One of the most exciting topics in nuclear physics is thus to study how the hadron properties are modified by the nuclear environment and how such modifications affect the properties of nuclei. Since nucleons and mesons are made of quarks, anti-quarks and gluons, one expects their internal structure to change when placed inside nuclear matter or atomic nuclei [1]. There is little doubt that, at sufficiently high nuclear density and/or temperature, quarks and gluons are the correct degrees of freedom. By contrast, the general success of conventional nuclear physics (with *effective* interactions) indicates that nucleons and mesons provide a good starting point for describing a nucleus at low energy. Therefore, a consistent nuclear theory describing the transition from nucleon and meson degrees of freedom to quarks and gluons is truly required to describe nuclei and nuclear matter over a wide range of density and temperature. Of course, theoretically, lattice QCD simulations may eventually give reliable information on the density and temperature dependence of hadron properties in nuclear medium. However, current simulations have mainly been performed for finite temperature systems with zero baryon density [2], which is very far from what is needed for the description of a finite nucleus. As a first step in this direction, it is therefore of great interest necessary to build a nuclear model which incorporates the internal quark and gluon degrees of freedom of hadrons themselves.

We know that explicit quark degrees of freedom are certainly necessary to understand deep-inelastic scattering (DIS) at momentum transfer of several GeV. In particular, the nuclear EMC effect [3] has suggested that it is vital to include some effects involving dynamics beyond the conventional nucleon-meson treatment of nuclear physics to explain the whole EMC effect [4, 5]. Furthermore, the search for evidence of some modification of nucleon properties in medium has recently been extended to the electromagnetic form factors of nucleon in

polarized ( $\vec{e}, e'\vec{p}$ ) scattering experiments on  $^{16}\text{O}$  and  $^4\text{He}$  nuclei at MAMI and JLab [6]. These experiments observed the double ratio of proton-recoil polarization-transfer coefficients in the scattering off nuclei with respect to the elastic  $^1\text{He}(\vec{e}, e'\vec{p})$  reaction at momentum transfers of several 100 MeV to a few GeV. It strongly hints at the need to include medium modifications of the proton electromagnetic form factors.

Some early attempts to construct a model which bridges the gap between conventional nuclear physics and the quark-gluon picture were made in the mid 80's. Using a covariant nontopological soliton model of the nucleon, Celenza *et al.* [7] discussed the effect of medium modification of the nucleon structure on its size to understand the nuclear EMC effect. They introduced a coupling between quarks and a scalar field generated by the nuclear environment, and predicted that the size of nucleon in a nucleus becomes larger than that of free nucleon. The increase in radius, of about 15% in an iron nucleus (Fe), was able to reproduce the observed nuclear structure functions. Stimulated by Celenza *et al.* [7], Wong investigated the effect of nuclear mean fields on quarks in a nucleon using the MIT bag model [8]. He pointed out that an attractive scalar potential makes quarks more relativistic by decreasing their masses in nuclear medium. Jandel and Peters also studied the change of the in-medium nucleon in size within the framework of the Friedberg-Lee nontopological-soliton bag model [9]. They reported that the swelling of the nucleon is about 30% at normal nuclear matter density.

In 1988, Guichon [10] developed a novel model for nuclear matter, in which quarks in non-overlapping nucleon bags interact *self-consistently* with (structureless) isoscalar-scalar ( $\sigma$ ) and isoscalar-vector ( $\omega$ ) mesons in the mean-field approximation (MFA). The mesons couple not to point-like nucleons but directly to confined quarks. He discussed a novel, possible mechanism for nuclear matter saturation in terms of quark degrees of freedom. (It should be noted here that Frederico *et al.* [11] studied a similar model for nuclear matter by using a harmonic oscillator potential for the quark confinement and discussed the dependence of the  $\sigma$ -nucleon coupling constant on nuclear density.) After that work, the model was studied further by Fleck *et al.* [12] and refined and extended by Saito and Thomas [13] in the 90's – the model is called the quark-meson coupling (QMC) model. (We also note that in the early 90's Banerjee [14] and Naar and Birse [15] studied nucleon properties in nuclear matter using the color-dielectric model, and that Mishra *et al.* [16] investigated a nonlocal  $\sigma$ - $\omega$  model in the relativistic Hartree approximation, including short distance vertex form factors.)

The QMC model may be viewed as an extension of Quantum Hadrodynamics (QHD) [17]. In studies of infinite nuclear matter, as a result of the quark- $\sigma$  scalar coupling, the internal structure of the nucleon is modified with respect to the free case. In particular, an attractive force associated with the  $\sigma$  meson exchange decreases the quark mass in matter, which leads to an enhancement of the small component of the confined quark wave function. Because of this enhancement, the quark scalar density in a nucleon, which is itself the source of the  $\sigma$  field, is reduced in matter compared with that in the free case. This can provide a new mechanism for the saturation of nuclear matter, where the quark structure of the nucleon plays a vital role [10]. The model can give a satisfactory description of the bulk properties of (symmetric) nuclear matter. Of particular interest is the fact that the decrease of the quark scalar density, depending on the density of nuclear matter, can provide a lower value of the incompressibility of nuclear matter than those obtained in approaches based on point-like nucleons such as QHD. This is a significant improvement on QHD at the same level of sophistication. A remarkable feature of this picture is that specific details of the model are mostly irrelevant: for example, the results do not depend on whether or not one uses the MIT bag model, all that is important is the confined quarks are treated relativistically. It also does not matter whether or not the sources of the repulsive and attractive forces are generated by the  $\omega$  and  $\sigma$ , respectively, all that is needed is that they have respectively Lorentz-vector and scalar character.

The original version of the QMC model consists of the nucleon,  $\sigma$  and  $\omega$  mesons. It is easy to include the (isovector-vector)  $\rho$  meson, which is vital to produce the correct symmetry energy, in addition to the usual ingredients [13]. It is also possible to incorporate the (isovector-scalar)  $\delta$  meson into the model. Such a model allows us to study the effect of charge symmetry breaking in nuclei [18]. In those cases, all the mesons are assumed to be structureless. This version is sometimes called the QMC-I model. However, it is true that the mesons are also built of quarks and anti-quarks and that they may change their character in matter. To incorporate the effect of meson structure, one can suppose that the vector mesons are again described by a relativistic quark model (like a bag) with *common* scalar and vector mean-fields in matter. In this case, the vector meson mass in matter will also depend on the scalar mean-field. The  $\sigma$  meson itself is, however, not readily represented by a simple quark model, because it couples strongly to the pseudoscalar ( $2\pi$ ) channel and

thus a direct treatment of chiral symmetry in medium is important. If, however, we choose an appropriate parametrization of the  $\sigma$  mass in matter, it is possible to construct a model in which the structure effects of both the nucleon and the mesons are included [19]. This is called the QMC-II model. QMC-I predicts a non-linear coupling between the nucleon and the  $\sigma$  meson and linear couplings of the vector mesons to the nucleon, while QMC-II yields many interaction terms because of the internal structure of the nucleon and mesons [19]. Extending this idea, one can find a novel, scaling mass formula for various hadrons in matter (see section 3.1.1).

In general, an effective field theory at low energy will contain an infinite number of interaction terms, which incorporate the compositeness of hadrons [20]. It is then expected to involve numerous couplings which may be nonrenormalizable. Manohar and Georgi [21] have proposed a systematic way to manage to organize such complicated, effective field theories, which is called *naive dimensional analysis* (NDA). NDA gives rules for assigning a coefficient of the appropriate size to any interaction term in an effective Lagrangian. After extracting the dimensional factors and some appropriate counting factors using NDA, the remaining dimensionless coefficients are all assumed to be of order unity. This is the so-called *naturalness* assumption. If naturalness is valid, we can control the effective Lagrangian, at least at the tree level. As seen in Ref. [22], QMC-I provides remarkably *natural* coupling constants, while in QMC-II the coupling constants are almost all *natural*. Therefore, the QMC model itself can be regarded as a *natural* effective field theory for nuclei.

One can investigate the relationship between QMC and QHD [23, 24]. Carrying out a re-definition of the scalar field in matter, it is possible to transform the QMC picture into a QHD-type model with a non-linear scalar potential (if we ignore the change in the internal quark wave function of the bound nucleon). Some potentials generated from the QMC model can be compared with those used in relativistic mean-field (RMF) models. The QMC model always predicts positive coefficients for the cubic and quartic terms in the non-linear scalar potential [19, 24], while in the RMF model those coefficients are parameterized phenomenologically and thus sometimes become negative. From the point of view of field theory, the coefficient of quartic term should be positive.

It is of interest to compare the QMC model with sophisticated versions of RMF models: for example, the recent version of QHD which was proposed by Furnstahl, Serot, Tang and Walecka [25]. This model is constructed in terms of nucleons, pions and the low-lying non-Goldstone bosons, and chiral symmetry is realized nonlinearly with a light scalar ( $\sigma$ ) meson included as a chiral singlet to describe the mid-range nucleon-nucleon attraction. This has a total of 16 coupling constants and they are almost *natural*. In this case, the coupling constants were determined so as to fit measured ground-state observables of several nuclei by solving the model equations for the nuclei simultaneously and minimizing the difference between the measured and calculated quantities using a nonlinear least-squares adjustment algorithm. Therefore, the coupling constants were fixed entirely phenomenologically. Such a phenomenological determination of the coupling constants is also typical of the ordinary RMF approach. In contrast, the QMC model has basically three coupling constants, which are determined to fit the saturation properties of nuclear matter, whereas the other coupling constants are automatically generated through a model for the structure of the hadrons. Therefore, the physical meaning of the coupling constants is quite clear. In the QMC model, the meson masses ( $\omega$ ,  $\rho$ , etc.) decrease in matter. However, in some RMF models, since the coupling constants were chosen phenomenologically, particular parameter sets lead to an increase of the effective meson masses in matter, which seems unlikely from the highlight of recent discussions [26, 27]. It should be noted that the chiral symmetry and its restoration have been recently discussed in the QMC model and that the pion cloud effect is studied in detail [28].

Furthermore, it is very remarkable that the QMC model can provide a many-body effective Hamiltonian in non-relativistic approximation [29]. It naturally leads to the appearance of many-body forces. In the conventional nuclear physics, the Skyrme effective forces are very popular and often used to estimate various properties of finite nuclei. However, there is no satisfactory interpretation of the parameters appearing in the Skyrme forces. Comparing the many-body Hamiltonian generated by the QMC model in the zero-range limit with that of the Skyrme effective forces, one can obtain a remarkable agreement between the Skyrme force and the effective interaction corresponding to the QMC model. It allows us to recognize that, indeed, the response of nucleon internal structure to the nuclear medium does play a vital role in nuclear structure.

There have been a lot of interesting applications to the properties of infinite nuclear matter and finite nuclei. It is possible to extend the QMC model of infinite nuclear matter to finite nuclei if we assume that

the meson fields do not vary rapidly across the interior of the nucleon in a nucleus and that the nucleon is not moving too rapidly – i.e., the Born-Oppenheimer approximation [30, 31]. It is, for example, possible to study the properties of strange, charm, and bottom hypernuclei (see section 3.3), as well as the bound states of various mesons and nuclei (see section 3.4). In this way we can investigate the properties of flavored hadrons in medium, as well as the partial restoration of chiral symmetry for heavy hadrons in a nuclear medium, where light quarks play crucial roles in those hadrons. We should emphasize again that, we do not have to determine various coupling constants for many hadrons in the QMC model. They are automatically determined at the quark level and this enables the QMC model to handle various hadrons in a systematic and unified manner based on the quark model. This strengthens the predictive power of the model enormously, once it has been calibrated using successfully using the available experimental data.

Furthermore, the QMC model predicts the variation of the nucleon form factors in nuclear matter (see section 4.1), which will certainly effect the analysis of electron scattering off nuclei [6, 32], including the polarization-transfer coefficients discussed at the top of this section. Recent experimental analysis [6] of results from Mainz and Jefferson Laboratory (JLab) do indeed seem to support such a variation of nucleon form factors in nuclei. The modification of nucleon structure in the nuclear medium is also expected to modify nuclear structure functions [33] (the nuclear EMC effect), which are measured by scattering with high-energy charged-leptons and/or neutrinos. We study such possibilities in section 4.2 based on empirically observed, Bloom-Gilman (quark-hadron) duality [34], which bridges between the low energy nucleon form factors with high energy deep-inelastic scattering nuclear structure functions.

The discrepancy between the calculated binding energy differences of mirror nuclei and those measured is a long-standing problem in nuclear physics, known as the Okamoto-Nolen-Schiffer (ONS) anomaly [35]. It is recognized that the ONS anomaly may not be understood by only the traditional approach, and conventional nuclear contributions to the anomaly are thought to be at the few percent level of the experimental findings. The effects of charge symmetry breaking (CSB) in the nuclear force, especially  $\rho$ - $\omega$  mixing, seemed to reduce this discrepancy [36]. However, the importance of the momentum dependence of the mixing amplitude has been pointed out using several different models [37, 38]. It suggests that the  $\rho$ - $\omega$  mixing amplitude at space-like momenta is quite different from the value at the  $\omega$  pole and implies that the nucleon-nucleon (NN) potential given by the off-shell amplitude of the  $\rho$ - $\omega$  mixing is very far from the ones used in the successful phenomenology. Thus, it may be difficult to explain the ONS anomaly by only the meson-mixing potentials. When the mass difference between  $u$  and  $d$  quarks is taken into account, the nucleon substructure may produce the difference between the meson couplings to proton and neutron, that leads to CSB in the NN interaction. It may be possible to extend the QMC model to study such CSB in nuclei [18, 39]. The change of the form factors due to the substructure effect of the nucleon may also give a previously unknown correction to the extraction of the Cabibbo-Kobayashi-Maskawa (CKM) matrix element,  $V_{ud}$ , from super-allowed Fermi  $\beta$ -decay [40, 41]. To draw more definite conclusions, there is, however, a need for further investigation.

In a recent helicity analysis of subthreshold  $\rho^0$  production on  $^2\text{H}$ ,  $^3\text{He}$  and  $^{12}\text{C}$  at low photo-production energies, the results are indicative of a large longitudinal  $\rho^0$  polarization and this signature is used to extract in-medium  $\rho_L^0$  invariant mass distributions for all three nuclei [42]. Then, the  $^2\text{H}$  and  $^3\text{He}$  data distributions support the role of  $N^*(1520)$  excitation in shaping the in-medium  $\rho_L^0$  invariant mass distribution, while the  $^{12}\text{C}$  distributions are consistent with quasi-free  $\rho_L^0$  production and the data support an in-medium modification of the  $\rho_L^0$  invariant mass distribution. The in-medium mass of the  $\rho$  meson predicted by the QMC model is consistent with the observed data [42, 43]. Two interesting experiments concerning the modification of the  $\omega$  mass in nuclear matter have also been performed very recently at the ELSA tagged photon facility (the CBELSA/TAPS collaboration) [44] and KEK [45]. Using the Crystal Barrel/TAPS experiment at ELSA, the in-medium modification of  $\omega$  meson was studied via the reaction  $\gamma + A \rightarrow \omega + X \rightarrow \pi^0\gamma + X'$ , and results obtained for Nb were compared to a reference measurement on a liquid hydrogen target. While for recoiling, long-lived mesons ( $\pi^0$ ,  $\eta$  and  $\eta'$ ), which decay outside of the nucleus, a difference in the lineshape for the two data samples was not observed, they found a significant enhancement toward lower masses for omega mesons with low momenta produced on the Nb target. For momenta less than 500 MeV/c, they have concluded that the in-medium  $\omega$  mass is about 722 MeV at  $0.6\rho_0$  (where  $\rho_0$  is the normal nuclear matter density), which is just the value predicted by the QMC model [19] (see also section 3.1.1). At KEK, the invariant mass spectra of  $e^+e^-$  pairs produced in 12-GeV proton-induced nuclear reactions were measured using the KEK Proton-

Synchrotron. On the low-mass side of the  $\omega$ -meson peak, a significant enhancement over the known hadronic sources has been observed. The mass spectra, including the excess, are well reproduced by a model that takes into account the density dependence of the vector meson mass modification.

Furthermore, in recent experimental work in relativistic heavy-ion collisions, the  $J/\psi$  suppression is thought to be a promising candidate as a signal of a quark-gluon plasma (QGP) and the experimental data show an anomalous result [46]. The modification of the  $D$  and  $\bar{D}$  meson properties in nuclear medium, derived within the QMC model, can lead to a large  $J/\Psi$  absorption cross section [47], which is required to explain the observed  $J/\Psi$  suppression in the microscopic, hadronic comover dissociation scenario, without assuming any formation of a QGP phase (see section 5.3). (In QMC, the mass modification of  $J/\Psi$  in nuclear medium is expected to be very moderate.)

These facts seem to indicate that the traditional nuclear/hadronic physics approach may have its limitations and suggest a need for the study of alternate approaches including subhadronic degrees of freedom. Exciting a single quark in the nucleon costs about 400 MeV. This is not significantly different from the energy required to excite a  $\Delta$ . It is also the same order of magnitude as the scalar and vector potentials required in QHD. Furthermore, the  $u$  and  $d$  quarks are very light compared to nucleon and mesons and should be able to respond faster to their environment. We know of *no* physical argument why this response should be ignored. It is, therefore, very important to consider and answer the following question: *Do quarks plays an important role in nuclei and nuclear matter ?* Our aim in this review article is to show how subnucleonic (subhadronic) degrees of freedom do indeed appear in nuclear physics.

This paper is organized as follows. We first review the foundation of the QMC model in section 2, in which the relationship between the QMC model and widespread nuclear models is also discussed. It is shown how the nucleon mass is modified by the nuclear environment. Several modified versions of the QMC model are also reviewed. In section 3, various properties of infinite nuclear matter and finite nuclei are summarized. We propose a new scaling formula for hadron masses in a nuclear medium. In particular, we study in detail the properties of strange, charm and bottom hypernuclei, which may be observed in forthcoming experiments. A new type of the spin-orbit force as well as the effects of Pauli blocking and channel coupling are also discussed. We review the effects of nucleon substructure on lepton-nucleus scattering in section 4. It is very interesting to study nucleon form factors in matter and nuclear structure functions because lepton-nucleus scattering can directly probe the quark substructure of in-medium nucleon. We compare several experimental results with the QMC predictions. In section 5, we summarize important implications predicted by the QMC model for hadronic reactions. In the last section, we give a summary and an outlook regarding future work.

## 2 Foundation of the QMC Model

### 2.1 *Non-relativistic treatment*

#### 2.1.1 *Classical consideration*

Following Guichon *et al.*, we first treat a nucleon in a nucleus classically [30]. We generally denote a coordinate in the nuclear rest frame (NRF) as  $(t, \vec{r})$ , while we define an instantaneous rest frame for a nucleon at each time  $t$  (IRF), which is denoted with primes  $(t', \vec{r}')$ :

$$\begin{aligned} r_L &= \vec{r} \cdot \vec{v} = r'_L \cosh \xi + t' \sinh \xi, \\ \vec{r}_\perp &= \vec{r}'_\perp, \\ t &= t' \cosh \xi + r'_L \sinh \xi. \end{aligned} \tag{1}$$

In the NRF, the nucleon follows a classical trajectory,  $\vec{R}(t)$ , and the instantaneous velocity of the nucleon is given by  $\vec{v} = d\vec{R}/dt$ . In Eq. (1),  $r_L$  and  $\vec{r}_\perp$  are respectively the components parallel and transverse to the velocity and  $\xi$  is the rapidity defined by  $\tanh \xi = |\vec{v}(t)|$ .

Let us suppose that quarks in the nucleon have *enough* time to adjust to the local fields in which the nucleon is moving [31]. It is exact if the fields are constant, because the motion of the nucleon has no acceleration. We shall examine this approximation for a typical nuclear environment. Assume that at  $t = 0$  the nucleon is at

$\vec{R}_0$ . After a short time  $t(\ll 1)$ , the coordinate of the nucleon can be described as

$$\vec{R}(t) = \vec{R}_0 + \vec{v}_0 t + \frac{1}{2} t^2 \vec{\alpha}_0, \quad (2)$$

where the velocity and acceleration at  $t = 0$  are respectively denoted by  $\vec{v}_0$  and  $\vec{\alpha}_0 = \vec{F}/M_N = -\vec{\nabla}V/M_N$  (with  $M_N$  the free nucleon mass and  $V$  potential). If we take a typical nuclear potential,  $V$ , as the Woods-Saxon form

$$V(r) = \frac{V_0}{1 + \exp\left[\frac{r-R_A}{a}\right]}, \quad (3)$$

with depth  $V_0 \sim -50$  MeV,  $a \sim 0.5$  fm (surface thickness is about 2 fm) and radius  $R_A \sim 1.2A^{1/3}$ , the maximum acceleration occurs at the nuclear surface, and it is

$$\vec{\alpha}_{max} = \frac{V_0}{4aM_N} \hat{R}, \quad (4)$$

where  $\hat{R}$  is a unit vector in the radial direction. Therefore, in the IRF, since the coordinates  $(t, \vec{R}_\perp, R_L)$  are transformed as Eq. (1), one finds  $R'_L = R_L \cosh \xi - t \sinh \xi$ . Assuming  $|\vec{v}_0| \ll 1$  and combining the transverse part, we get

$$\vec{R}'(t) \simeq \vec{R}'_0 + \frac{V_0}{8aM_N} t^2 \hat{R}, \quad (5)$$

which gives

$$R' - R'_0 \equiv (\vec{R}'(t) - \vec{R}'_0) \cdot \hat{R} = \frac{V_0}{8aM_N} t^2. \quad (6)$$

In the worst case, the departure from the initial position  $\vec{R}_0$ , relative to the typical size of the nucleon itself ( $R_N \sim 1$  fm) is then expressed as

$$\left| \frac{R'(t) - R'_0}{R_N} \right| \sim \frac{|V_0|}{8aM_N R_N} t^2 \sim \frac{t^2}{75}, \quad (7)$$

where  $t$  is in fm. Thus, as long as the time taken for the quark motion to change is less than  $\sim 9$  fm, the nucleon position in the IRF can be considered as *unchanged*. Since the typical time for an adjustment in the motion of the quarks is given by the inverse of the typical excitation energy, which is of order 0.5 fm (corresponding to the  $\Delta$  excitation), this is quite safe.

We begin by constructing an appropriate Lagrangian density in the IRF. As a nucleon model we adopt the static, spherical MIT bag [48]:

$$\mathcal{L}_0 = \bar{\psi}_q' (i\gamma \cdot \partial - m_q) \psi_q' - BV_B, \quad \text{for } |\vec{u}'| \leq R_B, \quad (8)$$

with  $B$  the bag constant,  $V_B$  the bag volume,  $R_B$  the bag radius,  $m_q$  the quark mass and  $\vec{u}'$  the position of the quark from the center of the bag in the IRF – we denote as  $u'$  the 4-vector:  $u' = (t', \vec{u}') = (t', \vec{r}' - \vec{R}')$ . The quark field in the IRF is expressed by  $\psi_q'(t', \vec{u}')$ , which satisfies the bag boundary condition at the surface  $|\vec{u}'| = R_B$ :  $(1 + i\vec{\gamma} \cdot \hat{u}')\psi_q' = 0$ .

We incorporate the interaction of the quark with the scalar ( $\sigma$ ) and vector ( $\omega$ ) mean fields, which are generated by the surrounding nucleons. In the NRF, they are functions of position:  $\sigma(\vec{r})$  and  $\omega^\mu = (\omega(\vec{r}), \vec{0})$  in MFA. Thus, in the IRF, these fields can be expressed by Lorentz transformation

$$\begin{aligned} \sigma_I(t', \vec{u}') &= \sigma(\vec{r}), \\ \omega_I(t', \vec{u}') &= \omega(\vec{r}) \cosh \xi, \\ \vec{\omega}'_I(t', \vec{u}') &= -\omega(\vec{r}) \hat{v} \sinh \xi, \end{aligned} \quad (9)$$

where the subscript  $I$  stands for the IRF. Thus, the interaction can be written as

$$\mathcal{L}_I = g_\sigma^q \bar{\psi}_q' \psi_q' \sigma_I(u') - g_\omega^q \bar{\psi}_q' \gamma_\mu \psi_q' \omega_I^\mu(u'), \quad \text{for } |\vec{u}'| \leq R_B, \quad (10)$$



where  $g_\sigma^q$  ( $g_\omega^q$ ) is the quark- $\sigma$  ( $\omega$ ) coupling constant. It is also possible to include the effect of  $\rho$  meson field (see section 2.1.5).

Now let us construct a Hamiltonian in the IRF. Suppose that at time  $t'$  the bag is located at  $\vec{R}'$  in the IRF, while, in the NRF, it is located at  $\vec{R}$  at time  $T$ . Using Eq. (1), for an arbitrary position  $\vec{r}'$  in the bag ( $\vec{r}' = \vec{u}' + \vec{R}'$ ) at the same time  $t'$ , we find

$$\begin{aligned} r_L &= R'_L \cosh \xi + t' \sinh \xi + u'_L \cosh \xi, \\ &= R_L + u'_L \cosh \xi, \\ \vec{r}_\perp &= \vec{R}'_\perp + \vec{u}'_\perp. \end{aligned} \quad (11)$$

From this relation, the  $\sigma$  and  $\omega$  fields are given by

$$\sigma_I(t', \vec{u}') = \sigma(R_L(T) + u'_L \cosh \xi, \vec{R}'_\perp(T) + \vec{u}'_\perp), \quad (12)$$

$$\omega_I^\mu(t', \vec{u}') = \eta^\mu \omega(R_L(T) + u'_L \cosh \xi, \vec{R}'_\perp(T) + \vec{u}'_\perp), \quad (13)$$

where  $\eta^\mu = (\cosh \xi, -\hat{v} \sinh \xi)$ .

For a while, suppose that the effect of finite size of the nucleon is negligible and that the mean fields in the IRF can be approximated by their values at  $\vec{R}(T)$  in the NRF, for example,  $\sigma_I \simeq \sigma(\vec{R}(T))$ . As the typical time scale for a change in the motion of the quark is  $\tau \sim 0.5$  fm, the relative change of the field during this time,  $\Delta\sigma$ , is

$$\Delta\sigma = |\sigma(\vec{R}(T + \tau)) - \sigma(\vec{R}(T))| = (\vec{v} \cdot \hat{R})\tau \left( \frac{d\sigma}{dR} \right). \quad (14)$$

It is then expected that the  $\sigma$  field roughly follows the nuclear density, and as long as it is constant in the interior of the nucleus,  $\Delta\sigma$  almost vanishes. The variation of the density occurs mainly at the surface where it drops to zero from the normal nuclear matter density,  $\rho_0$ , over a distance  $d$  of about 2 fm. Therefore, one can estimate  $|(d\sigma/dR)/\sigma|$  as approximately  $1/d$  at the surface. Furthermore, the factor  $(\vec{v} \cdot \hat{R})$  introduces a factor of  $1/3$ , because  $\vec{v}$  is isotropic. If we take  $|\vec{v}| \simeq k_F/M_N \sim 0.36$  ( $k_F \simeq 1.7$  fm $^{-1}$ ), the relative change of the  $\sigma$  field is then estimated to be

$$\frac{\Delta\sigma}{\sigma} \sim \frac{0.5 \times 0.36}{3 \times 2} \sim 3\%. \quad (15)$$

This value is quite small, implying that the Born-Oppenheimer approximation certainly works well in the nucleus and that we can treat the position  $\vec{R}(T)$  as a fixed parameter in solving the equation of motion for the quarks in matter. Clearly this amounts to neglecting terms of order  $v$  in the argument of  $\sigma$  and  $\omega$ . In order to be consistent we also neglect terms of order  $v^2$  – i.e., we replace  $u'_L \cosh \xi$  by  $u'_L$  in the argument.

### 2.1.2 Quantization at the quark level

In the IRF, the interaction Lagrangian density thus becomes

$$\mathcal{L}_I = g_\sigma^q \bar{\psi}_q' \psi_q'(u') \sigma(\vec{R} + \vec{u}') - g_\omega^q \bar{\psi}_q' \psi_q'(t', \vec{u}') [\gamma_0 \cosh \xi + \vec{\gamma} \cdot \hat{v} \sinh \xi] \psi_q'(t', \vec{u}') \omega(\vec{R} + \vec{u}'), \quad (16)$$

and the corresponding Hamiltonian is

$$H = \int_{V_B} d\vec{u}' \bar{\psi}_q' [-i\vec{\gamma} \cdot \vec{\nabla} + m_q - g_\sigma^q \sigma(\vec{R} + \vec{u}') + g_\omega^q (\gamma_0 \cosh \xi + \vec{\gamma} \cdot \hat{v} \sinh \xi) \omega(\vec{R} + \vec{u}')] \psi_q'(t', \vec{u}') + BV_B, \quad (17)$$

where the integral is performed within the bag volume  $V_B$ . The momentum operator is then given by

$$\vec{P} = \int_{V_B} d\vec{u}' \psi_q'^{\dagger} [-i\vec{\nabla}] \psi_q'. \quad (18)$$

Since the mean fields appreciably vary only near the nuclear surface, it makes sense to separate the Hamiltonian into two pieces,  $H = H_0 + H_1$ :

$$H_0 = \int_{V_B} d\vec{u}' \bar{\psi}_q' [-i\vec{\gamma} \cdot \vec{\nabla} + m_q - g_\sigma^q \sigma(\vec{R}) + g_\omega^q (\gamma_0 \cosh \xi + \vec{\gamma} \cdot \hat{v} \sinh \xi) \omega(\vec{R})] \psi_q'(t', \vec{u}') + BV_B, \quad (19)$$

$$H_1 = \int_{V_B} d\vec{u}' \bar{\psi}_q' [-g_\sigma^q(\sigma(\vec{R} + \vec{u}') - \sigma(\vec{R})) + g_\omega^q(\gamma_0 \cosh \xi + \vec{\gamma} \cdot \hat{u}' \sinh \xi)(\omega(\vec{R} + \vec{u}') - \omega(\vec{R}))] \psi_q'(t', \vec{u}'). \quad (20)$$

Then, it is possible to consider the latter Hamiltonian  $H_1$  as a perturbation.

We prepare a complete and orthogonal set of eigenfunctions for the quark field. They are denoted by  $\phi^\alpha$ , where  $\alpha$  is a collective symbol labeling the quantum numbers:

$$h\phi^\alpha(\vec{u}') \equiv (-i\gamma^0 \vec{\gamma} \cdot \vec{\nabla} + m_q^* \gamma^0) \phi^\alpha(\vec{u}') = \frac{\Omega_\alpha}{R_B} \phi^\alpha(\vec{u}'), \quad (21)$$

$$(1 + i\vec{\gamma} \cdot \hat{u}') \phi^\alpha(\vec{u}') = 0, \quad \text{at } |\vec{u}'| = R_B, \quad (22)$$

$$\int_{V_B} d\vec{u}' \phi^{\alpha\dagger} \phi^\beta = \delta^{\alpha\beta}, \quad (23)$$

with  $m_q^*$  a parameter. The lowest, positive eigenfunction is then given by

$$\phi^{0m}(t', \vec{u}') = \frac{\mathcal{N}}{4\pi} \begin{pmatrix} j_0(xu'/R_B) \\ i\beta_q \vec{\sigma} \cdot \hat{u}' j_1(xu'/R_B) \end{pmatrix} \chi_m, \quad (24)$$

with  $u' = |\vec{u}'|$  and  $\chi_m$  the spin function and

$$\Omega_0 = \sqrt{x^2 + (m_q^* R_B)^2}, \quad \beta_q = \sqrt{\frac{\Omega_0 - m_q^* R_B}{\Omega_0 + m_q^* R_B}}, \quad (25)$$

$$\mathcal{N}^{-2} = 2R_B^3 j_0^2(x) [\Omega_0(\Omega_0 - 1) + m_q^* R_B/2]/x^2, \quad (26)$$

where  $x$  is the eigenvalue for the lowest mode, which satisfies the boundary condition at the bag surface,  $j_0(x) = \beta_q j_1(x)$ .

Using this set, the quark field can be expanded as

$$\psi_q'(t', \vec{u}') = \sum_\alpha e^{-i\vec{k} \cdot \vec{u}'} \phi^\alpha(\vec{u}') b_\alpha(t'), \quad (27)$$

with  $b_\alpha$  an annihilation operator for the quark and  $\vec{k} = g_\omega^q \omega(\vec{R}) \hat{u}' \sinh \xi$ , which ensures the correct momentum for a particle in the vector field. Since the quark field satisfies

$$-i\gamma^0 \vec{\gamma} \cdot \vec{\nabla} \psi_q' = -i\gamma^0 \vec{\gamma} \cdot \vec{k} \psi_q' + \left( \frac{\Omega_\alpha}{R_B} - m_q^* \gamma^0 \right) \psi_q', \quad (28)$$

the free Hamiltonian and momentum operators are, respectively

$$H_0 = \sum_\alpha \left( \frac{\Omega_\alpha}{R_B} \right) b_\alpha^\dagger b_\alpha - \sum_{\alpha\beta} \langle \alpha | (g_\sigma^q \sigma(\vec{R}) - m_q + m_q^*) \gamma_0 | \beta \rangle b_\alpha^\dagger b_\beta + \hat{N}_q g_\omega^q \omega(\vec{R}) \cosh \xi + BV_B, \quad (29)$$

$$\vec{P} = \sum_{\alpha\beta} \langle \alpha | -i\vec{\nabla} | \beta \rangle b_\alpha^\dagger b_\beta - \hat{N}_q \vec{k}, \quad (30)$$

where  $\hat{N}_q (= \sum_\alpha b_\alpha^\dagger b_\alpha)$  is the quark number operator and

$$\langle \alpha | A | \beta \rangle = \int_{V_B} d\vec{u}' \phi^{\alpha\dagger}(\vec{u}') A \phi^\beta(\vec{u}'). \quad (31)$$

Choosing an effective quark mass as  $m_q^* = m_q - g_\sigma^q \sigma(\vec{R})$ , we find the leading part of the energy and momentum operators in the IRF

$$H_0^I = \sum_\alpha \frac{\Omega_\alpha(\vec{R})}{R_B} b_\alpha^\dagger b_\alpha + \hat{N}_q g_\omega^q \omega(\vec{R}) \cosh \xi + BV_B, \quad (32)$$

$$\vec{P}^I = \sum_{\alpha\beta} \langle \alpha | -i\vec{\nabla} | \beta \rangle b_\alpha^\dagger b_\beta - \hat{N}_q g_\omega^q \omega(\vec{R}) \hat{u}' \sinh \xi, \quad (33)$$

where the frequency  $\Omega$  depends on  $\vec{R}$  because the effective quark mass varies, depending on position through the  $\sigma$  field. If we quantize the  $b_\alpha$  in the usual way, the unperturbed Hamiltonian is diagonalized by number states  $|N_\alpha, N_\beta, \dots\rangle$  with  $N_\alpha$  the eigenvalue of the number operator  $b_\alpha^\dagger b_\alpha$  for the mode  $\{\alpha\}$ . Since we suppose that the nucleon should be described in terms of the three quarks in the lowest mode ( $\alpha = 0$ ) and should remain in that configuration as  $\vec{R}$  changes in matter, the gradient term in the momentum operator becomes zero because of parity conservation. Then, we obtain the energy and momentum in the IRF as

$$E_0^I = M_N^*(\vec{R}) + 3g_\omega^q \omega(\vec{R}) \cosh \xi, \quad (34)$$

$$\vec{P}^I = -3g_\omega^q \omega(\vec{R}) \hat{v} \sinh \xi, \quad (35)$$

with the effective nucleon mass

$$M_N^*(\vec{R}) = \frac{3\Omega_0(\vec{R})}{R_B} + BV_B. \quad (36)$$

Since we are treating the corrections to leading order in the velocity, the Lorentz transformation simply provides the expressions for the leading terms in the energy and momentum in the NRF as

$$E_0 = M_N^*(\vec{R}) \cosh \xi + 3g_\omega^q \omega(\vec{R}), \quad (37)$$

$$\vec{P} = M_N^*(\vec{R}) \vec{v} \sinh \xi. \quad (38)$$

This implies

$$E_0 = \sqrt{M_N^{*2}(\vec{R}) + \vec{P}^2} + 3g_\omega^q \omega(\vec{R}). \quad (39)$$

As usual, we here parameterize the sum of the center of mass (c.m.) correction and gluon fluctuation corrections to the bag energy by the familiar form,  $-z_0/R_B$ , where  $z_0$  is assumed to be *independent* of the nuclear density (see the next subsection). Then, the effective nucleon mass in matter takes the form

$$M_N^*(\vec{R}) = \frac{3\Omega_0(\vec{R}) - z_0}{R_B} + BV_B, \quad (40)$$

and the equilibrium condition is required as

$$\frac{dM_N^*(\vec{R})}{dR_B} = 0. \quad (41)$$

This is again justified by the Born-Oppenheimer approximation, according to which the internal structure of the nucleon has enough time to adjust the varying external field so as to stay in its ground state. We emphasize that the effective nucleon mass depends on position only through the scalar field. This result does not depend on the specific model of the nucleon, but is correct in *any* quark model in which the nucleon contains relativistic quarks which are linearly coupled to Lorentz-scalar and vector fields.

### 2.1.3 Correction due to the center of mass motion

Let us now consider the dependence of the c.m. correction on the external fields [30]. It turns out that this correction is only weakly dependent on the external field strength for the densities of interest. We estimate this c.m. correction for an external scalar field (note that a linearly coupled vector field does not alter the quark structure of the nucleon). Our aim here is not to obtain an exact expression for the c.m. correction to the MIT bag, but only to look for its dependence on the external field. Therefore, it is reasonable that we consider a model where the quark mass grows quadratically with the distance from the center of the bag, instead of the sharp boundary condition for the MIT bag. In this simple estimate, we further assume that the quark number is conserved, which allows us to formulate the problem in the first quantized form.

We now consider a model defined by the following first-quantized Hamiltonian:

$$H_{h.o.} = \sum_i^N \gamma_0(i) (\vec{\gamma}(i) \cdot \vec{p}_i + m(\vec{r}_i)), \quad \vec{p}_i = -i\vec{\nabla}_i, \quad (42)$$

with the quark mass  $m(\vec{r}) = m_q^* + Kr^2$  ( $K$  the strength of the harmonic oscillator potential), where  $m_q^*$  ( $= m_q - g_\sigma^q \sigma$ ) is the effective quark mass in the presence of the external scalar field.

Using the quark number  $N$ , we can define the intrinsic coordinates  $(\vec{\rho}, \vec{\pi})$  as

$$\vec{\pi}_i = \vec{p}_i - \frac{\vec{P}}{N}, \quad \vec{P} = \sum_i \vec{p}_i, \quad \sum_i \vec{\pi}_i = 0, \quad (43)$$

$$\vec{\rho}_i = \vec{r}_i - \vec{R}, \quad \vec{R} = \frac{1}{N} \sum_i \vec{r}_i, \quad \sum_i \vec{\rho}_i = 0. \quad (44)$$

Then we can separate the Hamiltonian into two pieces;

$$H_{h.o.} = H_{intr.} + H_{c.m.}, \quad (45)$$

$$H_{intr.} = \sum_i \gamma_0(i) (\vec{\gamma}(i) \cdot \vec{\pi}_i + m(\vec{\rho}_i)), \quad (46)$$

$$H_{c.m.} = \frac{\vec{P}}{N} \cdot \sum_i \gamma_0(i) \vec{\gamma}(i) + \sum_i \gamma_0(i) (m(\vec{r}_i) - m(\vec{\rho}_i)). \quad (47)$$

Here we note that the intrinsic Hamiltonian,  $H_{intr.}$ , commutes with the total momentum,  $\vec{P}$ , and the coordinate of the center of mass,  $\vec{R}$ , and that  $[H_{c.m.}, \vec{R}] = -i \sum_i \gamma_0(i) \vec{\gamma}(i)$ , where the r.h.s. can be identified with the time derivative of  $\vec{R}$ .

Now all we know are the eigenstates of  $H_{h.o.}$ , but we can consider  $H_{c.m.}$  as a correction of order  $1/N$  with respect to the leading term in the total energy. Therefore, we calculate its effect in first order perturbation method, that is

$$E_{intr.} = E_{h.o.} - E_{c.m.} = E_{h.o.} - \langle A | H_{c.m.} | A \rangle, \quad (48)$$

where  $|A\rangle$  is the eigenstate with its energy  $E_A$ . Thus, the energy due to the c.m. correction is

$$E_{c.m.} = \langle A | \frac{\vec{P}}{N} \cdot \sum_i \gamma_0(i) \vec{\gamma}(i) + 2K\vec{R} \cdot \sum_i \gamma_0(i) \vec{r}_i - K\vec{R}^2 \sum_i \gamma_0(i) | A \rangle. \quad (49)$$

Let  $|\alpha\rangle$  be the one body solutions, that is

$$\gamma_0(\vec{\gamma} \cdot \vec{p} + m(\vec{r})) \phi_\alpha = \Omega_\alpha \phi_\alpha. \quad (50)$$

Supposing that all the quarks are in the lowest mode, we then find

$$E_{c.m.} = \Omega_0 - m_q^* \langle 0 | \gamma_0 | 0 \rangle + K \langle 0 | \gamma_0 r^2 | 0 \rangle - \langle 0 | \gamma_0 | 0 \rangle \langle 0 | r^2 | 0 \rangle + \mathcal{O}(1/N). \quad (51)$$

To determine the wave function we solve Eq. (50) numerically and adjust the potential strength  $K$  so as to give  $\Omega_0 = 2.04$ , i.e., the lowest energy of the free bag (in units of the bag radius  $R_B = 1$  fm). We then find  $K = 1.74$ . We can now compute  $E_{c.m.}$  numerically (see Eq. (51)) as a function of  $m_q^*$ . We find that in the region of  $-1.5 < m_q^* < 0$  the value of  $E_{c.m.}$  is almost constant and its dependence on the external scalar field is very weak. Thus, for practical purposes, it is a very reasonable approximation to ignore the dependence of  $E_{c.m.}$  on the external field [30].

#### 2.1.4 Correction due to $H_1$ and Thomas precession

Here we return to the Hamiltonian Eq. (17) and estimate the perturbation term,  $H_1$  (Eq. (20)). Expanding the scalar and vector fields,  $\sigma(\vec{R} + \vec{u}')$  and  $\omega(\vec{R} + \vec{u}')$ , in powers of  $\vec{u}'$

$$\sigma(\vec{R} + \vec{u}') = \sigma(\vec{R}) + \vec{u}' \cdot \vec{\nabla}_R \sigma(\vec{R}) + \dots, \quad (52)$$

$$\omega(\vec{R} + \vec{u}') = \omega(\vec{R}) + \vec{u}' \cdot \vec{\nabla}_R \omega(\vec{R}) + \dots, \quad (53)$$

and computing the effect up to first order,  $H_1$  is given by

$$H_1 = \int_{V_B} d\vec{u}' \bar{\psi}_q' \vec{\gamma} \psi_q'(t', \vec{u}') \cdot \hat{v} g_\omega^q \sinh \xi \vec{u}' \cdot \vec{\nabla}_R \omega(\vec{R}), \quad (54)$$

where the scalar term and the vector term including  $\gamma_0$  vanish because of parity conservation. Then, the perturbation can be rewritten as

$$\langle (0)^3 | H_1 | (0)^3 \rangle = g_\omega^q \sum_{\alpha\beta} \langle (0)^3 | b_\alpha^\dagger b_\beta | (0)^3 \rangle \langle \alpha | \gamma_0 \vec{\gamma} \cdot \hat{v} \vec{u}' \sinh \xi | \beta \rangle \cdot \vec{\nabla}_R \omega(\vec{R}), \quad (55)$$

where we set  $\{\alpha\} = \{0, m_\alpha\}$  with  $m_\alpha$  the spin projection of the quark in the lowest mode  $\{0\}$ . Then, we find

$$\begin{aligned} \langle \alpha | \gamma_0 \vec{\gamma} \cdot \hat{v} \vec{u}' | \beta \rangle &= \int d\vec{u}' \phi^{0m_\alpha*} \gamma_0 (\vec{\gamma} \cdot \hat{v}) \vec{u}' \phi^{0m_\beta}, \\ &= -I(\vec{R}) \langle m_\alpha | \frac{\vec{\sigma}}{2} | m_\beta \rangle \times \hat{v}, \end{aligned} \quad (56)$$

with

$$I(\vec{R}) = \frac{4}{3} \int du' u'^3 f(u') g(u'), \quad (57)$$

where  $u' = |\vec{u}'|$ , and  $f$  and  $g$  are respectively the upper and lower components of the quark wave function and the factor  $4/3$  comes from the angular part of the integral with respect to  $\vec{u}'$ . If we use the wave function of the MIT bag, we find

$$I(\vec{R}) = \frac{R_B}{3} \left[ \frac{4\Omega_0 + 2m_q^* R_B - 3}{2\Omega_0(\Omega_0 - 1) + m_q^* R_B} \right]. \quad (58)$$

This integral,  $I(\vec{R})$ , depends on  $\vec{R}$  through the implicit dependences of the bag radius and eigenvalue on the local scalar field. Its value can be related to the nucleon magnetic moment  $\vec{\mu}$ :

$$\vec{\mu} = \frac{1}{2} \int d\vec{r} \vec{r} \times \psi_q^\dagger(r) \vec{\alpha} \psi_q(r). \quad (59)$$

The values of  $I$  in the free case,  $I_0$ , may then be expressed in terms of the nucleon isoscalar magnetic moment:  $I_0 = 3\mu_s/M_N$  with  $\mu_s = \mu_p + \mu_n$  and  $\mu_p = 2.79$  and  $\mu_n = -1.91$  the experimental values (all in units of  $\mu_N$ ). Using this value,  $H_1$  is rewritten by

$$\langle (0)^3 | H_1 | (0)^3 \rangle = \mu_s \left[ \frac{I(\vec{R}) M_N^*(\vec{R})}{I_0 M_N} \right] \frac{1}{M_N^{*2}(\vec{R}) R} \left[ \frac{d}{dR} 3g_\omega^q \omega(\vec{R}) \right] \vec{S} \cdot \vec{L}, \quad (60)$$

with  $\vec{S}$  the nucleon spin operator and  $\vec{L}$  its angular momentum.

This spin-orbit interaction is nothing but the interaction of the magnetic moment of the nucleon with the "magnetic" field of the  $\omega$  meson seen from the rest frame of the nucleon. This induces a rotation of the spin as a function of time. However, even if  $\mu_s$  were zero, the spin would nevertheless rotate because of Thomas precession [49], which is a relativistic effect independent of the structure

$$H_{prec} = -\frac{1}{2} \vec{v} \times \frac{d\vec{v}}{dt} \cdot \vec{S}, \quad (61)$$

where the acceleration up to lowest order in the velocity is given by

$$\frac{d\vec{v}}{dt} = -\frac{1}{M_N^*(\vec{R})} \vec{\nabla} [M_N^*(\vec{R}) + 3g_\omega^q \omega(\vec{R})]. \quad (62)$$

Combining this precession and the effect of  $H_1$ , we finally get the total spin orbit interaction to first order in the velocity

$$H_1 + H_{prec} = V_{s.o.}(\vec{R}) \vec{S} \cdot \vec{L}, \quad (63)$$

where

$$V_{s.o.}(\vec{R}) = -\frac{1}{2M_N^{*2}(\vec{R}) R} \left[ \left( \frac{d}{dR} M_N^*(\vec{R}) \right) + (1 - 2\mu_s \eta_s(\vec{R})) \left( \frac{d}{dR} 3g_\omega^q \omega(\vec{R}) \right) \right], \quad (64)$$

and

$$\eta_s(\vec{R}) = \frac{I(\vec{R}) M_N^*(\vec{R})}{I_0 M_N}. \quad (65)$$

### 2.1.5 Total Hamiltonian in the mean fields

It is not difficult to introduce the neutral  $\rho$  meson field. In the mean field approximation, only the neutral component is active. The interaction Lagrangian density may then be given by

$$\mathcal{L}_I^\rho = -g_\rho^q \bar{\psi}_q \gamma_\mu \frac{\tau_3}{2} \psi_q(u') \rho_I^\mu(u'), \quad (66)$$

where  $\rho_I^\mu$  is the neutral  $\rho$ -meson field in the IRF and  $\tau_3$  is the the third component of Pauli matrix acting on the quark field. If the mean field value of the time component of the  $\rho$  field is denoted by  $b(\vec{R})$  in the NRF, one can transpose the results for the  $\omega$  field. The only difference between the two fields comes from trivial isospin factors

$$3g_\omega^q \rightarrow g_\rho^q \frac{\tau_3^N}{2}, \quad \mu_s \rightarrow \mu_v = \mu_p - \mu_n, \quad (67)$$

where  $\tau_3^N/2$  is the nucleon isospin operator.

Because, in the NRF,  $E = \cosh \xi E^I + \sinh \xi P_L^I$  and  $P_L = \cosh \xi P_L^I + \sinh \xi E^I$ , one finally finds that the NRF energy-momentum of the nucleon moving in the meson fields is

$$E = M_N^*(\vec{R}) \cosh \xi + V(\vec{R}), \quad (68)$$

$$\vec{P} = M_N^*(\vec{R}) \hat{v} \sinh \xi, \quad (69)$$

with

$$V(\vec{R}) = V_c(\vec{R}) + V_{s.o.}(\vec{R}) \vec{S} \cdot \vec{L}, \quad (70)$$

$$V_c(\vec{R}) = 3g_\omega^q \omega(\vec{R}) + g_\rho^q \frac{\tau_3^N}{2} b(\vec{R}), \quad (71)$$

$$V_{s.o.} = -\frac{1}{2M_N^{*2}(\vec{R})R} \left( \Delta_\sigma + (1 - 2\mu_s \eta_s(\vec{R})) \Delta_\omega + (1 - 2\mu_v \eta_v(\vec{R})) \frac{\tau_3^N}{2} \Delta_\rho \right), \quad (72)$$

and

$$\Delta_\sigma = \frac{d}{dR} M_N^*(\vec{R}), \quad \Delta_\omega = \frac{d}{dR} 3g_\omega^q(\vec{R}), \quad \Delta_\rho = \frac{d}{dR} g_\rho^q(\vec{R}). \quad (73)$$

For a point-like nucleon, one has  $\mu_s = 1$  while the physical value is  $\mu_s = 0.88$ . Thus, in so far as the  $\omega$  contribution to the spin-orbit force is concerned, the point-like result has no problem. But, this is not the case for the  $\rho$  contribution, because we still have  $\mu_v = 1$  for the point-like particle but the observed value is  $\mu_v = 4.7$ . This structure is included in a very natural way in the QMC model.

Now let us consider how the model is quantized in the non-relativistic framework. Until now the motion of the nucleon has been treated as classical, but it is necessary to quantize it. The simple way to proceed may be to find a Lagrangian which can realize the energy-momentum expressions Eqs. (68) and (69). If we keep only terms up to those quadratic in the velocity, we find that the Lagrangian

$$L(\vec{R}, \vec{v}) = -M_N^*(\vec{R}) \sqrt{1 - v^2} - V_c(\vec{R}), \quad (74)$$

can produce the energy and momentum. Here we drop the spin dependent correction since it already involves the velocity. Then, the non-relativistic expression of the Lagrangian may be

$$L_{nr}(\vec{R}, \vec{v}) = \frac{1}{2} M_N^*(\vec{R}) v^2 - M_N^*(\vec{R}) - V_c(\vec{R}), \quad (75)$$

which leads to the Hamiltonian

$$H_{nr}(\vec{R}, \vec{P}) = \vec{P} \cdot \frac{1}{2M_N^*(\vec{R})} \vec{P} + M_N^*(\vec{R}) + V(\vec{R}), \quad (76)$$

where the spin-orbit interaction is re-inserted in  $V(\vec{R})$ . Thus, the nuclear, quantum Hamiltonian for the nucleus with atomic number  $A$  is given by

$$H_{nr} = \sum_{i=1}^A H_{nr}(\vec{R}_i, \vec{P}_i), \quad \vec{P}_i = -i\vec{\nabla}_i. \quad (77)$$

### 2.1.6 Equations for the meson fields

The equations of motion for the meson-field operators ( $\hat{\sigma}$ ,  $\hat{\omega}^\nu$ ,  $\hat{\rho}^\nu$ ) are given by

$$(\partial_\mu \partial^\mu + m_\sigma^2) \hat{\sigma} = g_\sigma^q \bar{\psi}_q \psi_q, \quad (78)$$

$$(\partial_\mu \partial^\mu + m_\omega^2) \hat{\omega}^\nu = g_\omega^q \bar{\psi}_q \gamma^\nu \psi_q, \quad (79)$$

$$(\partial_\mu \partial^\mu + m_\rho^2) \hat{\rho}^\nu = g_\rho^q \bar{\psi}_q \gamma^\nu \frac{\tau_3}{2} \psi_q, \quad (80)$$

where  $m_\sigma$ ,  $m_\omega$  and  $m_\rho$  are respectively the masses of  $\sigma$ ,  $\omega$  and (neutral)  $\rho$  mesons. We shall apply the mean field approximation to these meson fields. The mean fields are calculated as the expectation values with respect to the nuclear ground state  $|A\rangle$ :

$$\langle A | \hat{\sigma}(t, \vec{r}) | A \rangle = \sigma(\vec{r}), \quad (81)$$

$$\langle A | \hat{\omega}^\nu(t, \vec{r}) | A \rangle = \delta_{\nu,0} \omega(\vec{r}), \quad (82)$$

$$\langle A | \hat{\rho}^\nu(t, \vec{r}) | A \rangle = \delta_{\nu,0} b(\vec{r}). \quad (83)$$

Next, we need the expressions for the sources in Eqs. (78), (79) and (80)

$$\langle A | \bar{\psi}_q \psi_q(t, \vec{r}) | A \rangle, \quad \langle A | \bar{\psi}_q \gamma^\nu \psi_q(t, \vec{r}) | A \rangle, \quad \langle A | \bar{\psi}_q \gamma^\nu \frac{\tau_3}{2} \psi_q(t, \vec{r}) | A \rangle. \quad (84)$$

Since the sources are given by the sums of the source created by each nucleon in MFA, we can write

$$\bar{\psi}_q \psi_q(t, \vec{r}) = \sum_i \langle \bar{\psi}_q \psi_q(t, \vec{r}) \rangle_i, \quad \bar{\psi}_q \gamma^\nu \psi_q(t, \vec{r}) = \sum_i \langle \bar{\psi}_q \gamma^\nu \psi_q(t, \vec{r}) \rangle_i, \quad (85)$$

where  $\langle \dots \rangle_i$  is the matrix element in the nucleon  $i$  located at  $\vec{R}$  at time  $t$ . (For a while, we shall not present the expression of the source for the  $\rho$  meson because it is the same as that for the  $\omega$  except for trivial isospin factor.) Because we apply the Born-Oppenheimer approximation within the model, the sources are given by 3 quarks in the lowest state. In the IRF, one finds

$$\langle \bar{\psi}_q' \psi_q'(t', \vec{r}') \rangle_i = 3 \sum_m \bar{\phi}_i^{0,m}(\vec{u}') \phi_i^{0,m}(\vec{u}') \equiv 3s_i(\vec{u}'), \quad (86)$$

$$\langle \bar{\psi}_q' \gamma^\nu \psi_q'(t', \vec{r}') \rangle_i = 3\delta_{\nu,0} \sum_m \phi_i^{\dagger 0,m}(\vec{u}') \phi_i^{0,m}(\vec{u}') \equiv 3\delta_{\nu,0} w_i(\vec{u}'). \quad (87)$$

Note that the space component of the vector field vanishes because of parity conservation.

The Lorentz transformation between the IRF and NRF leads to

$$u'_{i,L} = (r_L - R_{i,L}) \cosh \xi_i, \quad \vec{u}'_{i,\perp} = \vec{r}_\perp - \vec{R}_{i,\perp}, \quad (88)$$

at the common time  $t$  in the NRF. Because of the Lorentz-scalar and vector characters, the sources are rewritten in the NRF as

$$\langle \bar{\psi}_q \psi_q(t, \vec{r}) \rangle_i = 3s_i((r_L - R_{i,L}) \cosh \xi_i, \vec{r}_\perp - \vec{R}_{i,\perp}), \quad (89)$$

$$\langle \bar{\psi}_q \gamma^0 \psi_q(t, \vec{r}) \rangle_i = 3w_i((r_L - R_{i,L}) \cosh \xi_i, \vec{r}_\perp - \vec{R}_{i,\perp}) \cosh \xi_i, \quad (90)$$

$$\langle \bar{\psi}_q \vec{\gamma} \psi_q(t, \vec{r}) \rangle_i = 3w_i((r_L - R_{i,L}) \cosh \xi_i, \vec{r}_\perp - \vec{R}_{i,\perp}) \hat{v} \sinh \xi_i. \quad (91)$$

$$(92)$$

These sources can be transformed

$$\langle \bar{\psi}_q \psi_q(t, \vec{r}) \rangle_i = \frac{3}{(2\pi)^3 \cosh \xi_i} \int d\vec{k} e^{i\vec{k} \cdot (\vec{r} - \vec{R}_i)} S(\vec{k}, \vec{R}_i), \quad (93)$$

$$\langle \bar{\psi}_q \gamma^0 \psi_q(t, \vec{r}) \rangle_i = \frac{3}{(2\pi)^3} \int d\vec{k} e^{i\vec{k} \cdot (\vec{r} - \vec{R}_i)} W(\vec{k}, \vec{R}_i), \quad (94)$$

$$\langle \bar{\psi}_q \vec{\gamma} \psi_q(t, \vec{r}) \rangle_i = \frac{3}{(2\pi)^3} \hat{v} \int d\vec{k} e^{i\vec{k} \cdot (\vec{r} - \vec{R}_i)} W(\vec{k}, \vec{R}_i), \quad (95)$$

with the sources in momentum space

$$S(\vec{k}, \vec{R}_i) = \int d\vec{u} e^{-i(\vec{k}_\perp \cdot \vec{u}_\perp + k_L u_L / \cosh \xi_i)} s_i(\vec{u}), \quad (96)$$

$$W(\vec{k}, \vec{R}_i) = \int d\vec{u} e^{-i(\vec{k}_\perp \cdot \vec{u}_\perp + k_L u_L / \cosh \xi_i)} w_i(\vec{u}). \quad (97)$$

Thus, the mean field expressions for the meson sources are given by

$$\langle A | \bar{\psi}_q \psi_q(t, \vec{r}) | A \rangle = \frac{3}{(2\pi)^3} \int d\vec{k} e^{i\vec{k} \cdot \vec{r}} \langle A | \sum_i (\cosh \xi_i)^{-1} e^{-i\vec{k} \cdot \vec{R}_i} S(\vec{k}, \vec{R}_i) | A \rangle, \quad (98)$$

$$\langle A | \bar{\psi}_q \gamma^0 \psi_q(t, \vec{r}) | A \rangle = \frac{3}{(2\pi)^3} \int d\vec{k} e^{i\vec{k} \cdot \vec{r}} \langle A | \sum_i e^{-i\vec{k} \cdot \vec{R}_i} W(\vec{k}, \vec{R}_i) | A \rangle, \quad (99)$$

$$\langle A | \bar{\psi}_q \vec{\gamma} \psi_q(t, \vec{r}) | A \rangle = 0. \quad (100)$$

Note that the velocity vector averages to zero.

The matrix element,  $\langle A | \sum_i \exp(-i\vec{k} \cdot \vec{R}_i) \cdots | A \rangle$ , in Eqs. (98) and (99) only remains when  $k$  is less than, or of order of the inverse of the nuclear radius. Furthermore, since  $u$  is bounded by the nucleon size, the argument of the exponential in Eqs. (96) and (97) can be ignored when the model is applied to large enough nuclei. In this approximation, we can simplify the sources further

$$\langle A | \bar{\psi}_q \psi_q(t, \vec{r}) | A \rangle = 3S(\vec{r})\rho_s(\vec{r}), \quad (101)$$

$$\langle A | \bar{\psi}_q \gamma^\nu \psi_q(t, \vec{r}) | A \rangle = 3\delta_{\nu,0}\rho_B(\vec{r}), \quad (102)$$

$$\langle A | \bar{\psi}_q \gamma^\nu \frac{\tau_3}{2} \psi_q(t, \vec{r}) | A \rangle = \delta_{\nu,0}\rho_3(\vec{r}), \quad (103)$$

with the scalar, baryon and isospin densities of the nucleon in the nucleus

$$\rho_s(\vec{r}) = \langle A | \sum_i \frac{M_N^*(\vec{R}_i)}{E_i - V(\vec{R}_i)} \delta(\vec{r} - \vec{R}_i) | A \rangle, \quad (104)$$

$$\rho_B(\vec{r}) = \langle A | \sum_i \delta(\vec{r} - \vec{R}_i) | A \rangle, \quad (105)$$

$$\rho_3(\vec{r}) = \langle A | \sum_i \frac{\tau_3^N}{2} \delta(\vec{r} - \vec{R}_i) | A \rangle. \quad (106)$$

Here we deduced the source for the  $\rho$  meson (the isospin density,  $\rho_3$ ) from that for the  $\omega$ . In Eq. (101),  $S(\vec{r})$  for the  $i$ -th nucleon (at  $\vec{r}$ ) is given by

$$S(\vec{r}) = S(\vec{0}, \vec{r}) = \int d\vec{u} s_i(\vec{u}) = \frac{\Omega_0/2 + m_q^* R_B (\Omega_0 - 1)}{\Omega_0 (\Omega_0 - 1) + m_q^* R_B / 2}, \quad (107)$$

in the MIT bag model. This has an implicit coordinate dependence through the local scalar field at  $\vec{r}$ .

Since these sources are time independent, the equations for the meson fields are finally given by

$$(-\nabla_r^2 + m_\sigma^2)\sigma(\vec{r}) = g_\sigma C(\vec{r})\rho_s(\vec{r}), \quad (108)$$

$$(-\nabla_r^2 + m_\omega^2)\omega(\vec{r}) = g_\omega \rho_B(\vec{r}), \quad (109)$$

$$(-\nabla_r^2 + m_\rho^2)\rho(\vec{r}) = g_\rho \rho_3(\vec{r}), \quad (110)$$

where the meson-nucleon coupling constants and  $C$  are respectively defined by

$$g_\sigma = 3g_\sigma^q S(\sigma = 0), \quad g_\omega = 3g_\omega^q, \quad g_\rho = g_\rho^q, \quad C(\vec{r}) = S(\vec{r})/S(\sigma = 0). \quad (111)$$

Thus, the mean fields carry the energy

$$E_{meson} = \frac{1}{2} \int d\vec{r} [(\vec{\nabla}\sigma)^2 + m_\sigma^2 \sigma^2 - (\vec{\nabla}\omega)^2 - m_\omega^2 \omega^2 - (\vec{\nabla}b)^2 - m_\rho^2 b^2]. \quad (112)$$



### 2.1.7 Self-consistent procedure

Let us summarize the model and review the procedure for the self-consistent calculation for finite nuclei:

1. Choose the bare quark mass,  $m_q$ , and construct a quark model of the nucleon so as to produce the free nucleon properties. For example, if we take the MIT bag model, the bag parameters,  $B$  and  $z_0$ , are fixed to fit the free nucleon mass and the bag radius.
2. Assume that the coupling constants and the masses of the mesons are known.
3. Calculate the nucleon properties,  $I(\sigma)$  (Eq. (57)) and  $S(\sigma)$  (Eq. (107)), at a given value of  $\sigma$ .
4. Guess initial forms of the densities,  $\rho_s(\vec{r})$ ,  $\rho_B(\vec{r})$ ,  $\rho_3(\vec{r})$ , in Eqs. (104)-(106).
5. For  $\rho_s(\vec{r})$ ,  $\rho_B(\vec{r})$  and  $\rho_3(\vec{r})$  fixed, solve Eqs. (108)-(110) for the meson fields.
6. Evaluate the effective nucleon mass,  $M_N^*$ , in the nucleus (for example, Eq. (40)) and the potential,  $V(\vec{r})$  (Eq. (70)). If we take the MIT bag model, the bag radius at each position in the nucleus is determined by the equilibrium condition, Eq. (41). For practical purposes, it is very convenient to make simple parameterizations for  $M_N^*$  and  $C(\vec{r})$  as functions of the value of the  $\sigma$  field at given position  $\vec{r}$ . The bag model enables us to make parameterizations which work very well at moderate densities (see section 3).
7. Solve the eigenvalue problem given by the nuclear Hamiltonian Eq. (77) and compute the shell states from which the densities,  $\rho_s(\vec{r})$ ,  $\rho_B(\vec{r})$ ,  $\rho_3(\vec{r})$ , can be evaluated.
8. Go to 5 and iterate until self-consistency is achieved.

## 2.2 Relativistic model

### 2.2.1 Relativistic treatment

To facilitate a comparison between QMC and the widely used Quantum Hadrodynamics (QHD) [17], we reformulate the model as a relativistic field theory [19, 30]. We make no attempt to justify the formulation of a local, relativistic field theory at a fundamental level because it is not possible for composite hadrons. Our point is to try to express the present idea in the framework of relativistic field theory at the mean field level. To do so, we first write a relativistic Lagrangian and check that it is equivalent to the non-relativistic formulation in an appropriate approximation. Since it is vital to consider the  $\sigma$  and  $\omega$  fields but less important to include the  $\rho$  field in a (isospin) symmetric nuclear medium, once again we omit the  $\rho$  contribution for a while.

Our basic result is that essentially the nucleon in a nuclear medium can be treated as a point-like particle with the effective mass  $M_N^*(\sigma(\vec{r}))$ , which depends on position through the local scalar field, moving in the vector potential  $g_\omega\omega(\vec{r})$ . Since, as already pointed out, the spin-orbit force due to the  $\omega$  is almost equivalent to that of a point-like Dirac nucleon, a possible Lagrangian density for the symmetric nuclear system may be written as

$$\mathcal{L} = \bar{\psi}[i\gamma \cdot \partial - M_N^*(\hat{\sigma}) - g_\omega\hat{\omega}^\mu\gamma_\mu]\psi + \mathcal{L}_{meson}, \quad (113)$$

where  $\psi$ ,  $\hat{\sigma}$  and  $\hat{\omega}$  are respectively the nucleon,  $\sigma$  and  $\omega$  field operators. The free meson Lagrangian density is

$$\mathcal{L}_{meson} = \frac{1}{2}(\partial_\mu\hat{\sigma}\partial^\mu\hat{\sigma} - m_\sigma^2\hat{\sigma}^2) - \frac{1}{2}\partial_\mu\hat{\omega}_\nu(\partial^\mu\hat{\omega}^\nu - \partial^\nu\hat{\omega}^\mu) + \frac{1}{2}m_\omega^2\hat{\omega}^\mu\hat{\omega}_\mu. \quad (114)$$

If we separate the effective nucleon mass as

$$M_N^*(\hat{\sigma}) = M_N - g_\sigma(\hat{\sigma})\hat{\sigma}, \quad (115)$$

and define the  $\sigma$ -field dependent (or position dependent) coupling constant,  $g_\sigma(\hat{\sigma})$ , one can check that  $g_\sigma(\sigma = 0)$  is the same as  $g_\sigma$  defined in Eq. (111). Furthermore, if we rewrite the Lagrangian density

$$\mathcal{L} = \bar{\psi}[i\gamma \cdot \partial - M_N + g_\sigma(\hat{\sigma})\hat{\sigma} - g_\omega\hat{\omega}^\mu\gamma_\mu]\psi + \mathcal{L}_{meson}, \quad (116)$$

it is very clear that the difference between the present model and QHD lies only in the fact that the substructure effect of the nucleon provides a *known* dependence of the scalar meson-nucleon coupling constant on the scalar field itself in a nuclear medium. It should be stressed that this dependence is not the same as that adopted in recent density-dependent hadron field theories [50], in which the meson-nucleon vertices are *assumed* to *phenomenologically* depend on the baryonic densities.

In MFA, we can replace the meson-field operators by their expectation values in the Lagrangian:  $\hat{\sigma} \rightarrow \sigma(\vec{r})$  and  $\hat{\omega}^\mu(\vec{r}) \rightarrow \delta_{\mu,0}\omega(\vec{r})$ . Then, the nucleon and meson fields satisfy the following equations:

$$(i\gamma \cdot \partial - M_N^*(\sigma) - g_\omega \gamma_0 \omega) \psi = 0, \quad (117)$$

$$(-\nabla_r^2 + m_\sigma^2) \sigma(\vec{r}) = - \left( \frac{\partial}{\partial \sigma} M_N^*(\sigma) \right) \langle A | \bar{\psi} \psi(\vec{r}) | A \rangle, \quad (118)$$

$$(-\nabla_r^2 + m_\omega^2) \omega(\vec{r}) = g_\omega \langle A | \psi^\dagger \psi(\vec{r}) | A \rangle, \quad (119)$$

where the derivative of the effective nucleon mass with respect to the scalar field is the response of the nucleon to the external scalar field - the so-called *scalar polarizability*. That is given in terms of the scalar density of a quark in the nucleon  $S(\sigma(\vec{r}))$  in Eq. (107):

$$\frac{d}{d\sigma} M_N^*(\sigma) = -C(\sigma) g_\sigma(\sigma=0) = -\frac{d}{d\sigma} (g_\sigma(\sigma) \sigma). \quad (120)$$

Note also that the sources in the r.h.s. of Eqs. (118) and (119) are, respectively, equal to the previously defined scalar ( $\rho_s$ ) and baryon ( $\rho_B$ ) sources.

It is possible to see that the present relativistic formulation can go back to the previous non-relativistic one (without the  $\rho$  coupling) under the following conditions: (1) only terms of second order in the velocity are kept, (2) second derivatives of the meson fields are ignored, (3) each field is small in comparison with the nucleon mass, (4) the isoscalar magnetic moment,  $\mu_s$ , is supposed to be unity.

To describe a nucleus with different numbers of protons and neutrons ( $Z \neq N$ ), it is necessary to include the  $\rho$ -meson contribution. Any realistic treatment of nuclear structure also requires the Coulomb interaction. Thus, an interaction Lagrangian density to be added to Eq. (116) at the quark level may be

$$\mathcal{L}_{\rho+\gamma} = -\bar{\psi}_q \left[ g_\rho^q \frac{\tau_3}{2} \gamma_\mu \rho^\mu - e \left( \frac{1}{6} + \frac{\tau_3}{2} \right) \gamma_\mu A^\mu \right] \psi_q, \quad (121)$$

(see also Eq. (66)). We saw in the previous section that this leads to both a central and spin-orbit potential for the nucleon in the NRF. Furthermore, for the isoscalar  $\omega$  contribution the potentials are well represented by a (point)  $\omega$ -nucleon coupling. However, for the  $\rho$ , the relativistic formulation *at the nucleon level* requires a strong tensor coupling ( $\sim \sigma^{\mu\nu} q_\nu$ ) if it is to reproduce the large isovector magnetic moment ( $\mu_v = 4.7$ ). In the present stage, we follow the usual procedure adopted in the Hartree treatment of QHD, namely, we only use a vector coupling for the  $\rho$ , with its coupling adjusted to give the bulk symmetry energy in MFA. (More precise discussion for the inclusion of the  $\rho$  meson remains as a future problem.) In this case, it is easy to get the expressions for the  $\rho$  and Coulomb fields by including trivial isospin factors:  $3g_\omega^q \omega(\vec{r}) \rightarrow g_\rho(\tau_3^N/2) b(\vec{r})$  or  $\rightarrow (e/2)(1 + \tau_3^N) A(\vec{r})$ . This is the first, relativistic version of the quark-meson coupling model - we shall call this QMC-I.

In summary, our effective Lagrangian density for the QMC-I model in MFA takes the form

$$\begin{aligned} \mathcal{L}_{QMC-I} = & \bar{\psi} [i\gamma \cdot \partial - M_N^*(\sigma(\vec{r})) - g_\omega \omega(\vec{r}) \gamma_0 - g_\rho \frac{\tau_3^N}{2} b(\vec{r}) \gamma_0 - \frac{e}{2} (1 + \tau_3^N) A(\vec{r}) \gamma_0] \psi \\ & - \frac{1}{2} [(\vec{\nabla} \sigma(\vec{r}))^2 + m_\sigma^2 \sigma(\vec{r})^2] + \frac{1}{2} [(\vec{\nabla} \omega(\vec{r}))^2 + m_\omega^2 \omega(\vec{r})^2] \\ & + \frac{1}{2} [(\vec{\nabla} b(\vec{r}))^2 + m_\rho^2 b(\vec{r})^2] + \frac{1}{2} (\vec{\nabla} A(\vec{r}))^2. \end{aligned} \quad (122)$$

The mean field description can be improved by the inclusion of exchange contribution (Fock terms) [51]. The inclusion of Fock terms allows us to explore the momentum dependence of meson-nucleon vertices and the role of pionic degrees of freedom in matter. It has been found that the Fock terms maintain the mean field predictions of the QMC model but that the Fock terms significantly increase the absolute values of the single-particle energy, 4-component scalar and vector potentials. This is particularly relevant for the spin-orbit splitting in finite nuclei (see also section 2.6).

### 2.2.2 Properties of the in-medium nucleon mass

We now consider the properties of the nucleon in a nuclear medium, based on the relativistic formulation developed in the previous section. In general, the Dirac equation for the quark field in matter may be written as (see also Eq. (21))

$$[i\gamma \cdot \partial - (m_q - V_s^q) - V_c(\vec{r}) - \gamma_0 V_v^q]\psi_q(\vec{r}) = 0, \quad (123)$$

where the quark feels the scalar  $V_s^q$  (like the  $\sigma$ ) and vector  $V_v^q$  (like the  $\omega$ ) potentials in nuclear matter, which are self-consistently generated by the medium, while  $V_c$  represents the confinement potential. As discussed in section 2.1.1, the scalar and vector potentials depend on the position of the nucleon, but they may be supposed to be constant inside the nucleon because the potentials do not vary much across it – this is the local density approximation (LDA) (see Ref. [31] for details).

As the nucleon is static, the time-derivative operator in the Dirac equation can be replaced by the quark energy,  $-i\epsilon_q$ . By analogy with the procedure applied to the nucleon in QHD [17], the Dirac equation, Eq. (123), can be rewritten in the same form as that in free space, with the effective quark mass  $m_q^*(= m_q - V_s^q)$  and the energy  $\epsilon^*(= \epsilon_q - V_v^q)$ , instead of  $m_q$  and  $\epsilon_q$  in the free case. In other words, the vector interaction has again *no effect* on the nucleon structure except for an overall phase in the quark wave function, which gives a shift in the nucleon energy. This fact *does not* depend on how to choose the confinement potential  $V_c$ . The nucleon energy (at rest),  $E_N^*$ , in the medium is then expressed by [19, 52]

$$E_N^* = M_N^*(V_s^q) + 3V_v^q, \quad (124)$$

where the effective nucleon mass  $M_N^*$  depends on *only* the scalar potential in the medium, as discussed in the non-relativistic treatment. We here again stress that the basic result in the QMC model is that, in the scalar ( $\sigma$ ) and vector ( $\omega$ ) meson fields, the nucleon behaves essentially as a point-like particle with an effective mass  $M_N^*$ , which depends on the position through only the  $\sigma$  field, moving in a vector potential generated by the  $\omega$  meson. This feature should hold in *any model* in which the nucleon contains *relativistic* quarks and the (middle- and long-range) *attractive* and (short-range) *repulsive* nucleon-nucleon (N-N) forces have *Lorentz-scalar* and *vector* characters, respectively.

We consider the nucleon mass in matter further. The nucleon mass is a function of the scalar field. Because the scalar field is small at low density the nucleon mass can be expanded in terms of  $\sigma$  as

$$M_N^* = M_N + \left(\frac{\partial M_N^*}{\partial \sigma}\right)_{\sigma=0} \sigma + \frac{1}{2} \left(\frac{\partial^2 M_N^*}{\partial \sigma^2}\right)_{\sigma=0} \sigma^2 + \dots \quad (125)$$

In the QMC model, the interaction Hamiltonian between the nucleon and the  $\sigma$  field at the quark level is given by  $H_{int} = -3g_\sigma^q \int d\vec{r} \bar{\psi}_q \sigma \psi_q$ , and the derivative of  $M_N^*$  with respect to  $\sigma$  is thus given by the quark-scalar density in the nucleon,  $-3g_\sigma^q S_N(\sigma)$  (see Eq. (107)). (Hereafter, we add the suffix  $N$  to the scalar density  $S$  and its ratio  $C$  to specify the nucleon.) Because of the negative value of  $\left(\frac{\partial M_N^*}{\partial \sigma}\right)$ , the nucleon mass decreases in matter at low density.

Furthermore, if we use Eq. (120), we find that

$$M_N^* = M_N - g_\sigma \sigma - \frac{1}{2} g_\sigma C'_N(0) \sigma^2 + \dots \quad (126)$$

In general, the scalar-density ratio,  $C_N$ , (or the scalar polarizability) is a decreasing function because the quark in matter is more relativistic than in free space. Thus,  $C'_N(0)$  takes a negative value, and hence the third term in the right hand side of Eq. (126) makes the mass larger. If the nucleon were structureless  $C_N$  would not depend on the scalar field, that is,  $C_N$  would be constant ( $C_N = 1$ ). Therefore, only the first two terms in the right hand side of Eq. (126) remain, which is exactly the same as the equation for the effective nucleon mass in QHD. By taking the heavy-quark-mass limit in QMC we can reproduce the QHD results [13]. We recall that this decrease in  $C_N$  constitutes a new saturation mechanism [10] – different from pure QHD – and is the main reason why the scalar coupling constant is somewhat smaller in QMC than in QHD. Finally, we note that it is possible to relate the mass reduction in the QMC model to the change of quark condensates in matter [13, 53, 54] (see section 3.1.2).

### 2.2.3 Effect of meson structure

Until now, we have studied only the effect of the nucleon substructure. It is, however, true that the mesons are also built of quarks and antiquarks, and that they may also change their properties in a nuclear medium. It may not be so difficult to include such effects in the present model [19]. To incorporate it, we suppose that the vector mesons are again described by a relativistic quark model with *common* scalar and vector mean fields, like the nucleon. Thus, the effective vector meson mass in matter,  $m_v^*(v = \omega, \rho)$ , again depends only on the value of scalar mean field in matter. However, for the  $\sigma$  meson it may not be easy to describe it by a simple quark model (like a bag) because it couples strongly to the pseudoscalar ( $2\pi$ ) channel, which requires a direct treatment of chiral symmetry in a nuclear medium. Since, according to the Nambu–Jona-Lasinio model [55, 56] or the Walecka model [57, 58], one might expect the  $\sigma$ -meson mass in medium  $m_\sigma^*$  to be less than in free space, we shall parameterize it using a quadratic function of the scalar field:

$$\left(\frac{m_\sigma^*}{m_\sigma}\right) = 1 - a_\sigma(g_\sigma\sigma) + b_\sigma(g_\sigma\sigma)^2, \quad (127)$$

with two, additional new parameters  $a_\sigma$  and  $b_\sigma$ .

Using these effective meson masses, one can construct a new Lagrangian density for finite nuclei, which involves the structure effects of not only the nucleons but also the mesons, in the MFA:

$$\begin{aligned} \mathcal{L}_{QMC-II} = & \bar{\psi}[i\gamma \cdot \partial - M_N^* - g_\omega\omega(\vec{r})\gamma_0 - g_\rho\frac{\tau_3^N}{2}b(\vec{r})\gamma_0 - \frac{e}{2}(1 + \tau_3^N)A(\vec{r})\gamma_0]\psi \\ & - \frac{1}{2}[(\vec{\nabla}\sigma(\vec{r}))^2 + m_\sigma^{*2}(\vec{r})\sigma(\vec{r})^2] + \frac{1}{2}[(\vec{\nabla}\omega(\vec{r}))^2 + m_\omega^{*2}(\vec{r})\omega(\vec{r})^2] \\ & + \frac{1}{2}[(\vec{\nabla}b(\vec{r}))^2 + m_\rho^{*2}(\vec{r})b(\vec{r})^2] + \frac{1}{2}(\vec{\nabla}A(\vec{r}))^2, \end{aligned} \quad (128)$$

where the masses of the mesons and the nucleon have a dependence on position through the scalar mean-field. We call this model QMC-II [19].

At low density, the vector-meson mass can be expanded in the similar manner to the nucleon case (Eq. (125)):

$$\begin{aligned} m_v^* &= m_v + \left(\frac{\partial m_v^*}{\partial \sigma}\right)_{\sigma=0} \sigma + \frac{1}{2} \left(\frac{\partial^2 m_v^*}{\partial \sigma^2}\right)_{\sigma=0} \sigma^2 + \dots, \\ &\simeq m_v - 2g_\sigma^q S_v(0)\sigma - g_\sigma^q S_v'(0)\sigma^2, \\ &\equiv m_v - \frac{2}{3}g_\sigma\Gamma_{v/N}\sigma - \frac{1}{3}g_\sigma\Gamma_{v/N}C_v'(0)\sigma^2, \end{aligned} \quad (129)$$

where  $m_v$  is the free mass and  $S_v(\sigma)$  is the quark-scalar density in the vector meson,

$$\left(\frac{\partial m_v^*}{\partial \sigma}\right) = -\frac{2}{3}g_\sigma\Gamma_{v/N}C_v(\sigma), \quad (130)$$

and  $C_v(\sigma) = S_v(\sigma)/S_v(0)$ . In Eqs. (129) and (130), we introduce a correction factor,  $\Gamma_{v/N}$ , which is given by  $S_v(0)/S_N(0)$ , because the coupling constant,  $g_\sigma$ , is defined specifically for the nucleon by Eq. (111).

Although the fields for the vector mesons satisfy the usual equations Eqs. (109) and (110) with their effective masses, instead of the free ones, the equation of motion for the  $\sigma$  is also modified by the effect of meson substructure. Since the quark and antiquark inside the mesons interact with the  $\sigma$  field, the source for the  $\sigma$  is given by not only the derivative of the nucleon mass with respect to  $\sigma$  but also those for the mesons in QMC-II. (Actual expression will be given in section 3.)

### 2.2.4 Naturalness

Here we check whether the concept of "naturalness" applies in the QMC model [22]. In general, an effective field theory at low energy will contain an infinite number of interaction terms, which incorporate the *compositeness* of hadrons. This is expected to involve numerous couplings which may not be renormalizable. Such an EFT requires an organizing principle to make sensible calculations.

Manohar and Georgi [21] have proposed a systematic way to manage such complicated, effective field theories called “naive dimensional analysis” (NDA). NDA gives rules for assigning a coefficient of the appropriate size to any interaction term in an effective Lagrangian. After extracting the dimensional factors and some appropriate counting factors using NDA, the remaining *dimensionless* coefficients are all assumed to be of order *unity*. This is the so-called *naturalness* assumption. If naturalness is valid, the effective Lagrangian can be truncated at a given order with a reasonable bound on the truncation error for physical observables. Then we can control the effective Lagrangian, at least at the tree level.

NDA has been already applied to QHD [25], where it was concluded that the relativistic Hartree approximation (RHA) in QHD leads to *unnaturally* large coefficients due to the treatment of the vacuum in terms of the excitation of  $N\bar{N}$ -pairs. This means that the loop expansion in QHD does not work as well as one would desire [59].

Here we use NDA to see whether the QMC model gives natural coefficients. In brief, NDA tells us the following: for the strong interaction there are two relevant scales, namely, the pion-decay constant  $f_\pi$  ( $= 93$  MeV) and a larger scale,  $\Lambda \sim 1$  GeV, which characterizes the mass scale of physics beyond the Goldstone bosons. The NDA rules indicate how those scales should appear in a given term in the effective Lagrangian. The rules are:

1. include a factor of  $1/f_\pi$  for each strongly interacting field,
2. assign an overall normalization factor of  $(f_\pi\Lambda)^2$ ,
3. multiply by factors of  $1/\Lambda$  to achieve dimension (mass)<sup>4</sup>,
4. include appropriate counting factors, e.g.  $1/n!$  for  $\phi^n$  (where  $\phi$  is a meson field).

Since the QMC Lagrangian in MFA is given in terms of the nucleon ( $\psi$ ), scalar ( $\sigma$ ) and vector ( $\omega$  and  $\rho$ ) meson fields, we can scale a generic Lagrangian component as

$$\mathcal{L} \sim c_{\ell mnp} \frac{1}{m!n!p!} \left( \frac{\bar{\psi}\Gamma(\tau/2)\psi}{f_\pi^2\Lambda} \right)^\ell \left( \frac{\sigma}{f_\pi} \right)^m \left( \frac{\omega}{f_\pi} \right)^n \left( \frac{b}{f_\pi} \right)^p (f_\pi\Lambda)^2, \quad (131)$$

where  $\Gamma$  and  $\tau$  stand for a combination of Dirac matrices and isospin operators. The overall coupling constant  $c_{\ell mnp}$  is dimensionless and of  $\mathcal{O}(1)$  if naturalness holds.

The QMC Lagrangian is given by

$$\mathcal{L}_{QMC} = \mathcal{L}_{free} + \mathcal{L}_{em} + \mathcal{L}_{QMC}^{int}, \quad (132)$$

where  $\mathcal{L}_{free}$  and  $\mathcal{L}_{em}$  stand for the free Lagrangian for the nucleon and mesons and the electromagnetic interaction, respectively, while  $\mathcal{L}_{QMC}^{int}$  involves (strong) interaction terms. For the QMC-I and QMC-II,  $\mathcal{L}_{QMC}^{int}$  is respectively given by Eqs. (122) and (128)

$$\mathcal{L}_{QMC-I}^{int} = \bar{\psi} \left[ (M_N - M_N^*(\sigma)) - g_\omega \gamma_0 \omega - g_\rho \left( \frac{\tau_3^N}{2} \right) \gamma_0 b \right] \psi, \quad (133)$$

and

$$\begin{aligned} \mathcal{L}_{QMC-II}^{int} &= \bar{\psi} \left[ (M_N - M_N^*(\sigma)) - g_\omega \gamma_0 \omega - g_\rho \left( \frac{\tau_3^N}{2} \right) \gamma_0 b \right] \psi \\ &\quad - \frac{1}{2} [m_\sigma^{*2}(\sigma) - m_\sigma^2] \sigma^2 + \frac{1}{2} [m_\omega^{*2}(\sigma) - m_\omega^2] \omega^2 \\ &\quad + \frac{1}{2} [m_\rho^{*2}(\sigma) - m_\rho^2] b^2, \end{aligned} \quad (134)$$

where the effective masses in the medium depend only on the scalar field.

Table 1: Interaction terms and corresponding (dimensionless) coupling constants. We take  $\Lambda = M_N$  in Eq. (131). A, B and C denote three types of parameterization of the  $\sigma$  mass in a medium (see section 3.1).

term	$c_{\ell mnp}$	QMC-I	A	B	C
$\bar{\psi}\sigma\psi$	$c_{1100}$	0.82	0.69	0.70	0.69
$\bar{\psi}\sigma^2\psi$	$c_{1200}$	-0.55	-0.40	-0.41	-0.40
$\bar{\psi}\gamma_0\omega\psi$	$c_{1010}$	-0.81	-0.58	-0.63	-0.64
$\bar{\psi}\left(\frac{\tau}{2}\right)\gamma_0 b\psi$	$c_{1001}$	-0.92	-0.83	-0.81	-0.80
$\sigma^3$	$c_{0300}$	—	0.40	0.67	1.0
$\sigma^4$	$c_{0400}$	—	-3.6	-2.2	-4.4
$\sigma^5$	$c_{0500}$	—	3.3	2.9	8.3
$\sigma^6$	$c_{0600}$	—	-22	-5.7	-22
$\sigma\omega^2$	$c_{0120}$	—	-0.77	-0.78	-0.76
$\sigma^2\omega^2$	$c_{0220}$	—	0.85	0.87	0.85
$\sigma^3\omega^2$	$c_{0320}$	—	-0.71	-0.73	-0.70
$\sigma^4\omega^2$	$c_{0420}$	—	0.39	0.41	0.39
$\sigma b^2$	$c_{0102}$	—	-0.75	-0.76	-0.75
$\sigma^2 b^2$	$c_{0202}$	—	0.84	0.86	0.84
$\sigma^3 b^2$	$c_{0302}$	—	-0.70	-0.73	-0.70
$\sigma^4 b^2$	$c_{0402}$	—	0.39	0.41	0.39

If the MIT bag model is used to describe the hadrons, one finds that the mass at nuclear density  $\rho_B$  is given by quite a simple form for the region of  $\rho_B \leq 3\rho_0$  [19]. The reduction of the mass from the free value,  $\delta M_j^* = M_j - M_j^*$ , is then given by

$$\delta M_j^* \simeq \frac{n_q}{3} g_\sigma \left[ 1 - \frac{a_j}{2} (g_\sigma \sigma) \right] \sigma, \quad (135)$$

where  $j = N, \sigma, \omega, \rho$ , and  $n_q$  is the number of light quarks in the hadron  $j$ , and  $a_j$  is a slope parameter for the hadron  $j$ , which is given by the second derivative of the mass with respect to the  $\sigma$  field (for details, see section 3.1.1).

There are several coupling constants to be determined in the QMC-I and QMC-II models. In section 3, we will explain in detail how these constants are fixed. Here, we merely present the values of the dimensionless coefficients,  $c_{\ell mnp}$ , in Eq. (131) for each interaction term in Table 1. (In the QMC-II model, we choose three parameter sets for the effective  $\sigma$ -meson mass in matter (see Eq. (127)). See for details section 3.1.) Using Eqs. (127) and (135), the QMC-I Lagrangian has four interaction terms, while the QMC-II Lagrangian offers 16 terms due to the internal structure of the nucleon *and* the mesons.

As seen in the table, the QMC-I model provides remarkably *natural* coupling constants, whose magnitudes lie in the range 0.5 – 1.0. In QMC-II, 14 or 15 of the 16 coupling constants can be regarded as *natural*. Only the large absolute values of  $c_{0500}$  for set C and  $c_{0600}$  for sets A - C are unnatural. Since the coefficients,  $c_{0500}$  and  $c_{0600}$ , are respectively proportional to  $a_\sigma b_\sigma$  and  $b_\sigma^2$ , we see that those unnaturally large numbers are associated with the parameterization of the  $\sigma$  mass in matter. In particular, a large value for the coefficient  $b_\sigma$  leads to unnatural values for  $c_{0500}$  and  $c_{0600}$ . In the present estimate, the reduction of the  $\sigma$ -meson mass in matter was the sole feature of the model which could not be calculated but was put in by hand. There is nothing within the QMC model itself which requires  $b_\sigma$  to be so large. Therefore, the QMC model itself can be regarded as a *natural* effective field theory for nuclei.

### 2.3 Relationship between the QMC model and conventional nuclear models

We shall consider the relationship between the QMC model and conventional nuclear approach. To this end we re-formulate the QMC model of a nucleus as a many body problem in the non-relativistic framework. This allows us to take the limit corresponding to a zero range force which can be compared to the familiar Skyrme force in conventional nuclear physics [29].

In the previous section 2.1.5, we have found the following expression for the classical energy of a nucleon with position ( $\vec{R}$ ) and momentum ( $\vec{P}$ ) (see Eq. (76)):

$$E_N(\vec{R}) = \frac{\vec{P}^2}{2M_N^*(\vec{R})} + M_N^*(\vec{R}) + g_\omega\omega(\vec{R}) + V_{so}, \quad (136)$$

To get the dynamical mass  $M_N^*(\vec{R})$  one has to solve a quark model of the nucleon (e.g., the bag model) in the field  $\sigma(\vec{R})$ . For the present purpose, it is sufficient to know that it is well approximated by the expression (see Eq. (126))

$$M_N^*(\vec{R}) = M_N - g_\sigma\sigma(\vec{R}) + \frac{d}{2} \left( g_\sigma\sigma(\vec{R}) \right)^2, \quad (137)$$

where  $d$  is a parameter – the bag model gives  $d = 0.22R_B$ . The last term, which represents the response of the nucleon to the applied scalar field – the scalar polarizability – is an essential element of the QMC model. From the numerical studies we know that the approximation Eq. (137) is quite accurate at moderate nuclear densities (see section 3).

The energy (136) is for one particular nucleon moving classically in the nuclear meson fields. The total energy of the system is then given by the sum of the energy of each nucleon and the energy carried by the fields (see Eq. (112)):

$$E_{tot} = \sum_i E_N(\vec{R}_i) + E_{meson}, \quad (138)$$

$$E_{meson} = \frac{1}{2} \int d\vec{r} \left[ (\vec{\nabla}\sigma)^2 + m_\sigma^2\sigma^2 - (\vec{\nabla}\omega)^2 - m_\omega^2\omega^2 \right]. \quad (139)$$

To simplify the expression for  $E_N(\vec{R})$ , we estimate the quantity  $g_\sigma\sigma$  using the field equations  $\delta E_{tot}/\delta\sigma(\vec{r}) = 0$ . Neglecting the velocity dependent terms, setting  $M_N^* \approx M_N - g_\sigma\sigma$  and neglecting  $(\vec{\nabla}\sigma)^2$  with respect to  $m_\sigma^2\sigma^2$ , we find the total energy

$$E_{tot} = E_{meson} + \sum_i \left( M_N + \frac{\vec{P}_i^2}{2M_N} + V_{so}(i) \right) - \int d\vec{r} \rho_s^{cl} \left( g_\sigma\sigma - \frac{d}{2}(g_\sigma\sigma)^2 \right) + \int d\vec{r} \rho^{cl} g_\omega\omega, \quad (140)$$

where we define the classical densities as  $\rho^{cl}(\vec{r}) = \sum_i \delta(\vec{r} - \vec{R}_i)$  and  $\rho_s^{cl}(\vec{r}) = \sum_i (1 - \vec{P}_i^2/2M_N^2) \delta(\vec{r} - \vec{R}_i)$ . This will be the starting point for the many body formulation of the QMC model.

To eliminate the meson fields from the energy, we use the equations for the mesons,  $\delta E_{tot}/\delta\sigma(\vec{r}) = \delta E_{tot}/\delta\omega(\vec{r}) = 0$ , and leave a system whose dynamics depends only on the nucleon coordinates. We first remark that, roughly speaking, the meson fields should follow the matter density. Therefore the typical scale for the  $\vec{\nabla}$  operator acting on  $\sigma$  or  $\omega$  is the thickness of the nuclear surface, that is about 1 fm. Therefore, it looks reasonable that we can consider the second derivative terms acting on the meson fields as perturbations. Then, starting from the lowest order approximation, we solve the equations for the meson fields iteratively, and neglect a small difference between  $\rho_s^{cl}$  and  $\rho^{cl}$  except in the leading term. When inserted into Eq. (140), the series for the meson fields generates  $N$ -body forces in the Hamiltonian. To complete the effective Hamiltonian, we now include the effect of the isovector  $\rho$  meson, which can be done by analogy with the  $\omega$  meson.

The quantum effective Hamiltonian finally takes the form

$$\begin{aligned} H_{QMC} = & \sum_i \frac{\vec{\nabla}_i \cdot \vec{\nabla}_i}{2M_N} + \frac{G_\sigma}{2M_N^2} \sum_{i \neq j} \vec{\nabla}_i \delta(\vec{R}_{ij}) \cdot \vec{\nabla}_i + \frac{1}{2} \sum_{i \neq j} [\vec{\nabla}_i^2 \delta(\vec{R}_{ij})] \left( \frac{G_\omega}{m_\omega^2} - \frac{G_\sigma}{m_\sigma^2} + \frac{G_\rho}{m_\rho^2} \frac{\vec{\tau}_i \cdot \vec{\tau}_j}{4} \right) \\ & + \frac{1}{2} \sum_{i \neq j} \delta(\vec{R}_{ij}) \left[ G_\omega - G_\sigma + G_\rho \frac{\vec{\tau}_i \cdot \vec{\tau}_j}{4} \right] + \frac{dG_\sigma^2}{2} \sum_{i \neq j \neq k} \delta^2(ijk) - \frac{d^2G_\sigma^3}{2} \sum_{i \neq j \neq k \neq l} \delta^3(ijkl) \end{aligned}$$

Table 2: QMC predictions (with  $m_\sigma = 600$  MeV) compared with the Skyrme force. See text for details.

	QMC	QMC(N=3)	SkIII
$t_0(\text{MeV fm}^3)$	-1082	-1047	-1129
$x_0$	0.59	0.61	0.45
$t_3(\text{MeV fm}^6)$	14926	12513	14000
$3t_1 + 5t_2(\text{MeV fm}^5)$	475	451	710
$5t_2 - 9t_1(\text{MeV fm}^5)$	-4330	-4036	-4030
$W_0(\text{MeV fm}^5)$	97	91	120
$K(\text{MeV})$	327	364	355

$$+ \frac{i}{4M_N^2} \sum_{i \neq j} A_{ij} \vec{\nabla}_i \delta(\vec{R}_{ij}) \times \vec{\nabla}_i \cdot \vec{\sigma}_i, \quad (141)$$

where  $G_i = g_i^2/m_i^2$  ( $i = \sigma, \omega, \rho$ ) and  $A_{ij} = G_\sigma + (2\mu_s - 1)G_\omega + (2\mu_v - 1)G_\rho \vec{\tau}_i \cdot \vec{\tau}_j/4$ . Here  $\vec{R}_{ij} = \vec{R}_i - \vec{R}_j$  and  $\vec{\nabla}_i$  is the gradient with respect to  $\vec{R}_i$  acting on the delta function. To shorten the equations, we used the notation  $\delta^2(ijk)$  for  $\delta(\vec{R}_{ij})\delta(\vec{R}_{jk})$  and analogously for  $\delta^3(ijkl)$ . Furthermore, we have dropped the contact interactions involving more than 4-bodies because their matrix elements vanish for antisymmetrized states.

To fix the free parameters,  $G_i$ , the volume and symmetry coefficients of the binding energy per nucleon of infinite nuclear matter,  $E_B/A = a_1 + a_4(N-Z)^2/A^2$ , are calculated and fitted so as to produce the experimental values. Using the bag model with the radius  $R_B = 0.8$  fm and the physical masses for the mesons and  $m_\sigma = 600$  MeV, one gets, in  $\text{fm}^2$ ,  $G_\sigma = 11.97$ ,  $G_\omega = 8.1$  and  $G_\rho = 6.46$ .

It is now possible to compare the present Hamiltonian with the effective Skyrme interaction. Since, in our formulation, the medium effects are summarized in the 3- and 4-body forces, we consider Skyrme forces of the same type, that is, without density dependent interactions. They are defined by a potential energy of the form

$$\begin{aligned} V = & t_3 \sum_{i < j < k} \delta(\vec{R}_{ij})\delta(\vec{R}_{jk}) + \sum_{i < j} \left\{ t_0(1 + x_0 P_\sigma) \delta(\vec{R}_{ij}) + \frac{1}{4} t_2 \vec{\nabla}_{ij} \cdot \delta(\vec{R}_{ij}) \vec{\nabla}_{ij} \right. \\ & \left. - \frac{1}{8} t_1 [\delta(\vec{R}_{ij}) \vec{\nabla}_{ij}^2 + \vec{\nabla}_{ij}^2 \delta(\vec{R}_{ij})] + \frac{i}{4} W_0 (\vec{\sigma}_i + \vec{\sigma}_j) \cdot \vec{\nabla}_{ij} \times \delta(\vec{R}_{ij}) \vec{\nabla}_{ij}^2 \right\}, \end{aligned} \quad (142)$$

with  $\nabla_{ij} = \nabla_i - \nabla_j$ . There is no 4-body force in Eq. (142). Comparison of Eq. (142) with the QMC Hamiltonian, Eq. (141), allows one to identify

$$t_0 = -G_\sigma + G_\omega - \frac{G_\rho}{4}, \quad t_3 = 3dG_\sigma^2, \quad x_0 = -\frac{G_\rho}{2t_0}. \quad (143)$$

To simplify the situation further, we restrict our considerations to doubly closed shell nuclei, and assume that one can neglect the difference between the radial wave functions of the single particle states with  $j = l + 1/2$  and  $j = l - 1/2$ . Then, by comparing the Hartree-Fock Hamiltonian obtained from  $H_{QMC}$  and that of Ref. [60] corresponding to the Skyrme force, we obtain the relations

$$3t_1 + 5t_2 = \frac{8G_\sigma}{M_N^2} + 4 \left( \frac{G_\omega}{m_\omega^2} - \frac{G_\sigma}{m_\sigma^2} \right) + 3 \frac{G_\rho}{m_\rho^2}, \quad (144)$$

$$5t_2 - 9t_1 = \frac{2G_\sigma}{M_N^2} + 28 \left( \frac{G_\omega}{m_\omega^2} - \frac{G_\sigma}{m_\sigma^2} \right) - 3 \frac{G_\rho}{m_\rho^2}, \quad (145)$$

$$W_0 = \frac{1}{12M_N^2} \left( 5G_\sigma + 5(2\mu_s - 1)G_\omega + \frac{3}{4}(2\mu_v - 1)G_\rho \right). \quad (146)$$

In Table 2, we compare our results with the parameters of the force SkIII [61], which is considered a good representative of density independent effective interactions. Instead of  $t_1$  and  $t_2$ , we show the combinations



$3t_1 + 5t_2$ , which controls the effective mass, and  $5t_2 - 9t_1$ , which controls the shape of the nuclear surface [60]. From the table, one sees that the level of agreement with SkIII is very impressive. An important point is that the spin orbit strength  $W_0$  comes out with approximately the correct value. The middle column (N=3) shows the results when we switch off the 4-body force. The main change is a decrease of the predicted 3-body force. Clearly this mocks up the effect of the attractive 4-body force which may then appear less important. However, this is misleading if we look at the incompressibility of nuclear matter,  $K$ , which decreases by as much as 37 MeV when we restore this 4-body force.

Now one can recognize a remarkable agreement between the phenomenologically successful Skyrme force (SkIII) and the effective interaction corresponding to the QMC model - a result which suggests that the response of nucleon internal structure to the nuclear medium does indeed play a vital role in nuclear structure.

## 2.4 Relationship between the QMC model and Quantum Hadrodynamics

Next, let us examine the relationship between the QMC-I model and QHD in detail [24]. The main difference between QMC and QHD at the *hadronic* level lies in the dependence of the nucleon mass on the scalar field in matter (see Eq. (126)). By re-defining the scalar field [23, 24], the QMC Lagrangian density can be cast into a form similar to that of a QHD-type mean-field model, in which the nucleon mass depends on the scalar field linearly (as in QHD), with self-interactions of the scalar field. It should be emphasized here that the QMC model explicitly provides how the quark structure changes inside the in-medium nucleon. Such information is necessarily not part of any QHD-type mean-field model generated through the re-definition of the scalar field.

In the QMC model, the nucleon mass in matter is given by a function of  $\sigma$ ,  $M_{N,QMC}^*(\sigma)$ , obtained from a quark model of the nucleon, while in QHD the mass depends on a scalar field linearly,  $M_{N,QHD}^* = M_N - g_0\phi$ , where  $\phi$  is a scalar field in a QHD-type model. Hence, to transform the QMC into a QHD-type model, we may re-define the scalar field of QMC as

$$g_0\phi(\sigma) = M_N - M_{N,QMC}^*(\sigma), \quad (147)$$

where  $g_0$  is a constant chosen so as to normalize the scalar field  $\phi$  in the limit  $\sigma \rightarrow 0$ :  $\phi(\sigma) = \sigma + \mathcal{O}(\sigma^2)$ . Thus,  $g_0$  is given by  $g_0 = -(\partial M_{N,QMC}^*/\partial\sigma)_{\sigma=0}$ , and we find  $g_0 = g_\sigma$ .

The contribution of the scalar field to the total energy,  $E_{scl}$ , can now be rewritten in terms of the new field  $\phi$  as

$$E_{scl} = \frac{1}{2} \int d\vec{r} [(\vec{\nabla}\sigma)^2 + m_\sigma^2\sigma^2] = \int d\vec{r} \left[ \frac{1}{2} h(\phi)^2 (\vec{\nabla}\phi)^2 + U_s(\phi) \right], \quad (148)$$

where  $U_s$  describes self-interactions of the scalar field:

$$U_s(\phi) = \frac{1}{2} m_\sigma^2 \sigma(\phi)^2 \quad \text{and} \quad h(\phi) = \left( \frac{\partial\sigma}{\partial\phi} \right) = \frac{1}{m_\sigma \sqrt{2U_s(\phi)}} \left( \frac{\partial U_s(\phi)}{\partial\phi} \right). \quad (149)$$

Note that in uniformly distributed nuclear matter the derivative term in  $E_{scl}$  does not contribute. Thus this term only affects the properties of finite nuclei [23]. Now, QMC *at the hadronic level* can be re-formulated in terms of the new scalar field  $\phi$ , and what we obtain has the same form as QHD, with the non-linear scalar potential  $U_s(\phi)$  and the coupling  $h(\phi)$  to the gradient of the scalar field. (Note that because this re-definition of the scalar field does not involve the vector interaction, the energy due to the  $\omega$  field is not modified.)

In general, the in-medium nucleon mass may be given by a complicated function of the scalar field. However, in the QMC with the bag model, the mass can be parameterized by a simple expression up to  $\mathcal{O}(g_\sigma^2)$  (see also Eq. (126)):

$$M_N^*/M_N \simeq 1 - ay + by^2, \quad (150)$$

where  $y (= g_\sigma\sigma/M_N)$  is a dimensionless scale and  $a$  and  $b$  are (dimensionless) parameters. This parameterization is accurate at moderate nuclear densities (see for details section 3.1.1).

Once the parameters  $a$  and  $b$  are fixed, we can easily re-define the scalar field using Eq. (147):

$$g_0 = ag_\sigma, \quad \phi(\sigma) = \sigma - d\sigma^2 \quad \text{and} \quad \sigma(\phi) = \frac{1 - \sqrt{1 - 4d\phi}}{2d}, \quad (151)$$

with  $d = bg_\sigma/aM_N$ . This satisfies the condition that  $\sigma \rightarrow 0$  in the limit  $\phi \rightarrow 0$ . The non-linear potential is thus calculated as

$$\begin{aligned} U_s(\phi) &= \frac{m_\sigma^2}{2} \left( \frac{\sigma(\phi) - \phi}{d} \right), \\ &= \frac{m_\sigma^2}{2} \phi^2 + g_\sigma r \left( \frac{m_\sigma^2}{M_N} \right) \phi^3 + \frac{5}{2} g_\sigma^2 r^2 \left( \frac{m_\sigma}{M_N} \right)^2 \phi^4 + \mathcal{O}(g_\sigma^3), \end{aligned} \quad (152)$$

where  $r = b/a$ . By contrast, the standard form of the non-linear scalar potential is usually given by

$$U_s(\phi) = \frac{1}{2} m_\sigma^2 \phi^2 + \frac{\kappa}{6} \phi^3 + \frac{\lambda}{24} \phi^4. \quad (153)$$

It is well known that the non-linear scalar potential given in Eq. (153) is vital to reproduce the bulk properties of finite nuclei and nuclear matter in relativistic mean field models.

We can estimate the parameters  $\kappa$  and  $\lambda$  in the QMC by comparing Eqs. (152) and (153). Because the parameters  $a$  and  $b$  are respectively about unity and 0.2 – 0.5 (see Table II in Ref. [24]), one finds  $\kappa \sim 20 - 40$  ( $\text{fm}^{-1}$ ) and  $\lambda \sim 80 - 400$ . Since the QMC predicts that both  $a$  and  $b$  are *always* positive, we can expect that the quark substructure of the in-medium nucleon provides a non-linear potential with *positive*  $\kappa$  and *positive*  $\lambda$  in the QHD-type mean-field model. By contrast, the parameters  $\kappa$  and  $\lambda$  phenomenologically determined in RMF models take wide range of values (for example, Ref. [25, 62, 63]), and the potentials in those models are then quite different from one another for large  $|\phi|$ . However, from the point of view of field theory, the coefficient of quartic term should be positive. The QMC model always yields a positive  $\lambda$ .

In general, the phenomenological potential may consist of a part that is due to the quark substructure of the nucleon, as well a piece involving inherent self-couplings of the scalar field in matter. It would therefore be very intriguing if the potential due to the internal structure of the nucleon could be inferred from analyses of experimental data in the future.

## 2.5 Modified quark-meson coupling model

As we have seen in the previous sections, the QMC model provides a simple and attractive framework to incorporate the quark structure of the nucleon in a nucleus. In the original QMC model, we chose to hold the bag constant at its free space value, even for nuclear matter. When a nucleon bag is put into the nuclear medium, the bag as a whole reacts to the environment. As a result, the bag constant might be modified. There is little doubt that at sufficiently high densities, the bag eventually melts away and quarks and gluons become the appropriate degrees of freedom. Thus, it seems reasonable that the bag constant be modified and decrease as the density increases. Moreover, the MIT bag constant may be related to the energy associated with chiral symmetry restoration, and the in-medium bag constant may drop relative to its free space value. This way of thinking leads to a modified version of the QMC model – called the modified quark-meson coupling (MQMC) model [23, 64, 65, 66]. In principle, the parameter  $z$  may also be modified in the nuclear medium. However, unlike the bag constant, it is unclear how  $z$  changes with the density as  $z$  is not directly related to chiral symmetry. Here we assume that the medium modification of  $z$  is small at low and moderate densities.

To reflect this physics, we introduce a direct coupling between the bag constant,  $B$ , in matter and the scalar mean field

$$\frac{B}{B_0} = \left[ 1 - g_\sigma^B \frac{4}{\delta} \frac{\sigma}{M_N} \right]^\delta, \quad (154)$$

where  $g_\sigma^B$  and  $\delta$  are new, real positive parameters and  $B_0$  is the free value of the bag constant. Note that  $g_\sigma^B$  differs from  $g_\sigma^q$  (or  $g_\sigma$ ) and that when  $g_\sigma^B = 0$  the original QMC model is recovered. This direct coupling is partially motivated from considering a non-topological soliton model for the nucleon where a scalar soliton field provides the confinement of the quarks. Roughly speaking, the bag constant in the MIT bag model mimics the effect of the scalar soliton field in the soliton model. In the limit  $\delta \rightarrow \infty$ , Eq. (154) reduces to an exponential form with a single parameter  $g_\sigma^B$ ,  $B/B_0 = \exp[-4g_\sigma^B \sigma/M_N]$ . In the limit of zero current quark mass and  $g_\sigma = 0$ , the nucleon mass scales like  $B^{1/4}$  from dimensional arguments. Then, from Eq. (154) we

get  $M_N^*/M_N = (B/B_0)^{1/4} = [1 - 4g_\sigma^B \sigma / \delta M_N]^{1/4}$ . One observes that the linear  $\sigma$ -nucleon coupling is just  $g_\sigma^B$  while  $\delta$  controls the non-linearities. For  $\delta = 4$ , the non-linearities vanish and the QHD-I is recovered but with a density dependent bag radius.

Alternative is a scaling model, which relates the in-medium bag constant to the in-medium nucleon mass directly through

$$\frac{B}{B_0} = \left[ \frac{M_N^*}{M_N} \right]^\kappa, \quad (155)$$

where  $\kappa$  is a real positive parameter ( $\kappa = 0$  corresponds to the usual QMC model). Note that in this model, the effective nucleon mass  $M_N^*$  and the bag constant  $B$  are determined self-consistently.

One notices that both Eqs. (154) and (155) give rise to a reduction of the bag constant in nuclear medium relative to its free-space value. While the scaling model is characterized by a single free parameter  $\kappa$ , it leads to a complicated and implicit relation between the bag constant and the scalar mean field. On the other hand, the direct coupling model features a straightforward coupling between the bag constant and the scalar mean field, which, however, introduces two free parameters,  $g_\sigma^B$  and  $\delta$ .

The most important feature is that the reduction of  $B$  relative to  $B_0$  leads to a decrease of  $M_N^*/M_N$  and an increase of the repulsive vector potential relative to their values in the original QMC model. In the MQMC model, the reduction of the bag constant in nuclear medium provides a new source of attraction as it effectively reduces  $M_N^*$ . Consequently, additional vector field strength is required to obtain the correct saturation properties of nuclear matter.

It can be seen that when the bag constant is reduced significantly in nuclear matter, the resulting magnitudes for  $M_N^* - M_N$  and  $U_v \equiv g_\omega \omega$  are qualitatively different from those obtained in the usual QMC model and could be  $\sim 700$  MeV and  $\sim 200$  MeV, respectively, for some parameter sets [64]. These values imply that large and canceling scalar and vector potentials for the nucleon can be produced in nuclear matter and they are comparable to those suggested by Dirac phenomenology [67]. These potentials also imply a strong nucleon spin-orbit potential and the essential features of relativistic nuclear phenomenology are recovered. The corresponding results for the nuclear matter incompressibility  $K$  are, however, larger than the value in the usual QMC model but smaller than that in QHD-I. The relationship among the QMC, MQMC and QHD is clarified and discussed in Ref. [23, 65, 66].

In the usual QMC model, the bag radius decreases slightly and the quark root-mean-square (rms) radius increases slightly in nuclear matter with respect to their free-space values. When the bag constant drops relative to its free-space value, the bag pressure decreases and hence the bag radius increases in the medium. When the reduction of the bag constant is significant, the bag radius in saturated nuclear matter is 25 – 30% larger than its free-space value. The quark rms radius also increases with density, with essentially the same rate as for the bag radius. This implies a “swollen” nucleon in nuclear medium. However, a 25 – 30% increase in the nucleon size is generally considered too large in comparison with the conclusion drawn from electron scattering data [68, 69]. The MQMC model has also been used to study many nuclear phenomena.

## 2.6 Variants of the QMC model

In the original QMC model, the MIT bag model was used to describe the nucleon structure. Although the basic idea of the QMC model is not altered, it is possible to replace the bag model with the constituent quark model. Toki *et al.* [70] have proposed a quark mean field (QMF) model for nucleons in nuclei, where the constituent quarks interact with the meson fields created by other nucleons and hence change the nucleon properties in nuclei (see also Ref. [51]). They have found very good nuclear matter properties with the use of the nonlinear self-energy terms for the meson fields. In particular, the spin-orbit splitting in finite nuclei becomes large due to the large reduction of the in-medium nucleon mass. In this picture, the nucleon size increases by about 7% at the normal nuclear matter density. This QMF model has been applied to various nuclear phenomena, for example, the effect of density-dependent coupling constants for finite nuclei [71],  $\Lambda$ -hyper nuclei [72], pentaquark  $\Theta^+$  in nuclear matter and  $\Theta^+$  hypernuclei [73].

Krein *et al.* [51] have also proposed a similar model, in which the constituent quark model is used to describe a nucleon. In addition to that, the exchange contribution and pionic effect have been calculated. As in QHD, the exchange effect is repulsive and the coupling of the mesons directly to the quarks in the nucleons introduces

Table 3: Bag constant and parameter  $z_0$  for several bag radii and quark masses.

$m_q(\text{MeV})$	0			5			10		
$R_N(\text{fm})$	0.6	0.8	1.0	0.6	0.8	1.0	0.6	0.8	1.0
$B^{1/4}(\text{MeV})$	211.3	170.3	144.1	210.9	170.0	143.8	210.5	169.6	143.5
$z_0$	3.987	3.273	2.559	4.003	3.295	2.587	4.020	3.317	2.614

a new effect on the exchange energies that provides an extra repulsive contribution to the binding energy. In this approach, the pionic effect is not small.

Recently, the QMC model has been extended to a model based on  $SU(3)_L \times SU(3)_R$  symmetry and scale invariance [74]. In this model it is possible to study strange hadronic matter, multi-strange hadronic system or strangelets, including  $\Lambda$ ,  $\Sigma$  and  $\Xi$  hyperons. The properties of hyperons in matter have been discussed with several types of confining potentials. The phase transition corresponding to chiral symmetry restoration in high density nuclear matter is also investigated.

Using the Nambu-Jona-Lasinio model to describe the nucleon as a quark-diquark state, it is also possible to discuss the stability of nuclear matter, based on the QMC idea [75]. This model has been applied to interesting nuclear phenomena including the high energy lepton-nucleus scattering [76, 77].

### 3 Properties of nuclei

In the previous section, we presented the basic idea of the QMC model, and saw various models relating to it. In this section, we are now in a position to report numerical results for various nuclear phenomena.

#### 3.1 Nuclear matter properties - saturation properties and incompressibility

Let us first consider the simplest version of the QMC model (QMC-I), which includes only the nucleon,  $\sigma$  and  $\omega$  mesons, and calculate the properties for symmetric nuclear matter [10, 13, 19, 52]. In this case, because of the uniform matter distribution, the sources of the meson fields are constant and can be related to the nucleon Fermi momentum  $k_F$  as

$$\rho_B = \frac{4}{(2\pi)^3} \int d\vec{k} \theta(k_F - k) = \frac{2k_F^3}{3\pi^2}, \quad (156)$$

$$\rho_s = \frac{4}{(2\pi)^3} \int d\vec{k} \theta(k_F - k) \frac{M_N^*}{\sqrt{M_N^{*2} + \vec{k}^2}}, \quad (157)$$

where  $M_N^*$  is the constant value of the effective nucleon mass at a given density. We here adopt the MIT bag model, and the bag constant  $B$  and the parameter  $z_0$  (which accounts for the sum of the c.m. and gluon fluctuation corrections) are determined so as to produce the free nucleon mass under the stationary condition with respect to the free bag radius,  $R_N$  (hereafter  $R_N$  denotes the nucleon bag radius in free space, see Eqs. (40) and (41)). In the following we treat the free bag radius as a variable parameter to test the sensitivity of our results to the free nucleon size. The results for  $B$  and  $z_0$  are shown in Table 3. The free quark mass may be chosen to be  $m_q = 0, 5, 10$  MeV. Let  $(\sigma, \omega)$  be the constant mean-values of the meson fields which are given by

$$\omega = \frac{g_\omega \rho_B}{m_\omega^2}, \quad (158)$$

$$\sigma = \frac{g_\sigma}{m_\sigma^2} C_N(\sigma) \frac{4}{(2\pi)^3} \int d\vec{k} \theta(k_F - k) \frac{M_N^*}{\sqrt{M_N^{*2} + \vec{k}^2}}, \quad (159)$$

where  $C_N(\sigma)$  is now the constant value of the scalar density ratio defined by Eq. (111).

Table 4: Coupling constants and calculated properties for symmetric nuclear matter at normal nuclear matter density (QMC-I). The effective nucleon mass,  $M_N^*$ , and the nuclear incompressibility,  $K$ , are quoted in MeV. The bottom row is for QHD [17].

$m_q(\text{MeV})$	$R_N(\text{fm})$	$g_\sigma^2/4\pi$	$g_\omega^2/4\pi$	$M_N^*$	$K$	$\delta R_N^*/R_N$	$\delta x_0^*/x_0$	$\delta r_q^*/r_q$
0	0.6	5.84	6.29	730	293	-0.02	-0.13	0.01
	0.8	5.38	5.26	756	278	-0.02	-0.16	0.02
	1.0	5.04	4.50	774	266	-0.02	-0.19	0.02
5	0.6	5.86	6.34	729	295	-0.02	-0.13	0.01
	0.8	5.40	5.31	755	280	-0.02	-0.16	0.02
	1.0	5.07	4.56	773	267	-0.02	-0.19	0.02
10	0.6	5.87	6.37	728	295	-0.02	-0.13	0.02
	0.8	5.42	5.36	753	281	-0.02	-0.16	0.02
	1.0	5.09	4.62	772	269	-0.02	-0.18	0.03
QHD	—	7.29	10.8	522	540			

Once the self-consistency equation for the  $\sigma$  has been solved, one can evaluate the total energy per nucleon

$$E^{tot}/A = \frac{4}{(2\pi)^3 \rho_B} \int d\vec{k} \theta(k_F - k) \sqrt{M_N^{*2} + \vec{k}^2} + \frac{m_\sigma^2 \sigma^2}{2\rho_B} + \frac{g_\omega^2 \rho_B}{2m_\omega^2}. \quad (160)$$

We then determine the coupling constants,  $g_\sigma$  and  $g_\omega$ , so as to fit the binding energy ( $-15.7$  MeV) per nucleon at the saturation density,  $\rho_0 = 0.15 \text{ fm}^{-3}$  ( $k_F^0 = 1.305 \text{ fm}^{-1}$ ), for symmetric nuclear matter. The coupling constants and some calculated properties of nuclear matter (for  $m_\sigma = 550$  MeV and  $m_\omega = 783$  MeV) at the saturation density are listed in Table 4. The last three columns show the relative changes (from their values at zero density) of the bag radius ( $\delta R_N^*/R_N$ ), the lowest eigenvalue ( $\delta x_0^*/x_0$ ) and the rms radius of the nucleon calculated by the quark wave function ( $\delta r_q^*/r_q$ ) at saturation density.

The most notable fact is that the calculated incompressibility,  $K$ , is well within the experimental range:  $K = 200 \sim 300$  MeV. Although the bag radius shrinks a little at finite density, the rms radius of the quark wave function actually *increases* by a few percent at saturation density. This seems consistent with the observed results [68, 69] (see also section 4.1). The saturation mechanism of the binding energy of nuclear matter is novel. In QHD, the  $\sigma$  and  $\omega$  couplings to the nucleon are really constant, while in the QMC the  $\sigma$ -N coupling is reduced by the effect of the internal structure of the nucleon, that is responsible for the saturation [10, 13].

Next let us consider the QMC-II model, including the effect of the meson structure (see section 2.2.3). For asymmetric nuclear matter ( $Z \neq N$ ), we take the Fermi momenta for protons and neutrons to be  $k_{F_i}$  ( $i = p$  or  $n$ ). This is defined by  $\rho_i = k_{F_i}^3/(3\pi^2)$ , where  $\rho_i$  is the density of protons or neutrons, and the total baryon density,  $\rho_B$ , is then given by  $\rho_p + \rho_n$ . From the Lagrangian density Eq. (128), the total energy per nucleon is then written

$$E^{tot}/A = \frac{2}{\rho_B (2\pi)^3} \sum_{i=p,n} \int^{k_{F_i}} d\vec{k} \sqrt{M_i^{*2} + \vec{k}^2} + \frac{m_\sigma^{*2}}{2\rho_B} \sigma^2 + \frac{g_\omega^2}{2m_\omega^{*2}} \rho_B + \frac{g_\rho^2}{8m_\rho^{*2}} \rho_3^2, \quad (161)$$

where the value of the  $\omega$  field is determined by baryon number conservation, Eq. (158), with the effective mass  $m_\omega^*$  instead of the free mass, and the  $\rho$  field value by the difference in proton and neutron densities,  $\rho_3 = \rho_p - \rho_n$ , as  $b = g_\rho \rho_3/(2m_\rho^{*2})$ .

In contrast, the  $\sigma$  field is given by a self-consistency condition (instead of Eq. (159)):

$$\begin{aligned} \sigma &= \frac{2g_\sigma}{(2\pi)^3 m_\sigma^{*2}} \left[ \sum_{i=p,n} C_i(\sigma) \int^{k_{F_i}} d\vec{k} \frac{M_i^*}{\sqrt{M_i^{*2} + \vec{k}^2}} \right] + g_\sigma \left( \frac{m_\sigma}{m_\sigma^*} \right) [a_\sigma - 2b_\sigma(g_\sigma \sigma)] \sigma^2 \\ &- \frac{2}{3} \left( \frac{g_\sigma}{m_\sigma^*} \right) \left[ \frac{g_\omega^2 \rho_B^2}{m_\omega^{*3}} \Gamma_{\omega/N} C_\omega(\sigma) + \frac{g_\rho^2 \rho_3^2}{4m_\rho^{*3}} \Gamma_{\rho/N} C_\rho(\sigma) \right]. \end{aligned} \quad (162)$$

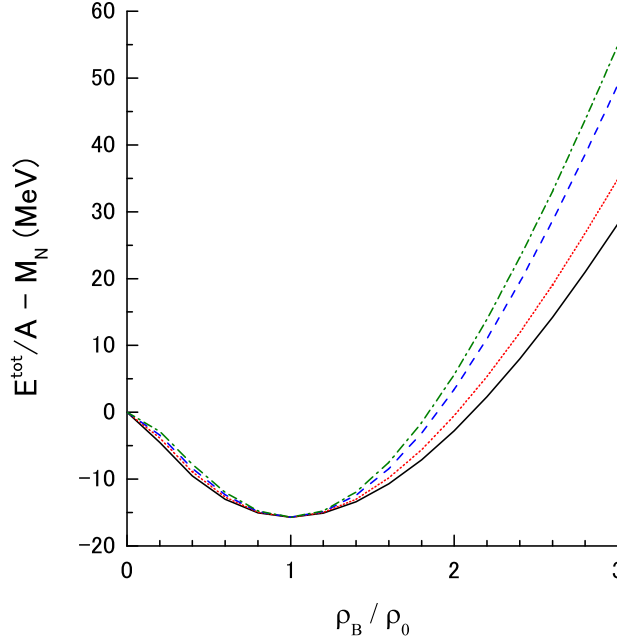


Figure 1: Energy per nucleon for iso-symmetric nuclear matter (for  $m_q = 5$  MeV and  $R_N = 0.8$  fm). The solid curve is for QMC-I, while the dotted (dashed) [dot-dashed] curve is for type A (B) [C] of QMC-II.

Here we used Eq. (127) to describe the  $\sigma$  mass in matter. Note that  $\Gamma_{v/N}$  ( $v = \omega$  or  $\rho$ ) is the correction factor to the scalar density ratio (see around Eq. (130)). In actual calculations using the bag model, we find that  $\Gamma_{\omega,\rho/N} = 0.9996$ , which may be replaced by unity for practical purposes [19].

Next we must fix the two parameters in the parameterization for the  $\sigma$  mass in matter (see Eq. (127)). For example, we here consider three parameter sets:

- (A)  $a_\sigma = 3.0 \times 10^{-4}$  (MeV $^{-1}$ ),  $b_\sigma = 100 \times 10^{-8}$  (MeV $^{-2}$ ),
- (B)  $a_\sigma = 5.0 \times 10^{-4}$  (MeV $^{-1}$ ),  $b_\sigma = 50 \times 10^{-8}$  (MeV $^{-2}$ ),
- (C)  $a_\sigma = 7.5 \times 10^{-4}$  (MeV $^{-1}$ ),  $b_\sigma = 100 \times 10^{-8}$  (MeV $^{-2}$ ).

The parameter sets A, B and C give about 2%, 7% and 10% decreases of the  $\sigma$  mass at saturation density, respectively.

We then determine the coupling constants. As in the QMC-I model,  $g_\sigma^2$  and  $g_\omega^2$  are fixed to fit the binding energy at the saturation density for symmetric nuclear matter. Furthermore, the  $\rho$ -meson coupling constant is used to reproduce the bulk symmetry energy, 35 MeV [78]. We take  $m_\rho = 770$  MeV. The coupling constants and some calculated properties for symmetric nuclear matter are listed in Table 5. In Fig. 1, we show the total energy per nucleon for iso-symmetric nuclear matter calculated in QMC-I and three types of QMC-II. We note that the nuclear incompressibility is higher than that in QMC-I. However, it is still much lower than in QHD. As in QMC-I, the bag radius of the nucleon shrinks a little, while its rms radius swells a little.

We here comment on other non-relativistic or relativistic calculations for nuclear matter. In non-relativistic approach, the Brueckner-Bethe-Goldstone formalism [79] or variation chain summation methods [80] with an effective two-body interaction like the Argonne  $v_{18}$  are often used to study the nuclear bulk properties. However, it is well known that a phenomenological three-body force like Urbana IX is vital to produce the empirical values of the saturation energy at  $\rho_0$  and the incompressibility. As discussed in section 2.3, the QMC model in

Table 5: Coupling constants and calculated properties for symmetric nuclear matter at normal nuclear matter density (QMC-II). We take  $m_q = 5$  MeV,  $R_N = 0.8$  fm and  $m_\sigma = 550$  MeV. The effective nucleon mass,  $M_N^*$ , and the nuclear compressibility,  $K$ , are quoted in MeV.

type	$g_\sigma^2/4\pi$	$g_\omega^2/4\pi$	$g_\rho^2/4\pi$	$M_N^*$	$K$	$\delta R_N^*/R_N$	$\delta x_0^*/x_0$	$\delta r_q^*/r_q$
A	3.84	2.70	5.54	801	325	-0.01	-0.11	0.02
B	3.94	3.17	5.27	781	382	-0.01	-0.13	0.02
C	3.84	3.31	5.18	775	433	-0.02	-0.14	0.02

non-relativistic limit has already involved many-body interactions which are generated by the response of the nucleon to the applied scalar field – the scalar polarizability. Thus, it would be very interesting to compare the role of three-body forces in the conventional calculations with the contact interactions, Eq. (142), in the non-relativistic QMC.

The relativistic Dirac-Brueckner approach is also often used to study the bulk nuclear matter properties. Using it, Dalen *et al.* [81] have calculated various properties of iso-asymmetric nuclear matter. They have obtained a reasonable saturation property for symmetric nuclear matter and calculated the mean-field effective coupling constants, which decrease with increasing nuclear density. We note that the origin of such changes is different from that of the coupling-constant change in QMC. In contrast, using the relativistic Brueckner-Hartree-Fock approach with explicit intermediate negative energy states (in the Gross approximation), Jong and Lenske [82] have pointed out that the intermediate anti-nucleons provide a large vector repulsion and the effective mean-field coupling constants increase with increasing nuclear density. Furthermore, to obtain a reasonable saturation result, it is vital to modify the nucleonic off-shell form factor, which may relate to the internal structure of the nucleon, compared with the free one. Although it may be uncertain whether the anti-nucleon degrees of freedom is relevant in the intermediate state, it would be very interesting that the in-medium form factor plays the important role even in the relativistic Brueckner-Hartree-Fock calculation.

### 3.1.1 A new scaling formula for hadron masses in nuclear matter

We have discussed the effective nucleon and  $\omega$  meson masses in detail in sections 2.2.2 and 2.2.3. Here we describe a new scaling formula for hadron masses in matter that is predicted by the QMC model.

In the QMC-II model, the  $\sigma$  and  $\omega$  masses are respectively given by Eqs. (127) and (129). The nucleon mass is also expressed by Eq. (126). At small density, the scalar field is approximated

$$g_\sigma \sigma \simeq 200 \text{ (MeV)} \left( \frac{\rho_B}{\rho_0} \right), \quad (163)$$

and we find

$$\left( \frac{M_N^*}{M_N} \right) \simeq 1 - 0.21 \left( \frac{\rho_B}{\rho_0} \right) \quad \text{and} \quad \left( \frac{m_v^*}{m_v} \right) \simeq 1 - 0.17 \left( \frac{\rho_B}{\rho_0} \right). \quad (164)$$

Since the ratio of the quark-scalar densities for the nucleon,  $C_N$  (see Eq. (126)), is well approximated by a linear function of  $g_\sigma \sigma$

$$C_N(\sigma) = 1 - a_N \times (g_\sigma \sigma), \quad (165)$$

Eq. (120) can be solved easily and the nucleon mass is then expressed as

$$M_N^* = M_N - g_\sigma \left[ 1 - \frac{a_N}{2} (g_\sigma \sigma) \right] \sigma. \quad (166)$$

It is also true that the ratio for the vector meson can be well described by a similar, linear function of  $g_\sigma \sigma$ :

$$C_v(\sigma) = 1 - a_v \times (g_\sigma \sigma). \quad (167)$$

In the QMC model, it is possible to calculate masses of other hadrons in matter. In particular, there is a considerable interest in studying the masses of hyperons in medium – e.g.  $\Lambda$ ,  $\Sigma$  and  $\Xi$ . For the hyperons

Table 6: Slope parameters for the hadrons ( $\times 10^{-4}$  MeV $^{-1}$ ). Types A, B, C correspond to those in the effective  $\sigma$  mass.

type	$a_N$	$a_\omega$	$a_\rho$	$a_\Lambda$	$a_\Sigma$	$a_\Xi$
A	9.01	8.63	8.59	9.27	9.52	9.41
B	8.98	8.63	8.58	9.29	9.53	9.43
C	8.97	8.63	8.58	9.29	9.53	9.43

themselves we again use the MIT bag model and assume that the strange quark in the hyperon does not directly couple to the scalar field in MFA, as one would expect if the  $\sigma$  meson represented a two-pion-exchange potential. It is also assumed that the addition of a single hyperon to nuclear matter of density  $\rho_B$  does not alter the values of the scalar and vector mean-fields – that is, we take the local-density approximation to the hyperons. For example, the mass of the strange quark  $m_s$  is taken to be  $m_s = 250$  MeV, and new  $z$ -parameters in the mass formula are again introduced to reproduce the free hyperon masses:  $z_\Lambda = 3.131$ ,  $z_\Sigma = 2.810$ , and  $z_\Xi = 2.860$ . Using those parameters, we can calculate the masses of  $\Lambda$ ,  $\Sigma$  and  $\Xi$  in nuclear matter and finite nuclei [19].

In general, we find that the effective hadron mass in medium is given by

$$\begin{aligned} M_j^* &= M_j + \left( \frac{\partial M_j^*}{\partial \sigma} \right)_{\sigma=0} \sigma + \frac{1}{2} \left( \frac{\partial^2 M_j^*}{\partial \sigma^2} \right)_{\sigma=0} \sigma^2 + \dots, \\ &\simeq M_j - \frac{n_q}{3} g_\sigma \Gamma_{j/N} \sigma - \frac{n_q}{6} g_\sigma \Gamma_{j/N} C_j'(0) \sigma^2, \end{aligned} \quad (168)$$

where  $j$  stands for  $N$ ,  $\omega$ ,  $\rho$ ,  $\Lambda$ ,  $\Sigma$ ,  $\Xi$ , etc.,  $n_q$  is the number of light quarks in the hadron  $j$ ,  $\Gamma_{j/N} = S_j(0)/S_N(0)$  with the quark-scalar density,  $S_j$ , in  $j$ , and the scalar density ratio,  $C_j(\sigma) = S_j(\sigma)/S_j(0)$ .

Using Eqs. (163) and (168), the hyperon masses at low density are given by

$$\left( \frac{M_\Lambda^*}{M_\Lambda} \right) \simeq 1 - 0.12 \left( \frac{\rho_B}{\rho_0} \right), \quad \left( \frac{M_\Sigma^*}{M_\Sigma} \right) \simeq 1 - 0.11 \left( \frac{\rho_B}{\rho_0} \right) \quad \text{and} \quad \left( \frac{M_\Xi^*}{M_\Xi} \right) \simeq 1 - 0.05 \left( \frac{\rho_B}{\rho_0} \right), \quad (169)$$

where we take  $\Gamma_{\Lambda, \Sigma, \Xi/N} = 1$ , because we find that the  $\Gamma$  factor for the hyperons is again quite close to unity.

The linear approximation to the quark-scalar density ratio,  $C_j$ , is again relevant to not only the nucleon and vector mesons but also the hyperons:

$$C_j(\sigma) = 1 - a_j \times (g_\sigma \sigma), \quad (170)$$

where  $a_j$  is a slope parameter for the hadron  $j$ . We list them in Table 6. We should note that the dependence of  $a_j$  on the hadron is quite weak, and it ranges around  $8.6 \sim 9.5 \times 10^{-4}$  (MeV $^{-1}$ ).

If we ignore the weak dependence of  $a_j$  on the hadron and take  $\Gamma_{j/N} = 1$  in Eq. (168), the effective hadron mass can be rewritten in a quite simple form:

$$M_j^* \simeq M_j - \frac{n_q}{3} g_\sigma \left[ 1 - \frac{a_j}{2} (g_\sigma \sigma) \right] \sigma, \quad (171)$$

where  $a \simeq 9.0 \times 10^{-4}$  (MeV $^{-1}$ ). This mass formula can reproduce the hadron masses in matter quite well over a wide range of  $\rho_B$ , up to  $\sim 3\rho_0$ . (See also Eq. (135).)

Since the scalar field is common to all hadrons, Eq. (171) leads to a new, simple scaling relationship among the hadron masses:

$$\left( \frac{\delta m_v^*}{\delta M_N^*} \right) \simeq \left( \frac{\delta M_\Lambda^*}{\delta M_N^*} \right) \simeq \left( \frac{\delta M_\Sigma^*}{\delta M_N^*} \right) \simeq \frac{2}{3} \quad \text{and} \quad \left( \frac{\delta M_\Xi^*}{\delta M_N^*} \right) \simeq \frac{1}{3}, \quad (172)$$

where  $\delta M_j^* \equiv M_j - M_j^*$ . The factors,  $\frac{2}{3}$  and  $\frac{1}{3}$ , in Eq. (172) come from the ratio of the number of light quarks in the hadron  $j$  to that in the nucleon. This means that the hadron mass modification in nuclear medium (the scalar potential) is practically determined by only the number of light quarks, which feel the common scalar



field generated by the surrounding nucleons in medium, and the corresponding strength of the scalar field (see also section 3.3).

Finally, we note recent experiments concerning the change of the in-medium meson masses. In an helicity analysis of subthreshold  $\rho^0$  production on  $^2\text{H}$ ,  $^3\text{He}$  and  $^{12}\text{C}$  at low photo-production energies [42], the data support an in-medium modification of the  $\rho^0$  invariant mass, with the result being consistent with the QMC model [42, 43]. Recently, the ELSA tagged photon facility [44] and KEK [45] have independently measured the in-medium  $\omega$  meson mass. Using the Crystal Barrel/TAPS experiment at ELSA, the in-medium modification of  $\omega$  meson was studied via the reaction  $\gamma + A \rightarrow \omega + X \rightarrow \pi^0\gamma + X'$ , and a significant change toward lower masses for  $\omega$  mesons produced on the Nb target was observed. For momenta less than 500 MeV/c, they concluded that the in-medium  $\omega$  mass was about 722 MeV at  $0.6\rho_0$ . This is just the value predicted by QMC-II [19]. From the 12 GeV  $p + A$  reactions at KEK, it was found that the in-medium mass is reduced by about  $m_\omega^*/m_\omega \sim 1 - 0.1(\rho_B/\rho_0)$ , which is also consistent with the QMC model.

### 3.1.2 Variations of quark and gluon condensates in nuclear matter

The QCD ground state is highly non-trivial, and the strong condensates of scalar quark-antiquark pairs  $\langle\bar{q}q\rangle$  and gluon fields  $\langle G_{\mu\nu}^a G^{a\mu\nu}\rangle$  may play important roles in a wide range of low-energy hadronic phenomena [83, 84, 85]. Therefore, it is quite interesting to study the density dependence of the condensates in nuclear matter [86]. The vacuum values of the lowest-dimensional quark and gluon condensates are typically given by [84]

$$Q_0 \equiv \langle\bar{q}q\rangle_0 \simeq -(225 \pm 25\text{MeV})^3, \quad (173)$$

$$G_0 \equiv \langle G_{\mu\nu}^a G^{a\mu\nu}\rangle_0 \simeq (360 \pm 20\text{MeV})^4. \quad (174)$$

Drukarev *et al.* [85], Cohen *et al.* [87] and Lutz *et al.* [88] have shown that the leading dependence on the nuclear density,  $\rho_B$ , of the quark condensate in nuclear matter,  $Q(\rho_B)$ , is given by the model-independent form:

$$\frac{Q(\rho_B)}{Q_0} \simeq 1 - \frac{\sigma_N}{f_\pi^2 m_\pi^2} \rho_B, \quad (175)$$

where  $\sigma_N$  is the pion-nucleon sigma term (empirically  $\sigma_N \simeq 45$  MeV [89]),  $m_\pi$  is the pion mass (138 MeV) and  $f_\pi \simeq 93$  MeV, the pion decay constant. Further, the strange quark content in the nucleon at finite density (and temperature) was studied in Ref. [90] using the Nambu–Jona-Lasinio (NJL) model, supplemented by an instanton induced interaction involving the in-medium quark condensates. The gluon condensate at finite density,  $G(\rho_B)$ , has also been discussed in Ref. [87].

We here consider the variations of quark and gluon condensates in nuclear matter within QMC-II (see also Refs. [13, 18, 19, 53, 54]). The total energy per nucleon is given by Eq. (161). The density-dependent quark condensate  $Q(\rho_B)$  is formally derived by applying the Hellmann–Feynman theorem to the chiral-symmetry-breaking quark mass term of the total Hamiltonian. One finds the relation for the quark condensate in nuclear matter at the baryon density  $\rho_B$ :

$$m_q(Q(\rho_B) - Q_0) = m_q \frac{d}{dm_q} \mathcal{E}(\rho_B), \quad (176)$$

where  $\mathcal{E}(\rho_B) = \rho_B(E^{\text{tot}}/A)$  (see Eq. (161)) and  $m_q$  is the average, current quark mass of the  $u$  and  $d$  quarks. The resulting value for  $Q/Q_0$  as a function of density is shown in Fig. 2 – dashed line. (We have chosen the quark mass to be  $m_q = 5$  MeV and the bag radius of the free nucleon  $R_N = 0.8$  fm, but the result is quite insensitive to these choices.)

Using Eq. (176), the Gell-Mann–Oakes–Renner relation and the explicit expression for the self-consistency condition of the  $\sigma$  field in nuclear matter Eq. (162) lead to the following explicit relation for the ratio of  $Q(\rho_B)$  to  $Q_0$ :

$$\begin{aligned} \frac{Q(\rho_B)}{Q_0} = 1 & - \left( \frac{\sigma_N}{m_\pi^2 f_\pi^2} \right) \left( \frac{m_\sigma^*}{g_\sigma} \right)^2 (g_\sigma \sigma) \left[ 1 - \frac{1}{g_\sigma} \left( \frac{dg_\sigma^q}{dm_q} \right) (g_\sigma \sigma) \right] \\ & - \left( \frac{\sigma_N \rho_0}{6S_N(0)m_\pi^2 f_\pi^2} \right) \rho_r^2 \left[ \frac{\rho_0}{m_\omega^{*2}} \left( \frac{dg_\omega^2}{dm_q} \right) + \frac{\rho_0}{4m_\rho^{*2}} (2f_p - 1)^2 \left( \frac{dg_\rho^2}{dm_q} \right) \right], \end{aligned} \quad (177)$$

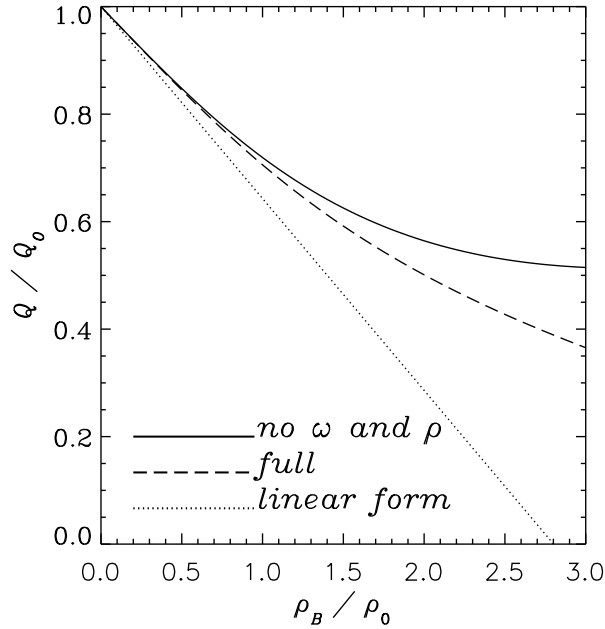


Figure 2: Quark condensate at finite density using parameter type B of QMC-II. The dashed and dotted curves are respectively for the full calculation in symmetric nuclear matter and the linear approximation, Eq. (179). The solid curve is the result corrected by removing the spurious  $\omega$  and  $\rho$  contributions.

where  $\rho_r = \rho_B/\rho_0$  and  $f_p = \rho_p/\rho_B$ . Because  $m_q$  enters only in the combination  $m_q - g_\sigma^q \sigma$ , which is generally regarded as the chiral-symmetry-breaking term in nuclear medium, we were able to evaluate  $(dm_\sigma^*/dm_q)$  in terms of the derivative of  $m_\sigma^*$  with respect to the applied scalar field  $\sigma$ .

In Eq. (177) we have followed the usual convention of identifying  $3m_q S_N(0)$ , which is the sigma commutator in the free MIT bag, as the experimental pion-nucleon sigma term,  $\sigma_N$ . It is well known that the meson cloud of the nucleon (mainly the pions), as well as its strange quark content contribute significantly to  $\sigma_N$  [91]. However, because we are concerned primarily with the variation of  $Q$  in matter from its free value,  $Q_0$ , it should be reasonable to replace  $\sigma_N$  in Eq. (177) by its empirical value. (We note that the main variation of  $Q$  in medium is generated by the  $\sigma$  mean-field.)

Clearly, from Eq. (177), the leading dependence of the quark condensate on the density is given by the scalar field:

$$\frac{Q(\rho_B)}{Q_0} \simeq 1 - \frac{\sigma_N}{m_\pi^2 f_\pi^2} \left( \frac{m_\sigma}{g_\sigma} \right)^2 (g_\sigma \sigma). \quad (178)$$

One can easily show that Eq. (178) reduces to the model-independent result, Eq. (175), to leading order in the density, so that for small  $\rho_r$  one has (for type B of QMC-II):

$$Q(\rho_B)/Q_0 \simeq 1 - 0.357\rho_r. \quad (179)$$

This is shown as the dotted line in Fig. 2.

Equation (177) also involves deviations of the quark-meson coupling constants with respect to  $m_q$ . In principle, if one could derive these coupling constants from QCD, their dependence on  $m_q$  would be given. Within the present model there is no reason to believe that the couplings should vary with  $m_q$ . This is especially so for the vector couplings since they involve conserved vector currents. On the other hand, we require that our model reproduces the correct saturation energy and density of nuclear matter whatever parameters are chosen for the free nucleon. As a consequence, the coupling constants depend on  $m_q$  in a way that has nothing

to do with chiral symmetry breaking. (For example, for type B of QMC-II, we find  $g_\sigma^q = 4.891 - 0.005880m_q + 1.200 \times 10^{-5}m_q^2$ ,  $g_\omega^2 = 39.59 + 0.03828m_q + 1.144 \times 10^{-3}m_q^2$  and  $g_\rho^2 = 66.3 - 0.02m_q$ , with  $m_q$  in MeV.)

In order to extract a physically meaningful result for  $Q/Q_0$  we should therefore remove the spurious contributions associated with  $\frac{dg_M^q}{dm_q}$  ( $M = \sigma, \rho, \omega$ ) in Eq. (177). In fact, the variation of  $g_\sigma^q$  with  $m_q$  is extremely small so we need only correct the  $\omega$  and  $\rho$  contributions. The final, corrected result is shown as the solid line in Fig.2. Even in MFA, our calculations show that the higher-order contributions in the nuclear density become very important and that they weaken the chiral symmetry restoration at high density. In QMC-II, the  $\sigma$  field in nuclear matter is suppressed at high density (for example,  $g_\sigma\sigma \simeq 200$  (300) MeV at  $\rho_0$  ( $3\rho_0$ )) because the quark scalar density,  $S_N$ , decreases significantly as the density rises, as a result of the change in the quark structure of the bound nucleon (see section 3.1). Since the reduction of the quark condensate is mainly controlled by the scalar field, it is much smaller than in the simple, linear approximation, Eq. (179). From the difference between the solid and dashed curves we see that the correction for the dependence of the coupling constants on  $m_q$  is significant and this should be born in mind in any phenomenological treatment.

We should note here that, from extensive studies of chiral perturbation theory for nuclear matter, especially the work of Birse [92], a reduction of the quark condensate from its vacuum value may *not* be enough to conclude that the chiral symmetry has been partially restored – in particular, if part of the change in  $\langle \bar{q}q \rangle$  arises from low-momentum pions. We note also that higher-order condensates may play an increasingly important role as the quark condensate tends to zero.

Next let us consider the in-medium gluon condensate. Cohen et al. [87] also developed a model-independent prediction of the gluon condensate that is valid to first order in the nuclear density through an application of the trace anomaly and the Hellmann–Feynman theorem. Following their approach, the ratio of the gluon condensate in nuclear matter  $G(\rho_B)$  to that in vacuum  $G_0$  is given by

$$G(\rho_B)/G_0 \simeq 1 - \left( \frac{8}{9G_0} \right) [\mathcal{E}(\rho_B) - 2m_q(Q(\rho_B) - Q_0) - m_s(Q_s(\rho_B) - Q_{s0})], \quad (180)$$

where  $m_s$  is the strange-quark mass and  $Q_s(\rho_B)$  ( $Q_{s0}$ ) is the strange-quark condensate in nuclear matter (in vacuum). Up to first order in the density, the change of the strange-quark condensate may be written in terms of the strange quark content of the nucleon in free space,  $\mathcal{S}$ :

$$m_s(Q_s(\rho_B) - Q_{s0}) = \mathcal{S}\rho_B + \mathcal{O}(\rho_B^2). \quad (181)$$

The strange quark content is commonly specified by the dimensionless quantity,  $y$ , defined by

$$y \equiv \frac{2\langle \bar{s}s \rangle_N}{\langle \bar{u}u + \bar{d}d \rangle_N}, \quad (182)$$

which leads to  $\mathcal{S} = (m_s/2m_q)\sigma_N y$ . Roughly speaking,  $y$  represents the probability to find  $s$  or  $\bar{s}$  in the nucleon and is a measure of the OZI-rule violation. If  $m_s/m_q \simeq 25$  and  $y \simeq 0.45$  [87], we get  $\mathcal{S} \simeq 250$  MeV. We note, however, that  $y \simeq 0.45$  is an extreme value. In the analysis below, we shall take care to examine the sensitivity to the full range of variation of  $y$ .

At very low  $\rho_B$ ,  $\mathcal{E}(\rho_B)$  can be expanded as [17]

$$\mathcal{E}(\rho_B) = M_N \rho_B \left[ 1 + \frac{3}{10M_N^2} \left( \frac{3\pi^2}{2} \right)^{2/3} \rho_B^{2/3} \right] + \mathcal{O}(\rho_B^2), \quad (183)$$

where the second term in the bracket is the non-relativistic Fermi-gas energy. Using the approximate form,  $g_\sigma\sigma \simeq 214$  (MeV)  $\times \rho_r$  (for type B), we find

$$2m_q(Q(\rho_B) - Q_0) = 214(\text{MeV}) \times \sigma_N \left( \frac{m_\sigma}{g_\sigma} \right)^2 \rho_r + \mathcal{O}(\rho_r^2). \quad (184)$$

Choosing the central value of  $G_0$  in Eq. (174), we then get the in-medium gluon condensate at low  $\rho_B$  (for type B):

$$G(\rho_B)/G_0 = 1 - (0.03892\rho_r + 0.001292\rho_r^{5/3}) + \mathcal{O}(\rho_r^2). \quad (185)$$

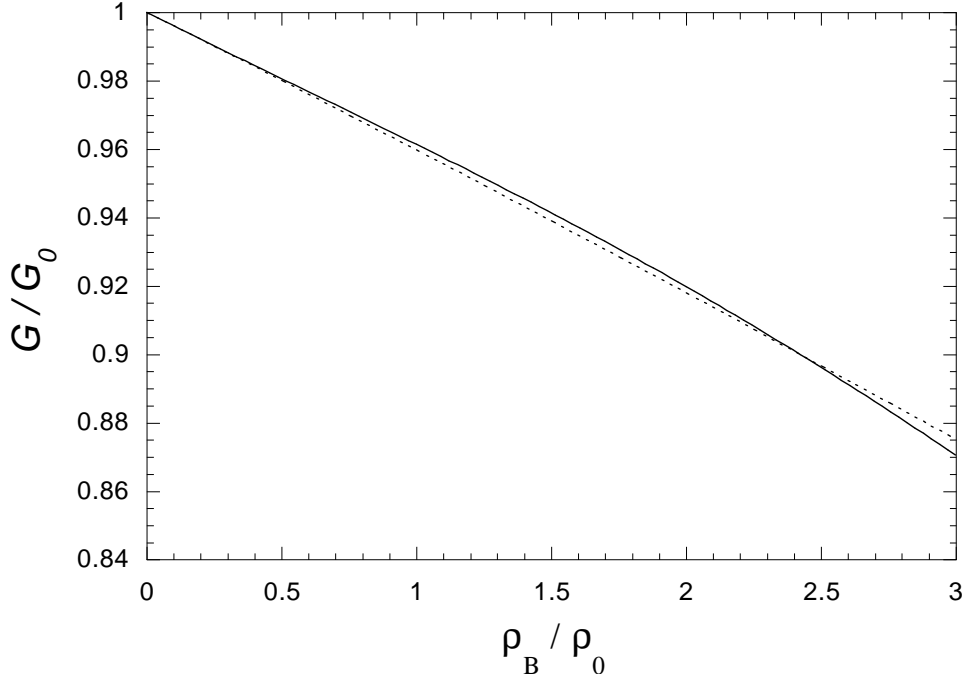


Figure 3: Gluon condensate at finite density using parameter type B. The solid and dotted curves are respectively for the full calculation in symmetric nuclear matter and the approximation, Eq. (185).

Our numerical results for the full calculation as well as the approximate calculation with Eq. (185) are shown in Fig. 3 (for  $m_q = 5$  MeV and  $R_N = 0.8$  fm). The reduction of the gluon condensate at finite density is not large; for example, it is reduced by only 4% at  $\rho_0$ . The approximation of Eq. (185) works very well for a wide range of the nuclear density, which may imply that the effect of higher-order contributions (in powers of the density) is small for the gluon condensate. However, one should keep in mind that the in-medium gluon condensate evaluated here contains a large uncertainty, originating from the uncertainty in the value for the strange quark content of the nucleon in free space. We note that if we assume a vanishing strange quark content of the nucleon in free space ( $\mathcal{S} = 0$  or  $y = 0$ ), the gluon condensate would be reduced by about 6% at  $\rho_0$ .

Finally, we relate the quark condensate to the variation of the hadron mass in nuclear matter. In QMC-II, the hadron mass at low  $\rho_B$  is simply given in terms of the scalar field (see Eq. (171)):

$$M_j^* \simeq M_j - \frac{n_q}{3}(g_\sigma \sigma), \quad (186)$$

where  $j(= N, \omega, \rho, \Lambda, \text{etc.})$ . Since the quark condensate at low  $\rho_B$  is also determined by the scalar field, we find a simple relation between the variations of the hadron mass and the quark condensate:

$$\delta M_j^* \simeq \left( \frac{m_\pi^2 f_\pi^2}{3\sigma_N} \right) \left( \frac{g_\sigma}{m_\sigma} \right)^2 n_q \left( 1 - \frac{Q(\rho_B)}{Q_0} \right) \approx 200(\text{MeV}) \times n_q \left( 1 - \frac{Q(\rho_B)}{Q_0} \right), \quad (187)$$

where  $\delta M_j^* = M_j - M_j^*$ .

However, as shown in Ref. [92], we know that the nucleon mass in matter cannot depend in any simple way on the quark condensate alone because the leading non-analytic contribution (LNAC) to the pion-nucleon sigma term – the term of order  $m_\pi^3$  – should *not* appear in the nucleon-nucleon interaction [93]. To discuss this problem further, we have to include pions self-consistently in the QMC model, which is a future study.

We note that in Ref. [18] the effect of  $\delta$  meson on the quark condensates and a measure of isospin symmetry breaking in the in-medium quark condensates are also discussed in details.

### 3.1.3 Nuclear matter at finite temperature and neutron stars

Song and Su extended the QMC model to include the effect of finite temperature [94], and applied the resulting EOS for nuclear matter to the liquid-gas phase transition. In their calculations, they simply added the thermal distribution functions for the nucleon and anti-nucleon to the energy-momentum expressions and the self-consistency condition. They found that the EOS at finite temperature is much softer than that in QHD and is comparable to that in the Zimanyi-Moszkowski model [62]. Furthermore, they have found that the critical temperature of the liquid-gas phase transition becomes lower in the QMC than in QHD.

Panda *et al.* have also studied hot nuclear matter within the framework of the QMC model [95]. In their calculations, the possible single-particle quark and antiquark energies at finite temperature  $T$  are summed up in the bag energy. The quark (antiquark) energy in the orbit  $(n, \kappa)$  ( $n$  specifies the number of nodes) is estimated as

$$\epsilon_{\pm}^{n\kappa} = \Omega^{n\kappa} \pm g_{\omega}^q \omega R_N, \quad (188)$$

where

$$\Omega^{n\kappa} = (x_{n\kappa}^2 + R_N^2 m_q^{*2})^{1/2} \quad (189)$$

with  $m_q^* = m_q - g_{\sigma}^q \sigma$ . The eigenvalue  $x_{n\kappa}$  is given by the boundary condition at the bag surface. The total energy from the quarks and antiquarks then reads

$$E_{tot} = 3 \sum_{n,\kappa} \frac{\Omega^{n\kappa}}{R_N} \left[ \frac{1}{e^{(\epsilon_{+}^{n\kappa}/R_N - \mu_q)/T} + 1} + \frac{1}{e^{(\epsilon_{-}^{n\kappa}/R_N + \mu_q)/T} + 1} \right], \quad (190)$$

with  $\mu_q$  the chemical potential for the quark. The bag energy now becomes

$$E_{bag} = E_{tot} - \frac{z_0}{R_N} + \frac{4\pi}{3} R_N^3 B, \quad (191)$$

which reduces to the usual form at zero temperature. They also adopted the MQMC model to include the medium-dependent bag parameter:

$$B = B_0 \exp \left( -\frac{4g_{\sigma}^B \sigma}{M_N} \right), \quad (192)$$

with  $g_{\sigma}^B$  as an additional parameter (see section 2.5).

They have found that the scalar mean field at zero density attains a nonzero value at a temperature of 200 MeV similar to the Walecka model calculations for nuclear matter [96], which is indicative of a phase transition to a system with baryon-antibaryon pairs. There is a softening in the phase transition in this case as compared to the earlier calculations. This is because the thermal contributions from the quarks are dominant and lead to a rise of the effective nucleon mass with temperature. The nucleon bag shrinks in size with increasing temperature. The nucleon mass at finite temperature and zero baryon density is then appreciably different from that in vacuum. This approach has been applied to various nuclear and stellar problems: for example, rotating neutron stars in the Komatsu-Eriguchi-Hachisu method [97] and hybrid stars which consist of both hadron and quark matter [98]. Recently they have also studied kaon condensation in compact stars [99].

Zakout *et al.* have developed a QMC model at finite temperature in a similar manner. They have, however, included the effect of dilatons in their model [100]. Applying the effective potential with dilatons to nuclear matter, the nucleon properties at finite temperature are found to be appreciably different from those in cold nuclear matter. The dilaton potential improves the shape of the saturation curve at  $T = 0$  and significantly affects the properties of hot nuclear matter. Hot hypernuclear matter [101], neutron stars [102] and relativistic heavy ion reactions [103] have also been investigated in their approach.

## 3.2 Finite nuclei - $^{16}\text{O}$ , $^{40}\text{Ca}$ , $^{48}\text{Ca}$ , $^{90}\text{Zr}$ , $^{208}\text{Pb}$

To describe a finite nucleus with different numbers of protons and neutrons ( $Z \neq N$ ), it is necessary to include the contributions of the  $\rho$  meson explicitly. Any realistic treatment also needs the inclusion of Coulomb

force. The variation of the Lagrangian for QMC-I (see Eq. (122)) results in the following equations for static, spherically symmetric nuclei:

$$\begin{aligned}\frac{d^2}{dr^2}\sigma(r) + \frac{2}{r}\frac{d}{dr}\sigma(r) - m_\sigma^2\sigma(r) &= -g_\sigma C_N(\sigma(r))\rho_s(r) \\ &\equiv -g_\sigma C_N(\sigma(r)) \sum_{\alpha}^{occ} d_\alpha(r)(|G_\alpha(r)|^2 - |F_\alpha(r)|^2),\end{aligned}\quad (193)$$

$$\begin{aligned}\frac{d^2}{dr^2}\omega(r) + \frac{2}{r}\frac{d}{dr}\omega(r) - m_\omega^2\omega(r) &= -g_\omega\rho_B(r) \\ &\equiv -g_\omega \sum_{\alpha}^{occ} d_\alpha(r)(|G_\alpha(r)|^2 + |F_\alpha(r)|^2),\end{aligned}\quad (194)$$

$$\begin{aligned}\frac{d^2}{dr^2}b(r) + \frac{2}{r}\frac{d}{dr}b(r) - m_\rho^2b(r) &= -\frac{g_\rho}{2}\rho_3(r) \\ &\equiv -\frac{g_\rho}{2} \sum_{\alpha}^{occ} d_\alpha(r)(-)^{t_\alpha-1/2}(|G_\alpha(r)|^2 + |F_\alpha(r)|^2),\end{aligned}\quad (195)$$

$$\begin{aligned}\frac{d^2}{dr^2}A(r) + \frac{2}{r}\frac{d}{dr}A(r) &= -e\rho_p(r) \\ &\equiv -e \sum_{\alpha}^{occ} d_\alpha(r)(t_\alpha + \frac{1}{2})(|G_\alpha(r)|^2 + |F_\alpha(r)|^2),\end{aligned}\quad (196)$$

where  $d_\alpha(r) = (2j_\alpha + 1)/4\pi r^2$  and

$$\begin{aligned}\frac{d}{dr}G_\alpha(r) + \frac{\kappa}{r}G_\alpha(r) - [\epsilon_\alpha - g_\omega\omega(r) - t_\alpha g_\rho b(r) &- (t_\alpha + \frac{1}{2})eA(r) + M_N \\ &- g_\sigma(\sigma(r))\sigma(r)] F_\alpha(r) = 0,\end{aligned}\quad (197)$$

$$\begin{aligned}\frac{d}{dr}F_\alpha(r) - \frac{\kappa}{r}F_\alpha(r) + [\epsilon_\alpha - g_\omega\omega(r) - t_\alpha g_\rho b(r) &- (t_\alpha + \frac{1}{2})eA(r) - M_N \\ &+ g_\sigma(\sigma(r))\sigma(r)] G_\alpha(r) = 0.\end{aligned}\quad (198)$$

Here  $iG_\alpha(r)/r$  and  $-F_\alpha(r)/r$  are respectively the radial part of the upper and lower components of the solution to the Dirac equation for the nucleon ( $\epsilon_\alpha$  being the energy) under the normalization condition:

$$\int dr(|G_\alpha(r)|^2 + |F_\alpha(r)|^2) = 1. \quad (199)$$

As usual,  $\kappa$  specifies the angular quantum numbers and  $t_\alpha$  the eigenvalue of the isospin operator,  $\tau_3^N/2$ .  $C_N(\sigma)$  and  $g_\sigma(\sigma)$  are practically given by Eqs. (115), (165) and (166), i.e.,

$$g_\sigma(\sigma(\vec{r})) = g_\sigma \left[ 1 - \frac{a_N}{2} g_\sigma \sigma(\vec{r}) \right]. \quad (200)$$

The total energy of the system is then given by

$$\begin{aligned}E_{tot} &= \sum_{\alpha}^{occ} (2j_\alpha + 1) \epsilon_\alpha - \frac{1}{2} \int d\vec{r} [-g_\sigma C_N(\sigma(r))\sigma(r)\rho_s(r) \\ &+ g_\omega\omega(r)\rho_B(r) + \frac{1}{2}g_\rho b(r)\rho_3(r) + eA(r)\rho_p(r)].\end{aligned}\quad (201)$$

For the QMC-II model, the Lagrangian density, Eq. (128), leads

$$\begin{aligned}\frac{d^2}{dr^2}\sigma(r) + \frac{2}{r}\frac{d}{dr}\sigma(r) - m_\sigma^{*2}\sigma(r) &= -g_\sigma C_N\rho_s(r) - m_\sigma m_\sigma^* g_\sigma [a_\sigma - 2b_\sigma g_\sigma \sigma(r)]\sigma(r)^2 \\ &+ \frac{2}{3}g_\sigma [m_\omega^* \Gamma_{\omega/N} C_\omega \omega(r)^2 + m_\rho^* \Gamma_{\rho/N} C_\rho b(r)^2],\end{aligned}\quad (202)$$

$$\frac{d^2}{dr^2}\omega(r) + \frac{2}{r}\frac{d}{dr}\omega(r) - m_\omega^{*2}\omega(r) = -g_\omega\rho_B(r), \quad (203)$$

$$\frac{d^2}{dr^2}b(r) + \frac{2}{r}\frac{d}{dr}b(r) - m_\rho^{*2}b(r) = -\frac{g_\rho}{2}\rho_3(r). \quad (204)$$

Table 7: Model parameters for finite nuclei (QMC-I).

$m_q(\text{MeV})$	$R_N(\text{fm})$	$g_\sigma^2/4\pi$	$g_\omega^2/4\pi$	$g_\rho^2/4\pi$	$m_\sigma(\text{MeV})$
0	0.6	3.55	6.29	6.79	429
	0.8	2.94	5.26	6.93	407
	1.0	2.51	4.50	7.03	388
5	0.6	3.68	6.34	6.78	436
	0.8	3.12	5.31	6.93	418
	1.0	2.69	4.56	7.02	401
10	0.6	3.81	6.37	6.78	443
	0.8	3.28	5.36	6.92	428
	1.0	2.91	4.62	7.02	416

The photon field and nucleon wave functions are again given by Eqs. (196)-(198). Then, the total energy reads

$$\begin{aligned}
E_{tot} = & \sum_{\alpha}^{occ} (2j_{\alpha} + 1) \epsilon_{\alpha} - \frac{1}{2} \int d\vec{r} [-g_{\sigma} D(\sigma(r)) \sigma(r) \\
& + g_{\omega} \omega(r) \rho_B(r) + \frac{1}{2} g_{\rho} b(r) \rho_3(r) + e A(r) \rho_p(r)],
\end{aligned} \tag{205}$$

where

$$\begin{aligned}
D(\sigma(r)) = & C_N \rho_s(r) + m_{\sigma} m_{\sigma}^* [a_{\sigma} - 2b_{\sigma} g_{\sigma} \sigma(r)] \sigma(r)^2 \\
& - \frac{2}{3} [m_{\omega}^* \Gamma_{\omega/N} C_{\omega} \omega(r)^2 + m_{\rho}^* \Gamma_{\rho/N} C_{\rho} b(r)^2].
\end{aligned} \tag{206}$$

We are now in a position to show results for finite nuclei. We calculate the properties of  $^{16}\text{O}$ ,  $^{40}\text{Ca}$ ,  $^{48}\text{Ca}$ ,  $^{90}\text{Zr}$  and  $^{208}\text{Pb}$ . Firstly, we consider the QMC-I model [52]. Equations (193) to (199) give a set of coupled non-linear differential equations, which may be solved by a standard iteration procedure. The numerical calculation was carried out by modifying the technique described by Horowitz *et al.* [78, 104]. The calculation is achieved in at most 20 iterations when it is performed with a maximum radius of 12 (15) fm on a mesh of 0.04 fm for medium mass (Pb) nuclei.

There are seven parameters to be determined:  $g_{\sigma}$ ,  $g_{\omega}$ ,  $g_{\rho}$ ,  $e$ ,  $m_{\sigma}$ ,  $m_{\omega}$  and  $m_{\rho}$ . We first fix  $m_{\omega}$ ,  $m_{\rho}$  and  $e^2/4\pi (= 1/137.036)$  to be the experimental values. The coupling constants  $g_{\sigma}$  and  $g_{\omega}$  were fixed so as to produce the nuclear matter properties with  $m_{\sigma} = 550$  MeV in section 3.1. The  $\sigma$  meson mass, however, determines the range of the attractive interaction and changes in  $m_{\sigma}$  affect the nuclear-surface slope and its thickness. Therefore, we adjust  $m_{\sigma}$  to produce the root-mean-square (rms) charge radius of  $^{40}\text{Ca}$ :  $r_{ch}(^{40}\text{Ca}) = 3.48$  fm, the experimental value [105]. We here notice that variations of  $m_{\sigma}$  at fixed  $(g_{\sigma}/m_{\sigma})$  have no effect on the infinite nuclear matter properties. Therefore, keeping the ratio  $(g_{\sigma}/m_{\sigma})$  constant we vary  $m_{\sigma}$  to fit the rms charge radius of  $^{40}\text{Ca}$ . We expect that  $m_{\sigma}$  ranges around  $400 \sim 550$  MeV [31, 106]. The last parameter  $g_{\rho}$  is adjusted to yield the bulk symmetry energy per baryon of 35 MeV [78]. We summarize the parameters in Table 7.

In Fig. 4, we show the baryon and scalar densities as well as the effective nucleon mass in  $^{208}\text{Pb}$ . We expect that the baryon density in the interior of lead would be close to the saturation density of infinite nuclear matter,  $\rho_0$ . As seen in the figure, the calculated baryon density at the center is quite close to  $0.15 \text{ fm}^{-3}$ , which supports our choice of the parameters.

Next we show the charge density distributions calculated,  $\rho_{ch}$ , in comparison with those of QHD [17, 78] and the experimental data in Figs. 5–9. Having solved Eqs. (193)-(199), we obtain the *point*-proton and neutron densities in a nucleus. Thus, we should estimate the effect of proton form factor on the densities. (Note that our calculation shows the effect of neutron form factor is eventually small and ignored in the results.) One can calculate the charge density by a convolution of the point-proton density,  $\rho_p(\vec{r})$ , with the proton charge

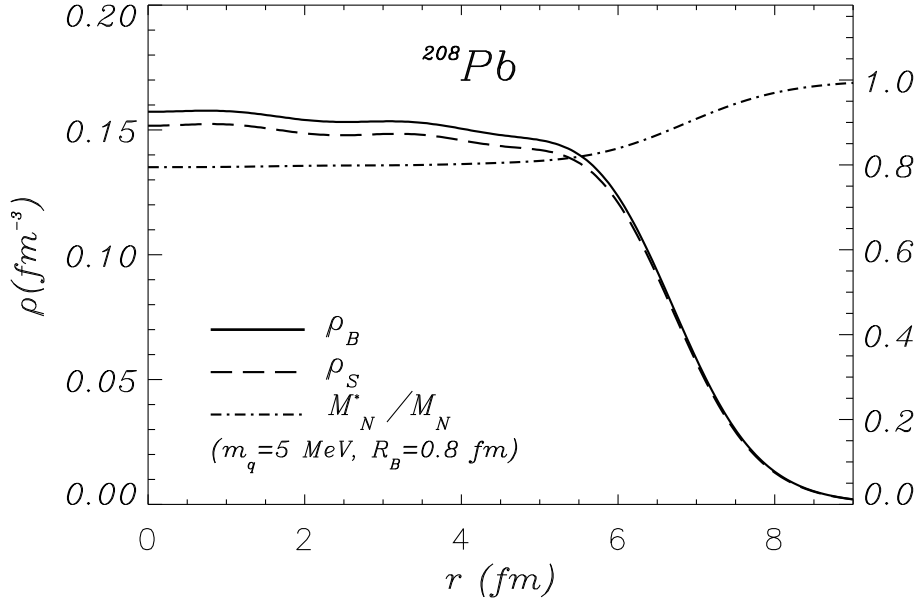


Figure 4: Model predictions for the effective nucleon mass, the baryon and scalar densities in  $^{208}\text{Pb}$  (for  $m_q = 5$  MeV and  $R_N = 0.8$  fm). The scale on the right vertical axis is for  $M_N^*/M_N$  (from Ref. [52]).

distribution,  $\rho_{ch}^p(\vec{r})$ :

$$\rho_{ch}(\vec{r}) = \int d\vec{r}' \rho_{ch}^p(\vec{r} - \vec{r}') \rho_p(\vec{r}'), \quad (207)$$

where we have used a Gaussian form for  $\rho_{ch}^p$

$$\rho_{ch}^p(\vec{r}) = (\beta/\pi)^{3/2} \exp(-\beta r^2). \quad (208)$$

The parameter  $\beta$ , which determines the proton size, is chosen so as to reproduce the experimental rms charge radius of the proton, 0.82 fm (i.e.,  $\beta = 2.231 \text{ fm}^{-2}$ ). In the QMC model, the rms radius of the nucleon in nuclear matter increases a little. However, since this amount is quite small, it can be ignored in the numerical calculations of nuclear parameters.

In Fig. 6, the charge density distribution for  $^{40}\text{Ca}$  is presented. The experimental data is taken from Ref. [107]. Once the rms charge radius of  $^{40}\text{Ca}$  is fitted by adjusting  $m_\sigma$ , the QMC model can reproduce  $\rho_{ch}(^{40}\text{Ca})$  quite well. As seen in the figures, the calculated charge densities lie almost within the experimental area. We note that the dependence of  $\rho_{ch}(^{40}\text{Ca})$  on the bag radius is quite weak [52].

It is interesting to see the quantum oscillations of the interior density in lead (see Fig. 8). This is probably a consequence of using a pure shell model, with no configuration mixing. The dependence of  $\rho_{ch}(^{208}\text{Pb})$  on the quark mass is again not strong. We note that the dependence of  $\rho_{ch}(^{208}\text{Pb})$  on the free nucleon size is also quite weak [52]. As seen in the figures, our model gives charge densities very close to those of QHD and still somewhat larger in the central region than those observed experimentally [108].

In Figs. 5 and 7, we show respectively the charge density distributions for  $^{16}\text{O}$  and  $^{90}\text{Zr}$ . For zirconium the calculated  $\rho_{ch}$  lies in between that of the non-relativistic density-dependent Hartree-Fock calculations [109] and that of QHD [78]. The experimental data for oxygen and zirconium are taken from Refs. [110] and [111]. (For both cases the dependence of  $\rho_{ch}$  on  $m_q$  and  $R_N$  is again weak.)

To see the isotope shift in charge density we have plotted  $r^2$  times the difference between  $\rho_{ch}(^{40}\text{Ca})$  and  $\rho_{ch}(^{48}\text{Ca})$  in Fig. 9. Its dependence on the bag radius is weak for a small quark mass while it becomes a little



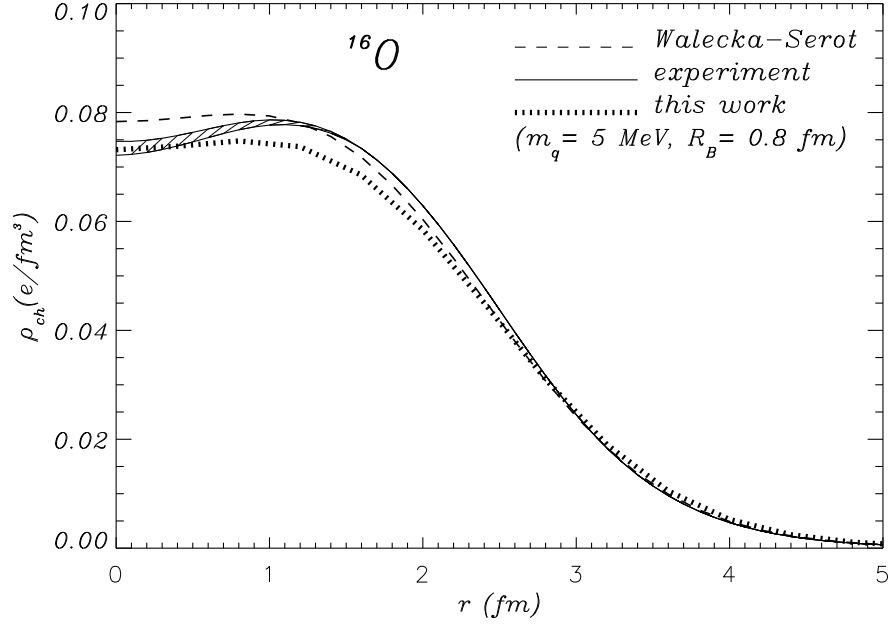


Figure 5: Same as Fig. 6 but for  $^{16}\text{O}$  (from Ref. [52]).

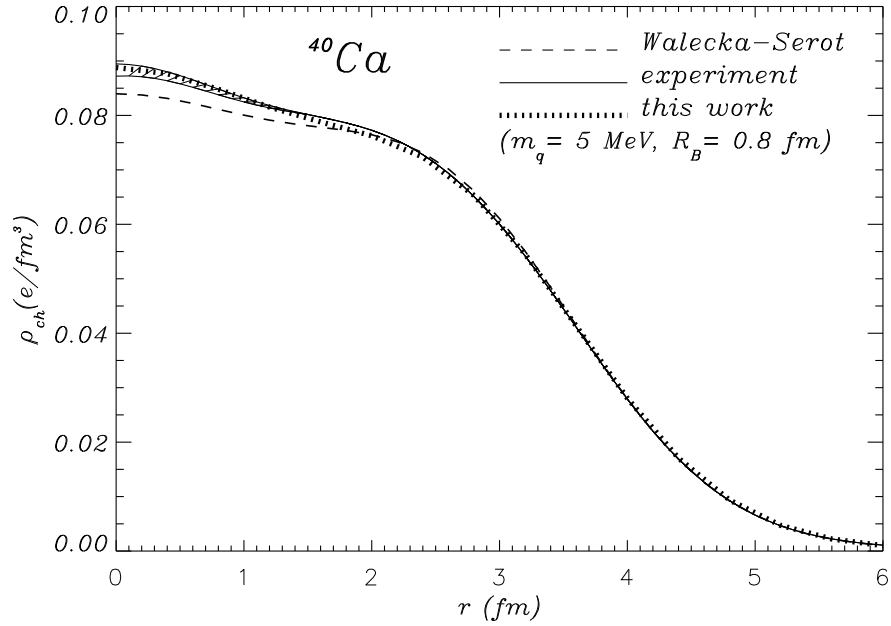


Figure 6: Charge density distribution for  $^{40}\text{Ca}$  (for  $m_q = 5 \text{ MeV}$  and  $R_N = 0.8 \text{ fm}$ ) compared with the experimental data (hatched area) and that of QHD (from Ref. [52]).

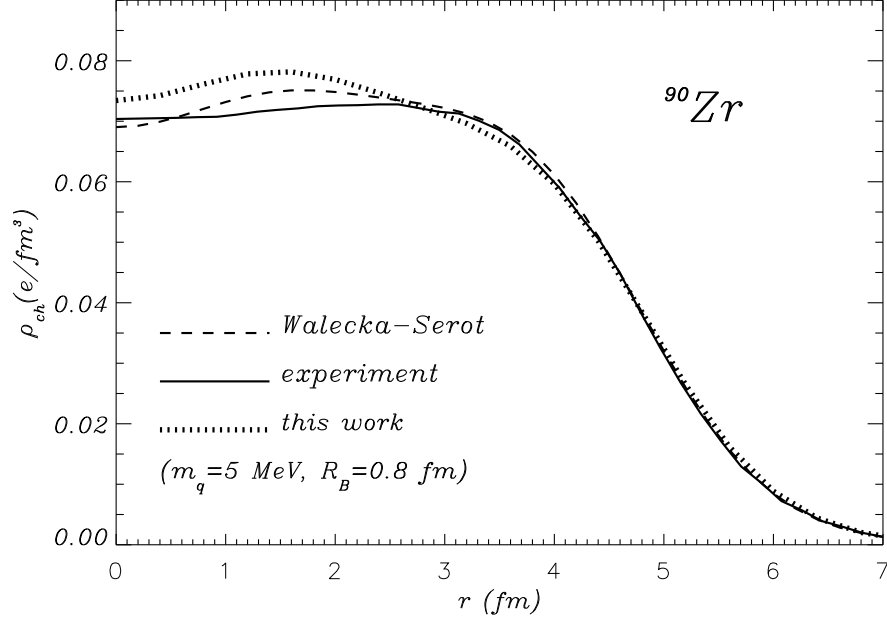


Figure 7: Same as Fig. 6 but for  $^{90}\text{Zr}$  (from Ref. [52]).

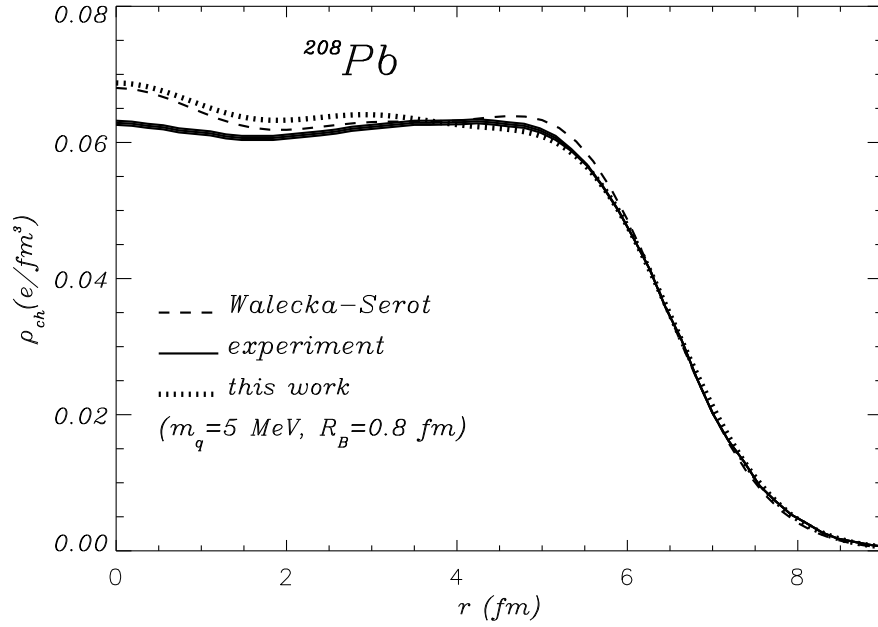


Figure 8: Same as Fig. 6 but for  $^{208}\text{Pb}$  (from Ref. [52]).

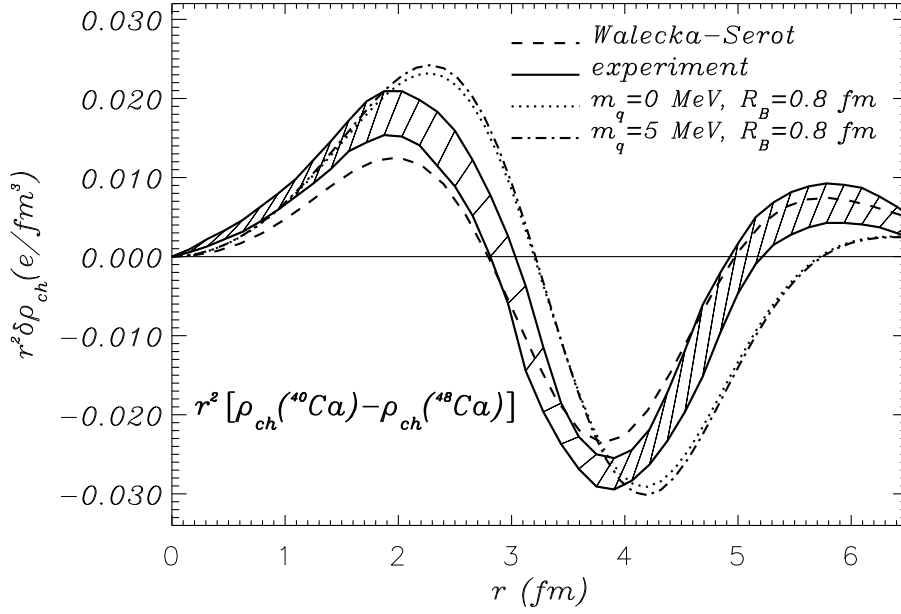


Figure 9: Isotope shift between  $\rho_{ch}(^{40}\text{Ca})$  and  $\rho_{ch}(^{48}\text{Ca})$  compared with the experimental data and that of QHD (for  $m_q = 0$  and 5 MeV with  $R_N = 0.8$  fm) (from Ref. [52]).

Table 8: Model parameters for finite nuclei for  $m_q = 5$  MeV and  $R_N = 0.8$  fm (QMC-II).

type	$g_\sigma^2/4\pi$	$g_\omega^2/4\pi$	$g_\rho^2/4\pi$	$m_\sigma(\text{MeV})$
A	1.67	2.70	5.54	363
B	2.01	3.17	5.27	393
C	2.19	3.31	5.18	416

stronger for  $m_q = 10$  MeV [52]. The experimental data is taken from Ref. [112]. (Note that in this case we also checked that including the charge distribution of the neutron had a small effect.)

In Figs. 10–12, we present the point-neutron density distributions,  $\rho_n$ , in calcium and lead. For  $^{40}\text{Ca}$ , since the dependence of  $\rho_n$  on  $m_q$  and  $R_N$  is again fairly weak, only the result for  $m_q = 5$  MeV and  $R_N = 0.8$  fm is shown, together with the empirical fit [113] to proton scattering data. We again find reasonable agreement with the data. For the isotope shift of  $\rho_n(^{48}\text{Ca}) - \rho_n(^{40}\text{Ca})$ , the calculated difference is closer to those of non-relativistic results than to those of QHD. The neutron density distribution in lead is shown in Fig. 12. Its behavior is again similar to that of QHD.

Next, let us show several numerical results for finite nuclei in the QMC-II model [19]. A set of coupled, nonlinear equations for the nucleon and meson fields are already obtained. The coupling constants  $g_\sigma$ ,  $g_\omega$  and  $g_\rho$  were fixed to describe the nuclear matter properties and the bulk symmetry energy per baryon of 35 MeV (see Table 5). Since the  $\sigma$  mass however determines the range of the attractive interaction, the nuclear-surface slope and its thickness, as in the QMC-I model, we again adjust  $m_\sigma$  to fit the measured rms charge radius of  $^{40}\text{Ca}$ ,  $r_{ch}(^{40}\text{Ca}) = 3.48$  fm [105]. (Notice that variations of  $m_\sigma$  at fixed  $(g_\sigma/m_\sigma)$  again have no effect on the infinite nuclear matter properties.) We summarize the parameters in Table 8.

We show the charge density distributions calculated,  $\rho_{ch}$ , of  $^{40}\text{Ca}$  and  $^{208}\text{Pb}$  in comparison with those of the experimental data in Figs. 13 and 14. As in the QMC-I model, we have used the convolution of the point-proton density with the proton charge distribution to calculate the charge distribution. For  $^{40}\text{Ca}$  the QMC-II model with parameter sets A and B give similar charge distributions to those in QMC-I, while the result of QMC-II

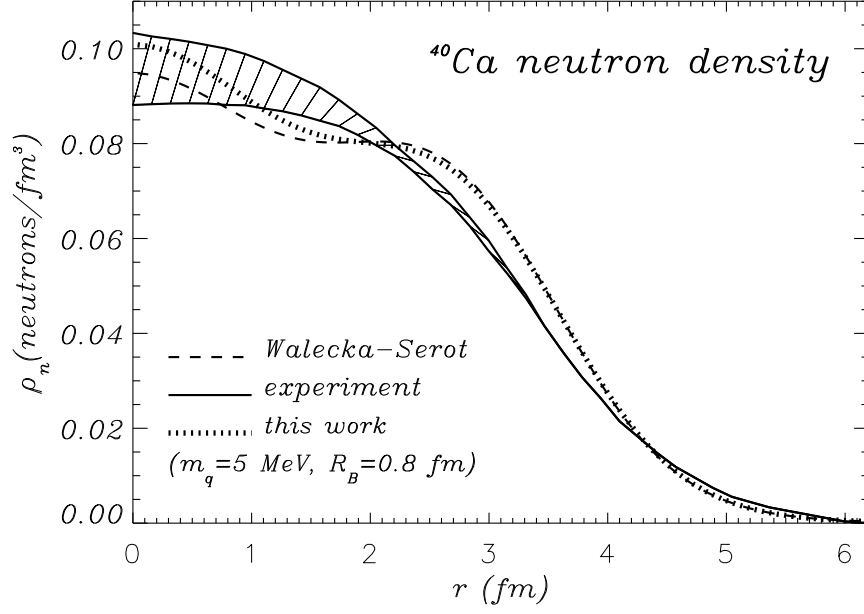


Figure 10: Point-neutron density distribution in  $^{40}\text{Ca}$  (for  $m_q = 5$  MeV and  $R_N = 0.8$  fm) compared with that of QHD and the empirical fit (from Ref. [52]).

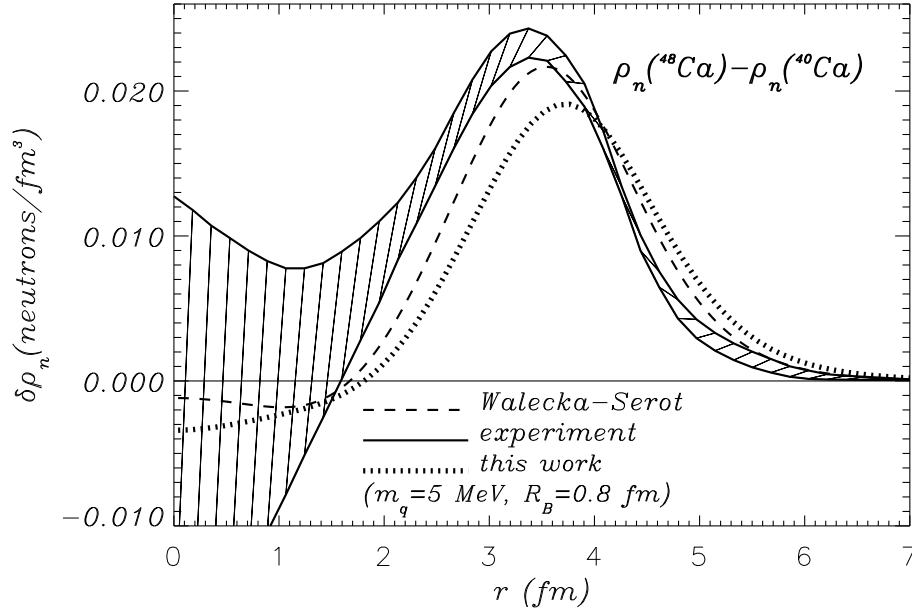


Figure 11: Difference between  $\rho_n(^{48}\text{Ca})$  and  $\rho_n(^{40}\text{Ca})$  compared with that of QHD and the empirical fit (for  $m_q = 5$  and  $R_N = 0.8$  fm) (from Ref. [52]).

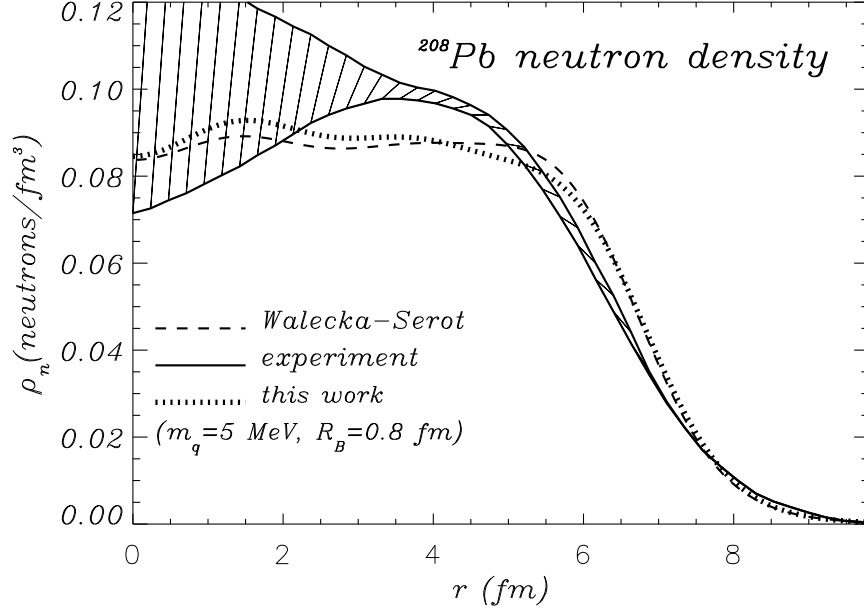


Figure 12: Same as Fig. 10 but for  $^{208}\text{Pb}$  (from Ref. [52]).

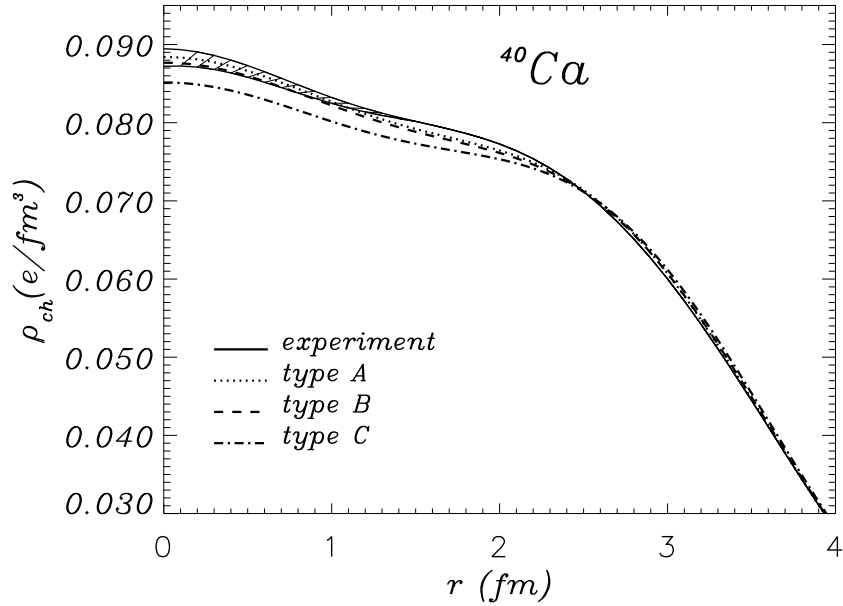


Figure 13: Charge density distribution for  $^{40}\text{Ca}$  (QMC-II) compared with the experimental data [107] (from Ref. [19]).

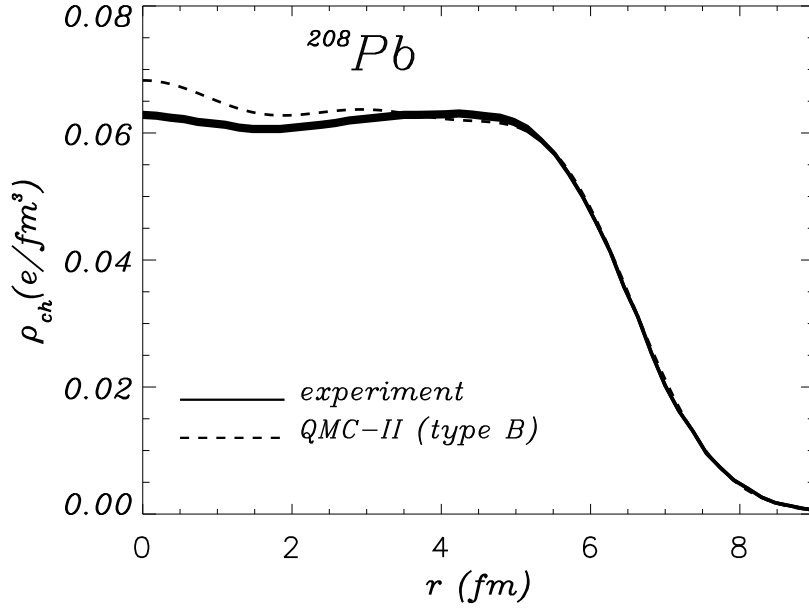


Figure 14: Same as Fig. 13 but for  $^{208}\text{Pb}$ . The parameter set B is used. The experimental data are taken from Ref. [108] (from Ref. [19]).

Table 9: Binding energy per nucleon  $E_B/A$  (in MeV), rms charge radius  $r_{ch}$  (in fm) and difference between  $r_n$  and  $r_p$  (in fm).  $m_q = 5$  MeV and  $R_N = 0.8$  fm. (\* fit)

Model	$-E_B/A$			$r_{ch}$			$r_n - r_p$		
	QMC-I	QMC-II	Exp.	QMC-I	QMC-II	Exp.	QMC-I	QMC-II	Exp.
$^{16}\text{O}$	5.84	5.11	7.98	2.79	2.77	2.73	-0.03	-0.03	0.0
$^{40}\text{Ca}$	7.36	6.54	8.45	3.48*	3.48*	3.48	-0.05	-0.05	$0.05 \pm 0.05$
$^{48}\text{Ca}$	7.26	6.27	8.57	3.52	3.47	3.53	0.23	0.24	$0.2 \pm 0.05$
$^{90}\text{Zr}$	7.79	6.99	8.66	4.27	4.26	4.28	0.11	0.12	$0.05 \pm 0.1$
$^{208}\text{Pb}$	7.25	6.52	7.86	5.49	5.46	5.49	0.26	0.27	$0.16 \pm 0.05$

with parameter set C is closer to that in QHD. From Fig. 14, we see that the present model also yields a charge distribution for  $^{208}\text{Pb}$  which is similar to those calculated using QMC-I or QHD.

In Figs. 15 and 16, we present the changes of the nucleon,  $\sigma$ ,  $\omega$  and hyperon ( $\Lambda$ ,  $\Sigma$  and  $\Xi$ ) masses in  $^{40}\text{Ca}$ . Because the interior density of  $^{40}\text{Ca}$  is higher than  $\rho_0$ , the effective hadron masses at the center become quite small. Using the local-density approximation and Eq. (171), the QMC-II model allows us to calculate the changes of the hyperon ( $\Lambda$ ,  $\Sigma$  and  $\Xi$ ) masses in a nucleus. Our quantitative calculations for the changes of the hyperon masses in finite nuclei may be quite important in forthcoming experiments concerning hypernuclei.

Table 9 gives a summary of the calculated binding energy per nucleon ( $E_B/A$ ), rms charge radii and the difference between nuclear rms radii for neutrons and protons ( $r_n - r_p$ ) for several closed-shell nuclei. Since the calculated properties do not depend strongly on  $m_q$  and  $R_N$ , we only list the values for the QMC-I and QMC-II models with  $m_q = 5$  MeV and  $R_N = 0.8$  fm. References for the experimental values can be found in Ref. [78]. While there are still some discrepancies between the results and data, the present models provide quite reasonable results. We note that the QMC model gives much larger binding energies (larger absolute values) per nucleon than those of QHD while still reproducing the rms charge radii for medium and heavy nuclei quite well.

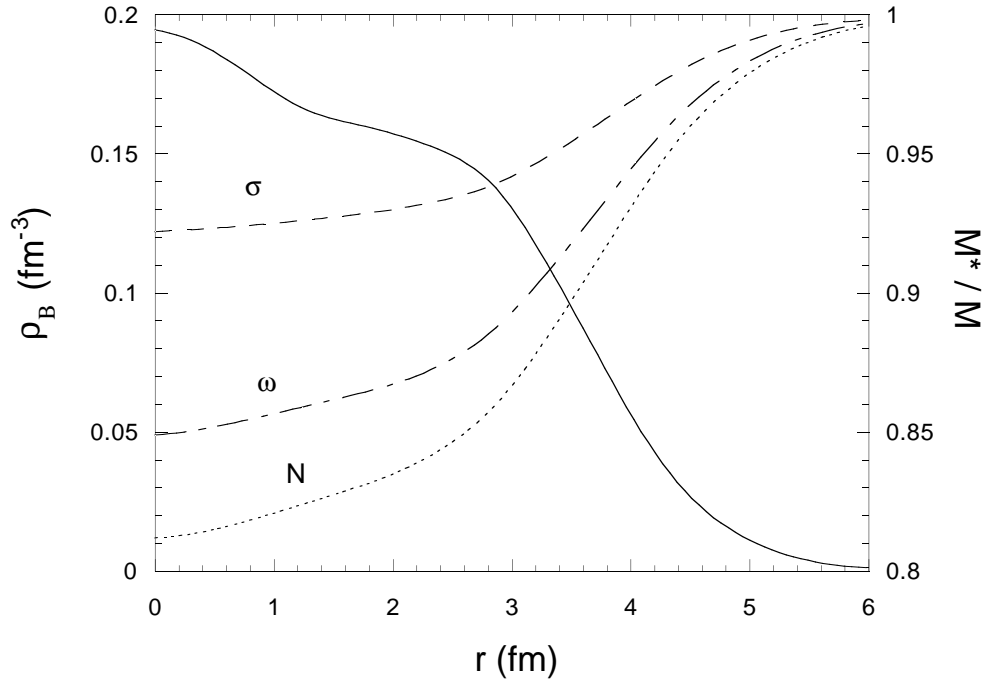


Figure 15: Changes of the nucleon,  $\sigma$  and  $\omega$  meson masses in  $^{40}\text{Ca}$ . The nuclear baryon density is also illustrated (solid curve). The right (left) scale is for the effective mass (the baryon density). The parameter set B is used (from Ref. [19]).

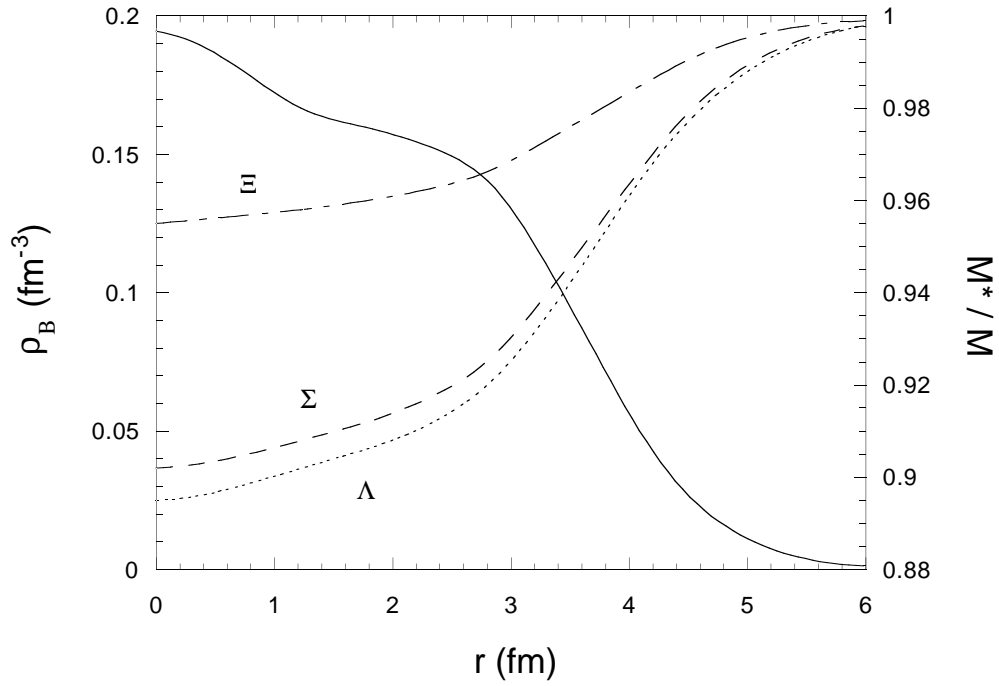


Figure 16: Same as Fig. 15 but for the hyperon ( $\Lambda$ ,  $\Sigma$  and  $\Xi$ ) masses in  $^{40}\text{Ca}$  (from Ref. [19]).

Table 10: Calculated proton and neutron spectra of  $^{40}\text{Ca}$  for QMC-I and QMC-II (type B) compared with the experimental data. We choose  $m_q = 5$  MeV and  $R_N = 0.8$  fm. All energies are in MeV.

Shell	neutron			proton		
	QMC-I	QMC-II	Expt.	QMC-I	QMC-II	Expt.
$1s_{1/2}$	43.1	41.1	51.9	35.2	33.2	$50 \pm 10$
$1p_{3/2}$	31.4	30.0	36.6	23.8	22.3	$34 \pm 6$
$1p_{1/2}$	30.2	29.0	34.5	22.5	21.4	$34 \pm 6$
$1d_{5/2}$	19.1	18.0	21.6	11.7	10.6	15.5
$2s_{1/2}$	15.8	14.7	18.9	8.5	7.4	10.9
$1d_{3/2}$	17.0	16.4	18.4	9.7	9.0	8.3

In Table 10, the calculated spectrum of  $^{40}\text{Ca}$  is presented. In Fig. 17, for example, the spectra of  $^{208}\text{Pb}$  calculated by the QMC-I is presented. Because of the relatively smaller scalar and vector fields in the present model than in QHD or RMF models, the spin-orbit splittings are smaller. The improvement over QHD in the binding energy per nucleon comes at the expense of a reduction in the spin-orbit force. We should note that there is a strong correlation between the effective nucleon mass and the spin-orbit force.

As a test of the sensitivity of the spin-orbit splitting to features of the model, we consider the case of a larger quark mass. For example, we have calculated the case  $m_q = 300$  MeV (and  $R_N = 0.8$  fm) which is a typical constituent quark mass. The calculated spectrum for  $m_q = 300$  MeV is also illustrated in Fig. 17 (QMCH). In this case, the various parameters were  $g_\sigma^2/4\pi = 5.58$ ,  $g_\omega^2/4\pi = 8.51$  (to satisfy the saturation condition),  $g_\rho^2/4\pi = 6.45$ ,  $m_\sigma = 497$  MeV (to fit the rms charge radius of  $^{40}\text{Ca}$ ),  $K = 334$  MeV and  $M_N^* = 674$  MeV at saturation density. We should record that the bag radius in this case increases by 7% at saturation density (which is relatively large). The slope parameter in Eq. (165) is  $a = 3.9 \times 10^{-4}$ . One can expect that a heavy quark mass gives a spectrum closer to those of QHD, because the effective nucleon mass is smaller than the value in case of the light quark mass. We can see from the figure that the calculated spectrum is somewhat closer to the experimental data. We note that the charge density distributions for  $^{40}\text{Ca}$  and  $^{208}\text{Pb}$  are also reproduced well in this case.

The problem concerning the spin-orbit force in the QMC model has also been studied in Refs. [31, 64]. This relatively small spin-orbit splittings may be somewhat recovered by including the exchange contributions (Fock terms) [51]. Alternative is the MQMC model [23, 64, 65, 66], in which we can get a small effective nucleon mass varying the bag constant in matter (see section 2.5) and produce large spin-orbit splittings correspondingly. In next section, we will again study the spin-orbit force in exotic nuclei in detail.

Recent RMF models (for example, see Refs. [63, 114]) are very successful to reproduce single-particle energy spectra of various nuclei (including spin-orbit splittings), because of several parameters for the nonlinear self-interaction terms. Furthermore, the density-dependent relativistic hadron field (DDRH) model [50] is attractive (see also Ref. [115]), because such an approach is also successful and thought to be related to the underlying microscopic description of nuclear interactions. However, we should emphasize that the idea of the QMC model is completely different from those density-dependent nuclear models, and that the vertices in QMC depend on the scalar field in matter, and this is caused by the substructure of nucleon.

### 3.3 Strange, charm and bottom hadrons in nucleus

In this section, we start from the mean-field Lagrangian density for strange, charm and bottom hypernuclei, and study first the properties of these hadrons in nuclear medium. Then, we study the properties of various hypernuclei with strange, charm and bottom hyperons.





the normal nuclei studied in section 3.2. Thus, we ignore also the  $\rho NN$  tensor coupling below.

A relativistic Lagrangian density for hypernuclei in the QMC model is given by [124, 125, 126]:

$$\mathcal{L}_{QMC}^Y = \mathcal{L}_{QMC} + \mathcal{L}_{QMC}^Y, \quad (209)$$

$$\begin{aligned} \mathcal{L}_{QMC} \equiv & \bar{\psi}_N(\vec{r}) \left[ i\gamma \cdot \partial - M_N^*(\sigma) - (g_\omega \omega(\vec{r}) + g_\rho \frac{\tau_3^N}{2} b(\vec{r}) + \frac{e}{2}(1 + \tau_3^N) A(\vec{r})) \gamma_0 \right] \psi_N(\vec{r}) \\ & - \frac{1}{2}[(\nabla \sigma(\vec{r}))^2 + m_\sigma^2 \sigma(\vec{r})^2] + \frac{1}{2}[(\nabla \omega(\vec{r}))^2 + m_\omega^2 \omega(\vec{r})^2] \\ & + \frac{1}{2}[(\nabla b(\vec{r}))^2 + m_\rho^2 b(\vec{r})^2] + \frac{1}{2}(\nabla A(\vec{r}))^2, \end{aligned} \quad (210)$$

$$\begin{aligned} \mathcal{L}_{QMC}^Y \equiv & \bar{\psi}_Y(\vec{r}) \left[ i\gamma \cdot \partial - M_Y^*(\sigma) - (g_\omega^Y \omega(\vec{r}) + g_\rho^Y I_3^Y b(\vec{r}) + e Q_Y A(\vec{r})) \gamma_0 \right] \psi_Y(\vec{r}), \\ & (Y = \Lambda, \Sigma^{0,\pm}, \Xi^{0,+}, \Lambda_c^+, \Sigma_c^{0,+,++}, \Xi_c^{0,+}, \Lambda_b), \end{aligned} \quad (211)$$

where  $\psi_N(\vec{r})$  and  $\psi_Y(\vec{r})$  are respectively the nucleon and the hyperon (strange, charm or bottom baryon) fields. Other notations are given in section 2.2.1.

In an approximation where the  $\sigma$ ,  $\omega$  and  $\rho$  fields couple only to the  $u$  and  $d$  light quarks, the coupling constants for the hyperon, are obtained as  $g_\omega^Y = (n_q/3)g_\omega$ , and  $g_\rho^Y \equiv g_\rho = g_\rho^q$ , with  $n_q$  being the total number of valence light quarks in the hyperon  $Y$ .  $I_3^Y$  and  $Q_Y$  are the third component of the hyperon isospin operator and its electric charge in units of the proton charge,  $e$ , respectively. The field dependent  $\sigma$ - $N$  and  $\sigma$ - $Y$  coupling strengths,  $g_\sigma(\sigma) \equiv g_\sigma^N(\sigma)$  and  $g_\sigma^Y(\sigma)$ , appearing in Eqs. (210) and (211), are defined by

$$M_N^*(\sigma) \equiv M_N - g_\sigma(\sigma)\sigma(\vec{r}), \quad (212)$$

$$M_Y^*(\sigma) \equiv M_Y - g_\sigma^Y(\sigma)\sigma(\vec{r}), \quad (213)$$

where  $M_N$  ( $M_Y$ ) is the free nucleon (hyperon) mass (see also Eq. (115)). Note that the dependence of these coupling strengths on the applied scalar field must be calculated self-consistently within the quark model [10, 13, 30, 52, 124]. Hence, unlike QHD [17], even though  $g_\sigma^Y(\sigma)/g_\sigma(\sigma)$  may be 2/3 or 1/3 depending on the number of light quarks in the hyperon in free space,  $\sigma = 0$  (even this is true only when their bag radii in free space are exactly the same), this will not necessarily be the case in a nuclear medium.

In the following, we consider the limit of infinitely large, uniform (symmetric) nuclear matter, where all scalar and vector fields become constant. In this limit, we can treat any single hadron (denoted by  $h$ ) embedded in the nuclear medium in the same way as for a hyperon. One simply may replace  $\mathcal{L}_{QMC}^Y$  in Eq. (211) by the corresponding Lagrangian density for the hadron  $h$ .

The Dirac equations for the quarks and antiquarks ( $q = u$  or  $d$ , and  $Q = s, c$  or  $b$ , hereafter) in the bag of hadron  $h$  in nuclear matter at the position  $x = (t, \vec{r})$  are given by [130, 131]:

$$\left[ i\gamma \cdot \partial_x - (m_q - V_\sigma^q) \mp \gamma^0 \left( V_\omega^q + \frac{1}{2} V_\rho^q \right) \right] \begin{pmatrix} \psi_u(x) \\ \psi_{\bar{u}}(x) \end{pmatrix} = 0, \quad (214)$$

$$\left[ i\gamma \cdot \partial_x - (m_q - V_\sigma^q) \mp \gamma^0 \left( V_\omega^q - \frac{1}{2} V_\rho^q \right) \right] \begin{pmatrix} \psi_d(x) \\ \psi_{\bar{d}}(x) \end{pmatrix} = 0, \quad (215)$$

$$[i\gamma \cdot \partial_x - m_Q] \psi_Q(x) \text{ (or } \psi_{\bar{Q}}(x)) = 0, \quad (|\vec{r}| \leq \text{bag radius}), \quad (216)$$

where we neglect the Coulomb force, and assume SU(2) symmetry for the light quarks ( $q = u = d$ ). The constant mean-field potentials in nuclear matter are defined by,  $V_\omega^q \equiv g_\omega^q \omega$  and  $V_\rho^q \equiv g_\rho^q b$ , with  $g_\sigma^q$ ,  $g_\omega^q$  and  $g_\rho^q$  the corresponding quark-meson coupling constants.

The normalized, static solution for the ground state quarks or antiquarks with flavor  $f$  in the hadron  $h$ , may be written,  $\psi_f(x) = N_f e^{-i\epsilon_f t / R_h^*} \psi_f(\vec{r})$ , where  $N_f$  and  $\psi_f(\vec{r})$  are the normalization factor and corresponding spin and spatial part of the wave function. The bag radius in medium for a hadron  $h$ ,  $R_h^*$ , is determined through the stability condition for the mass of the hadron against the variation of the bag radius [10, 13, 30]. The eigenenergies in units of  $1/R_h^*$  are given by,

$$\begin{pmatrix} \epsilon_u \\ \epsilon_{\bar{u}} \end{pmatrix} = \Omega_q^* \pm R_h^* \left( V_\omega^q + \frac{1}{2} V_\rho^q \right), \quad \begin{pmatrix} \epsilon_d \\ \epsilon_{\bar{d}} \end{pmatrix} = \Omega_q^* \pm R_h^* \left( V_\omega^q - \frac{1}{2} V_\rho^q \right), \quad \epsilon_Q = \epsilon_{\bar{Q}} = \Omega_Q. \quad (217)$$

Table 11: Current quark masses (input), coupling constants and the bag constant.

$m_{u,d}$	5 MeV	$g_\sigma^q$	5.69
$m_s$	250 MeV	$g_\omega^q$	2.72
$m_c$	1300 MeV	$g_\rho^q$	9.33
$m_b$	4200 MeV	$B^{1/4}$	170 MeV

The hadron masses in a nuclear medium  $m_h^*$  (free mass  $m_h$ ), are calculated by

$$m_h^* = \sum_{j=q,\bar{q},Q,\bar{Q}} \frac{n_j \Omega_j^* - z_h}{R_h^*} + \frac{4}{3} \pi R_h^{*3} B, \quad \left. \frac{\partial m_h^*}{\partial R_h} \right|_{R_h=R_h^*} = 0, \quad (218)$$

where  $\Omega_q^* = \Omega_{\bar{q}}^* = [x_q^2 + (R_h^* m_q^*)^2]^{1/2}$ , with  $m_q^* = m_q - g_\sigma^q \sigma$ ,  $\Omega_Q^* = \Omega_{\bar{Q}}^* = [x_Q^2 + (R_h^* m_Q)^2]^{1/2}$ , and  $x_{q,Q}$  being the lowest bag eigenfrequencies.  $n_q(n_{\bar{q}})$  and  $n_Q(n_{\bar{Q}})$  are the quark (antiquark) numbers for the quark flavors  $q$  and  $Q$ , respectively. The MIT bag quantities,  $z_h$ ,  $B$ ,  $x_{q,Q}$ , and  $m_{q,Q}$  are the parameters for the sum of the c.m. and gluon fluctuation effects, bag constant, lowest eigenvalues for the quarks  $q$  or  $Q$ , respectively, and the corresponding current quark masses.  $z_N$  and  $B$  ( $z_h$ ) are fixed by fitting the nucleon (the hadron) mass in free space. For the current quark masses we use  $(m_{u,d}, m_s, m_c, m_b) = (5, 250, 1300, 4200)$  MeV, where the values for  $m_c$  and  $m_b$  are the averaged values from Refs. [132] and [133], respectively, and these values were used in Refs. [125, 126]. Then, we obtain the bag constant  $B = (170 \text{ MeV})^4$ . The quark-meson coupling constants, which are determined so as to reproduce the saturation properties of symmetric nuclear matter are,  $(g_\sigma^q, g_\omega^q, g_\rho^q) = (5.69, 2.72, 9.33)$ , where  $g_\sigma \equiv g_\sigma^N \equiv 3g_\sigma^q S_N(0) = 3 \times 5.69 \times 0.483 = 8.23$  [52]. These are summarized in Table 11. (See also Eq. (111) and section 3.1.) The parameters  $z_h$ , and the bag radii  $R_h$  for various hadrons in free space, and some quantities calculated at normal nuclear matter density  $\rho_0 = 0.15 \text{ fm}^{-3}$  are listed in Table 12, together with the free space masses [132, 133, 134, 135].

However, in studies of the kaon system, we found that it was necessary to increase the strength of the vector coupling to the light quarks in the  $K^+$  (by a factor of  $1.4^2$ , i.e.,  $g_{K\omega}^q \equiv 1.4^2 g_\omega^q$ ) in order to reproduce the empirically extracted  $K^+$ -nucleus interaction [130]. This may be related to the fact that kaon is a pseudo-Goldstone boson, where treatment of the Goldstone bosons in a naive quark model is usually unsatisfactory. We also assume this,  $g_\omega^q \rightarrow 1.4^2 g_\omega^q$ , for the  $D$ ,  $\bar{D}$  [131] and  $B$  and  $\bar{B}$  mesons to obtain an upper limit on the corresponding binding. The scalar ( $V_s^h$ ) and vector ( $V_v^h$ ) potentials felt by the hadrons  $h$ , in nuclear matter are given by,

$$V_s^h = m_h^* - m_h, \quad (219)$$

$$V_v^h = (n_q - n_{\bar{q}}) V_\omega^q + I_3^h V_\rho^q, \quad (V_\omega^q \rightarrow \tilde{V}_\omega^q \equiv 1.4^2 V_\omega^q \text{ for } K, \bar{K}, D, \bar{D}, B, \bar{B}), \quad (220)$$

$$\simeq 41.8 \times (n_q - n_{\bar{q}}) \left( \frac{\rho_B}{\rho_0} \right) + 42.4 \times I_3^h \left( \frac{\rho_3}{\rho_0} \right) \quad (\text{MeV}) \quad \text{with} \quad \rho_0 = 0.15 \quad (\text{fm}^{-3}), \quad (221)$$

where  $I_3^h$  is the third component of isospin projection of the hadron  $h$ , and  $\rho_B = \rho_p + \rho_n$  ( $\rho_3 = \rho_p - \rho_n$ ) the baryon (isovector baryon) density with  $\rho_p$  and  $\rho_n$  being the proton and neutron densities, respectively. Thus, the vector potential felt by a heavy baryon with charm and bottom quarks, is equal to that of the strange hyperon with the same light quark configuration in QMC. (See also section 3.1.1 concerning the scalar potential.)

In Figs. 18 and 19 we show ratios of effective masses (free masses + scalar potentials) versus those of the free particles, for mesons and baryons, respectively. With increasing density the ratios decrease as expected, but this decrease in magnitude is, from larger to smaller: hadrons with only light quarks, with one strange quark, with one charm quark, and with one bottom quark. This is because their masses in free space are in the order from light to heavy. Thus, the net ratios for the decrease in masses (developing of scalar masses) compared to that of the free masses becomes smaller. This may be regarded as a measure of the role of light quarks in each hadron system in nuclear matter, in the sense of how much they contribute a partial restoration of chiral symmetry in the hadron. In Fig. 18 one can notice a somewhat anomalous behavior of the ratio for

Table 12: The bag parameters, various hadron masses and the bag radii in free space [at normal nuclear matter density,  $\rho_0 = 0.15 \text{ fm}^{-3}$ ]  $z_h, R_h$  and  $M_h$  [ $M_h^*$  and  $R_h^*$ ].  $M_h$  and  $R_N = 0.8 \text{ fm}$  in free space are inputs. Note that the quantities for the physical  $\omega, \phi, \eta$  and  $\eta'$  are calculated including the octet-singlet mixing effect, and that  $\omega$  and  $\rho$  below are standing for the physical particles and are different from those appearing in the Lagrangian density of QMC. (See section 3.4 for details.)

h	$z_h$	$M_h$ (MeV)	$R_h$ (fm)	$M_h^*$ (MeV)	$R_h^*$ (fm)
$N$	3.295	939.0	0.800	754.5	0.786
$\Lambda$	3.131	1115.7	0.806	992.7	0.803
$\Sigma$	2.810	1193.1	0.827	1070.4	0.824
$\Xi$	2.860	1318.1	0.820	1256.7	0.818
$\Lambda_c$	1.766	2284.9	0.846	2162.5	0.843
$\Sigma_c$	1.033	2452.0	0.885	2330.2	0.882
$\Xi_c$	1.564	2469.1	0.853	2408.0	0.851
$\Lambda_b$	-0.643	5624.0	0.930	5502.9	0.928
$\omega$	1.866	781.9	0.753	658.7	0.749
$\rho$	1.907	770.0	0.749	646.2	0.746
$K$	3.295	493.7	0.574	430.4	0.572
$K^*$	1.949	893.9	0.740	831.9	0.738
$\eta$	3.131	547.5	0.603	483.9	0.600
$\eta'$	1.711	957.8	0.760	896.5	0.758
$\phi$	1.979	1019.4	0.732	1018.9	0.732
$D$	1.389	1866.9	0.731	1804.9	0.730
$D^*$	0.849	2000.8	0.774	1946.7	0.772
$B$	-1.136	5279.2	0.854	5218.1	0.852

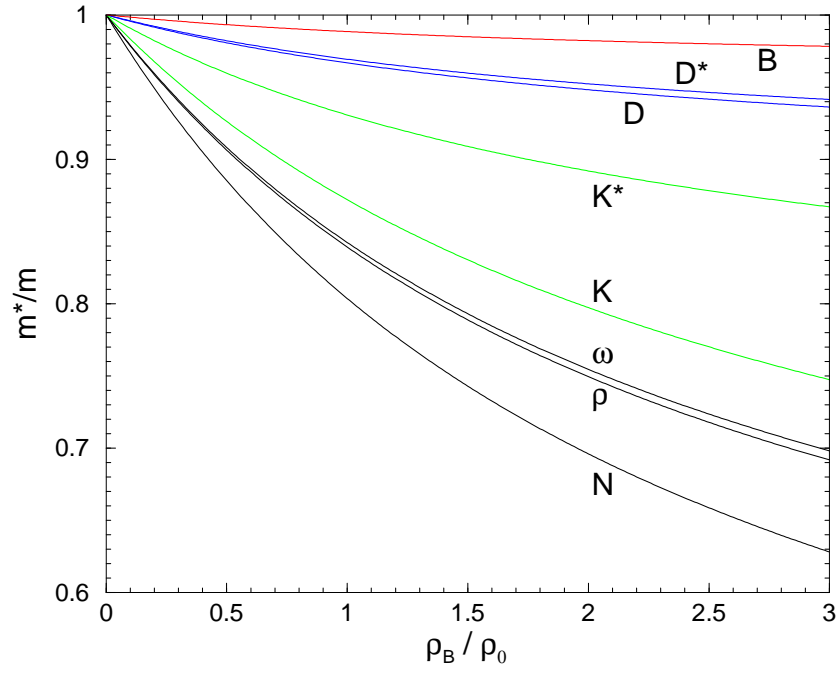


Figure 18: Effective mass ratios for mesons in symmetric nuclear matter ( $\rho_0 = 0.15 \text{ fm}^{-3}$ ).  $\omega$  and  $\rho$  stand for physical mesons which are treated in the quark model, and should not be confused with the fields appearing in the QMC model (from Ref. [125]).

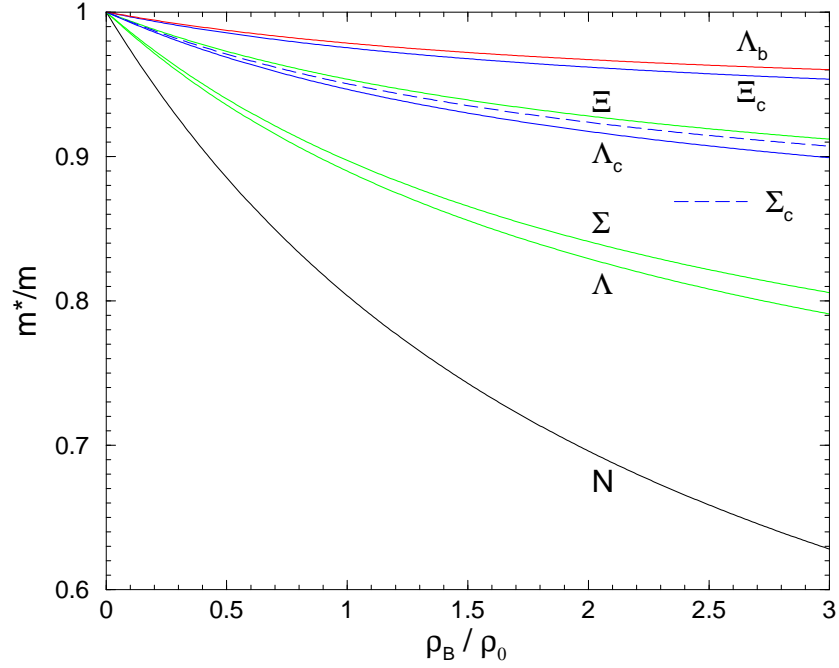


Figure 19: Effective mass ratios for baryons in symmetric nuclear matter. (from Ref. [125]).

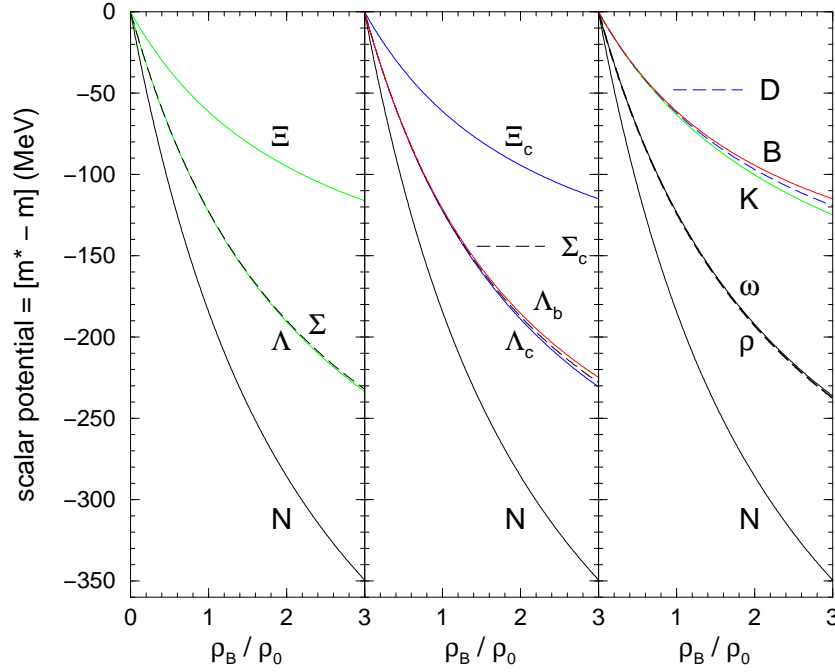


Figure 20: Scalar potentials for various hadrons in symmetric nuclear matter. (from Ref. [125]).

the kaon ( $K$ ) mass, which is related to what we meant by its pseudo-Goldstone boson nature – i.e., its mass in free space is relatively light,  $m_K \simeq 495$  MeV, and the relative reduction in its mass in-medium is large.

Perhaps it is much more quantitative and direct to compare the scalar potentials (see Eq. (219)) felt by each hadron in nuclear matter, with the calculated results shown in Fig. 20. These results confirm that the scalar potential felt by the hadron  $h$ ,  $V_s^h$ , follows a simple light quark number scaling rule:

$$V_s^h \simeq \left( \frac{n_q + n_{\bar{q}}}{3} \right) V_s^N = - \left( \frac{n_q + n_{\bar{q}}}{3} \right) \delta M_N^* = - \left( \frac{n_q + n_{\bar{q}}}{3} \right) (M_N - M_N^*), \quad (222)$$

where  $n_q$  ( $n_{\bar{q}}$ ) is the number of light quarks (antiquarks) in hadron  $h$  and  $V_s^N$  is the scalar potential felt by the nucleon (see Eq. (219)). This *scaling formula* for hadrons in nuclear matter is already discussed in section 3.1.1. It is interesting to notice that, the baryons with charm or bottom quarks ( $\Xi_c$  has the quark configuration,  $qsc$ ), show very similar features to those of the hyperons with one or two strange quarks. Then, we can expect that the hyperons with charm or bottom quarks, will also form charmed (bottom) hypernuclei as the strange hyperons do. (See Eq. (220), and recall that the repulsive vector potentials are the same for the corresponding strange hyperons with the same light quark configurations.)

In addition, as we discuss later (in section 3.4) in detail, the  $B^-$  meson will also certainly form meson-nucleus bound states, because it has the valence structure  $\bar{u}b$  and feels a strong attractive vector potential in addition to the attractive Coulomb force. This makes it much easier to bind in a nucleus compared to the  $D^0$  [131], which is  $c\bar{u}$  and is blind to the Coulomb force. This reminds us of a situation of the kaonic ( $K^-(\bar{u}s)$ ) atom [136, 137]. A study of  $B^-(\bar{u}b)$  atoms would be a fruitful experimental program. Such atoms will have the meson much closer to the nucleus and will thus probe even smaller changes in the nuclear density. This will provide complementary information to that given by  $D^-(\bar{c}d)$ -nucleus bound states, which give information on the vector potential in a nucleus [131] – again, see section 3.4.

Table 13: The slope parameters,  $a_j$  ( $j = N, \Lambda, \Sigma, \Xi, \Lambda_c, \Sigma_c, \Xi_c, \Lambda_b$ ). See also Table 6.

$a_j$	$\times 10^{-4} \text{ MeV}^{-1}$	$a_j$	$\times 10^{-4} \text{ MeV}^{-1}$
$a_N$	8.8	$a_{\Lambda_b}$	10.9
$a_\Lambda$	9.3	$a_{\Lambda_c}$	9.8
$a_\Sigma$	9.5	$a_{\Sigma_c}$	10.3
$a_\Xi$	9.4	$a_{\Xi_c}$	9.9

### 3.3.2 Mean-field equations of motion for strange, charm, and bottom hypernuclei

Next we consider the predictions for strange, charm and bottom hypernuclei. The Lagrangian density Eq. (209) leads to a set of equations of motion for the hypernuclear system:

$$[i\gamma \cdot \partial - M_N^*(\sigma) - (g_\omega \omega(\vec{r}) + g_\rho \frac{\tau_3^N}{2} b(\vec{r}) + \frac{e}{2}(1 + \tau_3^N) A(\vec{r})) \gamma_0] \psi_N(\vec{r}) = 0, \quad (223)$$

$$[i\gamma \cdot \partial - M_Y^*(\sigma) - (g_\omega^Y \omega(\vec{r}) + g_\rho I_3^Y b(\vec{r}) + e Q_Y A(\vec{r})) \gamma_0] \psi_Y(\vec{r}) = 0, \quad (224)$$

$$\begin{aligned} (-\nabla_r^2 + m_\sigma^2) \sigma(\vec{r}) &= - \left[ \frac{\partial M_N^*(\sigma)}{\partial \sigma} \right] \rho_s(\vec{r}) - \left[ \frac{\partial M_Y^*(\sigma)}{\partial \sigma} \right] \rho_s^Y(\vec{r}), \\ &\equiv g_\sigma Y_N(\sigma) \rho_s(\vec{r}) + g_\sigma^Y C_Y(\sigma) \rho_s^Y(\vec{r}), \end{aligned} \quad (225)$$

$$(-\nabla_r^2 + m_\omega^2) \omega(\vec{r}) = g_\omega \rho_B(\vec{r}) + g_\omega^Y \rho_B^Y(\vec{r}), \quad (226)$$

$$(-\nabla_r^2 + m_\rho^2) b(\vec{r}) = \frac{g_\rho}{2} \rho_3(\vec{r}) + g_\rho^Y I_3^Y \rho_B^Y(\vec{r}), \quad (227)$$

$$(-\nabla_r^2) A(\vec{r}) = e \rho_p(\vec{r}) + e Q_Y \rho_B^Y(\vec{r}), \quad (228)$$

where,  $\rho_s(\vec{r})$  ( $\rho_s^Y(\vec{r})$ ),  $\rho_B(\vec{r})$  ( $\rho_B^Y(\vec{r})$ ),  $\rho_3(\vec{r})$  and  $\rho_p(\vec{r})$  are the scalar, baryon, third component of isovector, and proton densities at position  $\vec{r}$  in the hypernucleus [30, 52, 124]. On the right hand side of Eq. (225),  $-[\partial M_N^*(\sigma)/\partial \sigma] \equiv g_\sigma C_N(\sigma)$  and  $-[\partial M_Y^*(\sigma)/\partial \sigma] \equiv g_\sigma^Y C_Y(\sigma)$ , where  $g_\sigma \equiv g_\sigma(\sigma = 0)$  and  $g_\sigma^Y \equiv g_\sigma^Y(\sigma = 0)$ , are new, characteristic features of QMC. At the hadronic level, the entire information on the quark dynamics is condensed into the effective couplings  $C_{N,Y}(\sigma)$  of Eq. (225) (see section 2.2). Furthermore, when  $C_{N,Y}(\sigma) = 1$ , which corresponds to a structureless nucleon or hyperon, the equations of motion given by Eqs. (223)-(228) can be identified with those derived from QHD [138, 139, 140], except for the terms arising from the tensor coupling and the non-linear scalar and/or vector field interactions, introduced beyond the naive QHD.

The explicit expressions for coupled differential equations to obtain various fields and hyperon and nucleon wave functions can be obtained [124] in a similar manner to those obtained for finite nuclei (see section 3.2), except for the additional modifications due to the embedded hyperon. It has been found that the function  $C_j(\sigma)$  ( $j = N, \Lambda, \Sigma, \Xi, \Lambda_c, \Sigma_c, \Xi_c, \Lambda_b$ ) can be parameterized as a linear form in the  $\sigma$  field,  $g_\sigma \sigma$ , for practical calculations [30, 52, 124, 126]:

$$C_j(\sigma) = 1 - a_j \times (g_\sigma \sigma), \quad (j = N, \Lambda, \Sigma, \Xi, \Lambda_c, \Sigma_c, \Xi_c, \Lambda_b). \quad (229)$$

The values obtained for  $a_j$  are listed in Table 13. (See also section 3.1.1 for some of the values calculated in QMC-II.) This parameterization works very well up to about three times normal nuclear matter density  $\rho_B \simeq 3\rho_0$ . Then, the effective masses for the baryon,  $j$ , in nuclear matter are well approximated by [30, 52, 124]:

$$M_j^* \simeq M_j - \frac{n_q}{3} g_\sigma \left[ 1 - \frac{a_j}{2} (g_\sigma \sigma) \right] \sigma, \quad (j = N, \Lambda, \Sigma, \Xi, \Lambda_c, \Sigma_c, \Xi_c, \Lambda_b), \quad (230)$$

with  $n_q$  being the number of light quarks in the baryon  $j$  (see Eq. (219) and section 3.1.1). The field strength,  $g_\sigma \sigma$ , versus baryon density can be found in Ref. [30].

### 3.3.3 Spin-orbit potential in the QMC model - strange hypernuclei

Here, we focus on the spin-orbit potential for a hyperon in the QMC model, where the internal structure of the hyperon gives one of the characteristic features not present in QHD-type models. As an illustrative example, we first discuss the spin-orbit potential for the  $\Lambda$ .

The origin of the spin orbit force for a composite nucleon moving through scalar and vector fields which vary with position was explained in section 2.1.4. The situation for the  $\Lambda$  is different in that, in an SU(6) quark model, the  $u$  and  $d$  quarks are coupled to spin zero, so that the spin of the  $\Lambda$  is carried by the  $s$  quark. As the  $\sigma$ -meson in QMC is viewed as a convenient parameterization of two-pion-exchange and the  $\omega$  and  $\rho$  are non-strange, it seems reasonable to assume that the  $\sigma$ ,  $\omega$  and  $\rho$  mesons couple only to the  $u$  and  $d$  quarks. The direct contributions to the spin-orbit interaction from these mesons then vanish due to the flavor-spin structure. Thus, the spin-orbit interaction,  $V_{S.O.}^\Lambda(\vec{r})\vec{S} \cdot \vec{L}$ , at the position  $\vec{r}$  for the  $\Lambda$  in a hypernucleus arises entirely from Thomas precession:

$$V_{s.o.}^\Lambda(\vec{r})\vec{S} \cdot \vec{L} = -\frac{1}{2}\vec{v}_\Lambda \times \frac{d\vec{v}_\Lambda}{dt} \cdot \vec{S} = -\frac{1}{2M_\Lambda^{*2}(r)r} \left( \frac{d}{dr}[M_\Lambda^*(r) + g_\omega^\Lambda \omega(r)] \right) \vec{S} \cdot \vec{L}, \quad (231)$$

where,  $\vec{v}_\Lambda = \vec{p}_\Lambda/M_\Lambda^*$ , is the velocity of the  $\Lambda$  in the rest frame of the  $\Lambda$  hypernucleus, and the acceleration,  $d\vec{v}_\Lambda/dt$ , is obtained from the Hamilton equations of motion applied to the leading order Hamiltonian, as explained in section 2.1.4. Because the contributions from the effective mass of the  $\Lambda$ ,  $M_\Lambda^*(r)$ , and the vector potential,  $g_\omega^\Lambda \omega(r)$ , are approximately equal and opposite in sign, we quite naturally expect a very small spin-orbit interaction for the  $\Lambda$  in a hypernucleus. (See section 3.2 for the spin-orbit splittings in normal nuclei.) Although the spin-orbit splittings for the nucleon calculated in QMC are already somewhat smaller than those calculated in QHD [17], we can expect much smaller spin-orbit splittings for the  $\Lambda$  in QMC. In order to include the spin-orbit potential of Eq. (231) approximately correctly, we added perturbatively the correction due to the vector potential,  $-\frac{2}{2M_\Lambda^{*2}(r)r} \left( \frac{d}{dr}g_\omega^\Lambda \omega(r) \right) \vec{S} \cdot \vec{L}$ , to the single-particle energies for the specified shell state obtained with the Dirac equation Eq. (224), by evaluating it with the corresponding shell-state wave function obtained for the  $\Lambda$ . (See also section 3.2.) This is necessary because the Dirac equation corresponding to Eq. (224) leads to a spin-orbit force which does not correspond to the underlying quark model, namely:

$$V_{s.o.}^\Lambda(\vec{r})\vec{S} \cdot \vec{L} = -\frac{1}{2M_\Lambda^{*2}(r)r} \left( \frac{d}{dr}[M_\Lambda^*(r) - g_\omega^\Lambda \omega(r)] \right) \vec{S} \cdot \vec{L}. \quad (232)$$

This correction to the spin-orbit force, which appears naturally in the QMC model, may also be modeled at the hadronic level of the Dirac equation by adding a tensor interaction, motivated by the quark model [141, 142]. In addition, one boson exchange model with underlying approximate SU(3) symmetry in strong interactions, also leads to weaker spin-orbit forces for the (strange) hyperon-nucleon ( $YN$ ) than that for the nucleon-nucleon ( $NN$ ) [143]. The very weak spin-orbit interaction for  $\Lambda$  hypernuclei, which had been phenomenologically suggested by Bouyssy and Hüfner [144], was first explained by Brockman and Weise [145] in a relativistic Hartree model, and directly confirmed later by experiment [146].

In the QMC model, the general expression for the spin-orbit potential felt by the nucleon or hyperon,  $j$  ( $j = N, \Lambda, \Sigma, \Xi$ ), may be expressed as [124] (see also section 2.1.5)

$$V_{s.o.}^j(\vec{r})\vec{S} \cdot \vec{L} = \frac{-1}{2M_j^{*2}(r)r} \left[ \Delta_\sigma^j + (G_j^s - 6F_j^s \mu_s \eta_j(r)) \Delta_\omega^j + (G_j^v - \frac{6}{5}F_j^v \mu_v \eta_j(r)) \Delta_\rho^j \right] \vec{S} \cdot \vec{L}, \quad (233)$$

with

$$\Delta_\sigma^j = \frac{d}{dr}M_j^*(r), \quad \Delta_\omega^j = \frac{d}{dr} \left( \frac{1}{3} \right) g_\omega \omega(r) = \Delta_\omega^q = \frac{d}{dr}g_\omega^q \omega(r), \quad \Delta_\rho^j = \frac{d}{dr}g_\rho b(r), \quad (234)$$

$$G_j^s = \langle j | \sum_{i=u,d} 1(i) | j \rangle, \quad G_j^v = \langle j | \sum_{i=u,d} \frac{1}{2} \tau_3(i) | j \rangle, \quad (235)$$

$$F_j^s = \frac{\langle j | \sum_{i=u,d} \frac{1}{2} \vec{\sigma}(i) | j \rangle}{\langle j | \frac{1}{2} \vec{\sigma}^j | j \rangle}, \quad F_j^v = \frac{\langle j | \sum_{i=u,d} \frac{1}{2} \vec{\sigma}(i) \frac{1}{2} \tau_3(i) | j \rangle}{\langle j | \frac{1}{2} \vec{\sigma}^j | j \rangle}, \quad (236)$$

$$\mu_s = \frac{1}{3}M_N I_0 = \frac{1}{5}\mu_v, \quad \eta_j(r) = \frac{I_j^* M_j^*(r)}{I_0 M_N}, \quad (237)$$

$$I_0 = \frac{R_N}{3} \frac{4\Omega_N + 2m_q R_N - 3}{2\Omega_N(\Omega_N - 1) + m_q R_N}, \quad I_j^* = \frac{R_j^*}{3} \frac{4\Omega_j^*(\sigma) + 2m_q^*(\sigma)R_j^* - 3}{2\Omega_j^*(\sigma)(\Omega_j^*(\sigma) - 1) + m_q^*(\sigma)R_j^*}. \quad (238)$$



Here  $\vec{r}$  is the position of the baryon  $j$  in the hypernucleus (nucleus), and the terms proportional to  $\mu_s$  and  $\mu_v$  are the anomalous contributions from the light quarks due to the finite size of the hyperon (nucleon). They are related to the magnetic moments of the proton,  $\mu_p$ , and the neutron,  $\mu_n$ , as  $\mu_s = \mu_p + \mu_n$  and  $\mu_v = \mu_p - \mu_n$ , with the experimental values,  $\mu_p = 2.79$  and  $\mu_n = -1.91$  (in nuclear magnetons). Note that  $\mu_s$  and  $\mu_v$ , together with the quantities  $I_0$  and  $I_j^*$  of Eq. (238), are calculated self-consistently in the QMC model. In addition, recall that the in-medium bag radius,  $R_j^*$ , and the lowest bag eigenenergy for the light quarks,  $\Omega_j^*/R_j^*$ , depend on  $j$  ( $j = N, \Lambda, \Sigma, \Xi, \Lambda_c, \Sigma_c, \Xi_c, \Lambda_b$ ) (see Table 12). The explicit expressions for the spin-orbit potentials for the octet baryons in the QMC model are given by:

$$V_{s.o.}^p(r) = \frac{-1}{2M_N^{*2}(r)r} \left[ \Delta_\sigma^N + 3(1 - 2\mu_s\eta_N(r))\Delta_\omega^N + \frac{1}{2}(1 - 2\mu_v\eta_N(r))\Delta_\rho \right], \quad (239)$$

$$V_{s.o.}^n(r) = \frac{-1}{2M_N^{*2}(r)r} \left[ \Delta_\sigma^N + 3(1 - 2\mu_s\eta_N(r))\Delta_\omega^N - \frac{1}{2}(1 - 2\mu_v\eta_N(r))\Delta_\rho \right], \quad (240)$$

$$V_{s.o.}^\Lambda(r) = \frac{-1}{2M_\Lambda^{*2}(r)r} \left[ \Delta_\sigma^\Lambda + 2\Delta_\omega^\Lambda \right], \quad (241)$$

$$V_{s.o.}^{\Sigma^+}(r) = \frac{-1}{2M_\Sigma^{*2}(r)r} \left[ \Delta_\sigma^\Sigma + 2(1 - 4\mu_s\eta_\Sigma(r))\Delta_\omega^\Sigma + (1 - \frac{4}{5}\mu_v\eta_\Sigma(r))\Delta_\rho \right], \quad (242)$$

$$V_{s.o.}^{\Sigma^0}(r) = \frac{-1}{2M_\Sigma^{*2}(r)r} \left[ \Delta_\sigma^\Sigma + 2(1 - 4\mu_s\eta_\Sigma(r))\Delta_\omega^\Sigma \right], \quad (243)$$

$$V_{s.o.}^{\Sigma^-}(r) = \frac{-1}{2M_\Sigma^{*2}(r)r} \left[ \Delta_\sigma^\Sigma + 2(1 - 4\mu_s\eta_\Sigma(r))\Delta_\omega^\Sigma - (1 - \frac{4}{5}\mu_v\eta_\Sigma(r))\Delta_\rho \right], \quad (244)$$

$$V_{s.o.}^{\Xi^0}(r) = \frac{-1}{2M_\Xi^{*2}(r)r} \left[ \Delta_\sigma^\Xi + (1 + 2\mu_s\eta_\Xi(r))\Delta_\omega^\Xi + \frac{1}{2}(1 + \frac{2}{5}\mu_v\eta_\Xi(r))\Delta_\rho \right], \quad (245)$$

$$V_{s.o.}^{\Xi^-}(r) = \frac{-1}{2M_\Xi^{*2}(r)r} \left[ \Delta_\sigma^\Xi + (1 + 2\mu_s\eta_\Xi(r))\Delta_\omega^\Xi - \frac{1}{2}(1 + \frac{2}{5}\mu_v\eta_\Xi(r))\Delta_\rho \right]. \quad (246)$$

The spin-orbit potentials for  $\Lambda_c, \Sigma_c, \Xi_c$  and  $\Lambda_b$  can be obtained in a similar way. However, because of the heavier (effective) masses for them and because the contribution from the  $\sigma$  and  $\omega$  fields for the spin-orbit potentials are very similar in magnitude to those for the strange hyperons, we expect that the contribution of the spin-orbit potential for charm and bottom hypernuclei should be negligible.

### 3.3.4 Pauli blocking and channel coupling effects

Next, we discuss the effects of Pauli blocking at the quark level, as well as the channel coupling. For the numerical results, these effects are included in the self-consistent calculation. When a hyperon sits in an orbital with the same quantum numbers as one already occupied by nucleons we need to include the effect of Pauli blocking at the quark level. Furthermore, there is an additional correction associated with the channel coupling,  $\Sigma N - \Lambda N$ . These effects will be included in specific ways at the hadronic level. More consistent treatments at the quark level have not yet been studied within the QMC model.

First, we consider the Pauli blocking effect. It seems natural to assume that this effect works repulsively in a way that the strength is proportional to the light quark baryonic (number) density of the core nucleons. One might then expect that the light quarks in the hyperon should feel a stronger repulsion at the position where the baryon density is large. As a consequence, the wave function of the hyperon (quark) will be suppressed in this region. Therefore, we assume that the Pauli blocking effect is simply proportional to the baryonic density. Then, the Dirac equation for the hyperon  $Y$ , Eq. (224), is modified by

$$[i\gamma \cdot \partial - M_Y^*(\sigma) - (\lambda_Y \rho_B(\vec{r}) + g_\omega^Y \omega(\vec{r}) + g_\rho I_3^Y b(\vec{r}) + eQ_Y A(\vec{r}))\gamma_0]\psi_Y(\vec{r}) = 0, \quad (247)$$

where,  $\rho_B(\vec{r})$  is the baryonic density at the position  $\vec{r}$  in the hypernucleus due to the core nucleons, and  $\lambda_Y$  is a constant to be determined empirically. In the present treatment, we chose this constant  $\lambda_Y$  for  $Y = \Lambda$ , in order to reproduce the empirical single-particle energy for the  $1s_{1/2}$  state in  $^{209}_{\Lambda}\text{Pb}$ , -27.0 MeV [147].

One might also imagine that this fitted value includes the attractive  $\Lambda N \rightarrow \Sigma N$  channel coupling effect for the  $\Lambda$  single-particle energies, because the value fitted is the experimentally observed one. However, for

$\Sigma$  hypernuclei, the repulsive  $\Sigma N \rightarrow \Lambda N$  channel coupling effect must be included in addition to this effective Pauli blocking, in a way to reproduce the relative repulsive energy shift in the single-particle energies for the  $\Sigma$ . The fitted value for the constant  $\lambda_\Lambda$  is  $\lambda_\Lambda = 60.25 \text{ MeV (fm)}^3$ . Then for the  $\Sigma$  and  $\Xi$  hypernuclei, we take the constants,  $\lambda_{\Sigma, \Xi}$ , corresponding to the effective Pauli blocking effect as,  $\lambda_\Sigma = \lambda_\Lambda$ , and  $\lambda_\Xi = \frac{1}{2}\lambda_\Lambda$ , by counting the total number of  $u$  and  $d$  quarks in these hyperons.

Next, we consider the channel coupling (strong conversion) effect additional to the Pauli blocking at the quark level. It is expected that the channel couplings,  $\Sigma N - \Lambda N$  and  $\Xi N - \Lambda \Lambda$ , generally exist in hypernuclei, with the former considered to be especially important [148, 149]. We consider first the  $\Sigma N - \Lambda N$  channel coupling. We estimate this effect using the Nijmegen potential [150] as follows. Including solely the effective Pauli blocking potential,  $\lambda_\Sigma \rho_B(r)$  ( $\lambda_\Sigma = \lambda_\Lambda = 60.25 \text{ MeV (fm)}^3$ ), we obtain the  $1s_{1/2}$  single-particle energy for in  $^{209}_{\Sigma}\text{Pb}$ ,  $-26.9 \text{ MeV}$  ( $\simeq -27.0 \text{ MeV}$  of observed value). This value does not contain entirely the effect of the correct channel coupling to the  $\Lambda$ . On the other hand, in a conventional first-order Brueckner calculation based on the standard choice of the single-particle potentials (cf. Ref. [151] for details) the binding energy for the  $\Sigma$  in nuclear matter with the Nijmegen potential [150] is,  $12.6 \text{ MeV}$ , for the case where the correct channel coupling effect to the  $\Lambda$  is omitted, namely, without the Pauli-projector in the  $\Lambda N$  channel. When the channel coupling to the  $\Lambda N$  is recovered and the Pauli-projector in the  $\Lambda N$  channel is included, the binding energy for the  $\Sigma$  in nuclear matter decreases to  $5.3 \text{ MeV}$ . Then, the decrease in the calculated binding energy for the  $\Sigma$ ,  $12.6 - 5.3 = +7.3 \text{ MeV}$ , may be taken as the net effect of the  $\Sigma N - \Lambda N$  channel coupling for the  $\Sigma$ . We include the effect by assuming the same form as that applied for the effective Pauli blocking via  $\lambda_\Sigma \rho_B(r)$ , and readjust the parameter  $\lambda_\Sigma = \lambda_\Lambda$  to  $\tilde{\lambda}_\Sigma \neq \lambda_\Sigma$  to reproduce this difference in the single-particle energy for the  $1s_{1/2}$  in  $^{209}_{\Sigma}\text{Pb}$ , namely,  $-19.6 = -26.9 + 7.3 \text{ MeV}$ . Here we should point out that the baryon density calculated in section 3.2, shows that the density around the center of the  $^{208}\text{Pb}$  nucleus is consistently close to that of nuclear matter within the model. The value obtained for  $\tilde{\lambda}_\Sigma$  in this way is,  $\tilde{\lambda}_\Sigma = 110.6 \text{ MeV (fm)}^3$ .

As for the  $\Xi N - \Lambda \Lambda$  channel coupling, the studies of Afnan and Gibson [152] show that the effect is very small for the calculated binding energy for  $^6_{\Lambda\Lambda}\text{He}$ . Although their estimate is not for large atomic number hypernuclei nor nuclear matter, we neglect the  $\Xi N - \Lambda \Lambda$  channel coupling effect in the calculation. For the effective Pauli blocking and the channel coupling effects for the corresponding charm and bottom hypernuclei, we apply exactly the same forms and the coupling constants as those obtained for the  $\Lambda$  and  $\Sigma$ .

### 3.3.5 Results for strange hypernuclei

First, we present the results for strange hypernuclei. In Tables 14 and 15, we list the single-particle energies calculated for  $^{17}_Y\text{O}$ ,  $^{41}_Y\text{Ca}$ ,  $^{49}_Y\text{Ca}$ ,  $^{91}_Y\text{Zr}$  and  $^{209}_Y\text{Pb}$  ( $Y = \Lambda, \Sigma^{\pm, 0}, \Xi^{-, 0}$ ) hypernuclei, together with the experimental data [147, 153] for the  $\Lambda$  hypernuclei. (A recent, extensive review on the progress of the  $\Lambda$  hypernuclear spectroscopy is made in Ref. [154].) We have searched for the single-particle states up to the highest level of the core neutrons in each hypernucleus, since the deeper levels are usually easier to observe in experiment. Concerning the single-particle energy levels for the  $\Lambda$  hypernuclei, the QMC model supplemented by the effective Pauli blocking effect employed at the hadronic level, reproduces the data reasonably well. For the reasons explained earlier, small spin-orbit splittings are found for the  $\Lambda$  hypernuclei.

It should be mentioned here that in the case of larger mass number  $\Sigma$  hypernuclei, no narrow states have been observed experimentally, although  $^4_\Sigma\text{He}$  was confirmed [155]. This experimental analysis [156] supports the suggestion made by Harada [157], that a large isospin dependent  $\Sigma$ -nucleus potential term may exist and the  $1/A$  ( $A$ : baryon number) dependence of that term reduces the likelihood of observing bound states for  $A > 5$ . The absence of heavier  $\Sigma$  hypernuclei may also arise from the width of  $\Sigma$  states associated with strong  $\Sigma - \Lambda$  conversion. Nevertheless, it may be interesting to compare the single-particle energies obtained for the charged hyperons,  $\Sigma^\pm$  and  $\Xi^-$ , and those of the neutral hyperons,  $\Sigma^0$  and  $\Xi^0$ . The present results imply that the Coulomb force is important for forming (or unforming) a bound state of the hyperon in hypernuclei. This was also discussed by Yamazaki et al. [158], in the context of the light  $\Sigma^-$  hypernuclei.

In Table 16 we show the calculated binding energy per baryon, root-mean-square (rms) charge radius ( $r_{ch}$ ) and rms radii of the strange hyperon ( $r_Y$ ), neutron ( $r_n$ ) and proton ( $r_p$ ) distributions. The results listed in Table 16 are calculated for the  $1s_{1/2}$  hyperon configuration in all cases. Here, one can again notice the important role of the Coulomb force. For example, the binding energy per baryon,  $E_B/A$ , for the  $\Sigma^-$  ( $\Sigma^+$ )

Table 14: Single-particle energies (in MeV) for  ${}^{17}_Y\text{O}$ ,  ${}^{41}_Y\text{Ca}$  and  ${}^{49}_Y\text{Ca}$  ( $Y = \Lambda, \Sigma^{\pm,0}, \Xi^{-,0}$ ) strange hypernuclei, calculated with the effective Pauli blocking and the  $\Sigma N - \Lambda N$  channel coupling. Experimental data are taken from Ref. [153]. Spin-orbit splittings are not well determined by the experiments.

	${}^{16}_{\Lambda}\text{O}$ (Expt.)	${}^{17}_{\Lambda}\text{O}$	${}^{17}_{\Sigma^-}\text{O}$	${}^{17}_{\Sigma^0}\text{O}$	${}^{17}_{\Sigma^+}\text{O}$	${}^{17}_{\Xi^-}\text{O}$	${}^{17}_{\Xi^0}\text{O}$
$1s_{1/2}$	-12.5	-14.1	-17.2	-9.6	-3.3	-9.9	-4.5
$1p_{3/2}$	-2.5 (1p)	-5.1	-8.7	-3.2	—	-3.4	—
$1p_{1/2}$	-2.5 (1p)	-5.0	-8.0	-2.6	—	-3.4	—
	${}^{40}_{\Lambda}\text{Ca}$ (Expt.)	${}^{41}_{\Lambda}\text{Ca}$	${}^{41}_{\Sigma^-}\text{Ca}$	${}^{41}_{\Sigma^0}\text{Ca}$	${}^{41}_{\Sigma^+}\text{Ca}$	${}^{41}_{\Xi^-}\text{Ca}$	${}^{41}_{\Xi^0}\text{Ca}$
$1s_{1/2}$	-20.0	-19.5	-23.5	-13.4	-4.1	-17.0	-8.1
$1p_{3/2}$	-12.0 (1p)	-12.3	-17.1	-8.3	—	-11.2	-3.3
$1p_{1/2}$	-12.0 (1p)	-12.3	-16.5	-7.7	—	-11.3	-3.4
$1d_{5/2}$		-4.7	-10.6	-2.6	—	-5.5	—
$2s_{1/2}$		-3.5	-9.3	-1.2	—	-5.4	—
$1d_{3/2}$		-4.6	-9.7	-1.9	—	-5.6	—
	—	${}^{49}_{\Lambda}\text{Ca}$	${}^{49}_{\Sigma^-}\text{Ca}$	${}^{49}_{\Sigma^0}\text{Ca}$	${}^{49}_{\Sigma^+}\text{Ca}$	${}^{49}_{\Xi^-}\text{Ca}$	${}^{49}_{\Xi^0}\text{Ca}$
$1s_{1/2}$		-21.0	-19.3	-14.6	-11.5	-14.7	-12.0
$1p_{3/2}$		-13.9	-11.4	-9.4	-7.5	-8.7	-7.4
$1p_{1/2}$		-13.8	-10.9	-8.9	-7.0	-8.8	-7.4
$1d_{5/2}$		-6.5	-5.8	-3.8	-2.0	-3.8	-2.1
$2s_{1/2}$		-5.4	-6.7	-2.6	—	-4.6	-1.1
$1d_{3/2}$		-6.4	-5.2	-3.1	-1.2	-3.8	-2.2
$1f_{7/2}$		—	-1.2	—	—	—	—

Table 15: Same as Table 17 but for  $^{91}_Y\text{Zr}$  and  $^{208}_Y\text{Pb}$  ( $Y = \Lambda, \Sigma^{\pm,0}, \Xi^{-,0}$ ). Experimental data are taken from Ref. [147]. Spin-orbit splittings are not well determined by the experiments. Double asterisks, \*\*, indicate the value used for fitting.

	$^{89}_\Lambda\text{Yb}$ (Expt.)	$^{91}_\Lambda\text{Zr}$	$^{91}_{\Sigma^-}\text{Zr}$	$^{91}_{\Sigma^0}\text{Zr}$	$^{91}_{\Sigma^+}\text{Zr}$	$^{91}_{\Xi^-}\text{Zr}$	$^{91}_{\Xi^0}\text{Zr}$
$1s_{1/2}$	-22.5	-23.9	-27.3	-16.8	-8.1	-22.7	-13.3
$1p_{3/2}$	-16.0 (1p)	-18.4	-20.8	-12.7	-5.0	-17.4	-9.7
$1p_{1/2}$	-16.0 (1p)	-18.4	-20.5	-12.4	-4.7	-17.4	-9.7
$1d_{5/2}$	-9.0 (1d)	-12.3	-15.4	-8.1	-0.9	-12.3	-5.4
$2s_{1/2}$		-10.8	-15.6	-6.5	—	-12.4	-3.9
$1d_{3/2}$	-9.0 (1d)	-12.3	-14.8	-7.5	-0.3	-12.4	-5.5
$1f_{7/2}$	-2.0 (1f)	-5.9	-10.2	-3.1	—	-7.5	-0.7
$2p_{3/2}$		-4.2	-10.1	—	—	-7.9	—
$1f_{5/2}$	-2.0 (1f)	-5.8	-9.4	-2.3	—	-7.6	-0.8
$2p_{1/2}$		-4.1	-9.9	—	—	-7.9	—
$1g_{9/2}$		—	-5.2	—	—	-3.3	—
	$^{208}_\Lambda\text{Pb}$ (Expt.)	$^{209}_\Lambda\text{Pb}$	$^{209}_{\Sigma^-}\text{Pb}$	$^{209}_{\Sigma^0}\text{Pb}$	$^{209}_{\Sigma^+}\text{Pb}$	$^{209}_{\Xi^-}\text{Pb}$	$^{209}_{\Xi^0}\text{Pb}$
$1s_{1/2}$	-27.0	-27.0**	-29.7	-19.6**	-10.0	-29.0	-19.2
$1p_{3/2}$	-22.0 (1p)	-23.4	-25.9	-16.7	-7.7	-25.3	-16.3
$1p_{1/2}$	-22.0 (1p)	-23.4	-25.8	-16.5	-7.5	-25.4	-16.3
$1d_{5/2}$	-17.0 (1d)	-19.1	-22.1	-13.3	-4.6	-21.6	-12.9
$2s_{1/2}$		-17.6	-21.7	-12.0	-2.1	-21.2	-12.0
$1d_{3/2}$	-17.0 (1d)	-19.1	-21.8	-13.0	-4.2	-21.6	-12.9
$1f_{7/2}$	-12.0 (1f)	-14.4	-18.2	-9.5	-0.9	-17.6	-9.2
$2p_{3/2}$		-12.4	-17.4	-7.8	—	-17.1	-8.0
$1f_{5/2}$	-12.0 (1f)	-14.3	-17.8	-9.0	-0.4	-17.7	-9.2
$2p_{1/2}$		-12.4	-17.2	-7.6	—	-17.1	-8.0
$1g_{9/2}$	-7.0 (1g)	-9.3	-14.3	-5.5	—	-13.6	-5.2
$1g_{7/2}$	-7.0 (1g)	-9.2	-13.6	-4.8	—	-13.7	-5.2
$1h_{11/2}$		-3.9	-4.9	-1.2	—	-9.7	-1.0
$2d_{5/2}$		-7.0	-7.5	—	—	-13.3	-3.8
$2d_{3/2}$		-7.0	-7.5	—	—	-13.3	-3.8
$1h_{9/2}$		-3.8	-4.8	—	—	-9.8	-1.0
$3s_{1/2}$		-6.1	-7.8	—	—	-8.3	-3.1
$2f_{7/2}$		-1.7	-5.8	—	—	-6.2	—
$3p_{3/2}$		-1.0	-3.4	—	—	-6.6	—
$2f_{5/2}$		-1.7	-5.8	—	—	-6.3	—
$3p_{1/2}$		-1.0	-3.3	—	—	-6.6	—
$1i_{13/2}$		—	—	—	—	-3.7	—

Table 16: Binding energy per baryon,  $E_B/A$  (in MeV), rms charge radius ( $r_{ch}$ ), and rms radii of the strange hyperon ( $r_Y$ ), neutron ( $r_n$ ), and proton ( $r_p$ ) (in fm) for  $^{17}_Y\text{O}$ ,  $^{41}_Y\text{Ca}$ ,  $^{49}_Y\text{Ca}$ ,  $^{91}_Y\text{Zr}$  and  $^{209}_Y\text{Pb}$  strange hypernuclei. The configuration of the strange hyperon,  $Y$ , is  $1s_{1/2}$  for all hypernuclei. For comparison, we also list the corresponding results for normal finite nuclei. Double asterisks, \*\*, indicate the value used for fitting.

hypernuclei	$-E_B/A$	$r_{ch}$	$r_Y$	$r_n$	$r_p$
$^{17}_{\Lambda}\text{O}$	6.37	2.84	2.49	2.59	2.72
$^{17}_{\Sigma^+}\text{O}$	5.91	2.82	3.15	2.61	2.70
$^{17}_{\Sigma^0}\text{O}$	6.10	2.83	2.79	2.60	2.71
$^{17}_{\Sigma^-}\text{O}$	6.31	2.84	2.49	2.59	2.72
$^{17}_{\Xi^0}\text{O}$	5.86	2.80	2.98	2.62	2.68
$^{17}_{\Xi^-}\text{O}$	6.02	2.81	2.65	2.61	2.69
$^{16}\text{O}$	5.84	2.79	—	2.64	2.67
$^{41}_{\Lambda}\text{Ca}$	7.58	3.51	2.81	3.31	3.42
$^{41}_{\Sigma^+}\text{Ca}$	7.33	3.50	3.43	3.32	3.41
$^{41}_{\Sigma^0}\text{Ca}$	7.44	3.51	3.14	3.31	3.41
$^{41}_{\Sigma^-}\text{Ca}$	7.60	3.51	2.87	3.31	3.41
$^{41}_{\Xi^0}\text{Ca}$	7.34	3.49	3.09	3.32	3.40
$^{41}_{\Xi^-}\text{Ca}$	7.45	3.50	2.84	3.32	3.40
$^{40}\text{Ca}$	7.36	3.48**	—	3.33	3.38
$^{49}_{\Lambda}\text{Ca}$	7.58	3.54	2.84	3.63	3.45
$^{49}_{\Sigma^+}\text{Ca}$	6.32	3.57	3.47	3.71	3.48
$^{49}_{\Sigma^0}\text{Ca}$	7.40	3.54	3.14	3.64	3.45
$^{49}_{\Sigma^-}\text{Ca}$	7.48	3.55	2.60	3.63	3.45
$^{49}_{\Xi^0}\text{Ca}$	7.32	3.53	3.14	3.65	3.43
$^{49}_{\Xi^-}\text{Ca}$	7.35	3.53	2.79	3.65	3.44
$^{48}\text{Ca}$	7.27	3.52	—	3.66	3.42
$^{91}_{\Lambda}\text{Zr}$	7.95	4.29	3.25	4.29	4.21
$^{91}_{\Sigma^+}\text{Zr}$	7.82	4.28	4.01	4.30	4.20
$^{91}_{\Sigma^0}\text{Zr}$	7.87	4.29	3.56	4.30	4.21
$^{91}_{\Sigma^-}\text{Zr}$	7.92	4.29	2.89	4.29	4.21
$^{91}_{\Xi^0}\text{Zr}$	7.83	4.28	3.54	4.30	4.20
$^{91}_{\Xi^-}\text{Zr}$	7.87	4.28	2.98	4.30	4.20
$^{90}\text{Zr}$	7.79	4.27	—	4.31	4.19
$^{209}_{\Lambda}\text{Pb}$	7.35	5.49	3.99	5.67	5.43
$^{209}_{\Sigma^+}\text{Pb}$	7.28	5.49	4.64	5.68	5.43
$^{209}_{\Sigma^0}\text{Pb}$	7.31	5.49	4.26	5.67	5.43
$^{209}_{\Sigma^-}\text{Pb}$	7.34	5.49	3.80	5.67	5.43
$^{209}_{\Xi^0}\text{Pb}$	7.30	5.49	3.96	5.68	5.43
$^{209}_{\Xi^-}\text{Pb}$	7.32	5.49	3.59	5.68	5.43
$^{208}\text{Pb}$	7.25	5.49	—	5.68	5.43

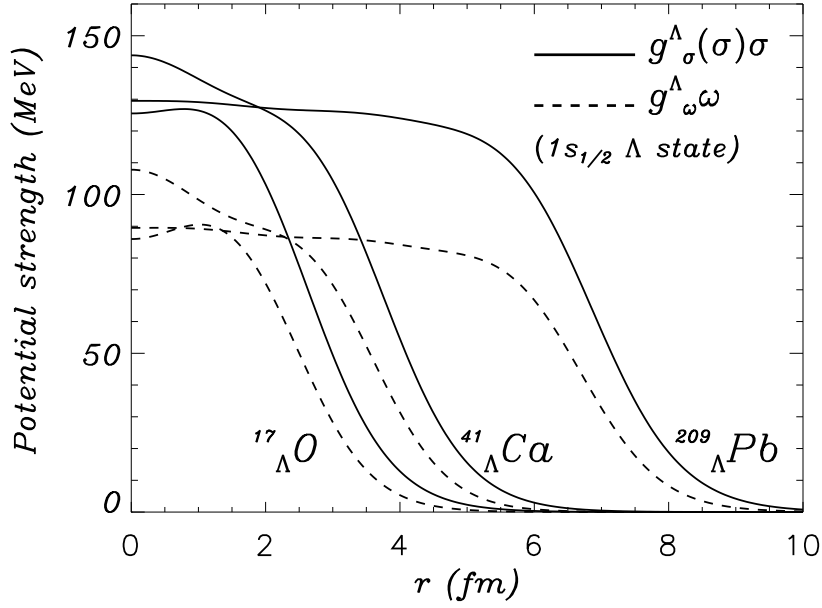


Figure 21: Potential strengths,  $g_\sigma^\Lambda(\sigma)$  and  $g_\omega^\Lambda$ , for  $\Lambda$  hypernuclei,  $^{17}_\Lambda\text{O}$ ,  $^{41}_\Lambda\text{Ca}$  and  $^{209}_\Lambda\text{Pb}$  for  $1s_{1/2}\Lambda$  state (from Ref. [124]).

hypernuclei is typically the largest (smallest) among the same atomic number strange hypernuclei, while the rms radii for the hyperon,  $r_{\Sigma^-}$  ( $r_{\Sigma^+}$ ) is mostly the smallest (largest) among the hypernuclei of the same atomic number.

To get an idea of the mass number dependence for the strange hypernuclei calculated, we show the absolute values of the scalar and vector potentials for the hyperons in  $^{17}_Y\text{O}$ ,  $^{41}_Y\text{Ca}$  and  $^{209}_Y\text{Pb}$  ( $Y = \Lambda, \Sigma^0, \Xi^0$ ) in Figs. 21 and 22.

We make one final remark concerning the  $\Sigma$  hypernuclei. Recent experiments [156] suggest that a strongly repulsive  $\Sigma$ -nucleus potential with a non-zero size of the imaginary part is best able to reproduce the measured spectra for middle and large baryon number hypernuclei. If we wish to be consistent with this result, we need to introduce an even stronger repulsive potential, either by the channel coupling effect, or based on the quark model analysis to reproduce the  $\Sigma$ -atom data without resorting to the channel coupling effect [159] for the  $\Sigma$  ( $\Sigma_c$ ) hypernuclei. In this case, the repulsion should be strong enough that it entails no bound state for the  $\Sigma$  hypernuclei with medium to large baryon number. This will need a more elaborate investigation in the future, using further accumulated experimental data and analyses. Thus, at present, our results for  $\Sigma$  hypernuclei are incomplete and we need further investigation.

### 3.3.6 Results for charm and bottom hypernuclei

Next, we present results for charm and bottom hypernuclei. The formation of  $\Lambda_c$  and/or  $\Lambda_b$  hypernuclei was first predicted in the mid-1970s by Tyapkin [160], and Dover and Kahana [161]. Later on, theoretical studies [162, 163] as well as suggestions concerning the possibility of experimental observation [164] were made. The study of charm and bottom hypernuclei can be made in the same way as those made for strange hypernuclei. Namely, the treatment of spin-orbit force, and the Pauli blocking and the channel coupling effects are included in the same way as those explained in sections 3.3.3 and 3.3.4. However, since the charm and bottom baryons are heavy compared to the typical magnitude of the potentials needed to form a nucleus, the contribution from the spin-orbit piece of the single-particle energies is negligible. As will be shown later, its typical contribution is of order 0.01 MeV, and even the largest case is  $\simeq 0.5$  MeV, for all the charm and bottom hypernuclear

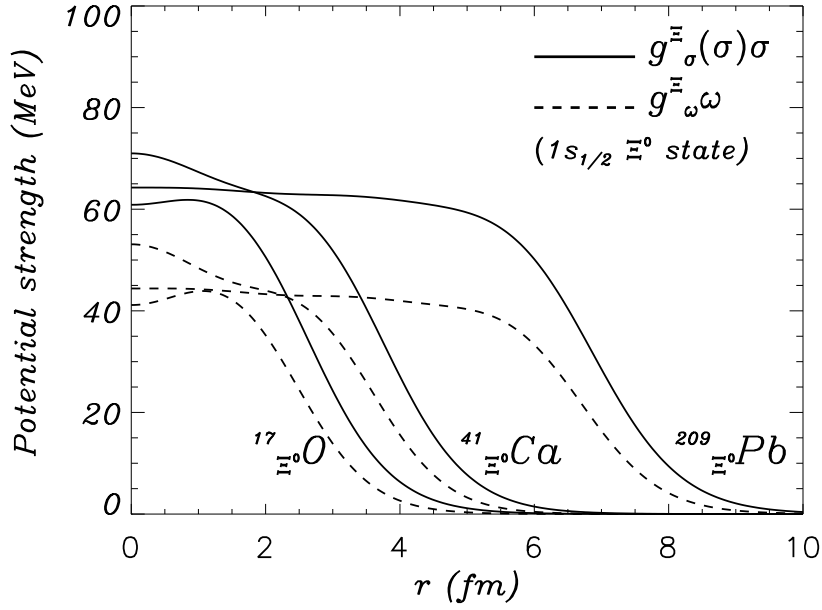


Figure 22: Same as Fig. 21 but for the  $\Xi^0$  hypernuclei (from Ref. [124]).

single-particle energies calculated. This can be understood when one considers the limit,  $M_j^* \rightarrow \infty$  in Eq. (233) for the cases of charm and bottom hypernuclei, where the quantity inside the square brackets varies smoothly from an order of hundred MeV to zero near the surface of the hypernucleus, and the derivative with respect to  $r$  is finite. Thus, the spin-orbit splittings are expected to be tiny.

Concerning the channel coupling for  $\Sigma_c N - \Lambda_c N$ , we treat it in the same phenomenological way as that for  $\Sigma N - \Lambda N$ , although the effect is expected to be smaller, since the mass difference for the former is larger. Thus, the channel coupling effect included for the  $\Sigma_c$  hypernuclei should be regarded as the limiting case. In addition, recall that the recent experimental results show no evidence for narrow width  $\Sigma$  hypernuclei for the medium to large mass region. This suggests that one should improve the present treatment of the Pauli blocking and the channel coupling effects in the QMC model, for the  $\Sigma_c$  (and  $\Sigma$ ) hypernuclei.

In Tables 17 and 18 we give the single particle energies calculated for  $^{17}_Y\text{O}$ ,  $^{41}_Y\text{Ca}$ ,  $^{49}_Y\text{Ca}$ ,  $^{91}_Y\text{Zr}$  and  $^{209}_Y\text{Pb}$  ( $Y = \Lambda, \Lambda_c^+, \Sigma_c^{0,+}, \Xi_c^{0,+}, \Lambda_b$ ) hypernuclei, together with the experimental data [153, 147] for the  $\Lambda$  hypernuclei.

As for the strange hypernuclei, we searched for single-particle states up to the same level as the highest state of the core neutrons in each hypernucleus, since the deeper levels are usually easier to observe in experiment. After a first look at the results shown in Tables 17 and 18 we notice:

1.  $\Sigma_c^{++}$  and  $\Xi_c^+$  hypernuclei are very unlikely to be formed under normal circumstances, while solid conclusions may not be drawn about  $^{49}_{\Sigma_c^{++}, \Xi_c^+}\text{Ca}$ . Although these results imply the formation of these hypernuclei, those numbers may be regarded within the uncertainties of the model and the approximations made in the calculation.
2.  $\Sigma_c^0$  and  $\Sigma_c^+$  hypernuclei may have some possibility to be formed. However, due to a peculiar feature that the correct  $1s_{1/2}$  state is not found in  $^{17}_\Sigma\text{O}$ ,  $^{49}_\Sigma\text{Ca}$  and  $^{91}_\Sigma\text{Zr}$ , one needs to take this statement with some caution. (For detailed discussion, see Ref. [126] and below.)
3.  $\Lambda_c^+, \Xi_c^0$  and  $\Lambda_b$  hypernuclei are expected to be quite likely to be formed in a realistic situation. However, for the  $\Lambda_b$  hypernuclei, it will be very difficult to achieve such a resolution to distinguish the states experimentally. The question of experimental observation is not tackled realistically.

Table 17: Single-particle energies (in MeV) for  $^{17}_Y\text{O}$ ,  $^{41}_Y\text{Ca}$  and  $^{49}_Y\text{Ca}$  ( $Y = \Lambda, \Lambda_c, \Sigma_c, \Xi_c, \Lambda_b$ ). Experimental data are taken from Ref. [153]. Spin-orbit splittings for the  $\Lambda$  hypernuclei are not well determined by the experiments.

	$^{16}_\Lambda\text{O}$ (Expt.)	$^{17}_\Lambda\text{O}$	$^{17}_{\Lambda_c^+}\text{O}$	$^{17}_{\Sigma_c^0}\text{O}$	$^{17}_{\Sigma_c^+}\text{O}$	$^{17}_{\Sigma_c^{++}}\text{O}$	$^{17}_{\Xi_c^0}\text{O}$	$^{17}_{\Xi_c^+}\text{O}$	$^{17}_{\Lambda_b}\text{O}$
$1s_{1/2}$	-12.5	-14.1	-12.8	—	-7.5	—	-7.9	-2.1	-19.6
$1p_{3/2}$	-2.5 (1p)	-5.1	-7.3	-10.7	-4.0	—	-3.5	—	-16.5
$1p_{1/2}$	-2.5 (1p)	-5.0	-7.3	-10.2	-3.6	—	-3.5	—	-16.5
	$^{40}_\Lambda\text{Ca}$ (Expt.)	$^{41}_\Lambda\text{Ca}$	$^{41}_{\Lambda_c^+}\text{Ca}$	$^{41}_{\Sigma_c^0}\text{Ca}$	$^{41}_{\Sigma_c^+}\text{Ca}$	$^{41}_{\Sigma_c^{++}}\text{Ca}$	$^{41}_{\Xi_c^0}\text{Ca}$	$^{41}_{\Xi_c^+}\text{Ca}$	$^{41}_{\Lambda_b}\text{Ca}$
$1s_{1/2}$	-20.0	-19.5	-12.8	-16.3	-6.3	—	-9.9	-1.0	-23.0
$1p_{3/2}$	-12.0 (1p)	-12.3	-9.2	-13.2	-4.1	—	-6.7	—	-20.9
$1p_{1/2}$	-12.0 (1p)	-12.3	-9.1	-12.9	-3.8	—	-6.7	—	-20.9
$1d_{5/2}$		-4.7	-4.8	-9.9	—	—	-3.3	—	-18.4
$2s_{1/2}$		-3.5	-3.4	-9.3	—	—	-2.8	—	-17.4
$1d_{3/2}$		-4.6	-4.8	-9.4	—	—	-3.3	—	-18.4
	—	$^{49}_\Lambda\text{Ca}$	$^{49}_{\Lambda_c^+}\text{Ca}$	$^{49}_{\Sigma_c^0}\text{Ca}$	$^{49}_{\Sigma_c^+}\text{Ca}$	$^{49}_{\Sigma_c^{++}}\text{Ca}$	$^{49}_{\Xi_c^0}\text{Ca}$	$^{49}_{\Xi_c^+}\text{Ca}$	$^{49}_{\Lambda_b}\text{Ca}$
$1s_{1/2}$		-21.0	-14.3	—	-7.4	-5.0	-7.8	-5.1	-24.4
$1p_{3/2}$		-13.9	-10.6	-7.2	-5.1	-3.4	-4.1	-2.8	-22.2
$1p_{1/2}$		-13.8	-10.6	-7.0	-4.9	-3.2	-4.1	-2.8	-22.2
$1d_{5/2}$		-6.5	-6.5	-4.0	-2.3	—	-0.9	—	-19.5
$2s_{1/2}$		-5.4	-5.3	-4.9	—	—	-1.5	—	-18.8
$1d_{3/2}$		-6.4	-6.4	-3.6	-1.9	—	-1.0	—	-19.5
$1f_{7/2}$		—	-2.0	—	—	—	—	—	-16.8



Table 18: Same as Table 17 but for  $^{91}_Y\text{Zr}$  and  $^{208}_Y\text{Pb}$  ( $Y = \Lambda, \Lambda_c, \Sigma_c, \Xi_c, \Lambda_b$ ). Experimental data are taken from Ref. [147]. The values given inside the brackets for  $^{91}_{\Sigma_c^0}\text{Zr}$  are those obtained by switching off both the Pauli blocking and the channel coupling effects simultaneously.

	$^{89}_{\Lambda}\text{Yb}$ (Expt.)	$^{91}_{\Lambda}\text{Zr}$	$^{91}_{\Lambda_c^+}\text{Zr}$	$^{91}_{\Sigma_c^0}\text{Zr}$	$^{91}_{\Sigma_c^+}\text{Zr}$	$^{91}_{\Sigma_c^{++}}\text{Zr}$	$^{91}_{\Xi_c^0}\text{Zr}$	$^{91}_{\Xi_c^+}\text{Zr}$	$^{91}_{\Lambda_b}\text{Zr}$
$1s_{1/2}$	-22.5	-23.9	-10.8	— (—)	-3.7	—	-9.3	—	-25.7
$1p_{3/2}$	-16.0 (1p)	-18.4	-8.7	-10.2 (-26.5)	-2.3	—	-6.6	—	-24.2
$1p_{1/2}$	-16.0 (1p)	-18.4	-8.7	-10.1 (-26.4)	-2.1	—	-6.7	—	-24.2
$1d_{5/2}$	-9.0 (1d)	-12.3	-5.8	-7.6 (-21.8)	—	—	-4.0	—	-22.4
$2s_{1/2}$		-10.8	-3.9	-8.1 (-23.0)	—	—	-3.9	—	-21.6
$1d_{3/2}$	-9.0 (1d)	-12.3	-5.8	-7.3 (-21.6)	—	—	-4.0	—	-22.4
$1f_{7/2}$	-2.0 (1f)	-5.9	-2.4	-5.1 (-17.1)	—	—	-1.3	—	-20.4
$2p_{3/2}$		-4.2	—	-5.0 (-16.5)	—	—	-1.3	—	-19.5
$1f_{5/2}$	-2.0 (1f)	-5.8	-2.4	-4.7 (-16.8)	—	—	-1.4	—	-20.4
$2p_{1/2}$		-4.1	—	-4.9 (-16.3)	—	—	-1.3	—	-19.5
$1g_{9/2}$		—	—	-2.4 (-12.4)	—	—	—	—	-18.1
	$^{208}_{\Lambda}\text{Pb}$ (Expt.)	$^{209}_{\Lambda}\text{Pb}$	$^{209}_{\Lambda_c^+}\text{Pb}$	$^{209}_{\Sigma_c^0}\text{Pb}$	$^{209}_{\Sigma_c^+}\text{Pb}$	$^{209}_{\Sigma_c^{++}}\text{Pb}$	$^{209}_{\Xi_c^0}\text{Pb}$	$^{209}_{\Xi_c^+}\text{Pb}$	$^{209}_{\Lambda_b}\text{Pb}$
$1s_{1/2}$	-27.0	-27.0	-5.2	-7.5	—	—	-6.7	—	-27.4
$1p_{3/2}$	-22.0 (1p)	-23.4	-4.1	-6.6	—	—	-5.4	—	-26.6
$1p_{1/2}$	-22.0 (1p)	-23.4	-4.0	-6.5	—	—	-5.5	—	-26.6
$1d_{5/2}$	-17.0 (1d)	-19.1	-2.4	-5.3	—	—	-3.9	—	-25.4
$2s_{1/2}$		-17.6	—	—	—	—	-3.3	—	-24.7
$1d_{3/2}$	-17.0 (1d)	-19.1	-2.4	-5.1	—	—	-4.0	—	-25.4
$1f_{7/2}$	-12.0 (1f)	-14.4	—	-3.8	—	—	-2.2	—	-24.1
$2p_{3/2}$		-12.4	—	—	—	—	-1.4	—	-23.2
$1f_{5/2}$	-12.0 (1f)	-14.3	—	-3.5	—	—	-2.3	—	-24.1
$2p_{1/2}$		-12.4	—	—	—	—	-1.5	—	-23.2
$1g_{9/2}$	-7.0 (1g)	-9.3	—	-2.1	—	—	—	—	-22.6
$1g_{7/2}$	-7.0 (1g)	-9.2	—	-1.8	—	—	—	—	-22.6
$1h_{11/2}$		-3.9	—	—	—	—	—	—	-21.0
$2d_{5/2}$		-7.0	—	—	—	—	—	—	-21.7
$2d_{3/2}$		-7.0	—	—	—	—	—	—	-21.7
$1h_{9/2}$		-3.8	—	—	—	—	—	—	-21.0
$3s_{1/2}$		-6.1	—	—	—	—	—	—	-21.3
$2f_{7/2}$		-1.7	—	—	—	—	—	—	-20.1
$3p_{3/2}$		-1.0	—	—	—	—	—	—	-19.6
$2f_{5/2}$		-1.7	—	—	—	—	—	—	-20.1
$3p_{1/2}$		-1.0	—	—	—	—	—	—	-19.6
$1i_{13/2}$		—	—	—	—	—	—	—	-19.3

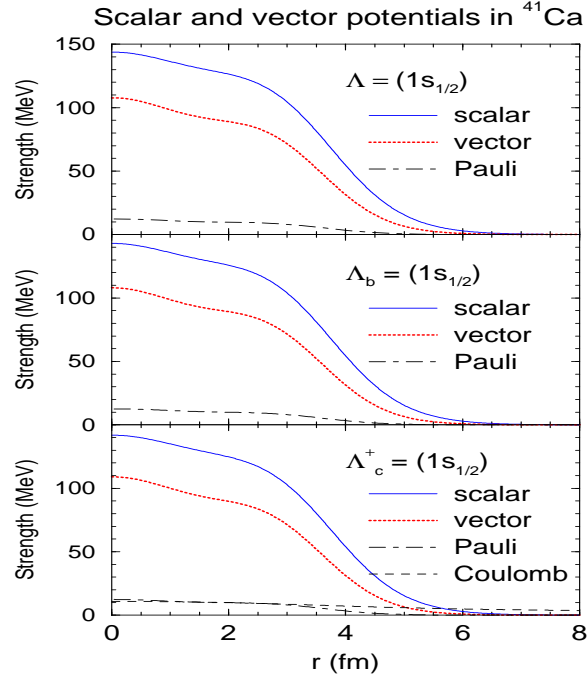


Figure 23: Potential strengths for  $1s_{1/2}$  state felt by the  $\Lambda$ ,  $\Lambda_c^+$  and  $\Lambda_b$  in  $^{41}_Y\text{Ca}$  ( $Y = \Lambda, \Lambda_c^+, \Lambda_b$ ). "Pauli" stands for the effective, repulsive, potential representing the Pauli blocking at the quark level plus the  $\Sigma_{c,b}N - \Lambda_{c,b}N$  channel coupling, introduced phenomenologically at the baryon level [124] (see section 3.3.4) (from Ref. [126]).

4. The Coulomb force plays a crucial role in forming (unforming) hypernuclei, by comparing the single-particle energies among/between the members within each multiplet,  $(\Lambda, \Lambda_c^+, \Lambda_b)$ ,  $(\Sigma_c^0, \Sigma_c^+, \Sigma_c^{++})$ , and  $(\Xi_c^0, \Xi_c^+)$  hypernuclei.

We comment shortly on the  $^{17}_{\Sigma_c^0}\text{O}$ ,  $^{49}_{\Sigma_c^0}\text{Ca}$  and  $^{91}_{\Sigma_c^0}\text{Zr}$  hypernuclei. The  $1s_{1/2}$  state for these hypernuclei were not found. It was concluded in Ref. [126] that this is caused by the strong isospin dependent  $\rho$  mean field in the very central region of these hypernuclei. Some related discussion will be given later.

Next, in Figs. 23, 24, 25 and 26 we show the potential strengths for  $1s_{1/2}$  state in  $^{41}_Y\text{Ca}$  and  $^{209}_Y\text{Pb}$  ( $Y = \Lambda, \Lambda_c^+, \Lambda_b, \Sigma_c^{0,+}, \Xi_c^0$ ). Recall that the effects are different for the  $\Lambda_c$  and  $\Sigma_c$  as they are true for the  $\Lambda$  and  $\Sigma$ . As in the limit of nuclear matter in section 2.2, the scalar and vector potentials for the heavy baryons are also quite similar to the strange hyperons with the same light quark numbers in the corresponding hypernuclei. This feature also holds for the  $\Sigma_c$  and  $\Sigma$  in the corresponding hypernuclei, except for a contribution due to the difference in charges, where the Coulomb force affects the baryon density distributions and then the vector and scalar potentials are also slightly modified. Thus, as far as the total baryon density distributions and the scalar and vector potentials are concerned, among/between the members within each multiplet,  $(\Lambda, \Lambda_c, \Lambda_b)$ ,  $(\Sigma, \Sigma_c)$  and  $(\Xi, \Xi_c)$  hypernuclei, they show quite similar features. However, in realistic nuclei, the Coulomb force plays a crucial role as mentioned before, and the single-particle energies thus obtained show very different features within each hypernuclear multiplet. Of course, the mass differences within the multiplet are also the dominant source for the differences in the single-particle energies calculated.

The baryon density distributions for hyperon  $Y$  for  $1s_{1/2}$  state, in  $^{41}_Y\text{Ca}$  and  $^{209}_Y\text{Pb}$  ( $Y = \Lambda, \Lambda_c^+, \Lambda_b, \Sigma_c^{0,+}, \Xi_c^0$ ), are shown in Figs. 27 and 28. One notices in Fig. 27 that the heavier hyperon,  $\Lambda_b$  is much more localized in the central region of the hypernucleus than  $\Lambda_c^+$  and  $\Lambda$ . In addition, the Coulomb force pushes the  $\Lambda_c^+$  away from the central region in the  $^{209}_{\Lambda_c^+}\text{Pb}$  hypernucleus. Next, it is interesting to compare the  $\Sigma_c^0$  and  $\Xi_c^0$  probability density distributions in Fig. 28. Due to the Pauli blocking and the channel coupling effects, the probability density distributions for the  $\Sigma_c^0$  are pushed away from the origin compared to those for the  $\Xi_c^0$  in both  $^{41}_{\Sigma_c^0}\text{Ca}$  and  $^{209}_{\Sigma_c^0}\text{Pb}$ . In particular, the  $\Sigma_c^0$  density distribution in  $^{209}_{\Sigma_c^0}\text{Pb}$  is really pushed away from the central region, and thus

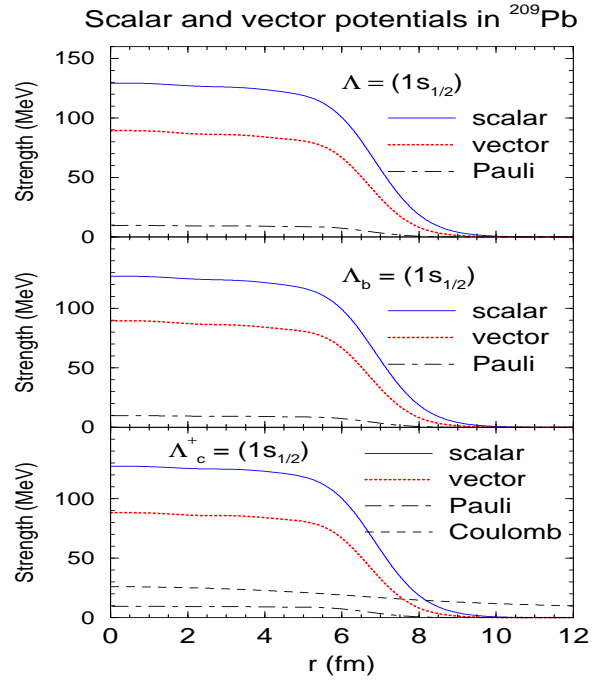


Figure 24: Same as Fig. 23, but for  $^{209}_{\text{Y}}\text{Pb}$  (from Ref. [126]).

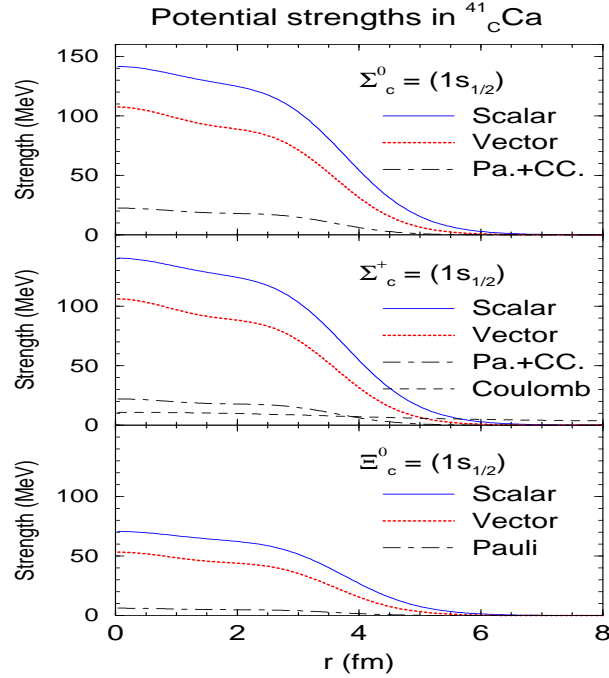


Figure 25: Potential strengths for the  $\Sigma_c^{0,+}$  and  $\Xi_c^0$  in  $^{41}_{\text{Y}}\text{Ca}$  ( $Y = \Sigma_c^{0,+}, \Xi_c^0$ ) for  $1s_{1/2}$  state (from Ref. [126]).

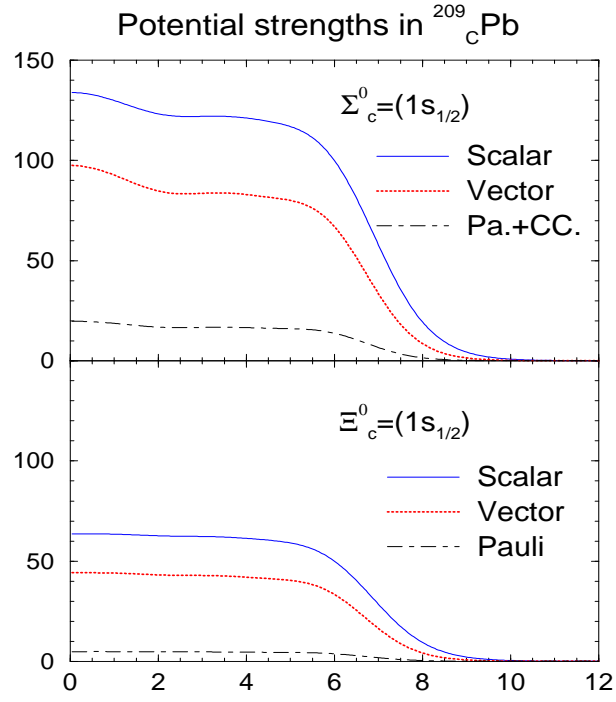


Figure 26: Same as Fig. 25 but for  $^{209}_{\text{C}}\text{Pb}$  ( $C = \Sigma_c^0, \Xi_c^0$ ) (from Ref. [126]).

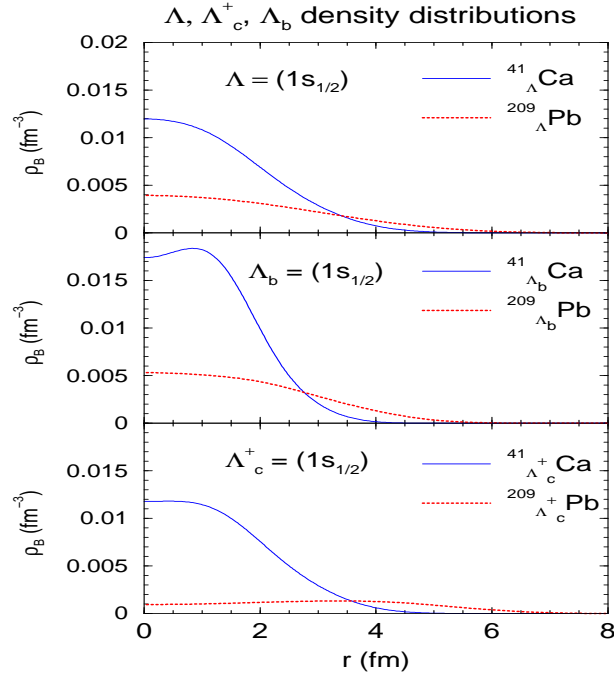


Figure 27:  $\Lambda, \Lambda_c^+$  and  $\Lambda_b$  baryon (probability) density distributions for  $1s_{1/2}$  state in  $^{41}_Y\text{Ca}$  and  $^{209}_Y\text{Pb}$  ( $Y = \Lambda, \Lambda_c^+, \Lambda_b$ ) (from Ref. [126]).

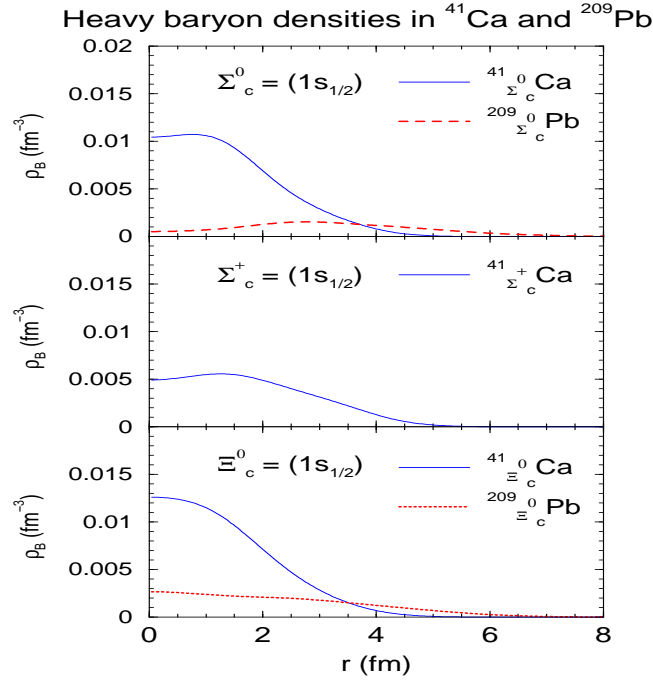


Figure 28:  $\Sigma_c^{0,+}$  and  $\Xi_c^0$  baryon (probability) density distributions for  $1s_{1/2}$  state in  ${}^{41}_Y\text{Ca}$  and  ${}^{209}_Y\text{Pb}$  ( $Y = \Sigma_c^{0,+}, \Xi_c^0$ ) (from Ref. [126]).

loses much of the character of a typical  $1s_{1/2}$  state wave function. This fact shows that the isospin dependent  $\rho$ -meson mean field for the  $\Sigma_c^0$   $1s_{1/2}$  state in the central region of the neutron rich nuclei is very strong. This may explain why the correct  $1s_{1/2}$  state is not found in  ${}^{49}_{\Sigma_c^0}\text{Ca}$  and  ${}^{91}_{\Sigma_c^0}\text{Zr}$ , where the (isospin asymmetric) baryon density distributions in central region of these nuclei are expected to be larger than those for  ${}^{209}_{\Sigma_c^0}\text{Pb}$  – as in the case of normal nuclei. (In the case of  ${}^{17}_{\Sigma_c^0}\text{O}$ , we expect that the size of the nucleus is much smaller and the  $\Sigma_c^0$  is more sensitive to the isospin dependent  $\rho$ -meson mean field, due to the higher baryon density and the limitation of the mean field approximation, than those for the  ${}^{209}_{\Sigma_c^0}\text{Pb}$ .) On the contrary, it is rather surprising that the  $\Xi_c^0$  probability density distribution is higher and localized more in the central region than those for the  $\Sigma_c^{0,+}$ , although one can naively expect that they have an opposite characteristic, because of the smaller scalar attractive potential for the  $\Xi_c^0$ . Thus, the effects of the Pauli blocking, and particularly the channel coupling, play an important role in giving rise to these different features.

Finally, we show in Table 19 the binding energy calculated per baryon,  $E_B/A$ , rms charge radius ( $r_{ch}$ ), and rms radii of the hyperons ( $r_Y, Y = \Lambda, \Lambda_c, \Sigma_c, \Xi_c, \Lambda_b$ ), neutron ( $r_n$ ) and proton ( $r_p$ ) for the  $1s_{1/2}$  hyperon configuration. At a first glance, it is very clear that the rms radius for the  $\Lambda_b$  is very small compared to those for other baryons within hypernuclei with the same baryon number – as one would expect, because of its heavy mass. On the other hand,  $r_{ch}$  and/or  $r_p$  for the  $\Lambda_b$  hypernuclei are usually the largest of all the hypernuclei calculated. This implies that the protons in the core nucleus are relatively more pushed away than in the other hypernuclei, although such a feature is not seen for  $r_n$ . The radii,  $r_{ch}$ ,  $r_n$  and  $r_p$ , may be grouped in similar magnitudes for all heavy baryon hypernuclei and  $\Lambda$  hypernuclei within the same baryon number multiplet ( ${}^{41}_Y\text{Ca}$  and  ${}^{49}_Y\text{Ca}$  in Table 19 may be grouped together), reflecting the fact that the effect of the embedded baryon on these quantities are of order,  $\simeq M_Y/[(A-1)M_N + M_Y]$ . As for the binding energy per baryon, the energy of  $\Lambda_b$  hypernuclei is usually the largest among hypernuclei with the same baryon number. One of the largest contributions for this is the single-particle energy of the  $1s_{1/2}$  state, even after divided by the total baryon number.

Although there can be numerous speculations on the implications of the present results we would like to emphasize that our calculations indicate that the  $\Lambda_c^+, \Xi_c^0$ , and  $\Lambda_b$  hypernuclei would exist in realistic experimental conditions, but there may be lesser possibilities for the  $\Sigma_c^0$  and  $\Sigma_c^+$  hypernuclei. Furthermore, it is very

Table 19: Binding energy per baryon,  $E_B/A$  (in MeV), rms charge radius ( $r_{ch}$ ), and rms radii of the  $\Lambda$  and heavy baryons,  $r_Y$ , neutron,  $r_n$ , and proton,  $r_p$  (in fm) for  $^{17}_Y\text{O}$ ,  $^{41}_Y\text{Ca}$ ,  $^{49}_Y\text{Ca}$ ,  $^{91}_Y\text{Zr}$  and  $^{209}_Y\text{Pb}$  ( $Y = \Lambda, \Lambda_c, \Sigma_c, \Xi_c, \Lambda_b$ ). The configurations of the  $\Lambda$  and heavy baryon  $Y$ , are  $1s_{1/2}$  for all hypernuclei.

hypernuclei	$-E_B/A$	$r_{ch}$	$r_Y$	$r_n$	$r_p$
$^{17}_{\Lambda}\text{O}$	6.37	2.84	2.49	2.59	2.72
$^{17}_{\Lambda^+}\text{O}$	6.42	2.85	2.19	2.58	2.73
$^{17}_{\Lambda_c^+}\text{O}$	6.10	2.83	2.57	2.60	2.71
$^{17}_{\Sigma_c^+}\text{O}$	6.01	2.81	2.34	2.61	2.69
$^{17}_{\Xi_c^0}\text{O}$	5.84	2.81	2.70	2.61	2.69
$^{17}_{\Xi_c^+}\text{O}$	6.69	2.87	1.81	2.57	2.75
$^{17}_{\Lambda_b}\text{O}$					
$^{41}_{\Lambda}\text{Ca}$	7.58	3.51	2.81	3.31	3.42
$^{41}_{\Lambda^+}\text{Ca}$	7.58	3.51	2.66	3.31	3.42
$^{41}_{\Lambda_c^+}\text{Ca}$	7.54	3.51	2.79	3.31	3.42
$^{41}_{\Sigma_c^0}\text{Ca}$	7.42	3.50	3.21	3.31	3.41
$^{41}_{\Sigma_c^+}\text{Ca}$	7.43	3.49	2.76	3.32	3.40
$^{41}_{\Xi_c^0}\text{Ca}$	7.32	3.49	3.11	3.32	3.39
$^{41}_{\Xi_c^+}\text{Ca}$	7.72	3.53	2.22	3.30	3.43
$^{41}_{\Lambda_b}\text{Ca}$					
$^{49}_{\Lambda}\text{Ca}$	7.58	3.54	2.84	3.63	3.45
$^{49}_{\Lambda^+}\text{Ca}$	7.54	3.54	2.67	3.63	3.45
$^{49}_{\Lambda_c^+}\text{Ca}$	7.39	3.54	3.17	3.64	3.44
$^{49}_{\Sigma_c^+}\text{Ca}$	6.29	3.57	3.62	3.71	3.47
$^{49}_{\Sigma_c^{++}}\text{Ca}$	7.34	3.53	2.57	3.65	3.43
$^{49}_{\Xi_c^0}\text{Ca}$	7.32	3.53	3.19	3.65	3.43
$^{49}_{\Xi_c^+}\text{Ca}$	7.64	3.56	2.16	3.63	3.46
$^{49}_{\Lambda_b}\text{Ca}$					
$^{91}_{\Lambda}\text{Zr}$	7.95	4.29	3.25	4.29	4.21
$^{91}_{\Lambda^+}\text{Zr}$	7.85	4.29	3.34	4.30	4.21
$^{91}_{\Lambda_c^+}\text{Zr}$	7.77	4.29	4.03	4.30	4.21
$^{91}_{\Sigma_c^+}\text{Zr}$	7.78	4.28	3.01	4.30	4.20
$^{91}_{\Xi_c^0}\text{Zr}$	7.93	4.30	2.63	4.29	4.22
$^{91}_{\Lambda_b}\text{Zr}$					
$^{209}_{\Lambda}\text{Pb}$	7.35	5.49	3.99	5.67	5.43
$^{209}_{\Lambda^+}\text{Pb}$	7.26	5.49	4.74	5.68	5.43
$^{209}_{\Lambda_c^+}\text{Pb}$	6.95	5.51	4.88	5.70	5.45
$^{209}_{\Sigma_c^0}\text{Pb}$	7.24	5.49	4.44	5.68	5.43
$^{209}_{\Xi_c^0}\text{Pb}$	7.48	5.49	3.45	5.66	5.43
$^{209}_{\Lambda_b}\text{Pb}$					

unlikely that the  $\Sigma_c^{++}$  and  $\Xi_c^+$  hypernuclei will be formed. Experiments at facilities like Japan Hadron Facility (JHF) would provide quantitative input to gain a better understanding of the interactions of heavy baryons with nuclear matter. Experiments at colliders such as RHIC, LHC and Fermilab could provide additional data to establish the formation and decay of such heavy baryon hypernuclei. A combination of these data inputs and a careful analysis, with the present calculations being considered as a first step, would give a valuable information about the physical implications for the presence of heavy quarks in finite nuclei or dense nuclear matter.

### 3.4 Meson-nucleus bound states

In this section we discuss the meson-nucleus bound states for  $\omega, \eta, \eta'$  [165, 166] first, and next  $D(\bar{D})$  mesons [131]. Studies of meson-nucleus bound states in different approaches have also been made in Refs. [167, 168, 169, 170, 171, 172, 173, 174]. To avoid confusion with the isoscalar-vector ( $\omega$ ) field appearing in the Lagrangian density of the QMC-I model, we emphasize that the  $\omega$  meson appearing in this section is a physical one.

As mentioned in section 3.3.1, we can treat mesons in the same way as hyperons in hypernuclei, as long as the mesons contain light quarks (antiquarks). (However, the pion cannot be treated in a satisfactory manner in a constituent quark model usually, because of its highly collective nature and low mass, originating in its Goldstone boson nature.) To study the meson-nucleus bound states for  $\omega, \eta, \eta'$  and  $D(\bar{D})$  mesons, one may solve the Klein-Gordon equation for a given potential inside a nucleus, instead of solving the Dirac equation for a hyperon in the case for the hypernuclei. (For the  $\omega$  meson, solving the Proca equation becomes equivalent to solving the Klein-Gordon equation with the Lorentz condition, as will be explained later.)

First, we consider the  $\eta, \eta'$  and  $\omega$  meson-nucleus bound states. The physical states of the  $\eta, \eta', \phi$  and  $\omega$  mesons are the superpositions of the octet and singlet states:

$$\xi = \xi_8 \cos \theta_{P,V} - \xi_1 \sin \theta_{P,V}, \quad \xi' = \xi_8 \sin \theta_{P,V} + \xi_1 \cos \theta_{P,V}, \quad (248)$$

with

$$\xi_1 = \frac{1}{\sqrt{3}} (u\bar{u} + d\bar{d} + s\bar{s}), \quad \xi_8 = \frac{1}{\sqrt{6}} (u\bar{u} + d\bar{d} - 2s\bar{s}), \quad (249)$$

where  $(\xi, \xi')$  denotes  $(\eta, \eta')$  or  $(\phi, \omega)$ , with the mixing angles  $\theta_P$  or  $\theta_V$ , respectively [132, 133, 134, 135]. Then, the masses for these mesons in the nucleus at position  $\vec{r}$ , are calculated using the local density approximation:

$$m_{\eta,\phi}^*(\vec{r}) = \frac{2[a_{P,V}^2 \Omega_q^*(\vec{r}) + b_{P,V}^2 \Omega_s^*(\vec{r})] - z_{\eta,\phi}}{R_{\eta,\phi}^*} + \frac{4}{3} \pi R_{\eta,\phi}^{*3} B, \quad (250)$$

$$m_{\eta',\omega}^*(\vec{r}) = \frac{2[b_{P,V}^2 \Omega_q^*(\vec{r}) + a_{P,V}^2 \Omega_s^*(\vec{r})] - z_{\eta',\omega}}{R_{\eta',\omega}^*} + \frac{4}{3} \pi R_{\eta',\omega}^{*3} B, \quad (251)$$

$$\left. \frac{\partial m_j^*(\vec{r})}{\partial R_j} \right|_{R_j=R_j^*} = 0, \quad (j = \eta, \eta', \phi, \omega), \quad (252)$$

with

$$a_{P,V} = \frac{1}{\sqrt{3}} \cos \theta_{P,V} - \sqrt{\frac{2}{3}} \sin \theta_{P,V}, \quad b_{P,V} = \sqrt{\frac{2}{3}} \cos \theta_{P,V} + \frac{1}{\sqrt{3}} \sin \theta_{P,V}. \quad (253)$$

In practice, we use  $\theta_P = -10^\circ$  and  $\theta_V = 39^\circ$  [132, 133, 134, 135], neglecting any possible mass dependence and imaginary parts. We also assume that the values of the mixing angles do not change in medium. Then, the in-medium modification of the  $\phi$  meson mass is negligible, since the  $\phi - \omega$  mixing is nearly ideal. Thus, the  $\phi$  meson is not expected to form nuclear bound states in the QMC model and we will not discuss on the  $\phi$ -nucleus bound states below.

In Eqs. (250) and (251),  $z_{\eta,\eta',\phi,\omega}$  are the same as before, they parameterize the sum of the center-of-mass and gluon fluctuation effects, and are assumed to be independent of density. The quark-meson coupling constants,  $g_\sigma^q$ ,  $g_\omega^q$  and  $g_\rho^q$ , are given in Table 11, and other inputs, parameters, and some of the quantities calculated are listed in Table 12.

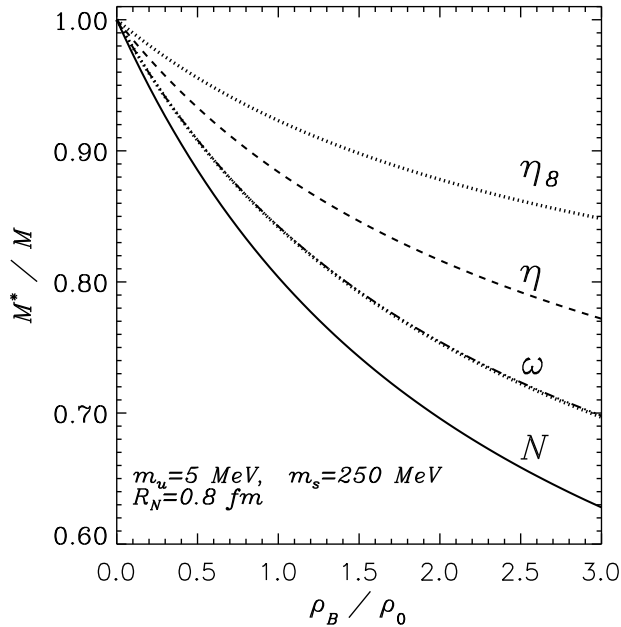


Figure 29: Effective masses of the nucleon, physical  $\eta$  and  $\omega$  mesons divided by their free values, and those correspond to the SU(3) quark model basis (the dotted lines), namely  $\omega = \frac{1}{\sqrt{2}}(u\bar{u} + d\bar{d})$  (ideal mixing) and  $\eta_8 = \frac{1}{\sqrt{6}}(u\bar{u} + d\bar{d} - 2s\bar{s})$ . The two cases for the  $\omega$  meson are almost degenerate ( $\rho_0 = 0.15 \text{ fm}^{-3}$ ) – from Ref. [165].

Because the vector potentials for the same flavor of quark and antiquark cancel each other, the potentials for these mesons are given respectively by  $m_{\eta, \eta', \phi, \omega}^* - m_{\eta, \eta', \phi, \omega}$ , where they will depend only on the distance from the center of the nucleus,  $r = |\vec{r}|$ . Before showing the potentials calculated for the  $\eta, \eta'$  and  $\omega$  mesons, we first show in Figs. 29 and 30 their effective masses divided by their free values, as well as those corresponding to  $\omega = \frac{1}{\sqrt{2}}(u\bar{u} + d\bar{d})$  (ideal mixing) and  $\eta_{1,8} = \xi_{1,8}$  in Eq. (249) for symmetric nuclear matter. One can easily see that the effect of the singlet-octet mixing is negligible for the  $\omega$  mass in matter, whereas it is important for the  $\eta$  and  $\eta'$  masses.

Next, as examples, we show the potentials for the mesons in  $^{26}\text{Mg}$  and  $^{208}\text{Pb}$  nuclei, respectively, in Figs. 31 and 32. Note that, although  $^6\text{He}$ ,  $^{11}\text{B}$  and  $^{26}\text{Mg}$  are not spherical, we have neglected the effect of deformation, which is expected to be small and irrelevant for the present discussion. (We do not expect that deformation should alter the calculated potentials by more than a few MeV near the center of the deformed nucleus, because the baryon (scalar) density there is also expected to be more or less the same as that for a spherical nucleus – close to normal nuclear matter density.) Around the center of each nucleus, the depth of the potentials are typically 60 and 130 MeV for the  $\eta$  and  $\omega$  mesons, respectively. In addition, we show the calculated potentials using QMC-II [19] in Fig. 32, for  $^{208}\text{Pb}$ , in order to estimate the ambiguities due to different versions of the QMC model. At the center of  $^{208}\text{Pb}$ , the potentials calculated using QMC-II are about 20 MeV shallower than those calculated using QMC-I. Note that in QMC-II the physical  $\omega$  meson is identified with the isoscalar-vector  $\omega$  field which mediates the interactions, while in QMC-I, it is the SU(6) quark model state and different from the isoscalar-vector  $\omega$  field. The potential for the  $\eta$  in QMC-II is calculated using the scalar  $\sigma$  field distribution in  $^{208}\text{Pb}$  obtained in the parameter set B.

It is interesting to compare the potentials, or equivalently the effective masses for the  $\eta$  and  $\omega$  in nuclear matter obtained in different approaches. In QMC-I, we get:

$$\frac{m_{\eta}^*}{m_{\eta}} \simeq 1 - 0.12 \left( \frac{\rho_B}{\rho_0} \right), \quad (254)$$



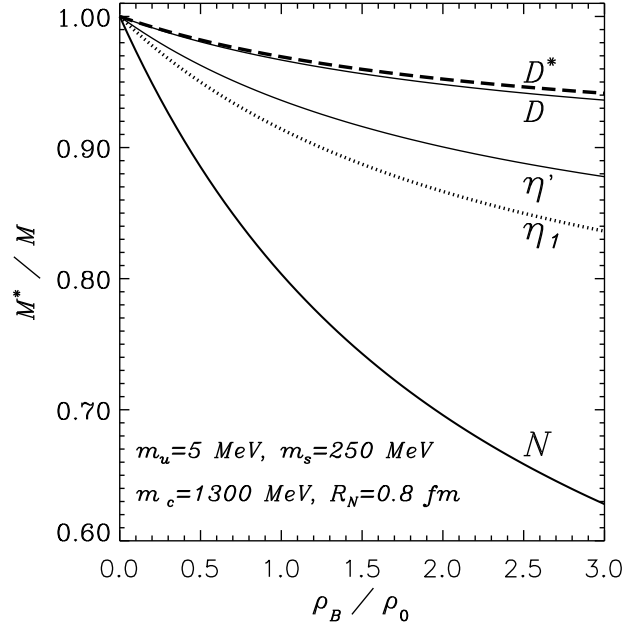


Figure 30: Same as caption of Fig. 29, but for physical  $\eta'$ ,  $D$  and  $D^*$  mesons, and that of the  $\eta_1$ , (the dotted lines), namely  $\eta_1 = \frac{1}{\sqrt{3}}(u\bar{u} + d\bar{d} + s\bar{s})$  (from Ref. [179]).

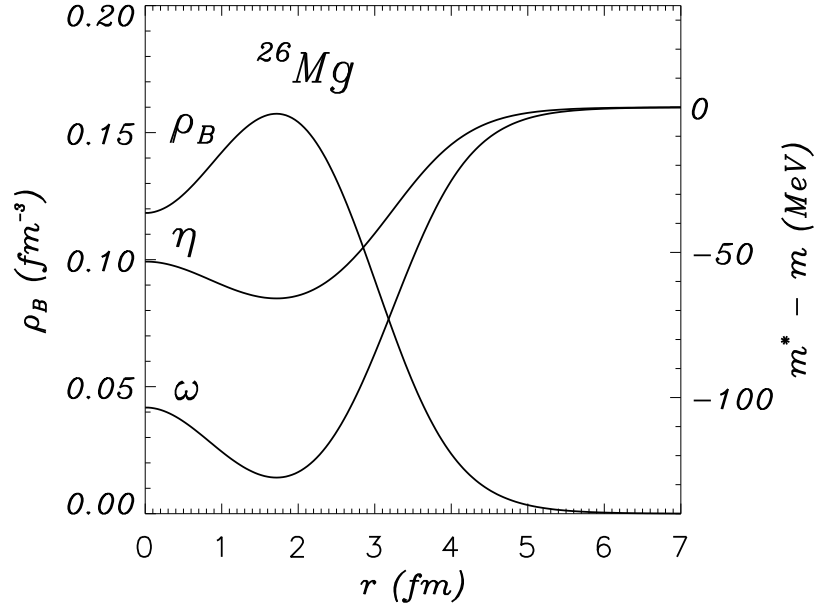


Figure 31: Potentials for the  $\eta$  and  $\omega$  mesons,  $(m_\eta^*(r) - m_\eta)$  and  $(m_\omega^*(r) - m_\omega)$ , calculated in QMC-I for  $^{26}\text{Mg}$  (from Ref. [165]).

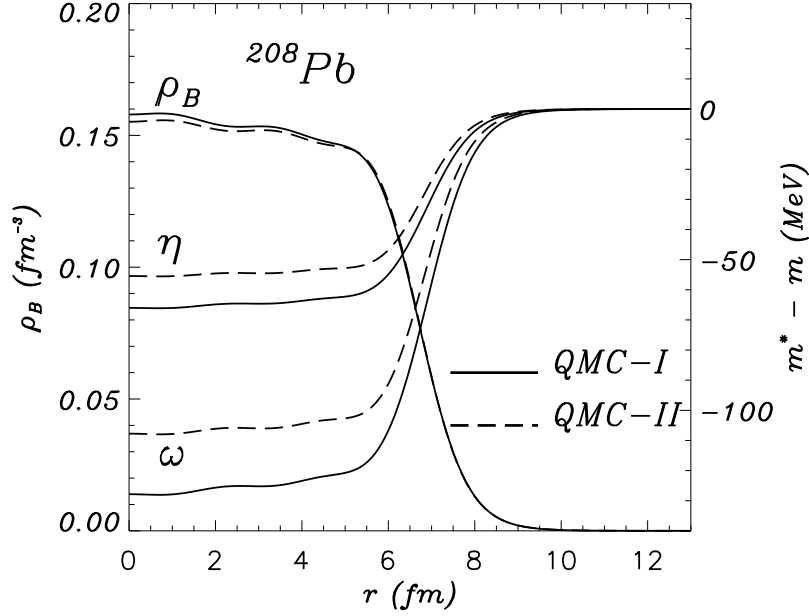


Figure 32: Same as Fig. 31 but for  $^{208}\text{Pb}$ . Potentials calculated in QMC-II are also shown (from Ref. [165]). (See section 3.1 for QMC-II.)

$$\frac{m_\omega^*}{m_\omega} \simeq 1 - 0.16 \left( \frac{\rho_B}{\rho_0} \right). \quad (255)$$

(See also Eq. (164) for the  $\omega$  obtained in QMC-II with using the approximated formula for the scalar field  $\sigma$ .) For the  $\eta$ , Waas and Weise [175] with a chiral SU(3) meson baryon Lagrangian, and Inoue and Oset [176] in a chiral unitary approach, both obtained:

$$\frac{m_\eta^*}{m_\eta} \simeq 1 - 0.05 \left( \frac{\rho_B}{\rho_0} \right), \quad (256)$$

which shows a slightly smaller downward shift for the effective  $\eta$ -meson mass, and thus entails a shallower potential than that obtained in QMC-I. However, Zhong, Peng and Ning [177] obtained a stronger downward shift compared to Eqs. (254) and (256), based on chiral perturbation theory. For the  $\omega$ , both based on QCD sum rules, Hatsuda and Lee [178] obtained:

$$\frac{m_\omega^*}{m_\omega} \simeq 1 - (0.18 \pm 0.054) \left( \frac{\rho_B}{\rho_0} \right), \quad (257)$$

while, Klingl, Kaiser and Weise [118] obtained:

$$\frac{m_\omega^*}{m_\omega} \simeq 1 - (0.16 \pm 0.6) \left( \frac{\rho_B}{\rho_0} \right). \quad (258)$$

They are very similar to those obtained in QMC-I and QMC-II. Thus, although approaches are different, they all predict the downward shift of the effective  $\eta$  and  $\omega$  masses in nuclear matter. For the  $\omega$ , this has been indeed confirmed independently by the ELSA tagged photon facility [44] and KEK [45] as mentioned in section 3.1.1. Then, one can expect a much realistic situation to find the  $\omega$ -nucleus bound states in near future.

Because the typical momentum of the bound  $\omega$  is low, it should be a very good approximation to neglect the possible energy difference between the longitudinal and transverse components of the  $\omega$  [58]. Then, after

imposing the Lorentz condition,  $\partial_\mu \phi^\mu = 0$ , solving the Proca equation becomes equivalent to solving the Klein-Gordon equation the same as for the  $\eta$  and  $\eta'$  mesons:

$$\left[ \nabla^2 + E_j^2 - m_j^{*2}(r) \right] \phi_j(\vec{r}) = 0, \quad (j = \eta, \eta', \omega), \quad (259)$$

where  $E_j$  is the total energy of the meson. An additional complication, which has so far been ignored, is the meson absorption in the nucleus, which requires a complex potential. At the moment, we have not been able to calculate the imaginary part of the potential (equivalently, the in-medium widths of the mesons) self-consistently within the model. In order to make a more realistic estimate for the meson-nucleus bound states, we include the widths of the mesons in the nucleus by assuming a specific form:

$$\tilde{m}_j^*(r) = m_j^*(r) - \frac{i}{2} \left[ (m_j - m_j^*(r)) \gamma_j + \Gamma_j^0 \right], \quad (j = \eta, \eta', \omega), \quad (260)$$

$$\equiv m_j^*(r) - \frac{i}{2} \Gamma_j^*(r), \quad (261)$$

where,  $m_j$  and  $\Gamma_j^0$  are the corresponding masses and widths in free space, and  $\gamma_j$  are treated as phenomenological parameters to describe the in-medium meson widths,  $\Gamma_j^*(r)$ . We have calculated the single-particle energies for several values of the parameter,  $\gamma_j$ , which cover the estimated ranges [165]. However, we will present the results for the values,  $(\gamma_\eta, \gamma_\omega) = (0.5, 0.2)$ , which are expected to be realistic. For the  $\eta'$ , although it is possible that the width in a nucleus becomes broader, we have neglected the width for simplicity in the initial calculation [166], and present the results for  $\gamma_{\eta'} = 0$ . (See Ref. [173] for a recent estimate of the  $\eta'$  width in a nucleus.)

In case the recoilless condition is achieved for meson production, as in the GSI experiment, we may expect that the energy dependence of the potentials would not be strong [180]. Thus we actually solve the following, modified Klein-Gordon equations:

$$\left[ \nabla^2 + E_j^2 - \tilde{m}_j^{*2}(r) \right] \phi_j(\vec{r}) = 0, \quad (j = \eta, \omega). \quad (262)$$

This is carried out in momentum space by the method developed in Ref. [181]. To confirm the results, we also calculated the single-particle energies by solving the Schrödinger equation. Calculated (complex) single-particle energies for the  $\eta, \eta'$  and  $\omega$  mesons,  $E_j^* = E_j + m_j - i\Gamma_j/2$ , ( $j = \eta, \eta', \omega$ ), obtained by solving the Klein-Gordon equation, are listed in Table 20. For a comparison, we also list the QHD results [182] for the  $\omega$  single-particle nuclear state energies, calculated using the potential estimated by QHD.

Although the specific form for the widths of the mesons in medium could not be calculated in this model yet, our results suggest that one should find  $\eta$ -  $\eta'$ - and  $\omega$ -nucleus bound states. From the point of view of uncertainties arising from differences between QMC-I and QMC-II, the present results for both the single-particle energies and calculated full widths should be no more than 20 % smaller in absolute value according to the estimate from the potential for the  $\omega$  in  $^{208}\text{Pb}$  in Fig. 32. Thus, for a heavy nucleus and relatively wide range of the in-medium meson widths, it seems inevitable that one should find such  $\eta$ - and  $\omega$ -nucleus bound states. Note that the correction to the real part of the single-particle energies from the width,  $\Gamma$ , can be estimated non-relativistically, to be of order of  $\sim \Gamma^2/8m_j$  (repulsive), which is a few MeV if we use  $\Gamma \simeq 100$  MeV.

Next, we discuss the  $D$  and  $\overline{D}$  meson-nucleus bound states, where the treatment is different from that for the  $\eta, \eta'$  and  $\omega$  cases due to the non-zero vector potential for them. In particular, the long range Coulomb interaction in the case of the  $D^-$ -nucleus bound state, needs special treatment. We again calculate the effective masses,  $m_j^*(\vec{r})$  ( $j = D, \overline{D}$ ), and mean field potentials,  $V_{\sigma, \omega, \rho}^q(\vec{r})$ , at position  $\vec{r}$  in the nucleus using the local density approximation. Note that the widths of the  $D$  and  $\overline{D}$  mesons in free space can be treated as zero in practice and we assume this for  $D^-$  and  $\overline{D}^0$  mesons in nuclei, because of their light quark content. We do not expect strong absorption for them. On the other hand, we expect that there should be strong absorption for  $D^+$  and  $D^0$  mesons and this is ignored in our main discussions below. However, to get some idea, nevertheless, we calculate  $D^0$  meson nuclear states, by forcing their widths to be zero. Thus, the highlight in the following is the  $D^-$ -nucleus bound states. The scalar and vector potentials, which depend only on the distance from the center of the nucleus,  $r = |\vec{r}|$ , are given by:

$$V_s^j(r) = m_j^*(r) - m_j, \quad (263)$$

Table 20: Calculated meson-nucleus bound state energies,  $E_j = \text{Re}(E_j^* - m_j)$ , and widths,  $\Gamma_j$  ( $j = \omega, \eta, \eta'$ ), (in MeV) in QMC [165] and those for the  $\omega$  in QHD, including the effect of  $\sigma$ - $\omega$  mixing [182]. The complex eigenenergies are given by,  $E_j^* = E_j + m_j - i\Gamma_j/2$ . (\* not calculated)

		$\Gamma_\eta^0 = 0$ $\gamma_\eta = 0.5$ (QMC)	$\Gamma_{\eta'}^0 = 0$ (QMC)	$\Gamma_\omega^0 = 8.43$ (MeV) $\gamma_\omega=0.2$ (QMC)	$\Gamma_\omega^0 = 8.43$ (MeV) $\gamma_\omega = 0.2$ (QHD)			
		$E_\eta$	$\Gamma_\eta$	$E_{\eta'}$	$E_\omega$	$\Gamma_\omega$	$E_\omega$	$\Gamma_\omega$
$^6_j\text{He}$	1s	-10.7	14.5	*	-55.6	24.7	-97.4	33.5
$^{11}_j\text{B}$	1s	-24.5	22.8	*	-80.8	28.8	-129	38.5
$^{26}_j\text{Mg}$	1s	-38.8	28.5	*	-99.7	31.1	-144	39.8
	1p	-17.8	23.1	*	-78.5	29.4	-121	37.8
	2s	—	—	*	-42.8	24.8	-80.7	33.2
$^{16}_j\text{O}$	1s	-32.6	26.7	-41.3	-93.4	30.6	-134	38.7
	1p	-7.72	18.3	-22.8	-64.7	27.8	-103	35.5
$^{40}_j\text{Ca}$	1s	-46.0	31.7	-51.8	-111	33.1	-148	40.1
	1p	-26.8	26.8	-38.5	-90.8	31.0	-129	38.3
	2s	-4.61	17.7	-21.9	-65.5	28.9	-99.8	35.6
$^{90}_j\text{Zr}$	1s	-52.9	33.2	-56.0	-117	33.4	-154	40.6
	1p	-40.0	30.5	-47.7	-105	32.3	-143	39.8
	2s	-21.7	26.1	-35.4	-86.4	30.7	-123	38.0
$^{208}_j\text{Pb}$	1s	-56.3	33.2	-57.5	-118	33.1	-157	40.8
	1p	-48.3	31.8	-52.6	-111	32.5	-151	40.5
	2s	-35.9	29.6	-44.9	-100	31.7	-139	39.5

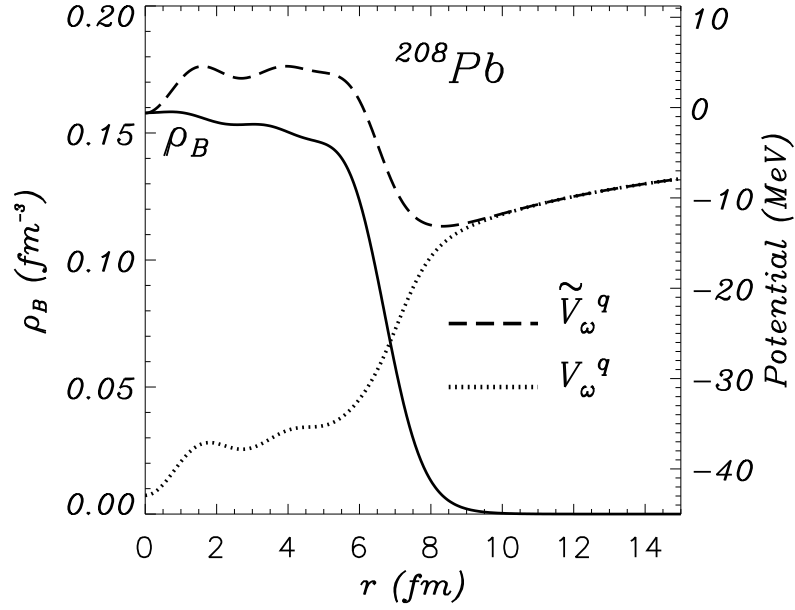


Figure 33: Sum of the scalar, vector and Coulomb potentials for the  $D^-$  meson in  $^{208}\text{Pb}$  for two cases,  $(m_{D^-}^*(r) - m_{D^-}) + \tilde{V}_\omega^q(r) + \frac{1}{2}V_\rho^q(r) - A(r)$  (the dashed line) and  $(m_{D^-}^*(r) - m_{D^-}) + V_\omega^q(r) + \frac{1}{2}V_\rho^q(r) - A(r)$  (the dotted line), where  $\tilde{V}_\omega^q(r) = 1.4^2 V_\omega^q(r)$  (from Ref. [131]).

$$V_v^{D^-}(r) = V_\omega^q(r) - \frac{1}{2}V_\rho^q(r) - A(r), \quad (264)$$

$$V_v^{\overline{D}^0}(r) = V_\omega^q(r) + \frac{1}{2}V_\rho^q(r), \quad (265)$$

$$V_v^{D^0}(r) = -\left(V_\omega^q(r) + \frac{1}{2}V_\rho^q(r)\right), \quad (266)$$

where  $A(r)$  is the Coulomb interaction between the meson and the nucleus. Note that the  $\rho$ -meson mean field potential,  $V_\rho^q(r)$ , is negative in a nucleus with a neutron excess, such as  $^{208}\text{Pb}$ . For the larger  $\omega$  meson coupling, suggested by  $K^+$ -nucleus scattering,  $V_\omega^q(r)$  is replaced by  $\tilde{V}_\omega^q(r) = 1.4^2 V_\omega^q(r)$ . (See Eq. (220).) In Fig. 33 we show the sum of the potentials for the  $D^-$  in  $^{208}\text{Pb}$  for the two choices of  $[V_s^{D^-}(r) + V_v^{D^-}(r)]$  (the dashed line corresponds to  $\tilde{V}_\omega^q(r)$  and the dotted line to  $V_\omega^q(r)$ ). Because the  $D^-$  meson is heavy and may be described well in the (non-relativistic) Schrödinger equation, one expects the existence of the  $^{208}\text{Pb}$  bound states just from inspection of the naive sum of the potentials, in a way which does not distinguish the vector or scalar Lorentz character.

Now we calculate the bound state energies for the  $D$  and  $\overline{D}$  in  $^{208}\text{Pb}$  nucleus, using the potentials calculated in QMC. There are several variants of the dynamical equation for a bound meson-nucleus system. Consistent with the mean field picture of QMC, we actually solve the Klein-Gordon equation:

$$[\nabla^2 + (E_j - V_v^j(r))^2 - m_j^{*2}(r)] \phi_j(\vec{r}) = 0, \quad (267)$$

where  $E_j$  is the total energy of the meson (the binding energy is  $E_j - m_j$ ). To deal with the long range Coulomb potential, we first expand the quadratic term (the zeroth component of Lorentz vector) as,  $(E_j - V_v^j(r))^2 = E_j^2 + A^2(r) + V_{\omega\rho}^2(r) + 2A(r)V_{\omega\rho}(r) - 2E_j(A(r) + V_{\omega\rho}(r))$ , where  $V_{\omega\rho}(r)$  is the combined potential due to  $\omega$  and  $\rho$  mesons ( $V_{\omega\rho}(r) = V_\omega^q(r) - \frac{1}{2}V_\rho^q(r)$  for  $D^-$ ). Then, Eq. (267) can be rewritten as an effective Schrödinger-like equation,

$$\left[-\frac{\nabla^2}{2m_j} + V_j(E_j, r)\right] \Phi_j(r) = \frac{E_j^2 - m_j^2}{2m_j} \Phi_j(r) \quad (268)$$

Table 21:  $D^-$ ,  $\overline{D}^0$  and  $D^0$  bound state energies (in MeV). The widths are all set to zero. Note that the  $D^0$  bound state energies calculated with  $\tilde{V}_\omega^q$  will be much larger (in absolute value) than those calculated with  $V_\omega^q$ .

state	$D^-(\tilde{V}_\omega^q)$	$D^-(V_\omega^q)$	$D^-(V_\omega^q, \text{no Coulomb})$	$\overline{D}^0(\tilde{V}_\omega^q)$	$\overline{D}^0(V_\omega^q)$	$D^0(V_\omega^q)$
1s	-10.6	-35.2	-11.2	unbound	-25.4	-96.2
1p	-10.2	-32.1	-10.0	unbound	-23.1	-93.0
2s	-7.7	-30.0	-6.6	unbound	-19.7	-88.5

where  $\Phi_j(r) = 2m_j\phi_j(r)$  and  $V_j(E_j, r)$  is an effective energy-dependent potential which can be split into three pieces (Coulomb, vector and scalar parts),

$$V_j(E_j, r) = \frac{E_j}{m_j}A(r) + \frac{2E_jV_{\omega\rho}^j(r) - (A(r) + V_{\omega\rho}^j(r))^2}{2m_j} + \frac{m_j^{*2}(r) - m_j^2}{2m_j}. \quad (269)$$

Note that only the first term in this equation is a long range interaction and thus needs special treatment, while the second and third terms are short range interactions. We would like to emphasize that no reduction has been made to derive the Schrödinger-like equation, so that all relativistic corrections are included in our calculation. The calculated meson-nucleus bound state energies for  $^{208}\text{Pb}$ , are listed in Table 21.

The results show that both the  $D^-$  and  $\overline{D}^0$  are bound in  $^{208}\text{Pb}$  with the usual  $\omega$  coupling constant. For the  $D^-$  the Coulomb force provides roughly 24 MeV of binding for the 1s state, and is strong enough to bind the system even with the much more repulsive  $\omega$  coupling (viz.,  $1.4^2V_\omega^q$ ). The  $\overline{D}^0$  with the stronger  $\omega$  coupling is not bound. Note that the difference between  $\overline{D}^0$  and  $D^-$  without the Coulomb force is due to the interaction with the  $\rho$  meson, which is attractive for the  $\overline{D}^0$  but repulsive for the  $D^-$ . For completeness, we also calculated the binding energies for the  $D^0$  setting a possible in-medium width to be zero. It is deeply bound because the  $\omega$  interaction with the light antiquarks is attractive. However, the expected large width associated with strong absorption may render it experimentally inaccessible. It is an extremely important experimental challenge to see whether it can be detected.

We show the eigenfunctions obtained for the Schrödinger-like equation in Fig. 34, together with the baryon density distribution in  $^{208}\text{Pb}$ . For the usual  $\omega$  coupling, the eigenstates (1s and 1p) are well within the nucleus, and behave as expected at the origin. For the stronger  $\omega$  coupling, however, the  $D^-$  meson is considerably pushed out of the nucleus. In this case, the bound state (an atomic state) is formed solely due to the Coulomb force. An experimental determination of whether this is a nuclear state or an atomic state would give a strong constraint on the  $\omega$  coupling. We note, however, that because it is very difficult to produce  $D$ -mesic nuclei with small momentum transfer, and the  $D$ -meson production cross section is small compared with the background from other channels, it will be a challenging task to detect such bound states experimentally [183].

In spite of possible model-dependent uncertainties, our results suggest that the  $D^-$  meson should be bound in  $^{208}\text{Pb}$  through two quite different mechanisms, namely, the scalar and attractive  $\sigma$  mean field even without the assistance of the Coulomb force in the case of the normal vector potential ( $V_\omega^q$ ), and solely due to the Coulomb force in the case of the stronger vector potential ( $\tilde{V}_\omega^q$ ). (We recall that the kaon is a pseudo-Goldstone boson and expected to be difficult to treat properly with the usual bag model. Thus, the analysis of Ref. [130] on the vector potential for the light quarks inside the kaon bag may not be applicable to the light quarks inside the  $D$ -meson.)

Thus, whether or not the  $\overline{D}^0$ - $^{208}\text{Pb}$  bound states exist would give new information as to whether the interactions of light quarks in a heavy meson are the same as those in a nucleon. The enormous difference between the binding energies of the  $D^0$  ( $\sim 100$  MeV) and the  $\overline{D}^0$  ( $\sim 10$  MeV) is a simple consequence of the presence of a strong Lorentz vector mean-field, while the existence of any binding at all would give us important information concerning the role of the Lorentz scalar  $\sigma$  field (and hence dynamical symmetry breaking) in heavy quark systems. In spite of the perceived experimental difficulties, we feel that the search for these bound systems should have a very high priority.

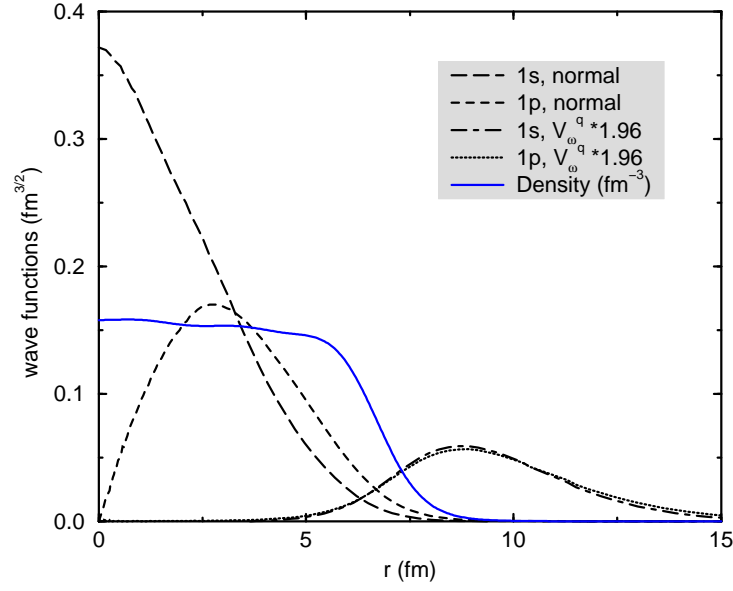


Figure 34: The Schrödinger-like bound state wave functions of the  $D^-$  meson in  $^{208}\text{Pb}$ , for two different  $\omega$  meson coupling strengths. See also the caption of Fig. 33. The wave function is normalized as follows:  $\int_0^\infty dr 4\pi r^2 |\Phi(r)|^2 = 1$  (from Ref. [131]).

## 4 Effects of nucleon substructure on lepton-nucleus scatterings

In this section, we summarize the applications of the QMC model to lepton-nucleus scattering, in which nucleon substructure effects in a medium may emerge. The highlight of this section is the comparison between the QMC model prediction and the experimental results for the bound proton electromagnetic form factors measured at the Thomas Jefferson Laboratory (JLab) [6].

### 4.1 Nucleon form factors

#### 4.1.1 Electromagnetic form factors

For an on-shell nucleon, the electric ( $G_E$ ) and magnetic ( $G_M$ ) form factors can be conveniently defined in the Breit frame by

$$\langle N_{s'}(\frac{\vec{q}}{2}) | J^0(0) | N_s(-\frac{\vec{q}}{2}) \rangle = \chi_{s'}^\dagger \chi_s G_E(Q^2), \quad (270)$$

$$\langle N_{s'}(\frac{\vec{q}}{2}) | \vec{J}(0) | N_s(-\frac{\vec{q}}{2}) \rangle = \chi_{s'}^\dagger \frac{i\vec{\sigma} \times \vec{q}}{2M_N} \chi_s G_M(Q^2), \quad (271)$$

where  $\chi_s$  and  $\chi_{s'}^\dagger$  are Pauli spinors for the initial and final nucleons respectively,  $\vec{q}$  is the three momentum transfer, and  $q^2 = -Q^2 = -\vec{q}^2$ . The major advantage of the Breit frame is that  $G_E$  and  $G_M$  are explicitly decoupled and can be determined by the time and space components of the electromagnetic current ( $J^\mu$ ), respectively. Note that, in the above definitions, both the initial and final states are physical states which incorporate meson clouds.

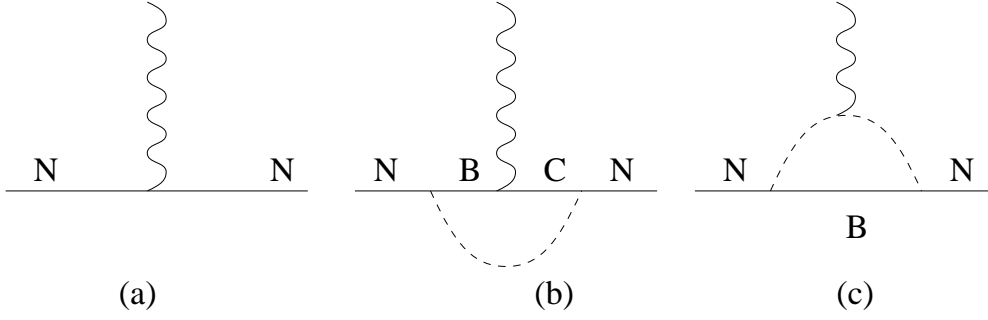


Figure 35: Diagrams illustrating various contributions included in the calculation of the nucleon form factors (up to one pion loop). The intermediate baryons  $B$  and  $C$  are restricted to the  $N$  and  $\Delta$ .

The electromagnetic current of the quark is given by

$$j^\mu(x) = \sum_q Q_q e \bar{\psi}_q(x) \gamma^\mu \psi_q(x), \quad (272)$$

where  $\psi_q(x)$  is the quark field operator for the flavor  $q$  and  $Q_q$  is its charge in units of the proton charge,  $e$ . This is represented by a diagram (a) in Fig. 35. The momentum eigenstate of a baryon is constructed by the Peierls-Thouless projection method [184, 185],

$$\Psi_{\text{PT}}(\vec{x}_1, \vec{x}_2, \vec{x}_3; \vec{p}) = N_{\text{PT}} e^{i\vec{p} \cdot \vec{x}_{\text{c.m.}}} \psi_q(\vec{x}_1 - \vec{x}_{\text{c.m.}}) \psi_q(\vec{x}_2 - \vec{x}_{\text{c.m.}}) \psi_q(\vec{x}_3 - \vec{x}_{\text{c.m.}}), \quad (273)$$

where  $N_{\text{PT}}$  is a normalization constant,  $\vec{p}$  the total momentum of the baryon, and  $\vec{x}_{\text{c.m.}} = (\vec{x}_1 + \vec{x}_2 + \vec{x}_3)/3$  is the center of mass of the baryon (we assume equal mass quarks here).

Using Eqs. (272) and (273), the nucleon electromagnetic form factors for the proton's quark core can be calculated by [184]

$$G_E(Q^2) = \int d^3r j_0(Qr) \rho_q(r) K(r) / D_{\text{PT}}, \quad (274)$$

$$G_M(Q^2) = (2M_N/Q) \int d^3r j_1(Qr) \beta_q j_0(\Omega_q r / R_N) j_1(\Omega_q r / R_N) K(r) / D_{\text{PT}}, \quad (275)$$

$$D_{\text{PT}} = \int d^3r \rho_q(r) K(r), \quad (276)$$

where  $D_{\text{PT}}$  is the normalization factor,  $\rho_q(r) \equiv j_0^2(\Omega_q r / R_N) + \beta_q^2 j_1^2(\Omega_q r / R_N)$ , and  $K(r) \equiv \int d^3x \rho_q(\vec{x}) \rho_q(-\vec{x} - \vec{r})$  is the recoil function to account for the correlation of the two spectator quarks.

Apart from the center-of-mass correction, it is also vital to include Lorentz contraction of the bag for the form factors at moderate momentum transfer [184, 186]. In the Breit frame, the photon-quark interaction can be reasonably treated as instantaneous. The final form of the form factors can be obtained through a simple rescaling [184], i.e.,

$$G_E(Q^2) = \left( \frac{M_N}{E_N} \right)^2 G_E^{\text{sph}} \left( \left( \frac{M_N}{E_N} \right)^2 Q^2 \right), \quad (277)$$

$$G_M(Q^2) = \left( \frac{M_N}{E_N} \right)^2 G_M^{\text{sph}} \left( \left( \frac{M_N}{E_N} \right)^2 Q^2 \right), \quad (278)$$

where  $E_N = \sqrt{M_N^2 + Q^2/4}$  and  $G_{M,E}^{\text{sph}}(Q^2)$  are the form factors calculated with the static spherical bag wave function. The scaling factor in the argument arises from the coordinate transformation of the struck quark and the factor in the front,  $(M_N/E_N)^2$ , comes from the reduction of the integral measure of two spectator



quarks in the Breit frame [186]. For the case of a bound nucleon (a nucleon in nuclear matter) we use the substitution [187],  $(M_N/E_N) \rightarrow (M_N^*/E_N^*)$  in Eqs. (277) and (278).

As is well-known, a realistic picture of the nucleon should include the surrounding meson cloud. Following the cloudy bag model (CBM) [188, 189], we limit our consideration on the meson cloud correction to the most important component, namely the pion cloud. For the pion cloud contribution we include up to one pion loop, namely, diagrams (b) and (c) in Fig. 35. As in free space, the pion field is a Goldstone boson field and acts to restore the chiral symmetry. The Lagrangian related to the pion field and its interaction, within the pseudoscalar quark-pion coupling scheme, is

$$\mathcal{L}_{\pi q} = \frac{1}{2}(\partial_\mu \vec{\pi})^2 - \frac{1}{2}m_\pi^2 \vec{\pi}^2 - \frac{i}{2f_\pi} \bar{\psi}_q \gamma_5 \vec{\tau} \cdot \vec{\pi} \psi_q \delta_S, \quad (279)$$

where  $\delta_S$  is a surface delta function of the bag,  $m_\pi$  the pion mass and  $f_\pi$  the pion decay constant. The electromagnetic current of the pion is

$$j_\pi^\mu(x) = -ie[\pi^\dagger(x)\partial^\mu \pi(x) - \pi(x)\partial^\mu \pi^\dagger(x)], \quad (280)$$

where  $\pi(x) = \frac{1}{\sqrt{2}}[\pi_1(x) + i\pi_2(x)]$  either destroys a negatively charged pion or creates a positively charged one. The detailed expressions for their contributions can be found in Ref. [184] with the following substitutions  $m_\pi \rightarrow m_\pi^*$ ,  $m_B \rightarrow m_B^*$ , and  $f_{\pi AB} \rightarrow f_{\pi AB}^*$ .

In principle, the existence of the  $\pi$  and  $\Delta$  inside the nuclear medium will also lead to some modification of their properties. Since the pion is well approximated as a Goldstone boson, the explicit chiral symmetry breaking is small in free space, and it should be somewhat smaller in nuclear medium [1]. While the pion mass would be slightly smaller in the medium, because the pion field has little effect on the form factors (other than  $G_{En}$ ), we use  $m_\pi^* = m_\pi$ . As the  $\Delta$  is treated on the same footing as the nucleon in the CBM, its mass should vary in a similar manner as that of the nucleon. Thus we assume that the in-medium and free space  $N - \Delta$  mass splitting are approximately equal, i.e.,  $m_\Delta^* - M_N^* \simeq m_\Delta - M_N$ . The physical  $\pi AB$  coupling constant is obtained by  $f^{AB} \simeq \left(\frac{f_0^{AB}}{f_0^{NN}}\right) f^{NN}$ . There are uncertain corrections to the bare coupling constant  $f_0^{NN}$ , such as the nonzero quark mass and the correction for spurious center of mass motion. Therefore, we use the renormalized coupling constant in our calculation,  $f^{NN} \simeq 3.03$ , which corresponds to the usual  $\pi NN$  coupling constant,  $f_{\pi NN}^2 \simeq 0.081$ . In the medium, the  $\pi NN$  coupling constant might be expected to decrease slightly due to the enhancement of the lower component of the quark wave function, but we shall ignore this density dependence in the present treatment and use  $f_{\pi NN}^* \simeq f_{\pi NN}$ .

The corrections for the center-of-mass motion and Lorentz contraction lead to significantly better agreement with data than was obtained in the original, static CBM calculations. For a detailed comparison with data we refer to Ref. [184]. This approach is sometimes called the improved cloudy bag model (ICBM). Our main results, namely the density dependence of the form factors in matter, relative to those in free space, are shown in Fig. 36. The charge form factors are much more sensitive to the nuclear medium density than the magnetic ones. The latter are nearly one order of magnitude less sensitive. Increasing density obviously suppresses the electromagnetic form factors for small  $Q^2$ . For a fixed  $Q^2$  (less than  $0.3 \text{ GeV}^2$ ), the form factors decrease almost linearly with respect to the nuclear baryon density,  $\rho$ . At  $Q^2 \sim 0.3 \text{ GeV}^2$ , the proton and neutron charge form factors are reduced by roughly 5% and 6% for  $\rho = 0.5\rho_0$ , and 8% for the normal nuclear density,  $\rho_0$ ; similarly, the proton and neutron magnetic form factors are 1% and 0.6% smaller for  $\rho = 0.5\rho_0$ , and 1.5% and 0.9% for the normal nuclear density.

The best experimental constraints on the changes in these form factors come from the analysis of  $y$ -scaling data. For example, in iron nucleus (Fe) the nucleon root-mean-square radius cannot vary by more than 3% [190]. However, in the kinematic range covered by this analysis, the  $eN$  cross section is predominantly magnetic, so this limit applies essentially to  $G_M$ . (As the electric and magnetic form factors contribute typically in the ratio 1:3 the corresponding limit on  $G_E$  would be nearer 10%.) For the QMC model considered here, the calculated increase in the root-mean-square radius of the magnetic form factors is less than 0.8% at  $\rho_0$ . For the electric form factors the best experimental limit seems to come from the Coulomb sum-rule, where a variation bigger than 4% would be excluded [69]. This is similar in size to the variations calculated here (e.g., 5.5% for  $G_E^p$  at  $\rho_0$ ) and not sufficient to reject them.

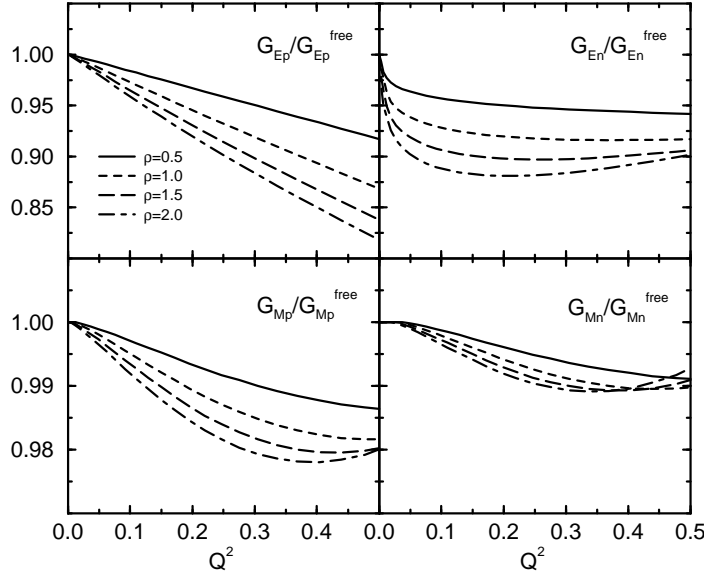


Figure 36: The nucleon electromagnetic form factors in the nuclear medium (relative to those in free space case) [187]. The free space bag radius is 1 fm and the density is quoted in units of the saturation density of symmetric nuclear matter,  $\rho_0 = 0.15 \text{ fm}^{-3}$ .

#### 4.1.2 The QMC predictions and Experimental results (EM interactions)

Now, we study the medium modification of the bound proton electromagnetic form factors in nuclei,  $^4\text{He}$ ,  $^{16}\text{O}$ , and  $^{40}\text{Ca}$  [191]. We emphasize that the bound proton electromagnetic form factors in  $^4\text{He}$  was predicted before the experimental data from JLab were taken. The quark wave function, as well as the nucleon wave function (both are Dirac spinors), are determined once a solution to equations of motion are found self-consistently. The orbital electromagnetic form factors for a bound proton, in local density approximation, are given by

$$G_{E,M}^\alpha(Q^2) = \int G_{E,M}(Q^2, \rho_B(\vec{r})) \rho_{p\alpha}(\vec{r}) d\vec{r}, \quad (281)$$

where  $\alpha$  denotes a specified orbit with appropriate quantum numbers, and  $G_{E,M}(Q^2, \rho_B(\vec{r}))$  is the density-dependent form factor of a “proton” immersed in nuclear matter with local baryon density,  $\rho_B(\vec{r})$ <sup>1</sup>. Using the nucleon shell model wave functions (Dirac spinors), the local baryon density and the local proton density in the specified orbit,  $\alpha$ , are easily evaluated as

$$\begin{aligned} \rho_B(\vec{r}) &= \sum_{\alpha}^{\text{occ}} d_{\alpha} \psi_{\alpha}^{\dagger}(\vec{r}) \psi_{\alpha}(\vec{r}), \\ \rho_{p\alpha}(\vec{r}) &= (t_{\alpha} + \frac{1}{2}) \psi_{\alpha}^{\dagger}(\vec{r}) \psi_{\alpha}(\vec{r}), \end{aligned} \quad (282)$$

where  $d_{\alpha} = (2j_{\alpha} + 1)$  refers to the degeneracy of nucleons occupying the orbit  $\alpha$  and  $t_{\alpha}$  is the eigenvalue of the isospin operator,  $\tau_3^N/2$ . Notice that the quark wave function only depends on the surrounding baryon density through the scalar  $\sigma$  field in the QMC model. Therefore, this part of the calculation of  $G_{E,M}(Q^2, \rho_B(\vec{r}))$  is the same as for nuclear matter [187, 193], as described in section 4.1.1. The notable medium modifications of the quark wave function inside the bound nucleon in QMC include a reduction of its frequency and an

<sup>1</sup>In a more sophisticated treatment, for example, using a full distorted wave calculation, the weighting may emphasize the nuclear surface somewhat more [192].

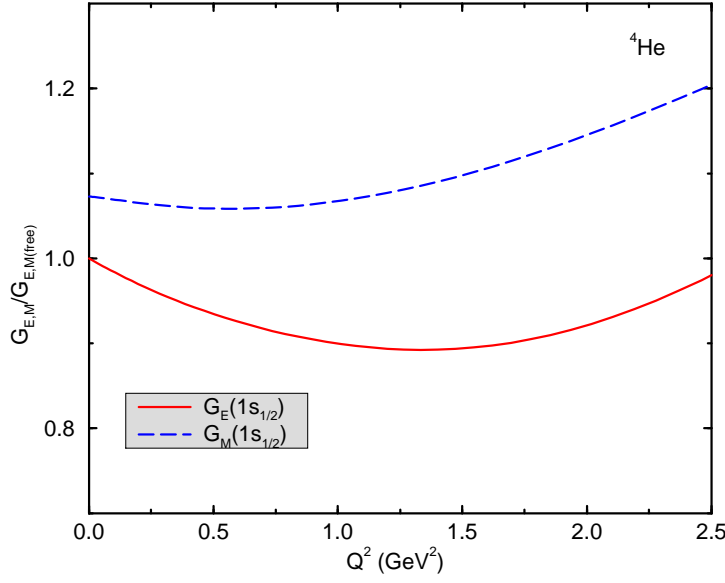


Figure 37: Ratio of in-medium to free space electric and magnetic form factors for the proton in  ${}^4\text{He}$ . (The free bag radius and current quark masses were respectively taken to be 0.8 fm and 5 MeV in all figures.) (Taken from Ref. [191].)

enhancement of the lower component of the Dirac spinor. As explained in section 4.1.1, the corrections arising from recoil and center of mass motion for the bag are made using the Peierls-Thouless projection method, combined with Lorentz contraction of the internal quark wave function and with the perturbative pion cloud added afterwards [184]. Note that possible off-shell effects [194] and meson exchange currents [195, 196] are ignored in the present approach. The resulting nucleon electromagnetic form factors agree with experiment quite well in free space [184]. Because of the limitations of the bag model the form factors are expected to be most reliable at low momentum transfer (say, less than 1  $\text{GeV}^2$ ). To cut down theoretical uncertainties, we prefer to show the ratios of the form factors with respect to corresponding free space values. Throughout this section, we use the renormalized  $\pi NN$  coupling constant,  $f_{\pi NN}^2 \simeq 0.0771$  [197]. The bag radius in free space and the current quark mass are taken to have the standard values, 0.8 fm and 5 MeV, respectively.

Fig. 37 shows the ratio of the electric and magnetic form factors for  ${}^4\text{He}$  (which has only one state,  $1s_{1/2}$ ) with respect to the free space values. As expected, both the electric and magnetic rms radii become slightly larger, while the magnetic moment of the proton increases by about 7%. Fig. 38 shows the ratio of the electric and magnetic form factors for  ${}^{16}\text{O}$  with respect to the free space values, which has one  $s$ -state,  $1s_{1/2}$ , and two  $p$ -states,  $1p_{3/2}$  and  $1p_{1/2}$ . For comparison, we also show in Fig. 38 the corresponding ratio of form factors (those curves with triangle symbols) using a variant of QMC where the bag constant is allowed to decrease by 10% [66] (see section 2.5). The momentum dependence of the form factors for the  $s$ -wave nucleon is more suppressed as the inner orbit in  ${}^{16}\text{O}$  experiences a larger average baryon density than in  ${}^4\text{He}$ . The magnetic moment for the  $s$ -orbit nucleon is similar to that in  ${}^4\text{He}$ , but it is reduced by 2 – 3% in the  $p$ -orbit. Since the difference between the two  $p$ -orbits is rather small, we do not plot the results for  $1p_{1/2}$ . Finally, Fig. 39 shows the ratio of the electric and magnetic form factors for  ${}^{16}\text{O}$  with respect to the free space values. For comparison, we also show in Fig. 39 the corresponding ratio of form factors (those curves with triangle symbols) using the MQMC model [66]. It is evident that the effect of a possible reduction in  $B$  is quite large and will severely reduce the electromagnetic form factors for a bound nucleon since the bag radius is quite sensitive to the value of  $B$ .

From the experimental point of view, it is more reliable to show the ratio,  $G_E/G_M$ , since it can be derived directly from the ratio of transverse to longitudinal polarization of the outgoing proton, with minimal systematic

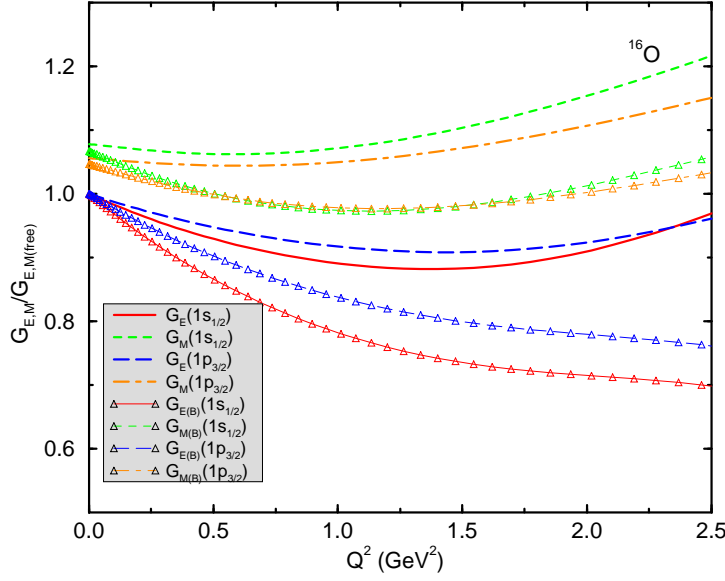


Figure 38: Ratio of in-medium to free space electric and magnetic form factors for the  $s$ - and  $p$ -shells of  $^{16}\text{O}$ . The curves with triangle symbols represent the corresponding ratio calculated in a variant of QMC with a 10% reduction of the bag constant,  $B$  (from Ref. [191]).

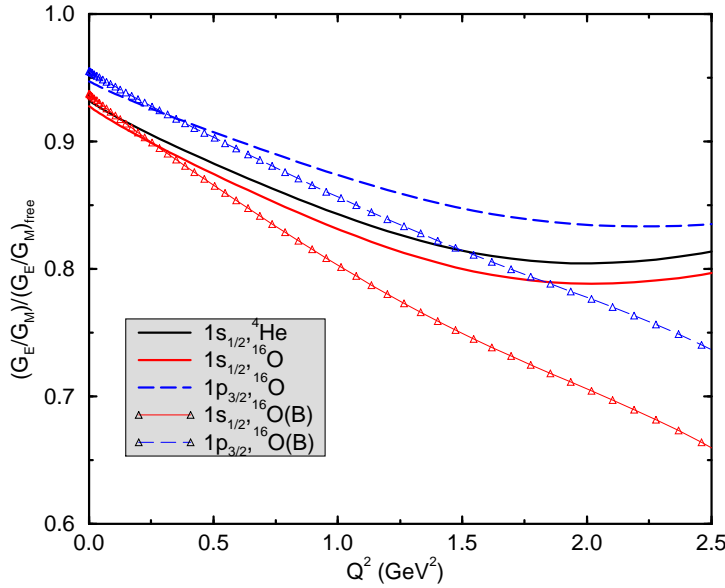


Figure 39: Ratio of electric and magnetic form factors in-medium, divided by the free space ratio. As in the previous figure, curves with triangle symbols represent the corresponding values calculated in a variant of QMC with a 10% reduction of  $B$  (from Ref. [191]).

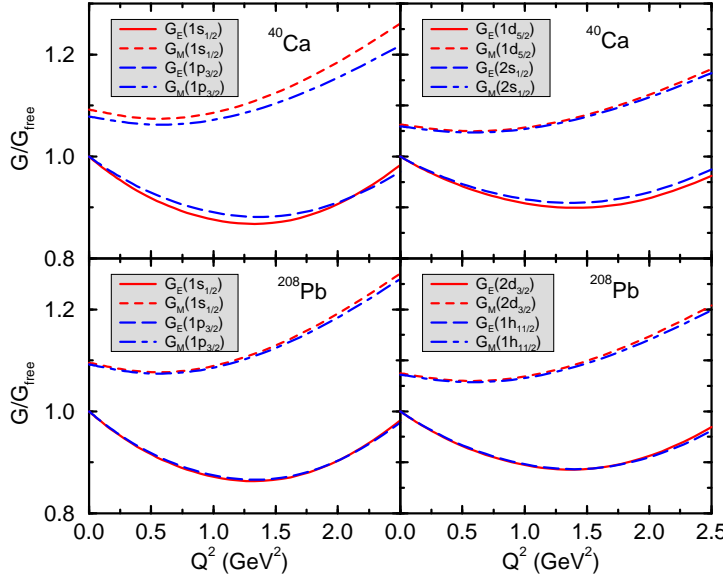


Figure 40: Ratio of in-medium to free space electric and magnetic form factors in specific orbits, for  $^{40}\text{Ca}$  and  $^{208}\text{Pb}$  (from Ref. [191]).

errors. We find that  $G_E/G_M$  runs from roughly 0.41 at  $Q^2 = 0$  to 0.28 and 0.20 at  $Q^2 = 1 \text{ GeV}^2$  and  $2 \text{ GeV}^2$ , respectively, for a proton in the  $1s$  orbit in  $^4\text{He}$  or  $^{16}\text{O}$ . The ratio of  $G_E/G_M$  with respect to the corresponding free space ratio is presented in Fig. 39. The result for the  $1s$ -orbit in  $^{16}\text{O}$  is close to that in  $^4\text{He}$  and 2% lower than that for the  $p$ -orbits in  $^{16}\text{O}$ . The effect on this ratio of ratios of a reduction in  $B$  by the maximum permitted from other constraints [190] is quite significant, especially for larger  $Q^2$ .

For completeness, we have also calculated the orbital electric and magnetic form factors for heavy nuclei such as  $^{40}\text{Ca}$  and  $^{208}\text{Pb}$ . The form factors for the proton in selected orbits are shown in Fig. 40. Because of the larger central baryon density of heavy nuclei, the proton electric and magnetic form factors in the inner orbits ( $1s_{1/2}$ ,  $1p_{3/2}$  and  $1p_{1/2}$  orbits) suffer much stronger medium modifications than those in light nuclei. That is to say, the  $Q^2$  dependence is further suppressed, while the magnetic moments appear to be larger. Surprisingly, the nucleons in peripheral orbits ( $1d_{5/2}$ ,  $2s_{1/2}$ , and  $1d_{3/2}$  for  $^{40}\text{Ca}$  and  $2d_{3/2}$ ,  $1h_{11/2}$ , and  $3s_{1/2}$  for  $^{208}\text{Pb}$ ) still show significant medium effects, comparable to those in  $^4\text{He}$ .

Finally, we would like to add some comments on the magnetic moment in a nucleus. In the present calculation, we have only calculated the contribution from the intrinsic magnetization (or spin) of the nucleon, which is modified by the scalar field in a nuclear medium [53]. As shown in the figures we have found that the intrinsic magnetic moment is enhanced in matter because of the change in the quark structure of the nucleon. We know, however, that there are several, additional contributions to the nuclear magnetic moment, such as meson exchange currents, higher-order correlations, etc. As is well known in relativistic nuclear models like QHD, there is a so-called magnetic moment problem in mean-field approximation [198]. To cure this problem, one must calculate the convection current matrix element within relativistic random phase approximation (RRPA) [199]. However, at high momentum transfer we expect that it should be feasible to detect the enhancement of the intrinsic spin contribution which we have predicted because the long-range correlations, like RRPA, should decrease much faster in that region.

So far, we have discussed the QMC model predictions on the bound proton electromagnetic form factors. Experimentally, the electromagnetic form factors of bound protons were studied in polarized ( $\vec{e}, e'\vec{p}$ ) scattering experiments on  $^{16}\text{O}$  and  $^4\text{He}$  [6] at MAMI and Thomas Jefferson Laboratory (JLab), respectively. We show in Fig. 41 the outcome of the “super ratio”,  $R/R_{\text{PWIA}}$ , which was made for the final analysis of the polarization

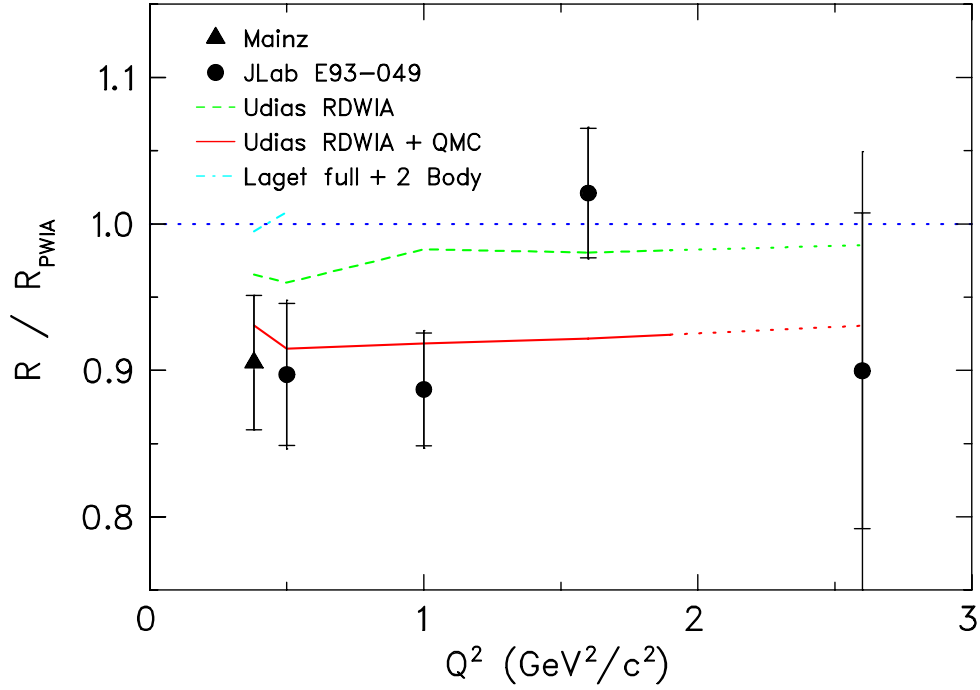


Figure 41: Super ratio  $R/R_{PWIA}$ , as a function of  $Q^2$ , taken from Ref. [6] (by private communication with S. Strauch). See caption of Fig. 1 in Ref. [6] for detailed explanations. In the figure, "Laget" and "Udias", respectively, correspond to the calculations reported in Refs. [200] and [201].

transfer measurements on  $^4\text{He}$  [6] performed at JLab. In Fig. 41,  $R_{PWIA}$  stands for the prediction based on the relativistic plane-wave impulse approximation (PWIA), and the measured ratio  $R$  is defined by:

$$R = \frac{(P'_x/P'_z)^{4\text{He}}}{(P'_x/P'_z)^{1\text{H}}}. \quad (283)$$

The analysis concluded that ratio of the electric ( $G_E^p$ ) to magnetic ( $G_M^p$ ) Sachs proton form factors differs by  $\sim 10\%$  in  $^4\text{He}$  from that in  $^1\text{H}$ . As can be seen from Fig. 41, conventional models employing free proton form factors, phenomenological optical potentials, and bound state wave functions, as well as relativistic corrections, meson exchange currents (MEC), isobar contributions and final state interactions [6, 200, 201, 202], all fail to account for the observed effect in  $^4\text{He}$ . Indeed, a better agreement with the data is obtained, in addition to these standard nuclear-structure corrections, the small correction associated with the change in the internal structure of the bound proton predicted by the QMC model is taken into account.

#### 4.1.3 Nucleon substructure effect on the longitudinal response functions

There is still considerable interest in the longitudinal response (LR) for quasielastic electron scattering off a nucleus. Within the framework of non-relativistic nuclear models and the impulse approximation, it may be difficult to reproduce the observed, quenched LR [203]. In the mid '80s, several groups calculated the LR function using QHD-I and argued that the contribution of the relativistic random-phase approximation (RRPA) is very vital in reducing the LR [204].

Since the nucleon has, however, the internal structure, it may affect the LR for electron scattering [205]. We first briefly review the calculation of the LR function for quasielastic electron scattering from (iso-symmetric) nuclear matter in QHD [204]. The starting point is the lowest order polarization insertion (PI),  $\Pi_{\mu\nu}$ , for the  $\omega$  meson. This describes the coupling of a virtual vector meson or photon to a particle-hole or nucleon-antinucleon

excitation:

$$\Pi_{\mu\nu}(q) = -ig_v^2 \int \frac{d^4k}{(2\pi)^4} \text{Tr}[G(k)\gamma_\mu G(k+q)\gamma_\nu], \quad (284)$$

where  $G(k)$  is the self-consistent nucleon propagator in relativistic Hartree approximation (RHA). One can separate the PI into two pieces: one is the density dependent part,  $\Pi_{\mu\nu}^D$ , and the other is the vacuum one,  $\Pi_{\mu\nu}^F$ . The former is finite, but the latter is divergent and must be renormalized [205].

In the Hartree approximation, where only the lowest one-nucleon loop is considered, the LR function,  $S_L^H$ , is then simply proportional to  $S_L^H(q) \propto G_{pE}^2(q)\Im\Pi_L(q)$ . Here,  $\Pi_L(= \Pi_{33} - \Pi_{00})$  is the longitudinal (L) component of the PI and  $G_{pE}$  is the proton electric form factor, which is usually parameterized by a dipole form in free space:  $G_{pE}(Q^2) = 1/(1 + Q^2/0.71)^2$  with the space-like four-momentum transfer,  $Q^2 = -q^2$ , in units of  $\text{GeV}^2$ .

In RRPA, the L component of the PI,  $\Pi_L^{RPA}$ , involves the sum of the ring diagrams to all orders. It involves the  $\sigma$ - $\omega$  mixing in the nuclear medium [38, 204, 205], and is given by

$$\Pi_L^{RPA}(q) = \frac{(1 - \Delta_0\Pi_s)\Pi_L + \Delta_0\Pi_m^2}{\epsilon_L}, \quad (285)$$

where  $\epsilon_L$  is the L dielectric function [57, 58, 205] and  $\Delta_0$  is the free  $\sigma$ -meson propagator. Here  $\Pi_s$  and  $\Pi_m$  are respectively the scalar and the time component of the mixed PIs. The vacuum component of the scalar PI is again divergent and we need to renormalize it [57, 58, 205]. For the mixed PI there is no vacuum polarization and it vanishes at zero density.

To discuss the effect of changes in the internal structure of the nucleon, we can consider the following modifications to QHD:

1. Meson-nucleon vertex form factor

Since both the mesons and nucleons are composite they have finite size. As the simplest example, we take a monopole form factor,  $F_N(Q^2)$ , at the vertex with a cut off parameter,  $\Lambda_N = 1.5 \text{ GeV}$  [205].

2. Modification of the proton electric form factor

We have studied the electromagnetic form factors of the nucleon in nuclear medium, using the QMC model (see section 4.1.1). The main result of that calculation is that the ratio of the electric form factor of the proton in medium to that in free space decreases essentially linearly as a function of  $Q^2$ , and that it is accurately parameterized as  $R_{pE}(\rho_0, Q^2) \equiv G_{pE}(\rho_0, Q^2)/G_{pE}(Q^2) \simeq 1 - 0.26 \times Q^2$  at  $\rho_0$  [187, 205].

3. Density dependence of the coupling constants

In the QMC model, the confined quark in the nucleon couples to the  $\sigma$  field which gives rise to an attractive force. As a result, the coupling between the  $\sigma$  and nucleon is expected to be reduced at finite density. The coupling between the vector meson and nucleon remains constant because it is related to the baryon number.

To study the LR of nuclear matter, we first have to solve the nuclear ground state within RHA. To take into account the modifications 1 and 3, we replace the  $\sigma$ - and  $\omega$ -nucleon coupling constants in QHD by:  $g_s \rightarrow g_s(\rho_B) \times F_N(Q^2)$  and  $g_v \rightarrow g_v \times F_N(Q^2)$ , where the density dependence of  $g_s(\rho_B)$  is given by solving the nuclear matter problem self-consistently in QMC [205]. Requiring the usual saturation condition for nuclear matter, we found the coupling constants:  $g_s^2(0) = 61.85$  and  $g_v^2 = 62.61$  (notice that  $g_s$  decreased by about 9% at  $\rho_0$ ). In the calculation we fix the quark mass,  $m_q$ , to be 5 or 300 MeV [13, 30],  $m_\sigma = 550 \text{ MeV}$  and  $m_\omega = 783 \text{ MeV}$ , while the bag parameters are chosen so as to reproduce the free nucleon mass with the bag radius  $R_N = 0.8 \text{ fm}$  (see section 3.1). Within RHA, this yields the effective nucleon mass  $M^*/M = 0.81$  at  $\rho_0$  and the incompressibility  $K = 281 \text{ MeV}$ .

Our result is shown in Fig. 42. The dotted curve is the result of the Hartree approximation, where the proton electric form factor is the same as in free space. The dashed curve is the result of the full RRPA, without the modifications 1 and 2. The dot-dashed curve shows the result of the full RRPA with the meson-nucleon form factor but  $R_{pE} = 1$ . The upper (lower) solid curve shows the result of the full RRPA for  $m_q = 5$  (300) MeV, including all modifications. Because of the density dependent coupling, the reduction of the response function from the Hartree result, caused by the full RRPA, is much smaller than that in QHD. In contrast,

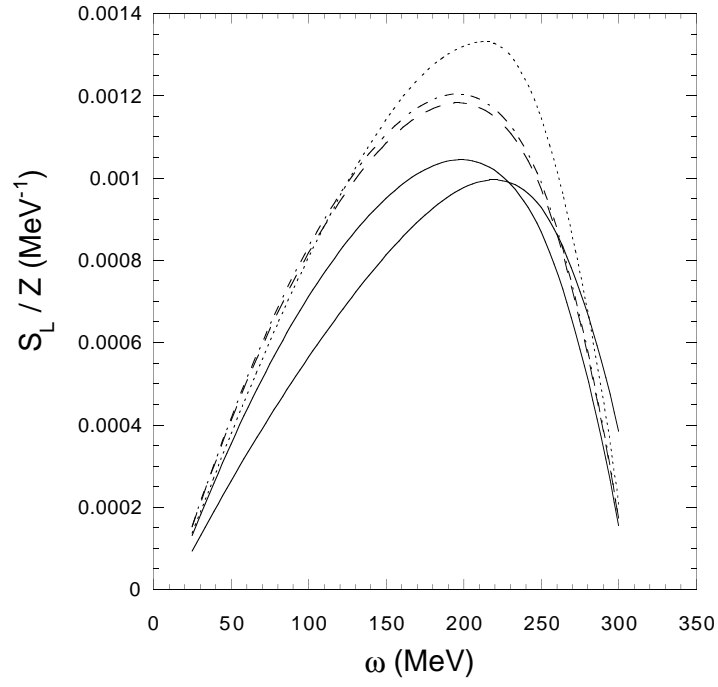


Figure 42: LR functions in the QMC model. We fix  $q = 550$  MeV and  $\rho_B = \rho_0$  (from Ref. [205]) – see text for details.

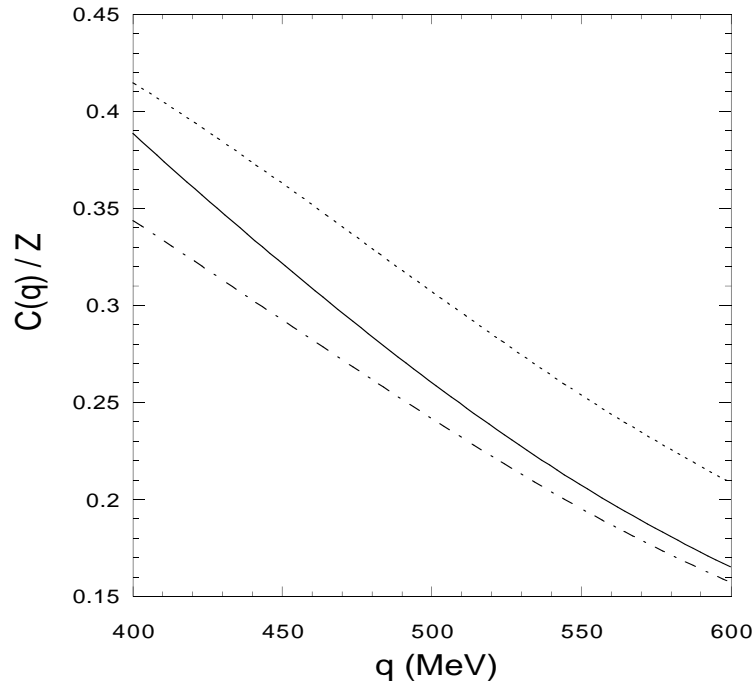


Figure 43: Coulomb sum,  $C(q)/Z$ , at  $\rho_0$  (from Ref. [205]) – see text for details.



the modification of the proton electric form factor is very significant, yielding a much bigger reduction in the response. We can see that the effect of the meson-nucleon form factor is relatively minor.

It is also interesting to see the quark mass dependence of the LR. As an example, we consider the case of  $m_q = 300$  MeV. In comparison with the case  $m_q = 5$  MeV, it is a little smaller and the peak position is shifted to the higher energy transfer side. This is related to the smaller effective nucleon mass in the case  $m_q = 300$  MeV than when  $m_q = 5$  MeV.

The Coulomb sum,  $C(q) = \int_0^q dq_0 S_L(q, q_0)$ , is shown in Fig. 43 as a function of three-momentum transfer,  $q = |\vec{q}|$ . For high  $q$ , the strength is about 20% lower in the full calculation (the solid and dot-dashed curves are for  $m_q = 5$  and 300 MeV, respectively) than for the Hartree response with  $R_{pE} = 1$  (the dotted curve). For low  $q$ , the full calculation with the constituent quark mass remains much lower than the Hartree result, while in case of the light quark mass it gradually approaches the Hartree one. This difference is caused by that the effective nucleon mass for  $m_q = 5$  MeV being larger in matter than that for  $m_q = 300$  MeV.

It also seems appropriate to comment on the transverse response (TR) from nuclear matter. In Ref. [187], it was found that the in-medium modification of the nucleon magnetic form factor within QMC is very small. Therefore, one would expect the total change in the TR caused by RPA correlations and the effect of the variation of the structure of the nucleon to be much smaller than in the LR.

In summary, the reduction of the  $\sigma$ -nucleon coupling constant with density decreases the contribution of the RPA, while the modification of the proton electric form factor in medium reduces the LR considerably. The LR or the Coulomb sum is reduced by about 20% in total, with RPA correlations and the variation of the in-medium nucleon structure contributing about fifty-fifty. It will be interesting to extend this work to calculate both the LR and TR functions for finite nuclei, and compare directly with the experimental results [206].

#### 4.1.4 Axial form factors - neutrino-nucleus scattering

We first discuss the axial vector form factor of the bound nucleon and its application to neutrino-nucleus scattering. At the end of this section, we briefly summarize the scalar and vector form factors of the in-medium nucleon as well.

The extension to the in-medium modification of the bound nucleon axial form factor  $G_A^*(Q^2)$  can be made in a straightforward manner [207]. (Hereafter we denote the in-medium quantities by an asterisk \*.) Since the induced pseudoscalar form factor,  $G_P(Q^2)$ , is dominated by the pion pole and can be derived using the PCAC relation [188], we do not discuss it here. The relevant axial current operator is then simply given by

$$A_a^\mu(x) = \sum_q \bar{\psi}_q(x) \gamma^\mu \gamma_5 \frac{\tau_a}{2} \psi_q(x) \theta(R_B - r), \quad (286)$$

where  $\psi_q(x)$  is the quark field operator for flavor  $q$ . Similarly to the case of electromagnetic form factors, in the Breit frame the resulting bound nucleon axial form factor is given by ICBM [207]:

$$G_A^*(Q^2) = \left( \frac{M_N^*}{E_N^*} \right)^2 G_A^{\text{sph}*} \left( \left( \frac{M_N^*}{E_N^*} \right)^2 Q^2 \right), \quad (287)$$

$$G_A^{\text{sph}*}(Q^2) = \frac{5}{3} \int d^3r \left\{ \left[ j_0^2(\Omega_q r / R_N^*) - \beta_q^2 j_1^2(\Omega_q r / R_N^*) \right] j_0(Qr) \right. \\ \left. + 2\beta_q^2 j_1^2(\Omega_q r / R_N^*) [j_1(Qr) / Qr] \right\} K(r) / D_{PT}. \quad (288)$$

In Fig. 44 we show the in-medium axial vector form factor,  $G_A^*(Q^2)$ , divided by that in free space,  $G_A(Q^2)$ , calculated at nuclear densities  $\rho_B = (0.5, 0.7, 1.0, 1.5)\rho_0$  with  $\rho_0 = 0.15 \text{ fm}^{-3}$ . At  $Q^2 = 0$  the space component  $G_A^*(Q^2 = 0) \equiv g_A^*$  is quenched [208, 209] by about 10 % at normal nuclear matter density. The modification calculated here may correspond to the “model independent part” in meson exchange language, where the axial current attaches itself to one of the two nucleon legs, but not to the exchanged meson [208, 209]. This is because the axial current operator in Eq. (286) is a one-body operator which operates on the quarks and pions belonging to a bound nucleon. A more detailed discussion will be made later. The medium modification of the bound nucleon axial form factor  $G_A^*(Q^2)$  may be observed for instance in neutrino-nucleus scattering, similar to

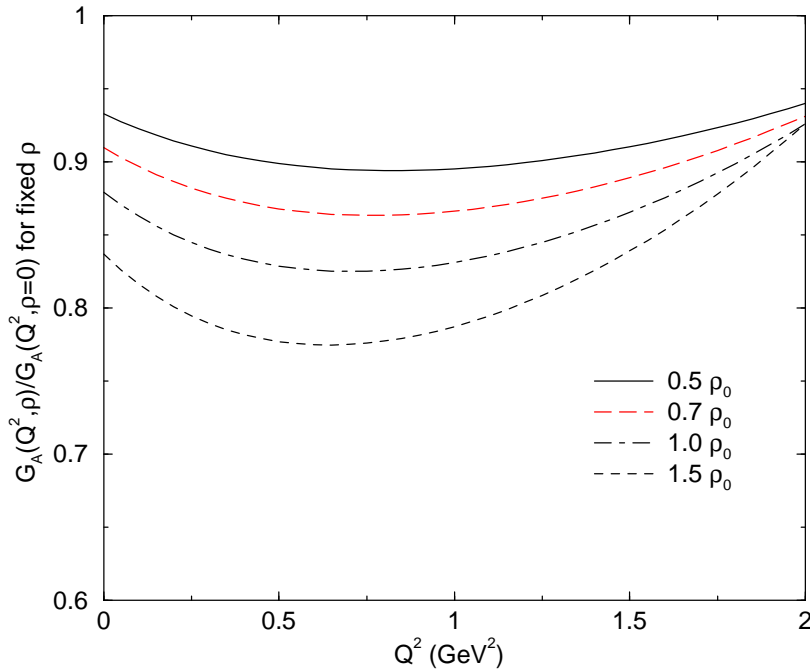


Figure 44: The ratio of in-medium to free axial form factors [207]. The free space value,  $G_A(0) = g_A = 1.14$  is used in the calculation.

that observed in the “EMC-type” experiments (see section 4.2.1), or in a similar experiment to the polarization transfer measurements performed on  $^4\text{He}$  [6]. However, at present the experimental uncertainties seem to be too large to detect such a medium effect directly. We should also note that the medium modification of the parity-violating  $F_3$  structure functions of a bound nucleon in deep-inelastic neutrino induced reactions can be extracted using the calculated in-medium axial form factor  $G_A^*(Q^2)$  and quark-hadron duality, as we will discuss in section 4.2.3.

Below, we study the effect of the bound nucleon form factors on neutrino-nucleus scattering [210].<sup>2</sup> As an example, we compute the inclusive  $^{12}\text{C}(\nu_\mu, \mu^-)X$  cross sections that have been measured by the LSND collaboration [211, 212, 213]. It is known that the existing calculations for the total cross section based on the nucleon and meson degrees of freedom overestimate the data by  $\sim 30\%$  to  $\sim 100\%$  [211, 212, 213, 214]. Because our aim is to focus on the effects due to the internal structure change of the bound nucleon, we use a relativistic Fermi gas model [215, 216], which is simple and transparent for the purpose, while implementing the bound nucleon form factors calculated in the QMC model. Thus, we do not include the other nuclear structure corrections [214, 217].

Of course, it is difficult to separate exactly the effects we consider here from the standard nuclear-structure corrections, particularly from meson exchange current (MEC). However, since the relevant current operators in this study are one-body quark (pion) operators acting on the quarks (pion cloud) in the nucleon, double counting with the model-dependent MEC [196, 209] (the current operators act on the exchanged mesons) is expected to be avoided. The same is also true for the model-independent meson pair currents, because they are based on the *anti-nucleon* degrees of freedom [196, 208, 209]. For the vector current, a double counting with MEC may be practically avoided because the analyses for the  $^4\text{He}(\vec{e}, e'\vec{p})^3\text{H}$  experiments [6] have shown. (See section 4.1.2.) For the axial-vector current, the quenching of the axial coupling constant ( $g_A = G_A(0)$ ) due to the model-independent meson pair currents was estimated [209] using a Fermi gas model. The quenching due to the pair currents amounts to only 2% at normal nuclear matter density, thus contributing negligibly to the cross section. Hence, the double counting from the interference between the axial-vector and vector currents

<sup>2</sup>Because the renormalization of axial-vector form factors are the same for the time and space components in this study (quenched), we will not discuss the time component.

is also expected to be small, in considering the analyses for the  ${}^4\text{He}(\bar{e}, e'\bar{p}){}^3\text{H}$  experiments. Thus, the effect we consider here, which originates from the change of the internal quark wave function, is additional to the standard nuclear-structure corrections.

Assuming G-parity (no second-class current), the charged-current vector and axial form factors for free nucleons with mass  $M_N$  are defined by:

$$\langle p's'|V_a^\mu(0)|ps\rangle = \bar{u}_{s'}(p') \left[ F_1(Q^2)\gamma^\mu + i\frac{F_2(Q^2)}{2M_N}\sigma^{\mu\nu}(p'-p)_\nu \right] \frac{\tau_a}{2}u_s(p), \quad (289)$$

$$\langle p's'|A_a^\mu(0)|ps\rangle = \bar{u}_{s'}(p') \left[ G_A(Q^2)\gamma^\mu + \frac{G_P(Q^2)}{2M_N}(p'-p)^\mu \right] \gamma_5 \frac{\tau_a}{2}u_s(p), \quad (290)$$

where  $Q^2 \equiv -(p' - p)^2$ , and other notations should be self-explanatory. The vector form factors,  $F_1(Q^2)$  and  $F_2(Q^2)$ , are related to the electric ( $G_E(Q^2)$ ) and magnetic ( $G_M(Q^2)$ ) Sachs form factors by the conserved vector current hypothesis. The induced pseudoscalar form factor,  $G_P(Q^2)$ , is dominated by the pion pole and can be calculated using the PCAC relation [188]. Nevertheless, the contribution from  $G_P(Q^2)$  to the cross section is proportional to (lepton mass) $^2/M_N^2$ , and small in the present study. We note that, since there is another vector in nuclear medium, the nuclear (matter) four-velocity, various other form factors may arise, in addition to those in Eqs. (289) and (290). The modification of the nucleon internal structure studied here may also be expected to contribute to such form factors. However, at this stage, information on such form factors is very limited and not well under control both in theoretically and experimentally. Thus, we focus on the in-medium changes of the free form factors given in Eqs. (289) and (290), and study their effects on neutrino-nucleus scattering.

As already discussed, the electromagnetic and axial vector form factors in nuclear medium in the Breit frame are calculated by ICBM [184]:

$$G_{E,M,A}^{QMC*}(Q^2) = \left( \frac{M_N^*}{E_N^*} \right)^2 G_{E,M,A}^{\text{sph}*} \left( \left( \frac{M_N^*}{E_N^*} \right)^2 Q^2 \right). \quad (291)$$

The explicit expressions for Eq. (291) are given in Eqs. (274), (275) and (288) with proper substitutions. The ICBM includes a Peierls-Thouless projection to account for center of mass and recoil corrections, and a Lorentz contraction of the internal quark wave function [184, 186].

Now we calculate the ratios of the bound to free nucleon form factors,  $[G_{E,M,A}^{QMC*}/G_{E,M,A}^{ICBM \text{ free}}]$ , to estimate the bound nucleon form factors. Using the empirical parameterizations in free space  $G_{E,M,A}^{\text{emp}}$  [218, 219], the bound nucleon form factors  $G_{E,M,A}^*$  are calculated by

$$G_{E,M,A}^*(Q^2) = \left[ \frac{G_{E,M,A}^{QMC*}(Q^2)}{G_{E,M,A}^{ICBM \text{ free}}(Q^2)} \right] G_{E,M,A}^{\text{emp}}(Q^2). \quad (292)$$

Note that the pion cloud effect is not included in the axial vector form factor in the present treatment [207]. However, the normalized  $Q^2$  dependence (divided by  $g_A = G_A(0) = 1.14$ ) relatively well reproduces the empirical parameterization [207]. Furthermore, the relative modification of  $G_A^*(Q^2)$  due to the pion cloud is expected to be small, since the pion cloud contribution to entire  $g_A$  is  $\sim 8\%$  [188] without a specific center-of-mass correction. In the calculation the standard values in the QMC model are used, i.e., the current quark mass  $m_q (= m_u = m_d) = 5$  MeV assuming SU(2) symmetry, and the free nucleon bag radius  $R_N = 0.8$  fm.

First, in Fig. 45 we show ratios of the bound to free nucleon form factors calculated as a function of  $Q^2$  for  $\rho_B = \rho_0 = 0.15 \text{ fm}^{-3}$  (the normal nuclear matter density) and  $0.668\rho_0$  (the Fermi momentum  $k_F = 225$  MeV for  ${}^{12}\text{C}$ ). The lower panels in Fig. 45 show the enhancement of momentum dependence of  $F_2^*(Q^2)$  and  $G_A^*(Q^2)$ , as well as the enhancement of  $F_2^*(0)$  and quenching of  $G_A^*(0)$  [53, 187, 207]. Although the modification of the  $Q^2$  dependence is small, we emphasize that this effect originates from change in the nucleon internal structure. The main origin of this new  $Q^2$  dependence is the effect of Lorentz contraction on the quark wave function, amplified by the reduced effective nucleon mass. (See also Eq. (291).) Note that, the relative change of the bound nucleon form factor  $F_2^*(Q^2)[G_E^{p*}(Q^2)]$  to that of the free nucleon is an enhancement [quenching] of  $\sim 8\%$  [4%] in  ${}^{12}\text{C}$  at  $Q^2 = 0.15 \text{ GeV}^2$ , and we are focusing on this relative change.

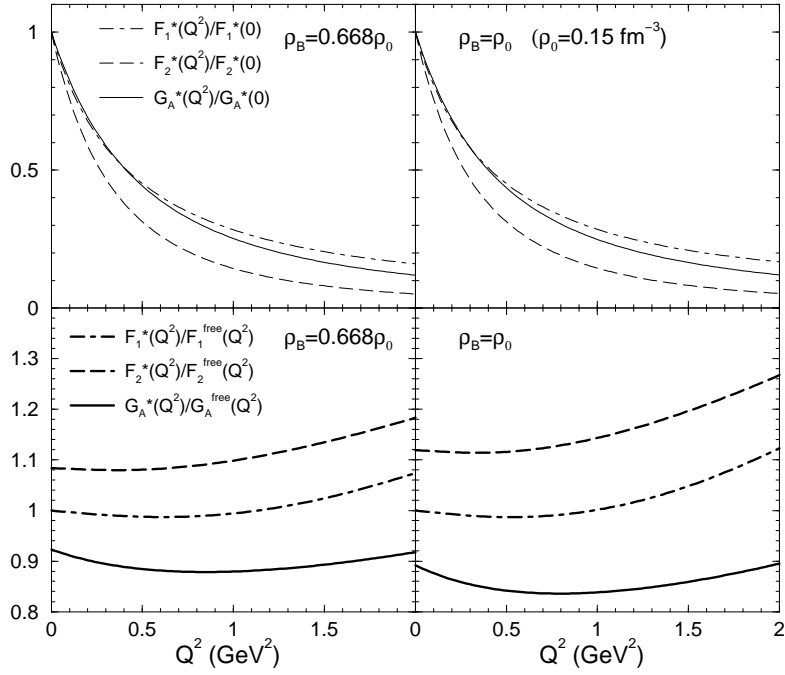


Figure 45: Calculated ratios for the bound nucleon form factors (from Ref. [210]).

Now, we investigate the effect of the bound nucleon form factors on charged-current neutrino-nucleus scattering. We compute the inclusive  $^{12}\text{C}(\nu_\mu, \mu^-)X$  differential and total cross sections, which have been measured by the LSND collaboration [211, 212, 213]. The formalism used in the calculation is described in Ref. [215], and that the empirical parameterizations of the electromagnetic [215, 218] and axial [207, 219] form factors for the free nucleon. (See Eq. (292).) A relativistic Fermi gas model is used implementing the bound nucleon form factors to calculate the differential cross section  $\langle d\sigma/dE_\mu \rangle$ , averaged over the LSND muon neutrino spectrum  $\Phi(E_{\nu_\mu})$  [215] for the full range of the LSND experimental spectrum [211, 212, 213],  $0 \leq E_{\nu_\mu} \leq 300$  MeV:

$$\left\langle \frac{d\sigma}{dE_\mu} \right\rangle = \frac{\int_0^\infty (d\sigma/dE_\mu) \Phi(E_{\nu_\mu}) dE_{\nu_\mu}}{\int_0^\infty \Phi(E_{\nu_\mu}) dE_{\nu_\mu}}. \quad (293)$$

Fig. 46 shows the result for  $\langle d\sigma/dE_\mu \rangle$  calculated using the nucleon masses,  $M_N$  and  $M_N^*$ . For the Fermi momentum  $k_F = 225$  MeV ( $\rho_B = 0.668\rho_0$ ) for  $^{12}\text{C}$ , we use the QMC calculated value,  $M_N^* = 802.8$  MeV. A moderate quenching of the cross section can be observed due to the in-medium form factors for both cases. Although the effective nucleon mass can account for, to some extent, the binding effect (the Hugenholtz-van Hove theorem [220]), there is an alternative to include the binding effect, i.e., the “binding energy”  $E_B$  is introduced and the available reaction energy  $E$  is replaced by  $E - E_B$ . In this case, we use the free nucleon mass in the calculation. Since  $E_B$  is an effective way of accounting for the binding effect [221], we regard  $E_B$  as a parameter and perform calculations for  $E_B = 20, 25$  and  $30$  MeV. (E.g.,  $E_B = 25 - 27$  MeV is commonly used for the  $^{16}\text{O}$  nucleus [222].) We emphasize that our aim is not to reproduce the LSND data, but to estimate the corrections due to the bound nucleon form factors.

In Fig. 47 we present the results of  $\langle d\sigma/dE_\mu \rangle$  for  $E_B = 20, 25$  and  $30$  MeV.

In both Figs. 46 and 47, the bound nucleon form factors reduce the differential cross section. In Fig. 47, as the binding energy  $E_B$  increases, the peak position shifts downward for both cases with the free and bound nucleon form factors. The similar tendency due to  $M_N^*$  is also seen in Fig. 46.

The total cross section is given by integrating Eq. (293) over the muon energy. We denote the cross section calculated with the free [bound] nucleon form factors,  $F_{1,2}(Q^2)$  and  $G_{A,P}(Q^2)$  [ $F_{1,2}^*(Q^2)$  and  $G_{A,P}^*(Q^2)$ ], as  $\langle \sigma(F, G) \rangle$  [ $\langle \sigma(F^*, G^*) \rangle$ ]. Thus,  $\langle \sigma(F, G) \rangle$  calculated with  $M_N$  and  $E_B = 0$  corresponds to the free Fermi gas model result. The results with  $E_B = 0$  and either  $M_N$  or  $M_N^*$  are listed in the top group rows in Table 22. The LSND experimental data [211, 212, 213] are also shown in the bottom group rows in Table 22. As

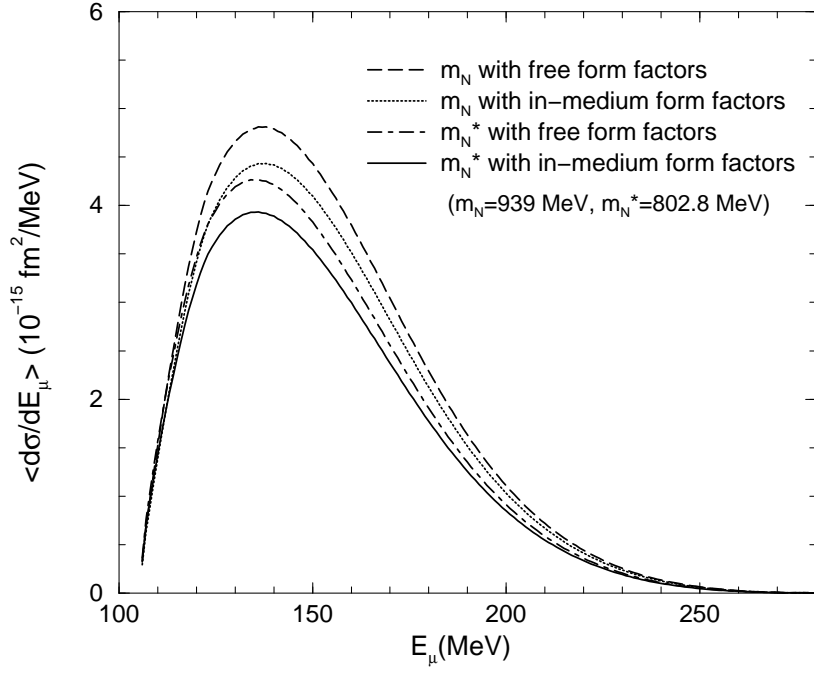


Figure 46: Angle-integrated inclusive  $^{12}\text{C}(\nu_\mu, \mu^-)X$  differential cross section as a function of the emitted muon energy  $E_\mu$  using  $E_B = 0$  for all cases (from Ref. [210]).

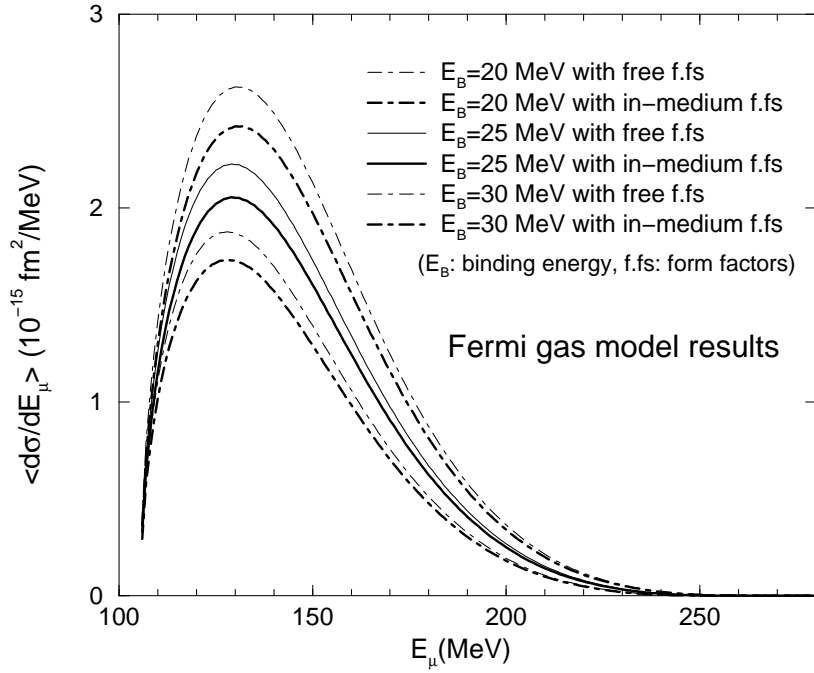


Figure 47: Same as Fig. 46, but using  $M_N = 939 \text{ MeV}$  for all cases (from Ref. [210]).

Table 22: Calculated total cross sections for  $^{12}\text{C}(\nu_\mu, \mu^-)X$ . See the text for notations.

Notation	Type of calculation	$E_B$ (MeV)	$\langle\sigma\rangle$ in $10^{-40} \text{ cm}^2$
$\langle\sigma(F, G)\rangle$	$M_N, F_{1,2}(Q^2), G_{A,P}(Q^2)$	0	32.5
$\langle\sigma(F^*, G^*)\rangle$	$M_N, F_{1,2}^*(Q^2), G_{A,P}^*(Q^2)$	0	30.0
$\langle\sigma(F, G)\rangle$	$M_N^*, F_{1,2}(Q^2), G_{A,P}(Q^2)$	0	28.4
$\langle\sigma(F^*, G^*)\rangle$	$M_N^*, F_{1,2}^*(Q^2), G_{A,P}^*(Q^2)$	0	26.2
$\langle\sigma(F^*, G)\rangle$	$M_N, F_{1,2}^*(Q^2), G_{A,P}(Q^2)$	0	33.5
$\langle\sigma(F, G^*)\rangle$	$M_N, F_{1,2}(Q^2), G_{A,P}^*(Q^2)$	0	29.1
$\langle\sigma(F, G)\rangle$	$M_N, F_{1,2}(Q^2), G_{A,P}(Q^2)$	20	16.1
$\langle\sigma(F^*, G^*)\rangle$	$M_N, F_{1,2}^*(Q^2), G_{A,P}^*(Q^2)$	20	14.8
$\langle\sigma(F, G)\rangle$	$M_N, F_{1,2}(Q^2), G_{A,P}(Q^2)$	25	13.2
$\langle\sigma(F^*, G^*)\rangle$	$M_N, F_{1,2}^*(Q^2), G_{A,P}^*(Q^2)$	25	12.2
$\langle\sigma(F, G)\rangle$	$M_N, F_{1,2}(Q^2), G_{A,P}(Q^2)$	30	10.7
$\langle\sigma(F^*, G^*)\rangle$	$M_N, F_{1,2}^*(Q^2), G_{A,P}^*(Q^2)$	30	9.9
Experiment [211] (2002)			$10.6 \pm 0.3 \pm 1.8$
Experiment [212] (1997)			$11.2 \pm 0.3 \pm 1.8$
Experiment [213] (1995)			$8.3 \pm 0.7 \pm 1.6$

expected [211, 212, 213], the free Fermi gas result overestimates the data by a factor of three. The results obtained using the bound nucleon form factors, with either  $M_N$  or  $M_N^*$ , similarly overestimate the LSND data. In order to make discussions more quantitative, we define a ratio:

$$R(\delta\sigma) \equiv [\langle\sigma(F, G)\rangle - \langle\sigma(F^*, G^*)\rangle] / \langle\sigma(F, G)\rangle. \quad (294)$$

For the total cross sections calculated with  $(M_N, M_N^*)$  and  $E_B = 0$ , we get  $R(\delta\sigma) = (7.7, 7.7)\%$ , respectively. Thus, the correction due to the bound nucleon form factors to the total cross section is not sensitive to  $M_N$  or  $M_N^*$  in the case of  $E_B = 0$ .

Next, we investigate which bound nucleon form factor gives dominant corrections to the total cross section. We calculate the total cross section with  $M_N$ , using the free and bound form factors for two cases,  $[F_{1,2}^*(Q^2)$  and  $G_{A,P}(Q^2)]$  and  $[F_{1,2}(Q^2)$  and  $G_{A,P}^*(Q^2)]$ . They are denoted by  $\langle\sigma(F^*, G)\rangle$  and  $\langle\sigma(F, G^*)\rangle$ , respectively. The results are given in the middle group rows in Table 22. Together with the results in the upper group rows in Table 22, we obtain inequalities for the total cross sections calculated with  $M_N$  and  $E_B = 0$ :

$$\langle\sigma(F, G^*)\rangle < \langle\sigma(F^*, G^*)\rangle < \langle\sigma(F, G)\rangle < \langle\sigma(F^*, G)\rangle. \quad (295)$$

This shows that the most dominant reduction is driven by the axial form factor,  $G_A^*(Q^2)$ . (The induced pseudoscalar form factor  $G_P(Q^2)$  gives only a few percent contribution when calculated using all free form factors.) Furthermore,  $F_{1,2}^*(Q^2)$  enhance the total cross section (mostly due to  $F_2^*(Q^2)$ ), as can be seen from the lower panel in Fig. 45.

The total cross sections for  $E_B = 20, 25$  and  $30$  MeV are listed in the bottom group rows in Table 22. The bound nucleon form factors for these cases also reduce the total cross section relative to those calculated with the free form factors. In addition, the results are rather sensitive to the values for  $E_B$ . However, we find  $R(\delta\sigma) = (8.1, 7.6, 7.5)\%$  for  $E_B = (20, 25, 30)$  MeV, respectively. Thus, the effect of the bound nucleon form factors to the reduction rate is again not sensitive to  $E_B$ . To draw a more definite conclusion, it is essential to perform a more precise, elaborate calculation within the framework of RPA [215] including the effect of bound nucleon form factors. However, even at the present stage, it is important to point out that the correction due to the in-medium form factors arising from the bound nucleon internal structure change, could be significant for a precise estimate of the charged-current neutrino-nucleus cross section.

Finally, we here comment on the scalar and vector form factors of the in-medium nucleon. Using the QMC model, it is possible to calculate the form factors at  $\sigma$ - and  $\omega$ -nucleon strong-interaction vertices in nuclear matter. In Ref. [223], the Peierls-Yoccoz projection technique is used to take account of center of mass and recoil corrections, and the Lorentz contraction is also applied to the internal quark wave function. The form factors are reduced by the nuclear medium relative to those in vacuum. At normal nuclear matter density and  $Q^2 = 1 \text{ GeV}^2$ , the reduction rate in the scalar form factor is about 15%, which is almost identical to that in the vector one. One can parameterize the ratios of the form factors in symmetric nuclear matter to those in vacuum as a function of nuclear density and momentum transfer [223].

## 4.2 Quark-hadron duality, the nuclear EMC effect and nuclear structure functions

### 4.2.1 The nuclear EMC effect

The European Muon Collaboration (EMC) effect tells us the fact that a nuclear structure function measured in deep inelastic scattering in the valence quark regime (Bjorken variable  $x \geq 0.3$ ) is considerably reduced compared with that of a free nucleon [224]. Despite much experimental and theoretical progress [3], no unique and universally accepted explanation of the EMC effect has yet emerged. Because the measurements in deep inelastic scattering are performed at very high momentum transfers, we can expect that the observed results really reflect quark degrees of freedom in a nucleus. The simple parton model interpretation is that a quark in the bound nucleon carries less momentum than in free space seems uncontested, but its underlying origin is still elusive.

The most popular explanation may be the conventional nuclear binding effect that is responsible for the depletion of the quark momentum in matter. It then suggests that the nuclear structure function,  $F_2^A(x)$ , can be expressed by the following convolution form:

$$\frac{F_2^A(x)}{A} = \int dy f_{N/A}(y) F_2^N(x/y), \quad (296)$$

where  $F_2^N$  is the free nucleon structure function, and the light front distribution function  $f_{N/A}(y)$ , which gives the probability that a nucleon carries a fractional momentum  $y$  of the nucleus  $A$ . If  $k^\mu$  is the momentum of a nucleon and  $P^\mu$  is the momentum of the target nucleus,  $y = (k^0 + k^3)A/P^+ = (k^0 + k^3)A/M_A = (k^0 + k^3)/\bar{M}_N$ , in which the nucleus is taken to be at rest with  $P^+ = M_A$  ( $M_A$  the nuclear mass). One can easily use conventional nuclear physics to obtain the probability that a nucleon carries a three momentum  $\vec{k}$  but if one uses only naive considerations, one faces a puzzle when deciding how to choose the value of  $k^0$ . Should one use the average separation energy or the average nucleon mass  $\bar{M}_N$ , or possibly the effective mass in the chosen many-body theory?

In the binding explanation,  $k^0$  is usually given by the free nucleon mass  $M_N$  minus the average separation energy  $\epsilon$ . Then,  $f_{N/A}(y)$  is narrowly peaked at  $y = 1 - \epsilon/M_N$  ( $\epsilon$  becomes as much as 70 MeV for infinite nuclear matter [225, 226]), which thus leads to a significant reduction in the value of the nuclear structure function (see also Ref. [227]). However, in any case, it is necessary to supply a derivation to avoid the need to arbitrarily choose a prescription for  $k^0$ .

To do this, one needs to develop the light front dynamics for nuclear system [228] because, in the parton model,  $x$  is the ratio of the plus component of the momentum of the struck quark to that of the target and it is the plus component of the momentum which was observed to be depleted by the EMC. In Ref. [4, 228], the function  $f_{N/A}(y)$  is shown to be the one which maintains the covariance of the formalism, and in which the nucleons carry the entire plus-momentum  $P^+$  of the nucleus. This result is obtained independently of the specific relativistic mean field theory used, so no such theory contains the binding effect discussed above. The only binding effect arises from the average binding energy of the nucleus (16 MeV for infinite nuclear matter and 8 MeV for a finite nucleus), and is far too small to explain the observed depletion of the structure function. This conclusion has also been obtained by Birse [229].

The generality of this result may be supported by the Hugenholtz-van Hove theorem [220], which states that the energy of the level at the Fermi surface,  $E_F$ , is equal to the nuclear mass divided by  $A$ :

$$E_F = M_A/A \equiv \bar{M}_N. \quad (297)$$

This theorem is the consequence of using the condition that the total pressure of the nucleus vanishes at equilibrium, and the assumption that nucleons are the only degrees of freedom contributing to the nuclear energy. Thus this theorem is a signal that  $P^+ = P_N^+$  or that nucleons account for the entire plus momentum of the nucleus.

Thus, the relativistic mean-field approach may lead to results in severe disagreement with experiment, i.e., the depth of the minimum in the EMC ratio is not monotonically decreasing with  $A$ , and it has a smaller magnitude than experiment [4]. Furthermore, the plus momentum distributions give  $\langle y \rangle \simeq 1$  which indicates that nearly all of the plus momentum is carried by the nucleons. In order to reproduce the data, the nucleon plus momentum must be decreased by some mechanism that becomes more important at larger  $A$ . Nucleon-nucleon correlations cannot take plus momentum from nucleons, and explicit mesonic components in the nuclear Fock state wave function carrying plus momentum are limited by Drell-Yan experiments [230]. Therefore, it appears that the nuclear EMC effect must be due to something outside of conventional nucleon-meson dynamics.

It is of great interest to apply the QMC model to explain the nuclear EMC effect, because the quarks in the bound nucleon respond to the nuclear environment and the quark eigenvalue,  $x_0$ , decreases in matter (see section 3.1). That should be responsible for the depletion of the quark momentum in a nucleus. In Ref. [231, 232], the quark momentum distribution function,  $q_A^{(2)}(x)$ , in nucleus  $A$  was calculated using the QMC model

$$q_A^{(2)}(x) = \int d^3r \rho_A(r) q_{N/A}^{(2)}(x, k_F(r)), \quad (298)$$

where, for simplicity, the local-density approximation is assumed and  $\rho_A$  is the nuclear density distribution ( $\rho_A(r) = 2/(3\pi^2)k_F(r)^3$ ,  $k_F$  the local Fermi momentum). The distribution of valence quarks in nuclear matter is then given by

$$q_{N/A}^{(2)}(x, k_F(r)) = \int_x^A dy f_{N/A}(y, k_F(r)) q_N^{(2)}(x/y, k_F(r), \mu^2), \quad (299)$$

where the Fermi motion is incorporated as a convolution of  $f_{N/A}$  with the quark distribution function of the bound nucleon,  $q_{N/A}^{(2)}$ , which is calculated in terms of the nucleon bag model [233] with the scalar and vector mean-fields generated by QMC. For a free nucleon, the dominant intermediate state is a two-quark bag, while for nuclei it is the two-quark bag state bound to the residual  $(A - 1)$  nuclear debris.

Using this framework, we have found that the usual impulse approximation, in which the interaction of the intermediate two-quark bag state with the rest of the nucleus is ignored, gives an overestimate of the nuclear EMC effect by a factor of two or three [231, 232]. In contrast, the inclusion of the interaction between the two-quark bag and the debris can provide a reasonable amount of the nuclear EMC effect [231, 232]. This outcome is physically very sensible. The nuclear binding is the result of the attractive scalar mean-field experienced by the three constituent quarks. By ignoring the binding of the pair of spectator quarks, that is, by treating the quarks as though they were free in the nucleus, it is assumed that the kinematics of the hard scattering of the quark struck by the virtual photon carries the binding of all three quarks. This is clearly not correct.

In Refs. [231, 232], the calculation is somewhat crude and needs to be made more realistic one. Nevertheless, the physical insight gained is much more general. Recently, Miller *et al.* have performed similar calculations using the QMC model supplemented by the chiral quark-soliton picture [5]. They concluded that their model can simultaneously describe the nuclear EMC effect and the related Drell-Yan experiments. Finally, we mention that Cloet *et al.* [77] have taken the covariant generalization the QMC model developed by Bentz and Thomas [75] and shown that not only does it reproduce the EMC effect in nuclear matter but that it predicts a nuclear effect on the proton spin structure function which is twice as large as in the unpolarized case. It is clearly very important to pursue this prediction experimentally as soon as possible.

#### 4.2.2 Bloom-Gilman duality and the nuclear EMC effect

The relationship between form factors and structure functions, or more generally between inclusive and exclusive processes, has been studied in a number of contexts over the years. Drell & Yan [234] and West [235] pointed out long ago that, simply on the basis of scaling arguments, the asymptotic behavior of elastic electromagnetic form factors as  $Q^2 \rightarrow \infty$  can be related to the  $x \rightarrow 1$  behavior of deep-inelastic structure functions.



Furthermore, the relationship between resonance (transition) form factors and the deep-inelastic continuum has been studied in the framework of quark-hadron, or Bloom-Gilman [34], duality: the equivalence of the averaged structure function in the resonance region and the scaling function which describes high  $W$  data. The high precision Jefferson Lab data [236] on the  $F_2$  structure function suggests that the resonance-scaling duality also exists locally, for each of the low-lying resonances, including surprisingly the elastic [237], to rather low values of  $Q^2$ . (For a recent extensive review on quark-hadron duality, see Ref. [238].)

In the context of QCD, Bloom-Gilman duality can be understood within an operator product expansion of moments of structure functions [239, 240]: the weak  $Q^2$  dependence of the low  $F_2$  moments can be interpreted as indicating that higher twist ( $1/Q^2$  suppressed) contributions are either small or cancel. However, while allowing the duality violations to be identified and classified according to operators of a certain twist, it does not explain why some higher twist matrix elements are intrinsically small.

Whatever the ultimate microscopic origin of Bloom-Gilman duality, for our purposes it will be sufficient to note the *empirical fact* that local duality is realized in lepton-proton scattering down to  $Q^2 \sim 0.5 \text{ GeV}^2$  at the 10-20% level for the lowest moments of the structure function. In other words, here we are not concerned about *why* duality works, but rather *that* it works.

Motivated by the experimental verification of local duality, one can use measured structure functions in the resonance region to directly extract elastic form factors [239]. Conversely, empirical electromagnetic form factors at large  $Q^2$  can be used to predict the  $x \rightarrow 1$  behavior of deep-inelastic structure functions [34, 241, 242, 243]. The assumption of local duality for the elastic case implies that the area under the elastic peak at a given  $Q^2$  is equivalent to the area under the scaling function, at much larger  $Q^2$ , when integrated from the pion threshold to the elastic point [34]. Using the local duality hypothesis, de Rújula et al. [239], and more recently Ent et al. [237], extracted the proton's magnetic form factor from resonance data on the  $F_2$  structure function at large  $x$ , finding agreement to better than 30% over a large range of  $Q^2$  ( $0.5 \lesssim Q^2 \lesssim 5 \text{ GeV}^2$ ). In the region  $Q^2 \sim 1$ – $2 \text{ GeV}^2$  the agreement was at the  $\sim 10\%$  level. An alternative parameterization of  $F_2$  was suggested in Ref. [244], which because of a different behavior in the unmeasured region  $\xi \gtrsim 0.86$ , where  $\xi = 2x/(1 + \sqrt{1 + x^2/\tau})$  is the Nachtmann variable, with  $\tau = Q^2/4M_N^2$ , led to larger differences at  $Q^2 \gtrsim 4 \text{ GeV}^2$ . However, at  $Q^2 \sim 1 \text{ GeV}^2$  the agreement with the form factor data was even better. As pointed out in Ref. [245], data at larger  $\xi$  are needed to constrain the structure function parameterization and reliably extract the form factor at larger  $Q^2$ . Furthermore, since we will be interested in *ratios* of form factors and structure functions only, what is more relevant for our analysis is not the degree to which local duality holds for the *absolute* structure functions, but rather the *relative* change in the duality approximation between free and bound protons.

Applying the argument in reverse, one can formally differentiate the local elastic duality relation [34] with respect to  $Q^2$  to express the scaling functions, evaluated at threshold,  $x = x_{\text{th}} = Q^2/(W_{\text{th}}^2 - M_N^2 + Q^2)$ , with  $W_{\text{th}} = M_N + m_\pi$ , in terms of  $Q^2$  derivatives of elastic form factors. Explicit explanations and derivations will be given in section 4.2.3 for the case of the bound nucleon. In Refs. [34, 242] the  $x \rightarrow 1$  behavior of the neutron to proton structure function ratio was extracted from data on the elastic electromagnetic form factors. (Nucleon structure functions in the  $x \sim 1$  region are important as they reflect mechanisms for the breaking of spin-flavor SU(6) symmetry in the nucleon [246].) Extending this to the case of bound nucleons [247], one finds that as  $Q^2 \rightarrow \infty$  the ratio of bound to free proton structure functions is:

$$\frac{F_2^{p*}}{F_2^p} \rightarrow \frac{dG_M^{p*2}/dQ^2}{dG_M^{p2}/dQ^2}. \quad (300)$$

At finite  $Q^2$  there are corrections to Eq. (300) arising from  $G_E^p$  and its derivatives, as discussed in Ref. [242]. (In this analysis we use the full,  $Q^2$  dependent expressions [242, 243].) Note that in the nuclear medium, the value of  $x$  at which the pion threshold arises is shifted:

$$x_{th} \rightarrow x_{th}^* = \left( \frac{m_\pi(2M_N + m_\pi) + Q^2}{m_\pi(2(M_N^* + 3V_\omega^q) + m_\pi) + Q^2} \right) x_{th}, \quad (301)$$

where  $V_\omega^q = g_\omega^q \omega$  is the vector potential felt by the nucleon and (consistent with chiral expectations and phenomenological constraints) we have set  $m_\pi^* = m_\pi$ . However, the difference between  $x_{th}$  and  $x_{th}^*$  has a negligible effect on the results for most values of  $x$  considered.

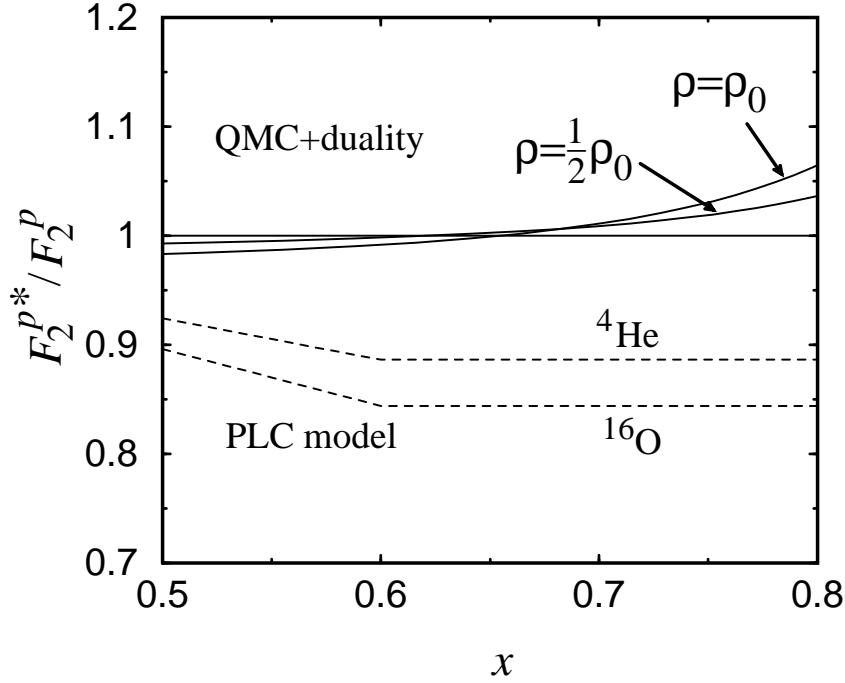


Figure 48: In-medium to free proton  $F_2$  structure function ratio as a function of  $x$  at threshold,  $x = x_{th}$ , extracted from the polarization transfer data [6] within the QMC model and local duality, at nuclear matter density,  $\rho = \rho_0$ , and at  $\rho = \frac{1}{2}\rho_0$  (solid) with  $\rho_0 = 0.15 \text{ fm}^{-3}$ . For comparison the results of the PLC suppression model [248] are shown for  $^4\text{He}$  and  $^{16}\text{O}$  (dashed) (from Ref. [247]).

Using the duality relations between electromagnetic form factors and structure functions, in Fig. 48 we plot the ratio  $F_2^{p*}/F_2^p$  as a function of  $x$ , with  $x$  evaluated at threshold,  $x = x_{th}$  (solid lines). Note that at threshold the range of  $Q^2$  spanned between  $x = 0.5$  and  $x = 0.8$  is  $Q^2 \approx 0.3\text{--}1.1 \text{ GeV}^2$ . Over the range  $0.5 \lesssim x \lesssim 0.75$  the effect is almost negligible, with the deviation of the ratio from unity being  $\lesssim 1\%$  for  $\rho = \frac{1}{2}\rho_0$  and  $\lesssim 2\%$  for  $\rho = \rho_0$  ( $\rho_0 = 0.15 \text{ fm}^{-3}$ ). For  $x \gtrsim 0.8$  the effect increases to  $\sim 5\%$ , where, larger  $x$  corresponds to larger  $Q^2$ , and the analysis in terms of the QMC model becomes unreliable for  $x \gtrsim 0.9$ . However, in the region where the analysis can be considered reliable, the results based on the bound nucleon form factors inferred from the polarization transfer data [6] and local duality imply that the nucleon structure function undergoes small modification in medium.

It is instructive to contrast this result with models of the EMC effect in which there is a large medium modification of nucleon structure. For example, let us consider the model of Ref. [248], where it is assumed that for large  $x$  the dominant contribution to the structure function is given by the point-like configurations (PLC) of partons which interact weakly with the other nucleons. The suppression of this component in a bound nucleon is assumed to be the main source of the EMC effect. This model represents one of the extreme possibilities that the EMC effect is solely the result of deformation of the wave function of bound nucleons, without attributing any contribution to nuclear pions or other effects associated with nuclear binding [249]. Given that this model has been so successfully applied to describe the nuclear EMC effect, it is clearly important to examine its consequences elsewhere.

The deformation of the bound nucleon structure function in the PLC suppression model is governed by the function [248]:

$$\delta(k) = 1 - 2(k^2/2M_N + \epsilon_A)/\Delta E_A, \quad (302)$$

where  $k$  is the bound nucleon momentum,  $\epsilon_A$  is the nuclear binding energy, and  $\Delta E_A \sim 0.3\text{--}0.6 \text{ GeV}$  is a

nucleon excitation energy in the nucleus. For  $x \gtrsim 0.6$  the ratio of bound to free nucleon structure functions is then given by [248]:

$$\frac{F_2^{N*}(k, x)}{F_2^N(x)} = \delta(k). \quad (303)$$

The  $x$  dependence of the suppression effect is based on the assumption that the point-like configuration contribution in the nucleon wave function is negligible at  $x \lesssim 0.3$  ( $F_2^{N*}/F_2^N = 1$ ), and for  $0.3 \lesssim x \lesssim 0.6$  one linearly interpolates between these values [248]. The results for  ${}^4\text{He}$  and  ${}^{16}\text{O}$  are shown in Fig. 48 (dashed lines) for the average values of nucleon momentum,  $\langle k^2 \rangle$ , in each nucleus. The effect is a suppression of order 20% in the ratio  $F_2^{N*}/F_2^N$  for  $x \sim 0.6$ – $0.7$ . In contrast, the ratios extracted on the basis of duality, using the QMC model constrained by the  ${}^4\text{He}$  polarization transfer data [6], show almost no suppression ( $\lesssim 1$ – $2\%$ ) in this region. (See section 4.1.2.) Thus, for  ${}^4\text{He}$ , the effect in the PLC suppression model is an order of magnitude too large at  $x \sim 0.6$ , and has the opposite sign for  $x \gtrsim 0.65$ .

Although the results extracted from the polarization transfer measurements [6] rely on the assumption of local duality, we stress that the corrections to duality have been found to be typically less than 20% for  $0.5 \lesssim Q^2 \lesssim 2 \text{ GeV}^2$  [236, 244]. The results therefore appear to rule out large bound structure function modifications, such as those assumed in the point-like configuration suppression model [248], and instead point to a small medium modification of the intrinsic nucleon structure, complemented by standard binding effects.

As a consistency check on the analysis, one can also examine the change in the form factor of a bound nucleon that would be implied by the corresponding change in the structure function in medium. Namely, from the local duality relation [239, 243]:

$$\left[G_M^p(Q^2)\right]^2 \approx \frac{2 - \xi_0}{\xi_0^2} \frac{(1 + \tau)}{(1/\mu_p^2 + \tau)} \int_{\xi_{\text{th}}}^1 d\xi F_2^p(\xi), \quad (304)$$

one can extract the magnetic form factor by integrating the  $F_2^p$  structure function over  $\xi$  between threshold,  $\xi = \xi_{\text{th}}$ , and  $\xi = 1$ . Here  $\xi_0 = \xi(x = 1)$ , and  $\mu_p$  is the proton magnetic moment. In Fig. 49 we show the PLC model predictions for the ratio of the magnetic form factor of a proton bound in  ${}^4\text{He}$  to that in vacuum, derived from Eqs. (303) and (304), using the parameterization for  $F_2^p(\xi)$  from Ref. [237], and an estimate for the in-medium value of  $\mu_p^*$  shown in Fig. 37. Taking the average nucleon momentum in the  ${}^4\text{He}$  nucleus,  $k = \langle k \rangle$ , the result is a suppression of about 20% in the ratio  $G_M^{p*}/G_M^p$  at  $Q^2 \sim 1$ – $2 \text{ GeV}^2$  (solid curve). Since the structure function suppression in the PLC model depends on the nucleon momentum (Eq. (302)), we also show the resulting form factor ratio for a momentum typical in the  $(\vec{e}, e'\vec{p})$  experiment,  $k = 50 \text{ MeV}$  (long dashed). As expected, the effect is reduced, however, it is still of the order 15% since the suppression also depends on the binding energy, as well as on the nucleon mass, which changes with density rather than with momentum. In contrast, the QMC calculation, which is consistent with the MAMI and JLab  ${}^4\text{He}$  quasi-elastic data [6] (see section 4.1.2), produces a ratio which is typically 5–10% *larger* than unity (dashed). Without a very large compensating change in the in-medium electric form factor of the proton (which seems to be excluded by  $y$ -scaling constraints), the behavior of the magnetic form factor implied by the PLC model + duality would produce a large *enhancement* of the polarization transfer ratio, rather than the observed small suppression [6].

In the context of the QMC model, the change in nucleon form factors allowed by the data imply a modification of the in-medium structure function of  $\lesssim 1$ – $2\%$  at  $0.5 \lesssim x \lesssim 0.75$  for all nuclear densities between nuclear matter density,  $\rho = \rho_0$ , and  $\rho = \frac{1}{2}\rho_0$ . While the results rely on the validity of quark-hadron duality, the empirical evidence suggests that for low moments of the proton's  $F_2$  structure function the duality violations due to higher twist corrections are  $\lesssim 20\%$  for  $Q^2 \gtrsim 0.5 \text{ GeV}^2$  [236], and decrease with increasing  $Q^2$ .

The results place rather strong constraints on models of the nuclear EMC effect, especially on models which assume that the EMC effect arises from a large deformation of the nucleon structure in medium. For example, we find that the PLC suppression model [248] predicts an effect which is about an order of magnitude larger than that allowed by the data [6], and has a different sign. The findings therefore appear to disfavor models with large medium modifications of structure functions as viable explanations for the nuclear EMC effect, although it would be desirable to have more data on a variety of nuclei and in different kinematic regions.

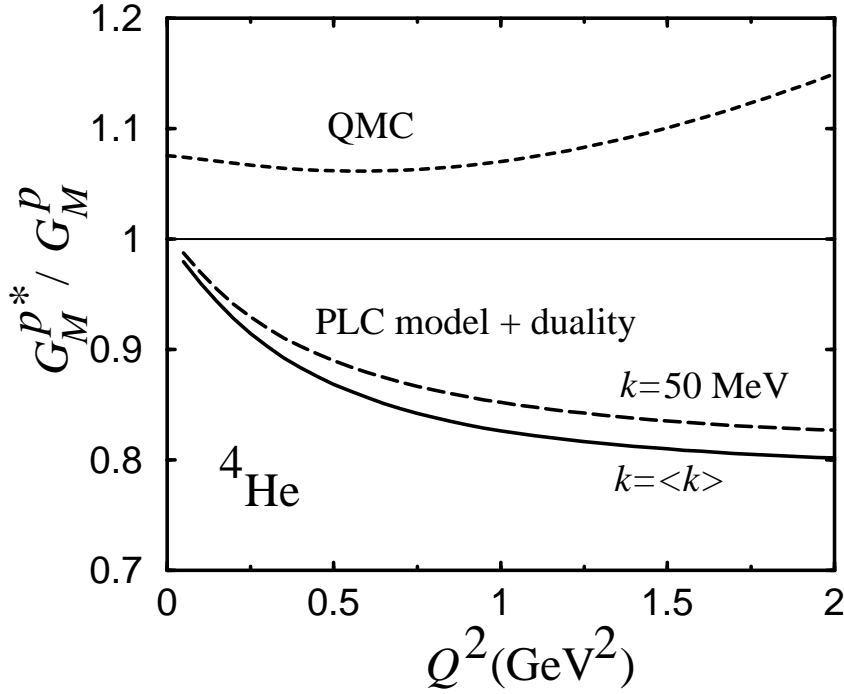


Figure 49: Ratio of in-medium to free proton magnetic form factors, extracted from the PLC suppression model [248] for the EMC ratio in  ${}^4\text{He}$ , using the  $F_2^p$  data from Refs. [236, 237] and local duality, for  $k = \langle k \rangle$  (solid) and  $k = 50 \text{ MeV}$  (long-dashed). The QMC model prediction (short-dashed) is shown for comparison (from Ref. [247]).

These results have other important practical ramifications. For instance, the PLC suppression model was used [250] to argue that the EMC effects in  ${}^3\text{He}$  and  ${}^3\text{H}$  differ significantly at large  $x$ , in contrast to calculations [251, 252] based on conventional nuclear physics using well-established bound state wave functions which show only small differences. Based on the findings presented here, one would conclude that the conventional nuclear physics description of the  ${}^3\text{He}/{}^3\text{H}$  system should indeed be a starting point for nuclear structure function calculations, as the available evidence suggests little room for large off-shell corrections. On top of this, we expect a small correction due to the change of the internal structure of the bound nucleon, as discussed in section 4.1.2, would indeed reflect the real explanation. Finally, let us stress that quark-hadron duality is a powerful tool with which to simultaneously study the medium dependence of both exclusive and inclusive observables, and thus provides an extremely valuable guide toward a consistent picture of the effects of the nuclear environment on nucleon substructure.

#### 4.2.3 Bloom-Gilman duality and the nuclear structure functions

As we discussed in section 4.2.2, we can study the nuclear structure functions at large Bjorken- $x$  based on the Bloom-Gilman duality [253]. Since, our main concern is to see the effect of the bound nucleon internal structure change included entirely in the bound nucleon form factors and the pion threshold in a nuclear medium, the elastic contribution to the bound nucleon structure functions for charged-lepton scattering may be given by [241, 242, 243]:

$$F_1^{BN*} = \frac{1}{2}(G_M^*)^2 \delta(x-1), \quad (305)$$

$$F_2^{BN*} = \frac{1}{1+\tau} \left[ (G_E^*)^2 + \tau (G_M^*)^2 \right] \delta(x-1), \quad (306)$$

$$g_1^{BN*} = \frac{1}{2(1+\tau)} G_M^* (G_E^* + \tau G_M^*) \delta(x-1), \quad (307)$$

$$g_2^{BN*} = \frac{\tau}{2(1+\tau)} G_M^* (G_E^* - G_M^*) \delta(x-1), \quad (308)$$

while those for (anti)neutrino scattering for an isoscalar nucleon,  $N \equiv \frac{1}{2}(p+n)$ , may be given by [254]:

$$F_1^{WNB N*} = \frac{1}{4} \left[ (G_M^{V*})^2 + (1+1/\tau)(G_A^*)^2 \right] \delta(x-1), \quad (309)$$

$$F_2^{WNB N*} = \frac{1}{2} \left[ \frac{(G_E^{V*})^2 + \tau(G_M^{V*})^2}{1+\tau} + (G_A^*)^2 \right] \delta(x-1), \quad (310)$$

$$F_3^{WNB N*} = G_M^{V*} G_A^* \delta(x-1), \quad (311)$$

where  $\tau = Q^2/4M_N^2$  ( $M_N$ , the free nucleon mass) and  $x$  the Bjorken variable.  $G_E^*$  [ $G_M^*$ ] is the bound nucleon electric [magnetic] Sachs form factor,  $G_{E,M}^{V*} = G_{E,M}^{p*} - G_{E,M}^{n*}$  the corresponding isovector electromagnetic form factors, and  $G_A^*$  is the (isovector) axial vector form factor [210, 254].

Using the Nachtmann variable,  $\xi = 2x/(1 + \sqrt{1+x^2/\tau})$ , local duality equates the scaling bound nucleon structure function  $F_2^*$  and the contribution from  $F_2^{BN*}$  of Eq. (306):

$$\int_{\xi_{th}^*}^1 F_2^*(\xi) d\xi = \int_{\xi_{th}^*}^1 F_2^{BN*}(\xi, Q^2) d\xi, \quad (312)$$

where  $\xi_{th}^*$  is the value at the pion threshold in a nuclear medium given below. Below, we consider symmetric nuclear matter, and we can assume that the pion mass in-medium ( $m_\pi^*$ ) is nearly equal to that in free space ( $m_\pi$ ), and  $\xi_{th}^*$  may be given by [247]:

$$\xi_{th}^* = \xi(x_{th}^*), \quad (313)$$

with

$$x_{th}^* = x_{th} \frac{m_\pi(2M_N + m_\pi) + Q^2}{m_\pi[2(M_N^* + 3V_\omega^q) + m_\pi] + Q^2}, \quad x_{th} = \frac{Q^2}{m_\pi(2M_N + m_\pi) + Q^2}, \quad (314)$$

where  $x_{th}^*$  [ $x_{th}$ ] is the Bjorken- $x$  at the pion threshold in medium [free space], and  $M_N^*$  and  $3V_\omega^q$  are respectively the effective mass and the vector potential of the bound nucleon. Inserting Eq. (306) into the r.h.s. of Eq. (312), we get [242, 243, 255]:

$$\int_{\xi_{th}^*}^1 F_2^*(\xi) d\xi = \frac{\xi_0^2}{4-2\xi_0} \left[ \frac{(G_E^*)^2 + \tau(G_M^*)^2}{1+\tau} \right], \quad (315)$$

where  $\xi_0 = \xi(x=1)$ . The derivative in terms of  $\xi_{th}^*$  in both sides of Eq. (315) with  $\xi_0$  fixed gives [242, 243, 254]:

$$F_2^*(\xi_{th}^*) \equiv F_2^*(x_{th}^*) = -2\beta^* \left[ \frac{(G_M^*)^2 - (G_E^*)^2}{4M_N^2(1+\tau)^2} + \frac{1}{1+\tau} \left( \frac{d(G_E^*)^2}{dQ^2} + \tau \frac{d(G_M^*)^2}{dQ^2} \right) \right], \quad (316)$$

where  $\beta^* = (Q^4/M_N^2)(\xi_0^2/\xi_{th}^{*3})[(2 - \xi_{th}^*/x_{th}^*)/(4 - 2\xi_0)]$ . Similarly, we get expressions for other bound nucleon structure functions at  $x = x_{th}^*$ :

$$F_1^*(x_{th}^*) = -\beta^* \frac{d(G_M^*)^2}{dQ^2}, \quad (317)$$

$$g_1^*(x_{th}^*) = -\beta^* \left[ \frac{G_M^*(G_M^* - G_E^*)}{4M_N^2(1+\tau)^2} + \frac{1}{1+\tau} \left( \frac{d(G_E^* G_M^*)}{dQ^2} + \tau \frac{d(G_M^*)^2}{dQ^2} \right) \right], \quad (318)$$

$$g_2^*(x_{th}^*) = -\beta^* \left[ \frac{G_M^*(G_E^* - G_M^*)}{4M_N^2(1+\tau)^2} + \frac{\tau}{1+\tau} \left( \frac{d(G_E^* G_M^*)}{dQ^2} - \frac{d(G_M^*)^2}{dQ^2} \right) \right], \quad (319)$$

$$F_1^{WN*}(x_{th}^*) = -\frac{\beta^*}{2} \left[ \frac{-(G_A^*)^2}{4M_N^2\tau^2} + \frac{d(G_M^{V*})^2}{dQ^2} + \frac{1+\tau}{\tau} \frac{d(G_A^*)^2}{dQ^2} \right], \quad (320)$$

$$F_2^{WN*}(x_{th}^*) = -\beta^* \left[ \frac{(G_M^{V*})^2 - (G_E^{V*})^2}{4M_N^2(1+\tau)^2} + \frac{1}{1+\tau} \left( \frac{d(G_E^{V*})^2}{dQ^2} + \tau \frac{d(G_M^{V*})^2}{dQ^2} \right) + \frac{d(G_A^*)^2}{dQ^2} \right], \quad (321)$$

$$F_3^{WN*}(x_{th}^*) = -\beta^* \frac{2G_M^{V*} G_A^*}{dQ^2}. \quad (322)$$

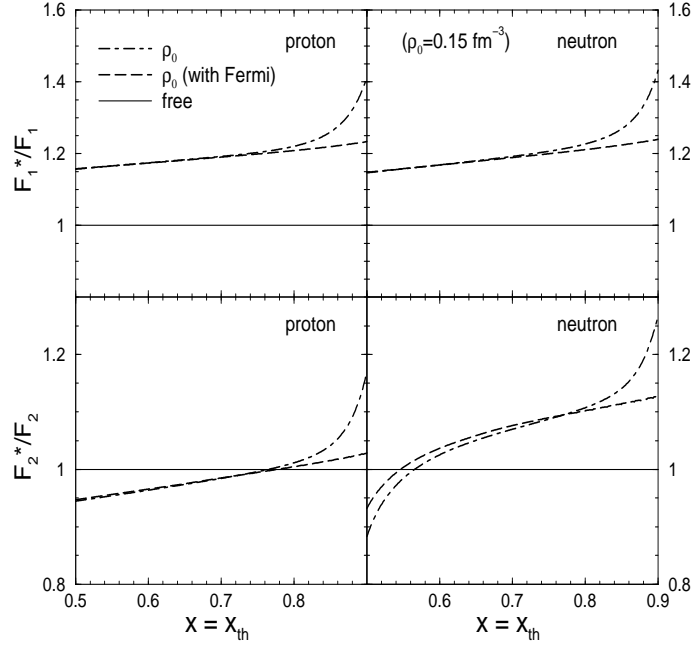


Figure 50: Ratios for the charged-lepton scattering structure functions  $F_{1,2}^*/F_{1,2}$ , those extracted using the bound and free nucleon form factors. Effect of Fermi motion is included by the convolution with the nucleon momentum distribution [4] for *both* the structure functions extracted using the free and bound nucleon form factors, and then ratios are calculated (the dashed lines denoted by "with Fermi") (from Ref. [253]).

First, we show in Figs. 50 and 51 ratios of the bound to free nucleon structure functions without the effect of Fermi motion (dash-dotted lines), calculated for the charged-lepton scattering for baryon densities  $\rho_B = \rho_0$  with  $\rho_0 = 0.15 \text{ fm}^{-3}$ .

Because  $x_{th} = (0.7, 0.9)$  in free space (see also Eq. (314)) correspond to  $Q^2 \simeq (0.65, 2.5) \text{ GeV}^2$ , we regard the results shown in the region,  $0.7 \lesssim x \lesssim 0.9$ , as the present local duality predictions. The corresponding  $Q^2$  range is also more or less within the reliability of the bound nucleon form factors calculated [6, 187, 210]. In the region,  $0.8 \lesssim x \lesssim 0.9$ , all the bound nucleon structure functions calculated,  $F_{1,2}^*$  and  $g_{1,2}^*$ , are enhanced relative to those in a free nucleon. (We have checked that also the enhancement becomes larger as the baryon density increases.) However, the depletion observed in the EMC effect, occurring just before the enhancement as  $x$  increases, is absent for all of them. Probably, the conventional binding effect, which is not entirely included in the present study, may produce some depletion [232]. (We may note also that the conclusion drawn by Smith and Miller [4], that the depletion of the deep inelastic nuclear structure functions observed in the valence quark regime, is due to some effect beyond the conventional nucleon-meson treatment of nuclear physics.) Thus, only the effect of the bound nucleon internal structure change introduced via the bound nucleon form factors and the pion threshold shift in the present local duality framework, cannot explain the observed depletion in the EMC effect for the relevant Bjorken- $x$  range  $0.7 \lesssim x \lesssim 0.85$ . However, it can explain a part of the enhancement at large Bjorken- $x$  ( $x \gtrsim 0.85$ ).

In order to see whether or not the conclusions drawn above are affected by Fermi motion, we also calculate the ratios by convoluting the nucleon momentum distribution obtained in Ref. [4] with the value  $\bar{M}_N = 931 \text{ MeV}$ . (See Eq. (297).) Namely, we convolute the nucleon momentum distribution with *both* the structure functions extracted using the free and bound nucleon form factors first, and then calculate ratios. The corresponding results are shown in Figs. 50 and 51 (dashed lines, denote by "with Fermi"). Note that, because the upper value of  $x_{th}(x_{th}^{max} \sim 0.91)$  is limited for a reliable extraction of the structure functions by the reliable  $Q^2$  range for the nucleon elastic form factors in the present case, we had to cut the contribution from the

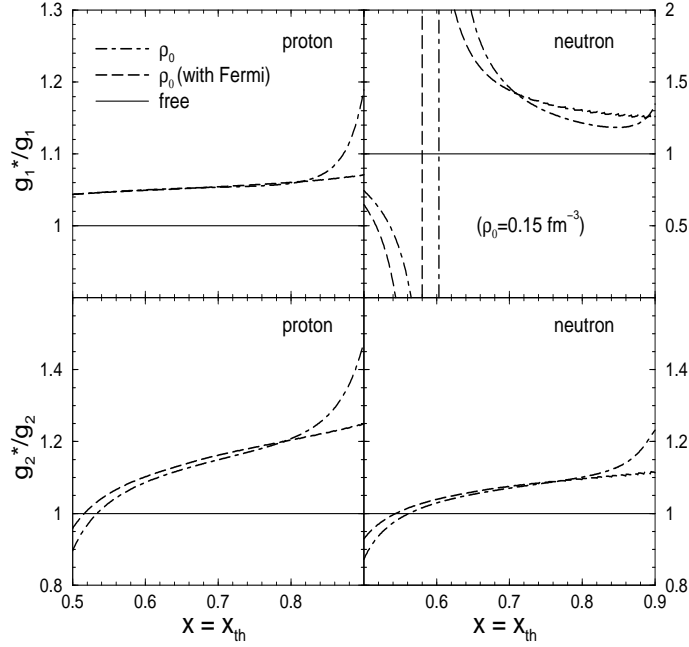


Figure 51: Same as Fig. 50, but for  $g_{1,2}^*/g_{1,2}$  (from Ref. [253]).

region,  $x_{th} \geq x_{th}^{max}$ , in the convolution integral. This would effectively suppress the enhanced part of the bound nucleon structure functions. The obtained results show a similar feature, except the region  $x_{th} \gtrsim 0.8$ . However, even the region  $x_{th} \gtrsim 0.8$ , the enhancement feature remains the same. Thus, we conclude that, the obtained enhancement of the bound nucleon structure functions  $F_{1,2}^*$  and  $g_{1,2}^*$  in the charged lepton scattering, is intrinsic and not smeared by the effect of Fermi motion. This is more obvious in the region  $0.7 \lesssim x_{th} \lesssim 0.8$ . In that region, the effect of Fermi motion is nearly canceled out in the ratios, as one could expect.

Next, we show in Fig. 52 the bound nucleon structure functions calculated from a charged current,  $F_{1,2,3}^{WN*}$ , together with those in vacuum for the (anti)neutrino scattering. For a reference, we show also  $\frac{18}{5}F_2^{\gamma N} \equiv \frac{18}{5}\frac{1}{2}(F_2^p + F_2^n)$  in vacuum for the charged-lepton scattering. The effect of Fermi motion is included in the same way as that was included in the charged-lepton scattering case. Similarly to the charged-lepton scattering case,  $F_{1,2,3}^{WN*}$  in symmetric nuclear matter are enhanced at large  $x$  without the effect of Fermi motion, but only in the region,  $0.85 \lesssim x \lesssim 0.9$ . This is due to the contribution from the in-medium axial vector form factor  $G_A^*$ . Although  $G_A^*$  falls off faster than the free space  $G_A$  in the range  $Q^2 \lesssim 1 \text{ GeV}^2$ , the  $Q^2$  dependence turns out to be slightly enhanced in the range  $Q^2 \gtrsim 1 \text{ GeV}^2$ , due to the Lorentz contraction of the internal quark wave function of the bound nucleon [210]. Then, the contribution from the  $Q^2 \gtrsim 1 \text{ GeV}^2$  region gives a suppression. (See Eqs. (320)-(322), but neglecting small contributions from the non-derivative terms with respect to  $Q^2$ , which are suppressed by  $\sim 1/\tau^2$  as  $Q^2$  increases.) With the effect of Fermi motion, the enhancement and quenching features at  $x_{th} \gtrsim 0.8$  are less pronounced because of the convolution procedure applied in the present treatment.

After having calculated  $F_2^*$  for both the charged-lepton and (anti)neutrino scattering, we can study also charge symmetry breaking in parton distributions focusing on the effect of the bound nucleon internal structure change. In free space, it was studied in Ref. [254] based on the local duality. A measure of charge symmetry breaking in parton distributions at  $x = x_{th}^*$  may be given by [254]:

$$\begin{aligned} & \left[ \frac{5}{6} F_2^{WN*}(x_{th}^*) - 3 F_2^{\gamma N*}(x_{th}^*) \right] \\ &= 3 \left\{ \frac{13}{18} \beta^* \left[ \frac{d(G_M^{p*})^2}{dQ^2} + \frac{d(G_M^{n*})^2}{dQ^2} \right] + \frac{5}{9} \beta^* \frac{d(G_M^{p*} G_M^{n*})}{dQ^2} - \frac{5}{18} \beta^* \frac{d(G_A^*)^2}{dQ^2} \right\}. \end{aligned} \quad (323)$$

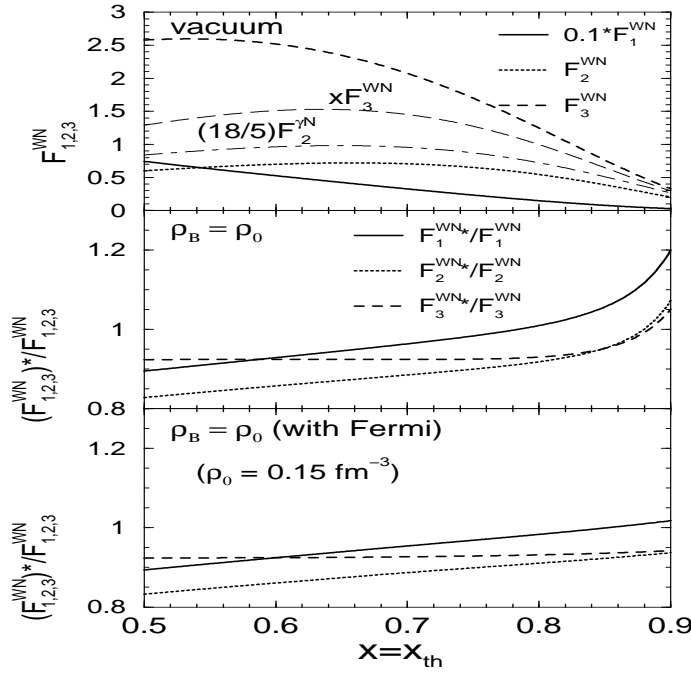


Figure 52: Structure functions calculated for (anti)neutrino scattering (for an isoscalar nucleon), for baryon density  $\rho_B = 0$  and  $\rho_0$ . For a reference,  $\frac{18}{5}F_2^{\gamma N} \equiv \frac{18}{5}\frac{1}{2}(F_2^p + F_2^n)$  for the charged-lepton scattering in vacuum is also shown (top panel). Ratios are shown for both with and without the effect of Fermi motion. (See also caption of Fig. 50 for the effect of Fermi motion.) (Taken from Ref. [253].)

In Fig. 53 we show normalized ratios, divided by  $\frac{1}{2} \left[ \frac{5}{6}F_2^{WN*} + 3F_2^{\gamma N*} \right]$ , for baryon densities  $\rho_B = 0$  and  $\rho_0$  with and without the effect of Fermi motion. The results show that the charge symmetry breaking in symmetric nuclear matter is enhanced due to the effect of the bound nucleon internal structure change. (We have checked that the breaking becomes larger as the baryon density increases.) Note that, because the quantity is the ratio by definition, it is very insensitive to the effect of Fermi motion in entire region of  $x_{th}$  considered. Thus, charge symmetry breaking looks to be more appreciable in nuclei than in the case of a free nucleon, and/or could affect fragmentation in heavy ion collisions. In particular, the results imply that the NuTeV anomaly [256], which was observed in the measurements using iron target, would be enhanced even more than the analysis made [254] in free space. (See e.g., Ref. [257] for detailed discussions.) However, the present status of experimental accuracies would not allow to detect the effect distinctly.

We summarize the results and conclusions of the present study based on the local quark-hadron duality:

1. The effect of the change of the bound nucleon internal structure in the nuclear medium is to enhance the structure functions at large Bjorken- $x$  ( $x \gtrsim 0.85$ ) for charged-lepton scattering and especially  $F_1^{WN}$  in (anti)neutrino scattering.
2. The  $x$  dependence of the bound nucleon structure functions obtained for the charged-lepton scattering and  $F_{2,3}^{WN}$  in (anti)neutrino scattering is different. Namely, the former [latter] is enhanced [quenched] in the region  $0.8 \lesssim x \lesssim 0.9$  [ $0.7 \lesssim x \lesssim 0.85$ ].
3. The effect of the change in the bound nucleon internal structure change cannot explain the depletion observed in the EMC effect (for the charged-lepton scattering) for the relevant Bjorken- $x$  range in this study,  $0.7 \lesssim x \lesssim 0.85$ , but it can explain a part of the enhancement occurring in the larger region of  $x$ .
4. Charge symmetry breaking in parton distributions in nuclei, or higher baryon densities, would be enhanced relative to that in free space by the internal structure change of a bound nucleon.



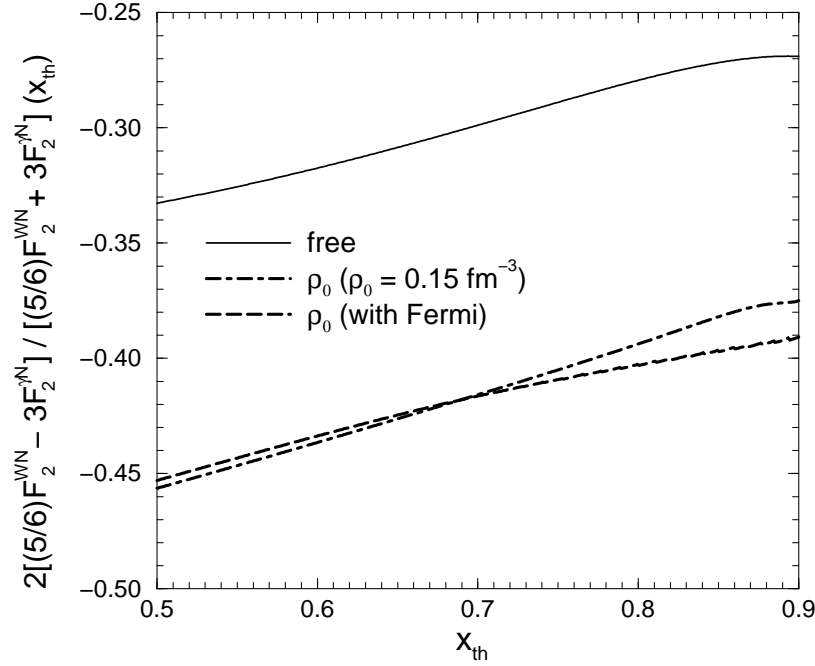


Figure 53: Normalized ratios, divided by  $\frac{1}{2} \left[ \frac{5}{6} F_2^{WN*} + 3 F_2^{\gamma N*} \right]$ , for charge symmetry breaking in parton distributions, for baryon densities  $\rho_B = 0$  and  $\rho_0$ , with and without the effect of Fermi motion. (See also caption of Fig. 50 for the effect of Fermi motion.) (Taken from Ref. [253].)

5. The conclusions obtained above are insensitive to the effect of Fermi motion in the treatment of the present study.

Finally, we note again that the present study has not included in a rigorous manner the conventional nuclear effects, such as binding and Fermi motion. However, even solely from the present results, we can conclude that, in addition to the conventional nuclear effects, the effect of a change in the internal structure of a bound nucleon may be appreciable in various nuclear structure functions at large Bjorken- $x$ .

## 5 Hadronic reactions in nuclear medium

We now turn to the study of how the internal structure changes of hadrons can have an impact on hadronic reactions. As examples, we discuss subthreshold kaon production,  $D$  and  $\bar{D}$  meson production in nucleus, and  $J/\psi$  suppression in heavy ion collisions in sections, 5.1, 5.2 and 5.3, respectively.

### 5.1 Subthreshold kaon production and in-medium effects

The properties of kaons in nuclear matter have recently attracted enormous interest because of their capacity to signal chiral symmetry restoration or give information on the possibility of kaon condensation in neutron stars [1, 258, 259, 260, 261]. Studies with a variety of models [130, 262, 263, 264] indicate that the antikaon potential is attractive while the kaons feel a repulsive potential in nuclear matter. The results from kaonic atoms [265], as well as an analysis [266, 267, 268, 269, 270] of the  $K^-$  production from heavy ion collisions [271, 272, 273, 274, 275], are in reasonable agreement with the former expectation for antikaons. However, the analysis of available data on  $K^+$  production from heavy ion collisions at SIS energies [273, 274, 275, 276] contradicted the predictions that the kaon potential is repulsive. The comparison between the heavy ion calculations and the data [268, 269, 270, 276, 277] indicated that the  $K^+$ -meson spectra were best described by neglecting any in-medium modification of the kaon properties. Furthermore, the introduction of even a

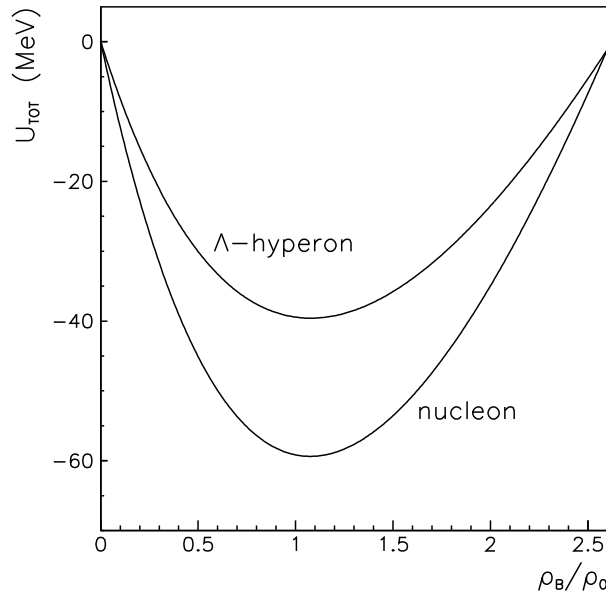


Figure 54: Total potential  $U_{tot}$  for nucleon and  $\Lambda$ -hyperon shown as a function of the baryon density,  $\rho_B$ , in units of the nuclear matter saturation density,  $\rho_0=0.15 \text{ fm}^{-3}$  (from Ref. [283]).

weakly repulsive  $K^+$ -nucleus potential usually resulted in a substantial underestimate of the experimental data on kaon production. However, subsequent studies including the in-medium modification of kaon property [278, 279, 280, 281, 282] all suggest that the repulsive  $K^+$ -nucleus potential can be consistently incorporated in kaon production simulations. The main uncertainties lie in the elementary kaon production cross sections which can not be constrained by experiments, those involving the  $\Delta(1232)$  resonance. They serve as dominant kaon production mechanisms. Keeping this point in mind, however, we would like to study the impact of property changes of kaon, nucleon, hyperons in nuclear medium on subthreshold kaon production in heavy ion collisions.

Since in heavy ion collisions at SIS energies [271, 272, 273, 274, 275] a lot of  $K^+$ -mesons are expected to be produced by secondary pions, we investigate the kaon production reactions,  $\pi+N \rightarrow Y+K$  ( $Y = \Lambda, \Sigma$  hyperons), in nuclear matter [283]. To do this, we combine the in-medium property changes of hadrons predicted by the QMC model with earlier studies of kaon production in free space. All parameters in the QMC model are fixed, as explained in section 3, and the effects of the medium on the reaction cross sections and *amplitudes* are calculated. The result is impressive in that *the medium effects explain the nuclear production data, without any adjustment of the parameters determined elsewhere, including the standard repulsive kaon-nucleus interaction.*

First, in Fig. 54, we show the total potential,  $U_{TOT} = V_s + V_v$  of Eqs. (219) and (220) for nucleon ( $N$ ) and  $\Lambda$  hyperon in symmetric nuclear matter. This indicates that both nucleon and hyperon potentials approach minima around normal nuclear matter density, which reflects the fact that around  $\rho_0$  the energy density of nuclear matter is minimized.

Next, in Fig. 55 we show the density dependence of the total  $K$  and  $K^*$ -meson potentials at zero momenta. The total kaon potential is repulsive as explained before, and depends substantially on the baryon density. (See Eq. (220).) The  $K^*$ -meson total potential is attractive at baryon densities below  $\simeq 2.7\rho_0$ . As for the pion, the Goldstone boson nature of it and the chiral symmetry suggest us that the pion mass modification in nuclear medium is marginal, as already mentioned before. Thus, we do not consider possible medium effects on the pion.

For the energy dependence of the cross section  $\pi N \rightarrow YK$  ( $Y = \Lambda, \Sigma$ ) we use the resonance model [284, 285], which could describe the energy dependence of the total cross sections,  $\pi N \rightarrow YK$ , quite well, and has been used widely in kaon production simulation codes [267, 268, 269, 277, 286, 287], and extend the model by

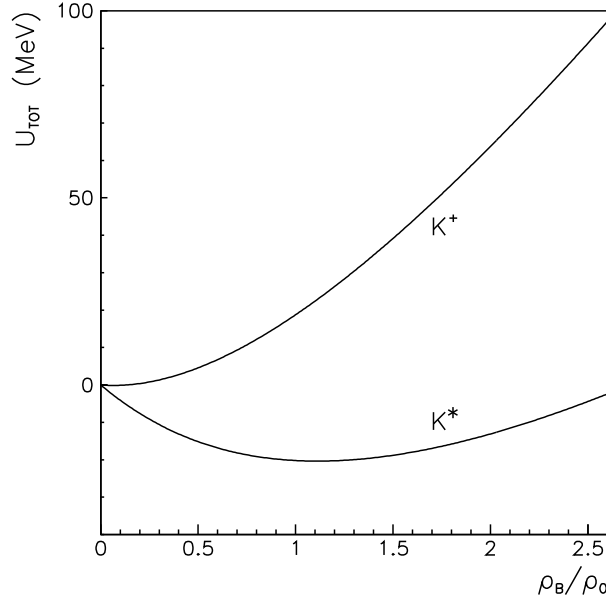


Figure 55: Total potential  $U_{tot}$  for  $K^+$  and  $K^*(892)^+$  mesons plotted as function of the baryon density,  $\rho_B$ , in units of saturation density,  $\rho_0=0.15 \text{ fm}^{-3}$  of the nuclear matter (from Ref. [283]).

including medium modification of the hadron properties, not only in the kinematic factors such as the flux and the phase space, but also in the reaction amplitudes. Kaon and hyperon production processes in  $\pi N$  collisions in the resonance model [284, 285] are shown in Figs. 56 and 57. Because different intermediate states and final states contribute to the  $\pi N \rightarrow \Lambda K$  and  $\pi N \rightarrow \Sigma K$  reactions, the in-medium modification of the reaction amplitudes for these reactions should also be different.

Now, we need to discuss the in-medium modification of the resonance masses, which enter the resonance propagators and modify the reaction amplitudes. At present it seems that there is no reliable estimate for the in-medium modification of masses for the higher mass baryon resonances.

Based on the QMC model, we assume that the light quarks in the baryon resonances are responsible for the mass modification in nuclear medium, as explained in section 3.3.1. However, there is a possibility that the excited state light quarks may couple differently to the scalar  $\sigma$  field from those in the ground states, although we expect that the difference should be small. Thus, we estimate the range for the in-medium baryon resonance masses by the following two extreme cases, i.e., (i) all light quarks including those in the excited states play the same role for the mass modification as those in the ground states, (ii) only the ground state light quarks play the role as in the usual QMC model. These two cases are expected to give the maximum and minimum limits for the mass modifications of the baryon resonances. Specifically, the range for the effective masses of the baryon resonance in medium is given:

$$M_{N(1650)} - \delta M_N^* \leq M_{N(1650)}^* \leq M_{N(1650)} - \frac{2}{3}\delta M_N^*, \quad (324)$$

$$M_{N(1710)} - \delta M_N^* \leq M_{N(1710)}^* \leq M_{N(1710)} - \frac{1}{3}\delta M_N^*, \quad (325)$$

$$M_{N(1720)} - \delta M_N^* \leq M_{N(1720)}^* \leq M_{N(1720)} - \frac{1}{3}\delta M_N^*, \quad (326)$$

$$M_{\Delta(1920)} - \delta M_N^* \leq M_{\Delta(1920)}^* \leq M_{\Delta(1920)} - \frac{1}{3}\delta M_N^*, \quad (327)$$

$$\text{with } \delta M_N^* = M_N - M_N^*. \quad (328)$$

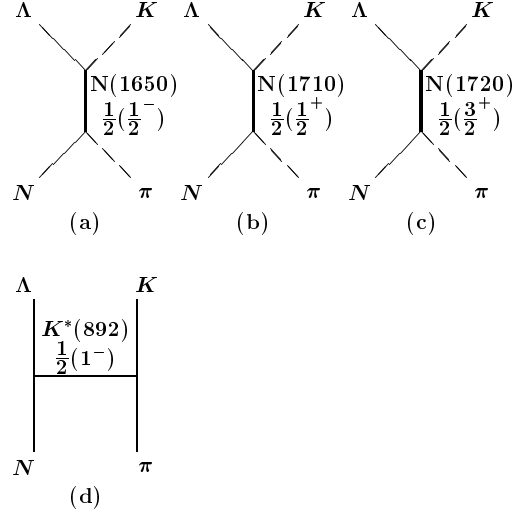


Figure 56: Processes included for the  $\pi N \rightarrow \Lambda K$  reactions.

These in-medium resonance masses may be expected to modify the resonance propagators in the reaction amplitudes. To avoid introducing extra unknown parameters, we approximate the in-medium resonance widths appearing in the propagator by the free space ones. From Eqs. (324)-(328), we will show results for the cross section calculated using the lower limit for the resonance masses. However, we have also performed the calculation using the upper limit for the resonance masses and confirmed that our conclusion remains the same.

The dispersion relation in nuclear matter relating the total energy  $E$  and the momentum  $\vec{p}$  of the particle  $h$  with free space mass  $m_h$  is written as

$$E = \sqrt{\vec{p}^2 + (m_h + V_s^h)^2} + V_v^h, \quad (329)$$

where  $V_s^h$ ,  $V_v^h$  denote the scalar and vector potentials in nuclear matter. (See Eqs. (219) and (220).) The threshold,  $\sqrt{s_{th}}$ , for the reaction  $\pi + N \rightarrow Y + K^+$  is given as the sum of the total energies of the final  $K^+$ -meson and  $Y$ -hyperon, taking their momenta to be zero and hence

$$\sqrt{s_{th}} = m_K + m_Y + V_s^K + V_s^Y + V_v^K + V_v^Y, \quad (330)$$

where now the upper indices denote kaons and hyperons. The solid lines in Fig. 58 show the  $K^+\Lambda$  and  $K^+\Sigma$  reaction thresholds,  $\sqrt{s_{th}}$ , as a function of the baryon density. Obviously, in free space the scalar and vector potentials vanish and the reaction threshold equals to the sum of the bare masses of the produced particles, which is shown by the dashed lines in Fig. 58 for the  $K^+\Lambda$  and  $K^+\Sigma$  final states.

It is important, that while the  $K^+$ -meson energy at zero momentum increases with the baryon density (see Fig. 55), because of the negative  $\Lambda$  and  $\Sigma$  potentials the reaction threshold in nuclear matter at  $\rho_B < 1.4\rho_0$  ( $\rho_0 = 0.15 \text{ fm}^{-3}$ ) is shifted below than that in free space. The maximal downward shift of the reaction threshold in nuclear matter occurs at baryon densities around  $\rho_B \simeq 0.6\rho_0$ . This value is the result of competition between the simple, linear dependence on density of the vector potentials and the more complicated, non-linear behavior

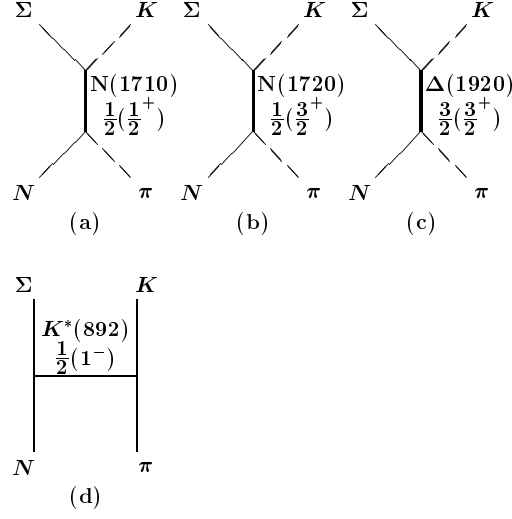


Figure 57: Processes included for the  $\pi N \rightarrow \Sigma K$  reactions.

of the scalar potentials. (A similar competition leads to the saturation of the binding energy of normal nuclear matter in the QMC model.) Furthermore, the maximum of the downward shift of the  $\pi + N \rightarrow Y + K^+$  reaction threshold amounts to roughly 30 MeV. We also found that at baryon densities  $\rho_B > 0.2 \text{ fm}^{-3}$  the strangeness production threshold in  $\pi N$  collisions is higher than the free space case.

Now we apply the resonance model to calculate the in-medium amplitudes, while keeping the coupling constant as well as the form factors at the values found in free space. While this assumption certainly cannot be completely correct in nuclear matter, there are no presently established ways to improve this part of our calculation. In principle, since we started from the reaction amplitude itself, it is possible to include in-medium modifications of the coupling constants as well as the form factors when reliable calculations of the changes of these quantities in nuclear matter become available. In the following calculations we include the vector and scalar potentials for the interacting (initial) nucleons and final kaons and hyperons, as well as for the intermediate baryonic resonances and  $K^*$ -meson.

Fig. 59 shows the results calculated for the differential cross section for the  $\pi^- + p \rightarrow \Lambda + K^0$  reaction at the invariant collision energy  $\sqrt{s} = 1683 \text{ MeV}$ . It is calculated both in free space (the solid line) and in nuclear matter, at baryon densities  $\rho_B = \rho_0$  (the dashed line) and  $\rho_B = 2\rho_0$  (the dotted line). For comparison, we also show in Fig. 59 the experimental data collected in free space [288, 289]. The important finding is that not only the absolute magnitude, but also the shape (the dependence on the  $\cos \theta$ ) of the  $\pi^- + p \rightarrow \Lambda + K^0$  differential cross section, depends on the baryon density.

One of the simplest ways to construct the in-medium reaction cross section is to take into account only the in-medium modification of the flux and phase space factors while leaving amplitude in matter the same as that in free space, without including any medium effect [290]. To shed more light on the problem of how the reaction amplitude itself is modified in nuclear matter, we show in Fig. 60 the reaction amplitudes squared in arbitrary units for the  $\pi^- + p \rightarrow \Lambda + K^0$  reaction, calculated at  $\sqrt{s} = 1.7 \text{ GeV}$  and  $1.9 \text{ GeV}$ , in free space (the solid lines),  $\rho_B = \rho_0$  (the dashed lines) and  $\rho_B = 2\rho_0$  (the dotted lines). Our calculation clearly indicates that

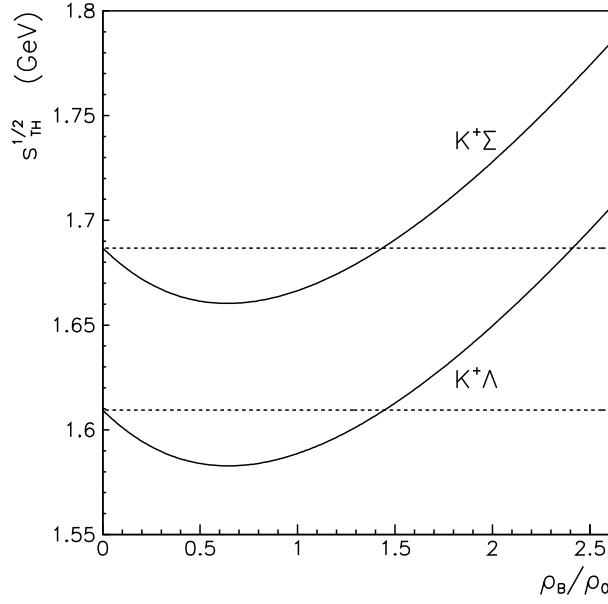


Figure 58: The threshold energy,  $\sqrt{s_{th}}$ , for  $K^+\Lambda$  and  $K^+\Sigma$  production given by their total in-medium energy at zero momentum, as a function of the baryon density  $\rho_B$  in units of saturation density of nuclear matter,  $\rho_0=0.15 \text{ fm}^{-3}$ . The solid lines indicate results calculated, while the dashed lines show the threshold in free space (from Ref. [283]).

the  $\pi^-+p\rightarrow\Lambda+K^0$  reaction amplitude in nuclear matter differs substantially from that in free space at these energies, and that the amplitudes depend on the baryon density.

Finally, the energy dependence of the total  $\pi^-+p\rightarrow\Lambda+K^0$  cross section is shown in Fig. 61, as a function of the invariant collision energy,  $\sqrt{s}$ . The experimental data in free space are taken from Ref. [291]. The calculations for free space are in reasonable agreement with the data, as shown by the solid line. The dashed line in Fig. 61 shows the results obtained for nuclear matter at  $\rho_B=\rho_0$ , while the dotted line is the calculation at  $\rho_B=2\rho_0$ . Clearly the total  $\pi^-+p\rightarrow\Lambda+K^0$  reaction cross section depends substantially on the baryon density. Furthermore, as already discussed previously, the reaction threshold at baryon density  $\rho_B=\rho_0$  is shifted downward as compared to that in free space, while at  $\rho_B=2\rho_0$  it is shifted upward.

It is obvious that heavy ion collisions probe a range of baryon densities from  $\rho_B=0$  up to several times normal nuclear matter density. The calculation of the time and spatial dependence of the baryon density distribution is a vital aspect of dynamical heavy ion simulations. However, a first estimate of the density averaged total  $\pi^-+p\rightarrow\Lambda+K^0$  cross section can be gained from Fig. 61. Of course, the data is only available in free space and should only be directly compared with the solid curve. Nevertheless, it is suggestive for the problem of in-medium production to note that a crude average of the in-medium cross sections over the range  $0<\rho_B<2\rho_0$  would be quite close to the free space cross section at energies around the free space threshold. This seems to provide a reasonable explanation of why the heavy ion calculations including [270, 276, 277] the  $\pi+p\rightarrow\Lambda+K$  cross section in free space, that is without a repulsive kaon potential, can reproduce the data [271, 272, 273, 274, 275]. A more quantitative calculation and discussion of this effect will be given later.

Next, we consider the  $\pi+N\rightarrow\Sigma+K$  reaction in nuclear matter. The  $\pi+N\rightarrow\Sigma+K$  reaction involves different dynamics in comparison with the  $\pi+p\rightarrow\Lambda+K$  reaction, because the reaction involves different intermediate baryonic resonances. For instance, although the  $N(1650)$  resonance couples to  $\Lambda N$  channel, it does not couple to the  $\Sigma N$  state. Moreover, the  $\Delta(1920)$  resonance couples to  $\Sigma N$  channel, but does not couple to the  $\Lambda N$  channel in the resonance model [284, 285]. For this reason, the dependence on the baryon density of the reaction in nuclear matter,  $\pi+N\rightarrow\Sigma+K$ , is quite different from that of  $\pi+N\rightarrow\Lambda+K$ .

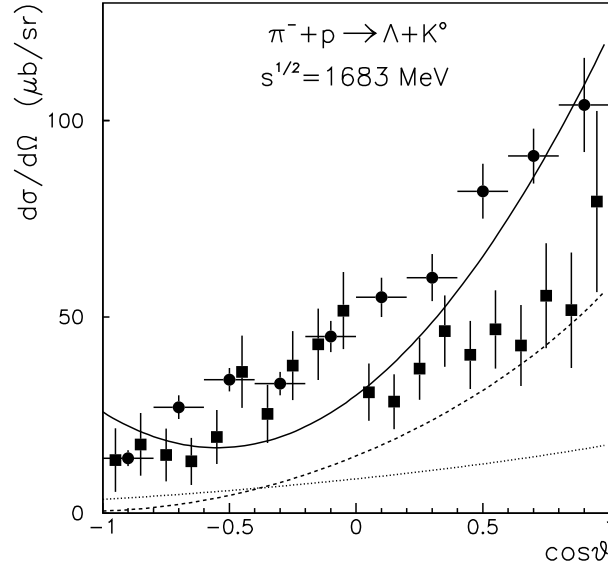


Figure 59: The  $\pi^- + p \rightarrow \Lambda + K^0$  differential cross section at invariant collision energy  $\sqrt{s}=1683$  MeV as a function of the  $\cos \theta$  of the kaon emission angle in the center of mass system. The experimental data are from Ref. [288] (the squares) and from Ref. [289] (the circles). The lines show our calculations in free space (solid) and in nuclear matter at baryon densities  $\rho_B=\rho_0$  (dashed) and  $\rho_B=2\rho_0$  (dotted), with  $\rho_0 = 0.15 \text{ fm}^{-3}$  (from Ref. [283]).

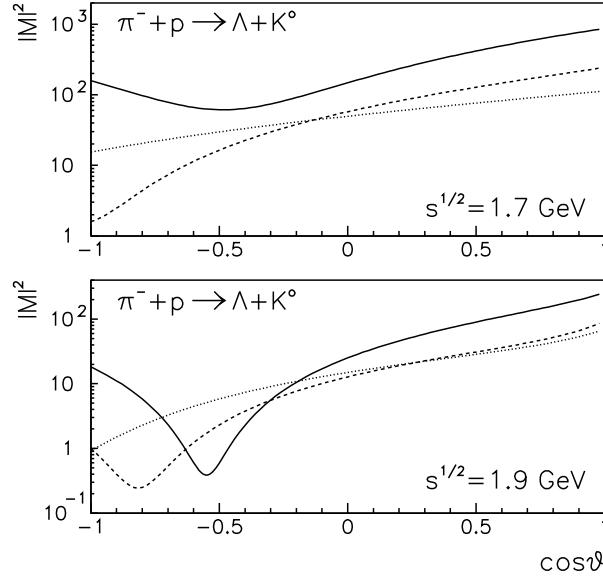


Figure 60: The (dimensionless) invariant amplitude squared for the  $\pi^- + p \rightarrow \Lambda + K^0$  reaction, as a function of the  $\cos\theta$  (the  $K^+$ -meson emission angle in the center of mass system), calculated for the invariant collision energies  $\sqrt{s}=1.7$  GeV (upper) and 1.9 GeV (lower). The lines show the result for free space (solid) and for nuclear matter at baryon densities  $\rho_B=\rho_0$  (dashed) and  $\rho_B=2\rho_0$  (dotted) (from Ref. [283]).



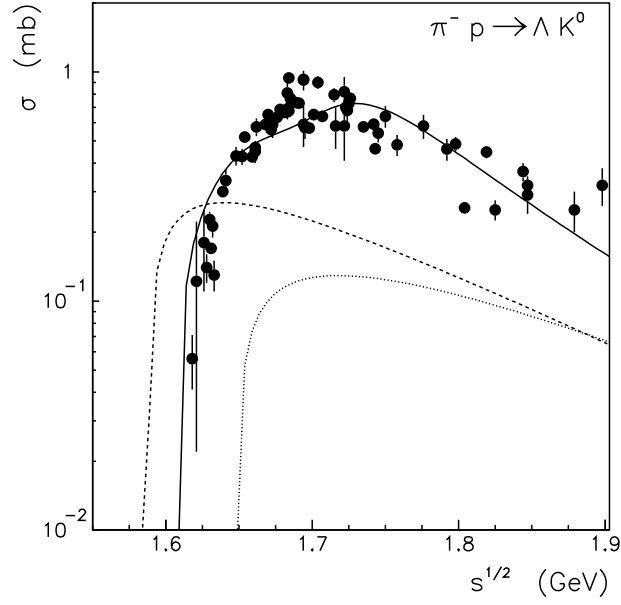


Figure 61: Energy dependence of the total cross section,  $\pi^- + p \rightarrow \Lambda + K^0$ , as a function of the invariant collision energy,  $\sqrt{s}$ , calculated for different baryon densities. The data in free space are taken from Ref. [291]. The lines correspond to the results calculated for free space (solid) and for nuclear matter at baryon densities  $\rho_B = \rho_0$  (dashed) and  $\rho_B = 2\rho_0$  (dotted). (Only the solid curve should be compared directly with the data.) (Taken from Ref. [283].)

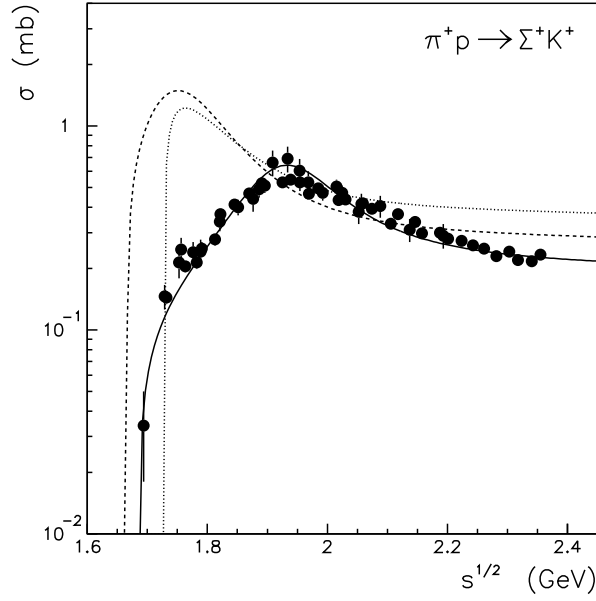


Figure 62: Energy dependence of the total cross section,  $\pi^+ + p \rightarrow \Sigma^+ + K^+$ , as a function of the invariant collision energy,  $\sqrt{s}$ , calculated for different baryon densities. The data in free space are taken from Ref. [291]. The lines indicate calculations for free space (solid) and for nuclear matter at baryon densities  $\rho_B = \rho_0$  (dashed) and  $\rho_B = 2\rho_0$  (dotted). (Taken from Ref. [283].)

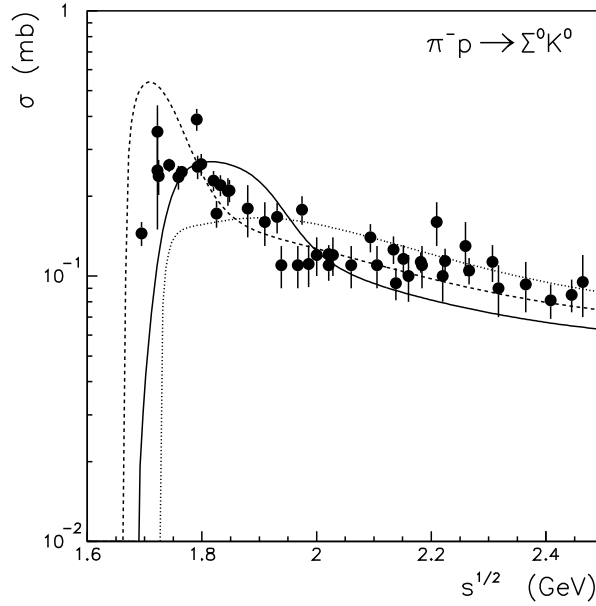


Figure 63: Energy dependence of the total cross section,  $\pi^- + p \rightarrow \Sigma^0 + K^0$ , as a function of the invariant collision energy,  $\sqrt{s}$ , calculated for different baryon densities. The data in free space are taken from Ref. [291]. The lines indicate the calculations for free space (solid) and for nuclear matter at baryon densities  $\rho_B = \rho_0$  (dashed) and  $\rho_B = 2\rho_0$  (dotted) (from Ref. [283]).

In Fig. 62 we show the energy dependence of the total cross section,  $\pi^+ + p \rightarrow \Sigma^+ + K^+$ , as a function of the invariant collision energy,  $\sqrt{s}$ . The experimental data in free space are taken from Ref. [291]. The free space data are well reproduced by the calculations in free space, as shown in Fig. 62 by the solid line. The dashed line indicates the results obtained for nuclear matter at baryon density  $\rho_B = \rho_0$ , while the dotted line shows the result at  $\rho_B = 2\rho_0$ .

Again, as already discussed previously, the density dependence of the hadron masses and the vector potentials leads to a shift of the reaction thresholds in nuclear matter. Because of the density dependence of the  $\Sigma$ -hyperon potential, the threshold at normal nuclear matter density ( $\rho_B = \rho_0$ ) is shifted downward compared with that in free space. At  $\rho_B = 2\rho_0$  the  $\Sigma K$  reaction threshold is shifted upward relative to the threshold in free space. Moreover, the magnitude of the  $\pi^+ + p \rightarrow \Sigma^+ + K^+$  cross section depends much more strongly on the density than the  $\pi^- + p \rightarrow \Lambda + K^0$  reaction.

Figs. 63 and 64 show the energy dependence of the total cross sections for the  $\pi^- + p \rightarrow \Sigma^0 + K^0$  and  $\pi^- + p \rightarrow \Sigma^- + K^+$  reactions, respectively. The data in free space [291] are well reproduced with the calculations in free space, which are indicated by the solid lines. The cross sections calculated for nuclear matter, except for  $\pi^- + p \rightarrow \Sigma^0 + K^0$  at  $\rho_B = 2\rho_0$ , are substantially enhanced in comparison with those in free space, at energies just above the in-medium reaction thresholds.

It is expected that in relativistic heavy ion collisions at SIS energies nuclear matter can be compressed up to baryonic densities of order  $\rho_B \simeq 3\rho_0$  [276]. The baryon density  $\rho_B$  available in heavy ion collisions evolves with the interaction time,  $t$ , and is given by the dynamics of the heavy ion collision. Moreover, the density is large in the very center of the collision. In the following estimates we investigate the density dependence of the production cross section for central central heavy ion collisions. However, it should be remembered that at the edges, where most particles are expected to be located, the density dependence of the strangeness production mechanism is not strong compared to that of the central zone of the collision. To calculate the  $K^+$ -meson production cross section averaged over the available density distribution we adopt the density profile function obtained in dynamical simulations [292] of  $Au+Au$  collisions at 2 AGeV and at impact parameter  $b=0$ . This

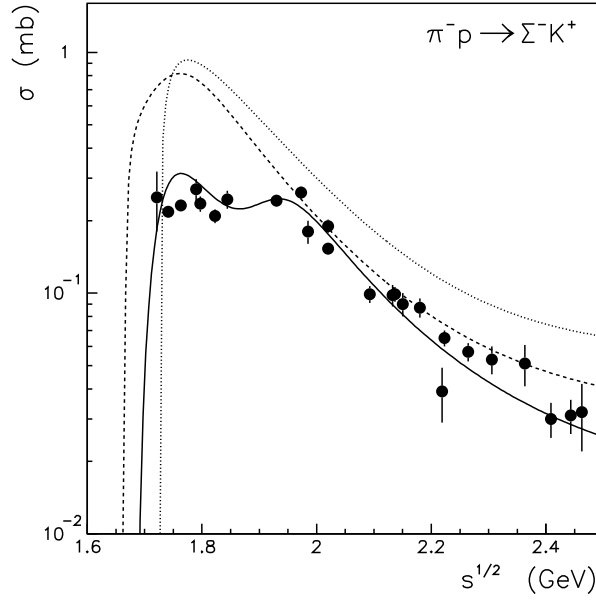


Figure 64: Energy dependence of the total cross section,  $\pi^- + p \rightarrow \Sigma^- + K^+$ , as a function of the invariant collision energy,  $\sqrt{s}$ , calculated for different baryon densities. The data in free space are taken from Ref. [291]. The lines indicate our calculations for free space (solid) and for nuclear matter at baryon densities  $\rho_B = \rho_0$  (dashed) and  $\rho_B = 2\rho_0$  (dotted) (from Ref. [283]).

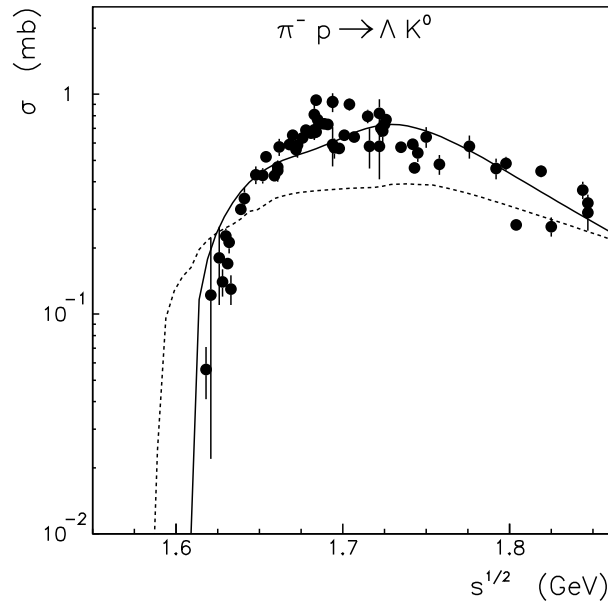


Figure 65: Energy dependence of the total cross section,  $\pi^- + p \rightarrow \Lambda + K^0$ , as a function of the invariant collision energy,  $\sqrt{s}$ . The data in free space are taken from Ref. [291]. The solid line indicates our calculation for free space. The dashed line shows the cross section calculated by averaging over the density function profile [292] given by the time evolution obtained for  $Au+Au$  collisions at 2 AGeV (see Eq. (331)) (from Ref. [283]).

can be parametrized as

$$\rho_B(t) = \rho_{max} \exp\left(\frac{[t - \bar{t}]^2}{\Delta t^2}\right), \quad (331)$$

where the parameters,  $\rho_{max}=3\rho_0$ ,  $\bar{t}=13$  fm and  $\Delta t=6.7$  fm, were fitted to the heavy ion calculations [292].

The total cross section for the  $\pi^- + p \rightarrow \Lambda + K^0$  reaction integrated over the time range  $5 \leq t \leq 23$  fm and weighted by the time dependent density profile given in Eq. (331), is shown by the dashed line in Fig. 65. The limits of the  $t$  integration were taken from the simulations of the  $Au+Au$  collision time evolution in Ref. [292]. The circles and solid line in Fig. 65 show the experimental data in free space [291] and the calculations in free space, respectively.

One can see that the total cross section averaged over the collision time (time dependent density profile) for the  $\pi^- + p \rightarrow \Lambda + K^0$  reaction is quite close to the result given in free space integrated up to energies above the production threshold, (i.e.,  $\sqrt{s} \simeq 1.7$  GeV). That the results shown in Fig. 65 actually explain why the heavy ion calculations with the free space kaon production cross section might quite reasonably reproduce the experimental data, will be discussed more quantitatively below.

As a matter of fact, the total cross section averaged over the time dependent density profile, shown by the dashed line in Fig. 65, should additionally be averaged over the invariant collision energy distribution available in heavy ion reactions. The number of meson-baryon collisions,  $N_{mB}$ , for the central  $Au+Au$  collisions at 2 AGeV is given in Ref. [293] as a function of the invariant collision energy,  $\sqrt{s}$ . It can be parametrized for  $\sqrt{s} > 1$  GeV as

$$\frac{dN_{mB}}{d\sqrt{s}} = N_0 \exp\left(\frac{[\sqrt{s} - \sqrt{s_0}]^2}{[\Delta\sqrt{s}]^2}\right), \quad (332)$$

where the normalization factor  $N_0=6 \times 10^4$  GeV $^{-1}$ , while  $\sqrt{s_0}=1$  GeV and  $\Delta\sqrt{s}=0.63$  GeV. Note that, at SIS energies  $N_{mB}$  is almost entirely given by the pion-nucleon interactions, and heavy meson and baryon collisions

contribute only to the high energy tail of the distribution in Eq. (332) – with quite small densities [293]. Finally, if we also average the calculated, in-medium, total cross section for  $\pi^- + p \rightarrow \Lambda + K^0$ , shown by the dashed line in Fig. 65, over the available energy distribution given in Eq. (332), we obtain an average total kaon production cross section of  $\langle K \rangle = 65 \mu\text{b}$  for central  $Au+Au$  collisions at 2 AGeV. This result is indeed compatible with the calculations using the free space total cross section of the  $\pi^- + p \rightarrow \Lambda + K^0$  reaction, which provide an average total kaon production cross section of  $\langle K \rangle = 71 \mu\text{b}$  for central  $Au+Au$  collisions at 2 AGeV. Note that the inclusion of even a slight modification of the  $K^+$  mass because of the nuclear medium (without the corresponding changes introduced here) leads to a substantial reduction of the inclusive  $K^+$  spectra (by as much as a factor of 2 or 3), compared to that calculated using the free space properties for the relevant hadrons [269].

We stress that at SIS energies reaction channels with a  $\Sigma$ -hyperon in the final state play a minor role, because of the upper limit of the energy available in the collisions. As was illustrated by Fig. 58, the downwardly shifted  $\pi + N \rightarrow \Sigma + K$  reaction threshold at small densities is still quite high compared to that for the reaction with a  $\Lambda$ -hyperon in the final state.

In summary, we averaged the kaon production cross section over the baryon density profile, which depends on the evolution time of the heavy ion collision, in order to evaluate the impact of our microscopic calculations on the heavy ion results. Furthermore, in order to compare with the experimental data more quantitatively, we calculated the effective total kaon production cross section by averaging over the invariant collision energy distributions available in heavy ion reactions. We found that at low collision energies, the density or time averaged  $K^+$ -meson production total cross section, calculated using the in-medium properties for the  $K^+$  meson, hyperons and relevant hadrons, is very close to that calculated using the total cross section given in free space.

Thus, the present results provide an explanation of why the analyses [268, 270, 276, 277] of available data on  $K^+$  production from heavy ion collisions at SIS energies [273, 274, 275, 276] for the  $K^+$  spectra, were able to be reasonably described when one neglected any in-medium modification of the kaon and hadronic properties – i.e., adopting the  $K^+$ -meson production cross section given in free space.

The conclusion of this section is that, if one accounts for the in-medium modification of the production amplitude (i.e., the in-medium properties of the  $K^+$ -meson and hadrons) correctly, it is possible to understand  $K^+$  production data in heavy ion collisions at SIS energies consistently as it should be, even if the  $K^+$ -meson feels the theoretically expected, repulsive mean field potential. Thus, it is very important to understand the  $K^+$  production data microscopically based on the in-medium dynamics, by including the in-medium changes of the  $K^+$ -meson and hadron properties in the reaction amplitudes. To include the in-medium properties of hadrons only in the purely kinematic effects, is not enough for the better understanding of the subthreshold kaon production in heavy ion collisions.

## 5.2 $D$ and $\bar{D}$ meson production in nuclei

Antiproton annihilation on nuclei provides new possibilities for studying open charm production, exploring the properties of charmed particles in nuclear matter and measuring the interaction of charmed hadrons.

Hatsuda and Kunihiro [56] proposed that the light quark condensates may be substantially reduced in hot and dense matter and that as a result hadron masses would be modified. At low density the ratio of the hadron mass in medium to that in vacuum can be directly linked to the ratio of the quark condensates [53, 178, 294, 295, 296]. Even if the change in the ratio of the quark condensates is small, the absolute difference between the in-medium and vacuum masses of the hadron is expected to be larger for the heavy hadrons. In practice, any detection of the modification of the mass of a hadron in matter deals with the measurement of effect associated with this absolute difference.

It was found in Refs. [120, 121, 123] that the in medium change of quark condensates is smaller for heavier quarks,  $s$  and  $c$ , than those for the light quarks,  $u$  and  $d$ . Thus the in-medium modification of the properties of heavy hadrons may be regarded as being controlled mainly by the light quark condensates. As a consequence we expect that charmed mesons, which consist of a light quark and heavy  $c$  quark, should serve as suitable probes of the in-medium modification of hadron properties.

As for the  $\bar{K}$  and  $K$ -mesons, with their quark contents  $\bar{q}s$  and  $q\bar{s}$  ( $q=u, d$  light quarks), respectively,

the  $D$  ( $\bar{q}c$ ) and  $\bar{D}$  ( $q\bar{c}$ ) mesons will satisfy different dispersion relations in nuclear matter because of the different sign of the  $q$  and  $\bar{q}$  vector coupling. Some experimental confirmation of this effect has come from measurements [266, 267, 270, 271, 273, 274, 297, 298, 299] of  $K^-$  and  $K^+$ -meson production from heavy ion collisions. The  $D^+$  and  $D^-$  production from  $\bar{p}A$  annihilation might yield an even cleaner signal for the in-medium modification of the  $D$  and  $\bar{D}$  properties.

Because of charm conservation,  $D$  and  $\bar{D}$  mesons are produced pairwise and can be detected by their semileptonic decay channels. The threshold for the  $\bar{p}N \rightarrow D\bar{D}$  reaction in vacuum opens at an antiproton energy around 5.57 GeV, but it is lowered in the  $\bar{p}A$  annihilation by the in-medium modification of the  $D$  and  $\bar{D}$  masses, as well as by Fermi motion.

The interaction of the  $D$ -mesons with nuclear matter is of special interest [300]. Note that the  $DN$  interaction should be very different from that of charmonia ( $J/\Psi N$ ), since the interaction between the nucleons and the heavy mesons which do not contain  $u$  and  $d$  quarks is expected to proceed predominantly through gluon exchange. On the other hand, as for  $\bar{K}$ -mesons, the  $D$ -mesons might be strongly absorbed in matter because of the charm exchange reaction  $DN \rightarrow \Lambda_c \pi$ , while the  $\bar{D}$ -mesons should not be absorbed. As will be shown later, the specific conditions of the  $D\bar{D}$  pair production in  $\bar{p}A$  annihilation provide a very clean and almost model independent opportunity for the experimental reconstruction of the charm-exchange mechanism.

As before, we calculate effective masses,  $m_D^*(r)$ , and mean field potentials,  $V_{\sigma,\omega,\rho}^q(r)$ , at position  $\vec{r}$  ( $r = |\vec{r}|$ ) in the nucleus. The scalar and vector potentials (neglecting the Coulomb force) felt by the  $D$  and  $\bar{D}$  mesons, which depend only on the distance from the center of the nucleus,  $r$ , are given by [301](see Eqs. (219) and (220)):

$$V_s^{D^\pm}(r) \equiv U_s(r) = m_D^*(r) - m_D, \quad (333)$$

$$V_v^{D^\pm}(r) = \mp(\tilde{V}_\omega^q(r) - \frac{1}{2}V_\rho^q(r)), \quad (334)$$

The  $\rho$ -meson mean field potential,  $V_\rho^q(r)$ , (and the Coulomb potential) which are small and expected to give a minor effect, will be neglected below. Note that  $\tilde{V}_\omega^q = 1.4^2 V_\omega^q$ , and also  $V_\rho^q$  is negative in a nucleus with a neutron excess.

For the following calculations we define the total potential as

$$U^{D^\pm}(r) = V_s(r) + V_v^{D^\pm}(r), \quad (335)$$

where  $V_s$  and  $V_v$  denote the scalar and vector potentials, respectively.

In Fig. 66 we show the total potentials for the  $D^-$  and  $D^+$ -mesons as a function of the nuclear radius calculated for  $^{12}C$  and  $^{197}Au$ . The in-medium dispersion relation, for the total energy  $E_{D^\pm}$  and the momentum  $p = |\vec{p}|$  of the  $D^\pm$ -meson is given by

$$E_{D^\pm}(r) = \sqrt{p^2 + (m_D + V_s(r))^2} + V_v^{D^\pm}(r), \quad (336)$$

where the bare  $D \equiv D^\pm$ -meson mass is  $m_D = 1.8693$  GeV [133, 134, 135]. Note that the total  $D^-$ -meson potential is repulsive, while the  $D^+$  potential is attractive, which is analogous to the case for the  $K^+$  and  $K^-$  mesons, respectively [130].

The amount of downward shift of the  $\bar{p}N \rightarrow D^+D^-$  reaction threshold in nuclei, associated with the in-medium modification of the  $D$  and  $\bar{D}$  scalar potentials and the vector potentials, is simply  $2V_s$ , and is shown in Fig. 66c) for  $^{12}C$  and  $^{197}Au$  as a function of the nuclear radius. The threshold reduction is quite large in the central region of these nuclei and should be detected as an enhanced production of the  $D^+D^-$  pairs. Note that a similar situation holds for the  $K^+$  and  $K^-$  production and, indeed, enhanced  $K^-$ -meson production in heavy ion collisions, associated with the reduction of the production threshold, has been partially confirmed experimentally [266, 267, 270, 271, 273, 274, 297, 298, 299].

The  $D\bar{D}$  production in antiproton-nucleus annihilation was calculated using the cascade model [302] adopted for  $\bar{p}A$  simulations. The detailed description of the initialization procedure as well as the interaction algorithm are given in Ref. [302]. The reaction zone was initialized with the use of the momentum dependent  $\bar{p}N$  total cross section, given as [303]:

$$\sigma_{\bar{p}N} = 38.4 + 77.6p^{-0.64} + 0.26(\ln p)^2 - 1.2 \ln p, \quad (337)$$

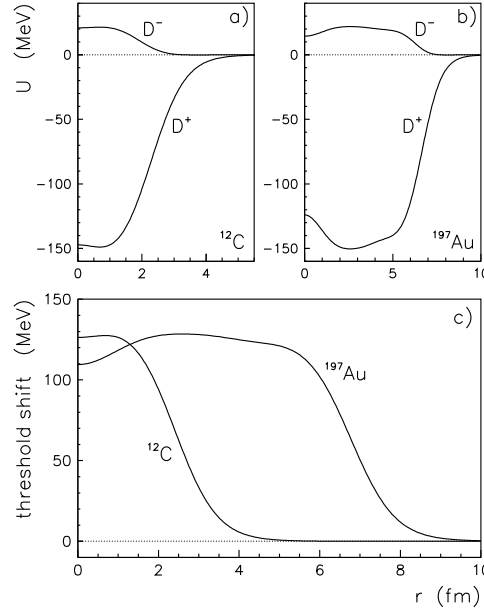


Figure 66: The  $D^-$  and  $D^+$  potentials calculated for  $^{12}\text{C}$  (a) and  $^{197}\text{Au}$  (b) as a function of the nuclear radius. We also show the downward shift in the threshold for  $D^+D^-$  production for  $^{12}\text{C}$  and  $^{197}\text{Au}$ , in (c) (from Ref. [301]).

where  $p$  denotes the antiproton laboratory momentum and the cross section was taken to be the same for the proton and the neutron target (in good agreement with the data [303]).

The  $\bar{p}N \rightarrow D\bar{D}$  cross section was calculated with quark-gluon string model proposed in Ref. [304]. In the following we will concentrate on the production of  $D^+$  and  $D^-$ -mesons and thus take into account only two possible reactions, namely  $\bar{p}p \rightarrow D^+D^-$  and  $\bar{p}n \rightarrow D^0D^-$ . Note that the relation,

$$4\sigma(\bar{p}p \rightarrow D^+D^-) = \sigma(\bar{p}n \rightarrow D^0D^-) \quad (338)$$

is due to the difference in the number of the quark planar diagrams [304].

Furthermore, to account for the  $D^-$  and  $D^+$ -meson propagation in nuclear matter one needs to introduce the relevant cross sections for elastic and inelastic  $DN$  scattering. Since no data for the  $DN$  interaction are available we use a diagrammatic approach illustrated by Fig. 67a,b). Let us compare the  $D^-N \rightarrow D^-N$  and the  $K^+N \rightarrow K^+N$  reactions in terms of the quark lines. Apart from the difference between the  $c$  and  $s$  quarks, both reactions are very similar and can be understood in terms of rearrangement of the  $u$  or  $d$  quarks. Thus, in the following calculations we assume that  $\sigma_{D^-N \rightarrow D^-N} = \sigma_{K^+N \rightarrow K^+N}$ .

The  $K^+N$  cross section was taken from Ref. [264], which gives a parametrization of the available experimental data. The total  $K^+N$  cross section, averaged over neutron and proton targets, is shown in Fig. 68a) by the dashed line - as a function of the kaon momentum in the laboratory system. Note, that within a wide range of kaon momentum  $\sigma_{K^+N}$  is almost constant and approaches a value of  $\simeq 20$  mb. We adopt the value  $\sigma_{D^-N} = 20$  mb, noting that it is entirely due to the elastic scattering channel.

Now, Fig. 67c,d) shows both the  $K^-N \rightarrow \Lambda_c\pi$  and  $D^+N \rightarrow \Lambda_c\pi$  processes, which are again quite similar in terms of the rearrangement of the  $s$  and  $c$  quarks, respectively. Thus we assume that  $\sigma_{D^+N \rightarrow \Lambda_c\pi} \simeq \sigma_{K^-N \rightarrow \Lambda_c\pi}$ .

The total  $K^-N$  cross section is shown by the solid line in Fig. 68. Again it is averaged over proton and the neutron and taken as a parametrization [264] of the experimental data. At low momenta the  $K^-N$  cross section shows resonance structures due to the strange baryonic resonances [134], while at high momenta it approaches a constant value. Apart from the contribution from these intermediate baryonic resonances the



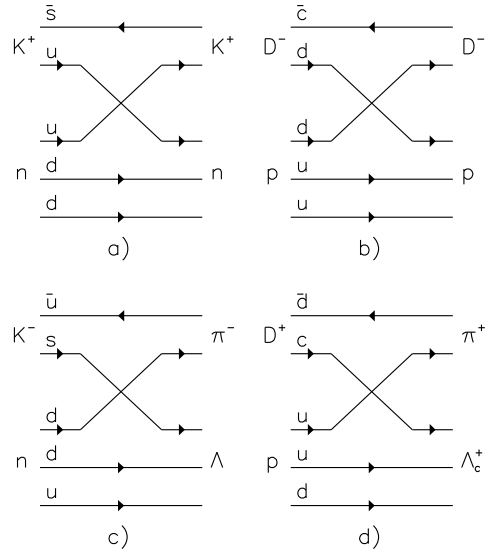


Figure 67: Quark diagrams for  $K^+n \rightarrow K^+n$  (a) and  $D^-p \rightarrow D^-p$  (b) elastic scattering and for  $K^-n \rightarrow \Lambda\pi^-$  (c),  $D^+p \rightarrow \Lambda_c^+\pi^+$  (d) inelastic scattering.

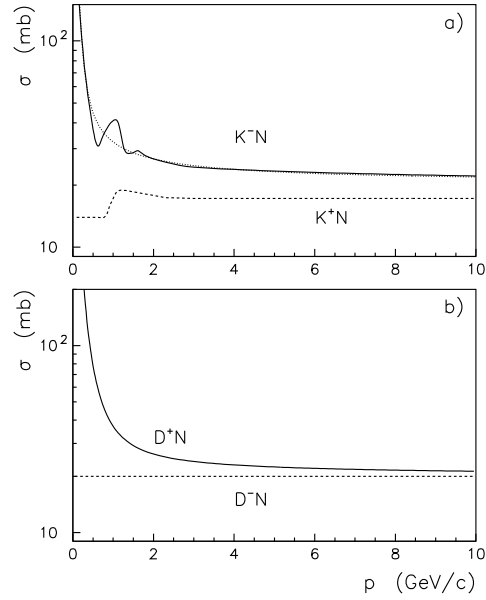


Figure 68: a) The total  $K^-N$  (solid) and  $K^+N$  (dashed line) cross sections obtained [264] as the best fit to the available experimental data [134] and shown as function of the kaon momentum. The dotted line show the result as explained in the text. b) The  $D^-N$  (dashed) and  $D^+N$  total cross sections used in the calculations (from Ref. [301]).

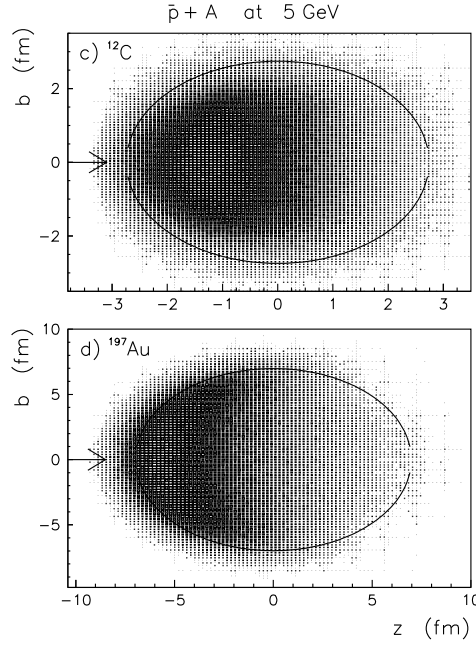


Figure 69: The plot of the annihilation zone for  $\bar{p}+^{12}\text{C}$  (a) and  $\bar{p}+^{197}\text{Au}$  (b) reactions at a beam energy of 5 GeV. The solid line indicates the rms radius of the target nucleus. The arrows show the direction of the antiproton beam (from Ref. [301]).

inelastic  $K^-N \rightarrow \Lambda\pi$  cross section can be written as

$$\sigma_{K^-N \rightarrow \Lambda\pi} = \frac{|M|^2}{16\pi s} \left[ \frac{(s - m_\Lambda^2 - m_\pi^2)^2 - 4m_\Lambda^2 m_\pi^2}{(s - m_K^2 - M_N^2)^2 - 4M_N^2 m_K^2} \right]^{1/2}, \quad (339)$$

where  $s$  is the square of the invariant collision energy and  $m_K$ ,  $M_N$ ,  $m_\Lambda$ ,  $m_\pi$  are the masses of kaon, nucleon,  $\Lambda$ -hyperon and pion, respectively. In Eq. (339) the  $|M|$  denotes the matrix element of the  $K^-N \rightarrow \Lambda\pi$  transition, which was taken as a constant. Now the total  $K^-N$  cross section is given as a sum of the cross section for the inelastic channel Eq. (339) and for the elastic one, where the latter was taken to be 20.5 mb. The dotted line in Fig. 68 shows our result for the total  $K^-N$  cross section obtained with  $|M|=11.64$  GeV·fm, which reproduces the trend of the data reasonably well.

A similar approach was used to construct the  $D^+N$  total cross section. It was assumed that at high momenta the  $D^+N$  elastic cross section equals the  $D^-N$  cross section, while the  $D^+N \rightarrow \Lambda_c^+ \pi$  cross section was calculated from Eq. (339), with appropriate replacements of the particle masses. The final results are shown in Fig. 68 and were adopted for the following calculations. We wish to emphasize that the status of the  $D$ -meson-nucleon interactions is still unknown and itself one of the important goals of the  $\bar{p}A \rightarrow D\bar{D}X$  studies. Our approach is necessary in order to estimate the expected sensitivity of the experimental measurements to the  $DN$  interaction and to study the possibility of evaluating the  $D^+N$  and  $D^-N$  cross sections.

In comparison to low energy antiprotons that annihilate at the periphery of the nucleus, because of the large  $\bar{p}N$  annihilation probability, antiprotons with energies above 3 GeV should penetrate the nuclear interior. They can therefore probe the nuclear medium at normal baryon density  $\rho_0$  and hence yield information about the in-medium properties of the particles. Indeed, as is illustrated by Fig. 66, the  $D$ -meson potential deviates strongly from zero in the interior of the nuclei considered. Figure 69 illustrates the reaction zone for the  $\bar{p}C$  and  $\bar{p}Au$  annihilations at an antiproton beam energy of 5 GeV. The plots are given as a functions of the impact parameter,  $b$ , and the  $z$ -coordinate, assuming that the beam is oriented along the  $z$ -axis, which is shown by arrows in Fig. 69. The annihilation zone is concentrated in the front hemisphere of the target nuclei. Actually

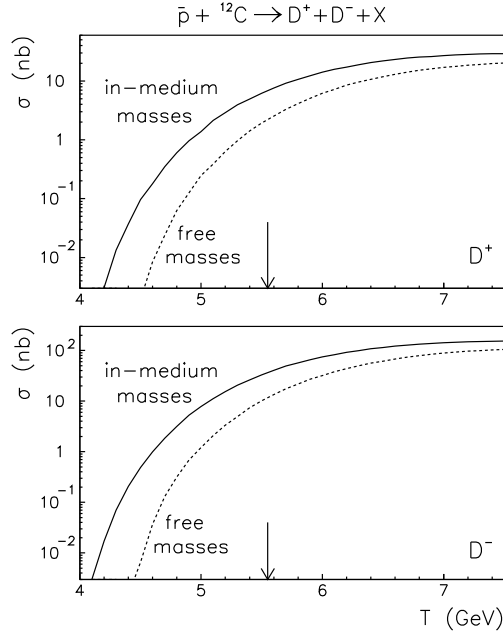


Figure 70: The total cross section for  $D^+$  and  $D^-$ -meson production in  $\bar{p}C$  annihilation as a function of the antiproton energy. The results are shown for calculations with free (dashed lines) and in-medium masses (solid lines) for the  $D$ -mesons. The arrow indicates the reaction threshold on a free nucleon (from Ref. [301]).

the antiprotons penetrate sufficiently deeply to test densities near that of normal nuclear matter and hence the shift in the  $D^+D^-$  production threshold should be manifest.

Now we calculate the total  $\bar{p}A \rightarrow D^+D^-X$  production cross section as function of the antiproton beam energy and show the results in Fig. 70 for a carbon target and in Fig. 71 for gold. The vacuum  $\bar{p}N \rightarrow D^+D^-$  cross section is also shown in Fig. 71. Note that the difference between the  $D^+$  and  $D^-$ -meson production rates is caused by the  $D^+$ -absorption in nuclear matter.

Obviously the production threshold is substantially reduced as compared to the antiproton annihilation on a free nucleon. Apparently, part of this reduction is due to the Fermi motion [305, 306, 307], however the results calculated with in-medium  $D$ -meson masses indicate a much stronger threshold reduction than those using free masses for the final  $D$ -mesons.

Note that, because of their relatively long mean life, the  $D$ -mesons decay outside the nucleus and their in-medium masses cannot be detected through a shift of the invariant mass of the decay products (unlike the leptonic decay of the vector mesons). Thus it seems that the modification of the  $D^+$  and  $D^-$ -meson masses in nuclear matter can best be detected experimentally as for the shift of the in-medium  $K^+$  and  $K^-$ -meson masses, namely as an enhanced  $D$ -meson production rate at energies below the threshold for the  $\bar{p}N \rightarrow D^+D^-$  reaction in free space.

We should further note that experimentally it may be difficult to distinguish whether such an enhancement is due to the modification of the  $D^+$  and  $D^-$ -meson masses in nuclear matter, or to the Fermi motion, or to other processes that are not yet included in our study. In principle, the high momentum component of the nuclear spectral function can provide sufficient energy for particle production far below the reaction threshold in free space [305]. However, the results in Refs. [306, 307] calculated with realistic spectral functions [225, 308, 309] indicate that such effects are actually negligible, while a more important contribution comes from multistep production mechanisms. For instance, the dominant contribution for  $K^+$  production in  $pA$  collisions comes from the secondary  $\pi N \rightarrow YK^+$  process, which prevails over the direct  $pN \rightarrow NYK^+$  reaction [306, 310]. Thus, the interpretation of the data depends substantially on the reliable determination of the production mechanism.

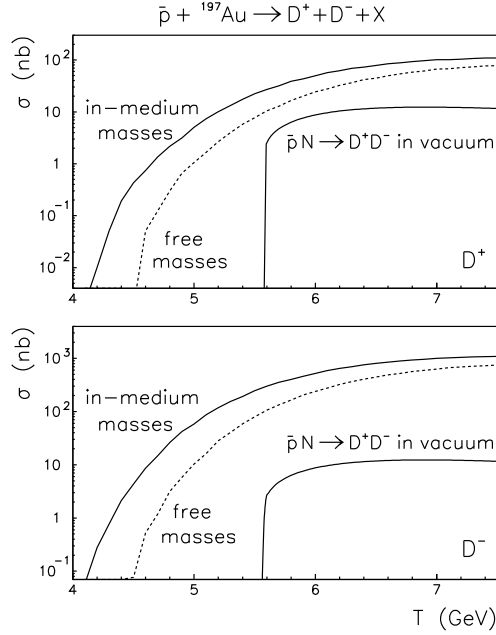


Figure 71: The total cross section for  $D^+$  and  $D^-$ -meson production in  $\bar{p}Au$  annihilation versus the antiproton energy. The results are shown for calculations with free (dashed lines) and in-medium masses (solid lines) for the  $D$ -mesons. For a comparison the  $\bar{p}N \rightarrow D^+ D^-$  cross section in free space is also indicated (from Ref. [301]).

We emphasize that an additional advantage of the  $D^+ D^-$  production in  $\bar{p}A$  annihilation is the possibility to reconstruct the production mechanism directly. Let us denote  $M_X$  as the missing mass of the target nucleon in the  $\bar{p}N \rightarrow D^+ D^-$  reaction. Obviously, in vacuum  $M_X$  is equal to the free nucleon mass and can be reconstructed for antiproton energies above the  $D^+ D^-$  production threshold. When analyzing  $M_X$  in  $\bar{p}A$  annihilations one expects the distribution  $d\sigma/dM_X$  to be centered close to the mass of the bound nucleon - below the free nucleon mass. The shape of the distribution  $d\sigma/dM_X$  reflects information of the spectral function of the nucleus [225, 308, 309].

The preceding discussion is based on the hypothesis that the reaction  $\bar{p}N \rightarrow D^+ D^-$  is the dominant mechanism for  $D^+ D^-$  pair production. By measuring both the  $D^+$  and  $D^-$  mesons one can directly check this hypothesis. Let us first neglect the  $D$ -meson interactions in the nuclear environment and analyze the  $M_X$  spectrum for  $\bar{p}C$  annihilation at 5 GeV. Fig. 72(a) shows the missing mass distribution calculated without (hatched histogram) and with the inclusion of the  $D^+$  and  $D^-$ -meson potentials in carbon nucleus  $^{12}C$ . Recall that the results calculated with free masses provide much smaller  $\bar{p}C \rightarrow D^+ D^- X$  production cross sections (see Fig. 70). Thus, for the purpose of the comparison, the result obtained without potentials is renormalized to those with in-medium masses in Fig. 72a). The arrow in Fig. 72a) indicates the density averaged mass of the bound nucleon in the carbon target [43]. Indeed, both histograms are centered around the expected value. However, the results calculated with the potentials shows a substantially wider distribution. This effect can be understood easily in terms of the downward shift of the  $D$ -meson production threshold in  $^{12}C$ .

Fig. 72(b) shows the  $M_X$  distribution calculated with in-medium masses, taking into account both  $D^+$  and  $D^-$ -meson interactions in the nuclear environment. Note that the distribution below  $M_X \simeq 0.75$  GeV results from secondary  $DN$  elastic rescattering and its strength is proportional to the  $DN$  elastic cross section. A deviation of the actual experimental missing mass distribution from those shown in Fig. 72(b) may directly imply a contribution from  $D^+ D^-$  reaction mechanisms, other than direct production.

In principle, the missing mass  $M_X$  reconstruction appears to be a very promising tool for the detection of the in-medium mass modification of the  $D^\pm$  mesons, although it requires a detailed knowledge of the nuclear

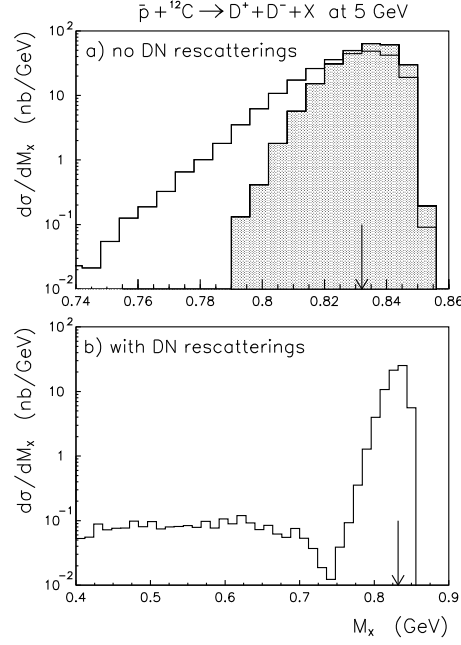


Figure 72: The missing mass distribution calculated for  $\bar{p}C$  annihilation at 5 GeV. The upper part shows the results obtained without (hatched histogram) and with account of the in-medium potentials (open histogram), but neglecting the  $D$ -meson interactions in the nucleus. The hatched histogram is normalized to the open histogram. The lower part shows the calculations with  $D^+$  and  $D^-$  potentials and with  $DN$  interactions (from Ref. [301]).

spectral function [225, 308, 309] as well as an accurate calculation of the  $M_X$  distribution.

In summarizing this section, we have shown that  $\bar{p}A$  annihilation at energies below the  $\bar{p}N \rightarrow D^+ D^-$  reaction threshold in free space offer reasonable conditions for detecting the changes in  $D$ -meson properties in nuclear environment. In-medium modification of the  $D$ -meson mass can be observed as an enhanced  $D^+ D^-$  production at antiproton energies below  $\simeq 5.5$  GeV. The advantage of the  $\bar{p}A \rightarrow D^+ D^- X$  reaction is the possibility to reconstruct directly the primary production mechanism and hence to avoid a misinterpretation that such an enhancement is due to the contribution from multistep production processes. The missing mass reconstruction allows one to separate the effect due to the high momentum component of the nuclear spectral function. Thus, the study of the in-medium modification of the  $D$ -meson mass is very promising, even with a target as light as carbon, where the total  $D^+ D^-$  mass reduction is sizable and the nuclear spectral function is under control [225, 308, 309]. Furthermore, we have shown that the  $\bar{p}A$  annihilation provides favorable conditions for studying the  $D$ -meson interaction in nucleus. The difference in the  $D^+$  and  $D^-$ -meson momentum spectra from antiproton annihilation on heavy nuclei provides a very clean signature for the charm exchange reaction  $D^+ N \rightarrow \Lambda_c^+ \pi$ , and thus can be used to determine the  $DN$  rescattering and absorption cross sections.

### 5.3 $J/\Psi$ suppression

There is a great deal of interest in possible signals of Quark-Gluon Plasma (QGP) formation (or precursors to its formation), and  $J/\Psi$  suppression has been considered to be one of the most promising candidates. Indeed, an anomalous result has been reported there [46, 311, 312]. On the other hand, there may be other mechanisms which produce an increase in  $J/\Psi$  absorption in a hot, dense medium. (For recent reviews on QGP, see e.g., Refs. [313, 314].) We are particularly interested in the rather exciting suggestion, based on the QMC model [10, 13], that the charmed mesons,  $D$ ,  $\bar{D}$ ,  $D^*$  and  $\bar{D}^*$ , should suffer substantial changes in their properties in a nuclear medium [131]. (See sections 3.3.1, 3.4 and 5.2.) This might be expected to have a considerable impact on charm production in heavy ion collisions.

In Ref. [131] it was found, for example, that at a density  $\rho_B = 3\rho_0$  ( $\rho_0 = 0.15 \text{ fm}^{-3}$ ) the  $D$ -meson would feel an attractive scalar potential of about 120 MeV and an attractive vector potential of about 250 MeV. (See sections 3.4 and 5.2.) These potentials are comparable to those felt by a  $K^-$ -meson [130, 263, 264, 315], while the total potential felt by the  $D$  is much larger than that for the vector mesons,  $\rho$ ,  $\omega$  and  $\phi$  [19, 53, 165]. Within QMC it is expected that the mass of the  $J/\Psi$  should only be changed by a tiny amount in nuclear matter [19, 53, 130, 165]. A similar result has also been obtained using QCD sum rules [120, 121].

In the light of these results, it seems that the charmed mesons, together with the  $K^-$ , are probably the best candidates to provide us information on the partial restoration of chiral symmetry. Both open charm production and the dissociation of charmonia in matter may therefore be used as new ways of detecting the modification of particle properties in a nuclear medium.

The suppression of  $J/\Psi$  production observed in relativistic heavy ion collisions, from  $p+A$  up to central  $S+U$  collisions, has been well understood in terms of charmonium absorption in the nuclear medium. However, recent data from  $Pb+Pb$  collisions show a considerably stronger  $J/\Psi$  suppression [311]. In an attempt to explain this “anomalous” suppression of  $J/\Psi$  production, many authors have studied one of two possible mechanisms, namely hadronic processes [316, 317, 318, 319, 320] and QGP formation [321] (see Ref. [46] for a review).

In the hadronic dissociation scenario [316] it is well known that the  $J/\Psi$  interacts with pions and  $\rho$ -mesons in matter, forming charmed mesons through the reactions,  $\pi + J/\Psi \rightarrow D^* + \bar{D}$ ,  $\bar{D}^* + D$  and  $\rho + J/\Psi \rightarrow D + \bar{D}$ . The absorption of  $J/\Psi$  mesons on pions and  $\rho$ -mesons has been found to be important (see Refs. [270, 317, 322] and references therein) in general and absolutely necessary in order to fit the data on  $J/\Psi$  production. Furthermore, the absorption on comovers should certainly play a more important role in  $S + U$  and  $Pb + Pb$  experiments, where hot, high density mesonic matter is expected to be achieved. However, recent calculations for the processes in free space [319], indicate a much lower cross sections than that necessary to explain the data for  $J/\Psi$  suppression.

$J/\Psi$  dissociation on comovers, combined with the absorption on nucleons, is the main mechanism proposed as an alternative to that of Matsui and Satz [321] – namely the dissociation of the  $J/\Psi$  in a QGP. Note that both the hadronic and QGP scenarios predict  $J/\Psi$  suppression but no mechanism has yet been found to separate them experimentally. Within the hadronic scenario the crucial point is the required dissociation strength. In

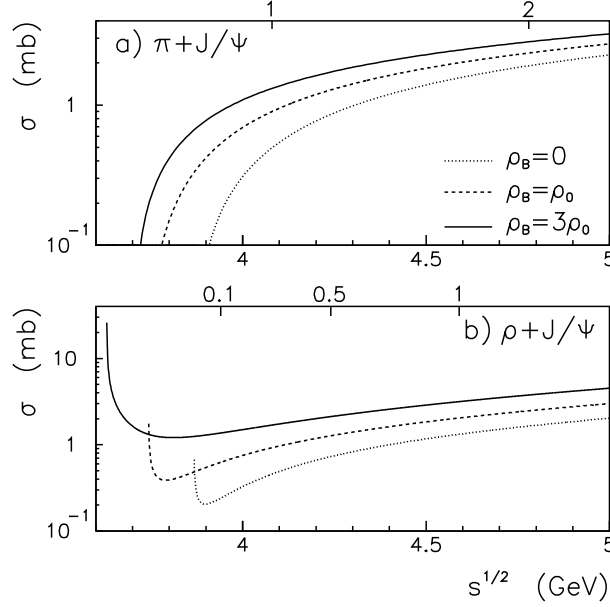


Figure 73:  $\pi+J/\Psi$  (a) and  $\rho+J/\Psi$  (b) dissociation cross sections as functions of the invariant collision energy,  $s^{1/2}$ . Results are shown for vacuum (the dotted line),  $\rho_0$  (the dashed line) and  $3\rho_0$  (the solid line) (from Ref. [47]).

particular, one needs a total cross section for the  $\pi, \rho+J/\Psi$  interaction of around  $1.5 \div 3$  mb in order to explain the data in heavy ion simulations [270]. Recent calculations [319] of the reactions  $\pi+J/\Psi \rightarrow D + \bar{D}^*, \bar{D} + D^*$  and  $\rho+J/\Psi \rightarrow D + \bar{D}$ , based on  $D$  exchange, indicate a much lower cross section than this.

The main uncertainty in the discussion of the  $J/\Psi$  dissociation on a meson gas is given by the estimates of the  $\pi, \rho+J/\Psi$  cross section [319]. The predictions available for the  $\pi+J/\Psi$  cross section are given in Refs. [318, 319]. Following the meson exchange model of Ref. [319], we show by the dotted line in Fig. 73 the  $\pi+J/\Psi$  (a) and  $\rho+J/\Psi$  (b) dissociation cross sections calculated in free space. Moreover, the upper axis of Fig. 73(a) indicates the  $\pi$ -meson kinetic energy,  $T_\pi$ , given in the  $J/\Psi$  rest frame, which indicates that the pions should be sufficiently hot to be above the  $DD^*$  production threshold and to dissociate the  $J/\Psi$ -meson. By taking a thermal pion gas with average  $T_\pi \simeq 150$  MeV, one might conclude that independent of the  $\pi+J/\Psi$  dissociation model used [318, 319], the rate of this process is small. However, this situation changes drastically when the in-medium potentials of the charmed mesons are taken into account, because they lower the  $\pi+J/\Psi \rightarrow \bar{D} + D^*$  threshold as will be shown later. The upper axis of Fig. 73(b) shows the  $\rho$ -meson kinetic energy  $T_\rho$  in the  $J/\Psi$  rest frame. As was discussed in Refs. [46, 270, 319], the  $J/\Psi$  dissociation might proceed on thermal  $\rho$ -mesons, because of the low  $\rho+J/\Psi \rightarrow \bar{D} + D^*$  reaction threshold.

As far as the meson properties in free space are concerned, the Bethe-Salpeter (BS) and Dyson-Schwinger (DS) approaches have been widely used [323]. The application of BS approach to the description of heavy-light quark systems allows one to describe the  $D$  and  $B$  meson properties in free space quite well [324]. The DS approach at finite baryon density was used [325] for the calculation of the in-medium properties of  $\rho$ ,  $\omega$  and  $\phi$  mesons. The modification of the  $\rho$  and  $\omega$  meson masses resulting from the DS equation is close to the calculations with the QMC model [10, 13, 19, 53, 165], while the  $\phi$ -meson mass reduction from Ref. [325] is larger than the QMC result. (See section 3.3.1.)

Based on the QMC model, the scalar and vector potentials felt by the  $D(D^+, D^0)$  and  $\bar{D}(D^-, \bar{D}^0)$  mesons in symmetric nuclear matter are given by [131]:

$$V_s^{D^\pm} \equiv U_s = m_D^* - m_D, \quad (340)$$

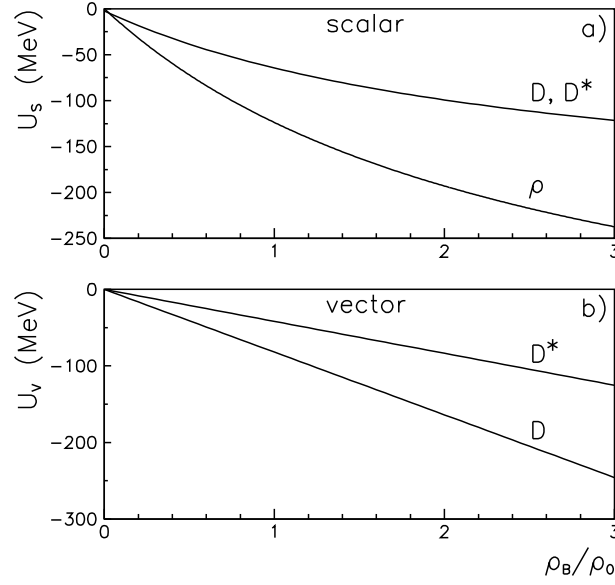


Figure 74: The scalar (a) and vector (b) potentials for the  $D$ ,  $D^*$  and  $\rho$  mesons, calculated for nuclear matter as functions of the baryon density, in units of the saturation density of nuclear matter,  $\rho_0=0.15 \text{ fm}^{-3}$ . Scalar potentials for  $D$  and  $D^*$  are indistinguishable (from Ref. [47]).

$$V_v^{D^\pm} \equiv \pm U_v = \mp(\tilde{V}_\omega^q - \frac{1}{2}V_\rho^q), \quad (341)$$

where,  $\tilde{V}_\omega^q = 1.4^2 V_\omega^q$ , which is assumed to be the same as that for the  $K^+$  and  $K^-$  mesons [130]. (See Eq. (220).) The isovector meson mean field potential,  $V_\rho^q$ , is zero in symmetric nuclear matter.

We show the  $D$ ,  $D^*$  and  $\rho$ -meson potentials used in further calculations in Fig. 74 as a function of the baryon density, in units of  $\rho_0=0.15 \text{ fm}^{-3}$ . Note that these potentials enter not only in the final state phase space (which becomes larger since the scalar masses are reduced in matter), but also in the reaction amplitude and the initial  $\rho$ -meson mass. (Recall the discussions in section 5.1 for subthreshold kaon production.) Furthermore, as observed earlier, the properties of the  $J/\Psi$  meson are not significantly altered in medium within QMC.

Note that the total  $D^-$ -meson potential is repulsive, while the  $D^+$  potential is attractive, which is analogous to the case for the  $K^+$  and  $K^-$  mesons, respectively [130, 263, 264, 315]. The threshold reduction is quite large when the nuclear density becomes large for the  $D^+D^-$  pairs. Note that a similar situation holds for the  $K^+$  and  $K^-$  production and, indeed, enhanced  $K^-$ -meson production in heavy ion collisions, associated with the reduction of the production threshold, has been partially confirmed experimentally [270, 274].

We first discuss the thermally averaged cross sections,  $\langle\sigma v\rangle$ , for  $\pi+J/\Psi$  and  $\rho+J/\Psi$  dissociation in Figs. 75 and 76, when the free masses are used for the charmed mesons and the in-medium potentials are set to zero. They are shown by the dotted lines. These results are needed for comparison with the calculations including the potentials. Since the pions are almost in thermal equilibrium, their energy spectrum is given by a Bose distribution with temperature,  $T$ , and chemical potential,  $\mu$ , where we have used the value,  $\mu=126 \text{ MeV}$  [326]. The thermally averaged  $\pi+J/\Psi$  cross section can be obtained by averaging over the  $\pi$ -spectrum at fixed  $J/\Psi$ -momentum. The dotted line in Fig. 75a) shows  $\langle\sigma v\rangle$  as a function of the pion gas temperature,  $T$ , which was calculated with zero  $J/\Psi$  momentum relative to the pion gas.

The shadowed area in Fig. 75a) indicates the temperature range corresponding to the pion densities  $0.2 - 0.8 \text{ fm}^{-3}$ , which are expected to be achieved in the heavy ion collisions presently under consideration. In vacuum the  $\pi+J/\Psi$  dissociation cross section is less than about  $0.3 \text{ mb}$ . The thermally averaged absorption



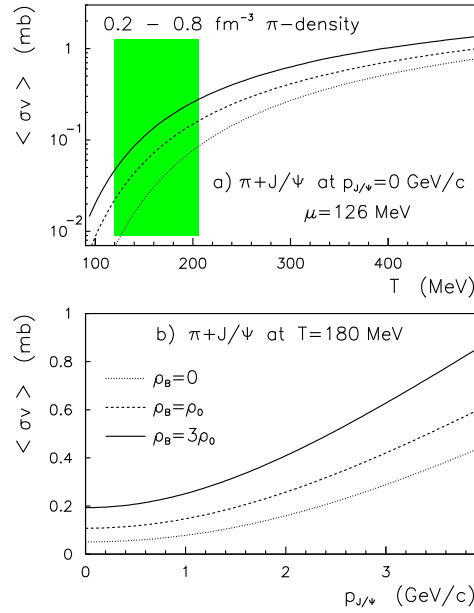


Figure 75: Thermally averaged  $\pi+J/\Psi$  absorption cross section as a function of the pion gas temperature,  $T$ , and chemical potential,  $\mu$ , at  $p_{J/\Psi}=0$  (a) and as a function of the  $J/\Psi$ -momentum at  $T=180$  MeV (b). The results are shown using the same notation as in Fig. 73. The shadowed area indicates the temperatures expected to be achieved in heavy ion collisions (from Ref. [47]).

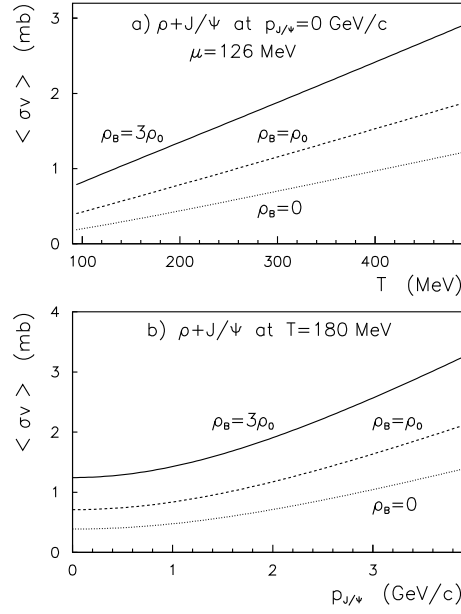


Figure 76: Thermally averaged  $\rho+J/\Psi$  absorption cross section as a function of the  $\rho$ -meson gas temperature  $T$  with  $p_{J/\Psi}=0$  (a) and as a function of the  $J/\Psi$ -momentum at  $T=180$  MeV (b). Notations are similar to Fig. 75 (from Ref. [47]).

cross section for temperature,  $T=180$  MeV, is shown in Fig. 75(b) (the dotted line) as a function of the  $J/\Psi$  momentum. The thermally averaged cross section which we find,  $\langle\sigma v\rangle$ , would be very difficult to detect with the present experimental capabilities.

A similar situation holds for the  $\rho+J/\Psi$  dissociation, as illustrated by the dotted line in Fig. 76. Indeed, the  $J/\Psi$  absorption on comovers seems to be negligible [319] in comparison with that needed to explain the  $J/\Psi$  suppression, provided that we use the vacuum properties of the charmed mesons. On the other hand, this situation changes dramatically when we consider the effect of the vector and scalar potentials felt by the charmed  $D$ ,  $D^*$  mesons and also  $\rho$  mesons (the vector potential is zero), as calculated using Eqs. (333), (334) and (219). The cross sections calculated for  $\pi, \rho+J/\Psi$  collisions with the in-medium potentials are shown in Fig. 73, for densities,  $\rho_0$  (the dashed line) and  $3\rho_0$  (the solid line). The dotted line in Fig. 73 indicates the free space cross sections.

Clearly the  $J/\Psi$  absorption cross sections are substantially enhanced for both the  $\pi+J/\Psi$  and  $\rho+J/\Psi$  reactions, not only because of the downward shift of the reaction threshold, but also because of the in-medium effect on the reaction amplitude. Moreover, now the  $J/\Psi$  absorption on comovers becomes density dependent – a crucial finding given the situation in actual heavy ion collisions. These effects have never been considered before. That is, this was the first calculation of the comover absorption cross section as a function of baryon density.

The thermally averaged, in-medium  $\pi+J/\Psi$  and  $\rho+J/\Psi$  absorption cross sections,  $\langle\sigma v\rangle$ , are shown by the dashed and solid lines in Figs. 75 and 76, respectively. We find that  $\langle\sigma v\rangle$  depends very strongly on the nuclear density. Even for  $p_{J/\Psi}=0$ , with a pion gas temperature of 120 MeV, which is close to the saturation pion density, the thermally averaged  $J/\Psi$  absorption cross section on the pion, at  $\rho_B=3\rho_0$ , is about a factor of 7 larger than that at  $\rho_B=0$  (i.e., with no effect of the in-medium modification – see Fig. 75(a)).

The thermally averaged  $\rho+J/\Psi$  dissociation cross section at  $\rho_B=3\rho_0$  becomes larger than 1 mb. Thus, the  $J/\Psi$  absorption on  $\rho$ -mesons should be appreciable, even though the  $\rho$ -meson density is expected to be small in heavy ion collisions. We note that dynamical calculations [270] suggest that the  $\rho$ -meson density should be around half of the pion density in  $Pb+Pb$  collisions.

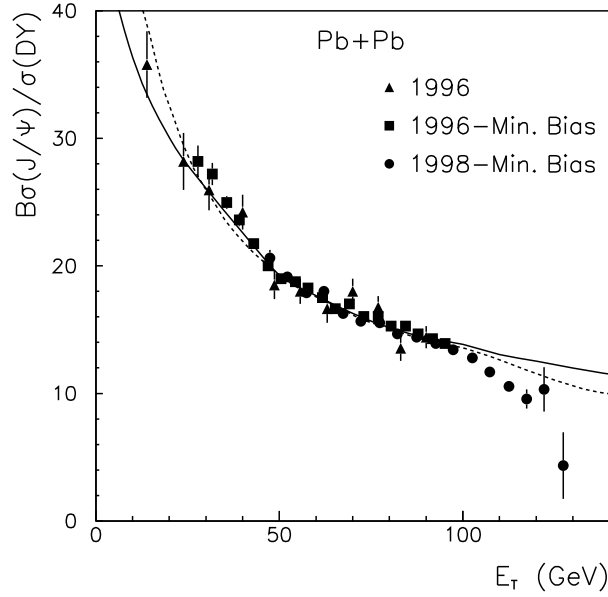


Figure 77: The ratio of the  $J/\Psi$  over Drell-Yan cross sections from  $Pb+Pb$  collisions as function of the transverse energy  $E_T$ . Data are from Ref. [311, 312]. The solid line shows our calculations with the density dependent cross section for  $J/\Psi$  absorption on comovers. The dashed line indicates the calculations with phenomenological cross section  $\langle\sigma v\rangle\simeq 1$  mb [320]. For both calculations the nuclear absorption cross section was taken as 4.5 mb (from Ref. [47]).

In order to compare our results with the NA38/NA50 data [311, 312] on  $J/\Psi$  suppression in  $Pb+Pb$  collisions, we have adopted the heavy ion model proposed in Ref. [317] with the  $E_T$  model from Ref. [320]. We introduce the absorption cross section on comovers as function of the density of comovers, while the nuclear absorption cross section is taken as 4.5 mb [320]. The final results are shown in Fig. 77. The dashed line in Fig. 77 shows the calculations with the phenomenological constant cross section for  $J/\Psi$  absorption on comovers  $\langle\sigma v\rangle\simeq 1$  mb and is identical to the results given in Ref. [320]. The solid line in Fig. 77 shows the calculations with the density dependent cross section  $\langle\sigma v\rangle$  for  $J/\Psi$  absorption on comovers calculated based on the QMC model. Both curves clearly reproduce the data [311] quite well, including most recent results from NA50 on the ratio of  $J/\Psi$  over Drell-Yan cross sections, as a function of the transverse energy up to  $E_T=100$  GeV. It is important to note that if one neglected the in-medium modification of the  $J/\Psi$  absorption cross section the large cross section  $\langle\sigma v\rangle\simeq 1$  mb could not be justified by microscopic theoretical calculations and hence the NA50 data [311, 312] could not be described.

Furthermore, we notice that our calculations with in-medium modified absorption provide a significant improvement in the understanding of the data [311] compared to the models quoted by NA50 [312]. The basic difference between our results and those quoted by NA50 [312] is that in previous heavy ion calculations [46, 270, 317] the cross section for  $J/\Psi$  absorption on comovers was taken as a free parameter to be adjusted to the data [311, 312] and was never motivated theoretically.

To summarize this section, we have studied  $J/\Psi$  dissociation in a gas of  $\pi$  and  $\rho$  mesons taking into account the density dependence of the scalar and vector potentials which the mesons feel in nuclear matter. We have shown a substantial density dependence of the  $J/\Psi$  absorption rate as a result of the changes in the properties of the charmed mesons in-medium. This aspect has never been considered before when analyzing  $J/\Psi$  suppression in heavy ion collisions. Moreover, when we introduce density dependent cross sections on comovers, based on the QMC model, into a heavy ion calculation, the result achieves a very good agreement

with the NA50 data [311, 312] up to transverse energy of about 100 GeV.

## 6 Summary and outlook

We have studied various nuclear phenomena, starting at the quark level, using a self-consistent model for nuclear physics, namely the QMC model. Although there are many kinds of relativistic mean-field theory for nuclear physics, only the QMC model incorporates explicit quark degrees of freedom into nuclear many-body systems. As discussed in section 2.4, at the *hadronic* level, it is certainly possible to cast the QMC model into a form similar to that of a QHD-type mean-field model by re-defining the scalar field. However, at the same time, the QMC model can describe how the internal structure of hadrons changes in a nuclear medium. That is the greatest advantage of the present model and it opens a tremendous number of opportunities for future work.

Since the discovery of QCD as the fundamental theory of the strong interaction, numerous attempts have been made to derive the nuclear force within quark models. The QMC model stands between the traditional meson-exchange picture and the hard core quark models, namely, it is a mean-field model in the sense of QHD but with the couplings of  $\sigma$  and  $\omega$  mesons to confined quarks, rather than to the point-like nucleon. After a considerable amount of work, one finds that the effect of the internal, quark structure of the nucleon is absorbed into the scalar polarizability in the effective nucleon mass in matter. It is the dependence of the scalar polarizability on the scalar field in matter (or it is numerically equivalent to the dependence on nuclear density) that is the heart of the QMC model and leads to the novel, saturation mechanism of the binding energy of nuclear matter as a function of density.

Because the scalar polarizability plays the important role in the QMC model, it is of great interest to study whether the dependence of the scalar polarizability on the scalar field can be extracted from the fundamental theory, i.e., QCD. In Ref. [327], it is shown that the remarkable progress in resolving the problem of chiral extrapolation of lattice QCD data gives one confidence that the pion loop contributions are under control. In the case of the nucleon, one can then use this control to estimate the effect of applying a chiral invariant scalar field to the nucleon, i.e., to estimate the scalar polarizability of the nucleon. The resulting value is in excellent agreement with the range found in the QMC model, which is vital to describe many phenomena in nuclear physics. Thus, in a very real sense, the results presented in Ref. [327] provide a direct connection between the growing power to compute hadron properties from QCD itself and fundamental properties of atomic nuclei. Further work in this direction is very important and will be a focus for our field in the coming years.

It is also of great interest to perform more realistic calculations for nuclear systems. Feldmeier [328] proposed a molecular dynamics approach to solve the many-body problem of interacting identical fermions with spin 1/2 approximately. The interacting system is represented by an antisymmetrized many-body wave function consisting of single-particle states which are localized in phase space. The equations of motion for the parameters characterizing the many-body state (e.g. positions, momenta and spin of the particles) are derived from a quantum variational principle. This is called the fermionic molecular dynamics (FMD) model. Later, based on FMD, a powerful technique to treat a fermionic system was developed by Horiuchi *et al.* [329] and applied not only to nuclear structure but also nuclear reactions. This is sometimes called the antisymmetrized molecular dynamics (AMD). In AMD, basis wave functions of the system are given by Slater determinants where the spatial part of each single-particle wave function is a Gaussian wave packet. The model has a remarkable feature that the wave function can represent various clustering structures as well as shell-model-like structures, although no inert cores and no clusters are assumed. Therefore, it is possible to calculate nuclear systems in a model-independent way. Although the formulation of AMD is non-relativistic, if we choose a proper nuclear force and adopt the non-relativistic version of the QMC model (see section 2.1), it would be possible to construct a more realistic nuclear model which covers a wide range of nuclei from stable to unstable ones. This may be a new challenge and provide a further connection between quark degrees of freedom (QCD) and conventional nuclear physics.

As seen through this article, many nuclear phenomena now seem to indicate that the traditional approach may have its limitations and suggest a need for subnucleonic degrees of freedom. There is no doubt that hadrons consist of quarks, antiquarks and gluons and that they can respond to the environment and change

their characters in matter. We would like to emphasize here that *quarks play an important role in nuclei and nuclear matter*.

### **Acknowledgment**

We would like to thank P.A.M. Guichon, J. Haidenbauer, Hungchong Kim, G. Krein, D.H. Lu, W. Melnitchouk, A. Sibirtsev, and F.M. Steffens for valuable discussions and collaborations. This work was partly supported by Academic Frontier Project (Holcs, Tokyo University of Science, 2005) of MEXT. It was also supported in part by DOE contract DE-AC05-84ER40150, under which SURA operates Jefferson Laboratory.

# References

- [1] G.E. Brown and M. Rho, *Phys. Rev. Lett.* 66 (1991) 2720
- [2] Lattice 2004, *Nucl. Phys. B - Proceedings Supplements* 140 (2005) 3;  
QCD Down Under, *Nucl. Phys. B - Proceedings Supplements* 141 (2005) 1
- [3] R.P. Bickerstaff and A.W. Thomas, *J. Phys. G* 15 (1989) 1523;  
M. Arneodo, *Phys. Rep.* 240 (1994) 301;  
D.F. Geesaman, K. Saito, and A.W. Thomas, *Annu. Rev. Nucl. Part. Sci.* 45 (1995) 337;  
G. Piller and W. Weise, *Phys. Rep.* 330 (2000) 1
- [4] G.A. Miller and J.R. Smith, *Phys. Rev. C* 65 (2002) 015211 (*Phys. Rev. C* 66 (2002) 049903(E));  
J.R. Smith and G.A. Miller, *Phys. Rev. C* 65 (2002) 055206
- [5] J.R. Smith and G.A. Miller, *Phys. Rev. Lett.* 91 (2003) 212301
- [6] S. Strauch (Jefferson Lab E93-049 Collaboration), *Eur. Phys. J. A* 19 (2004) 153;  
S. Strauch *et al.*, *Phys. Rev. Lett.* 91 (2003) 052301
- [7] L.S. Celenza, A. Rosenthal, and C.M. Shakin, *Phys. Rev. Lett.* 53 (1984) 892; *Phys. Rev. C* 31 (1985) 232
- [8] C.W. Wong, *Nucl. Phys. A* 435 (1985) 669
- [9] M. Jandel and G. Peters, *Phys. Rev. D* 30 (1984) 1117
- [10] P.A.M. Guichon, *Phys. Lett. B* 200 (1988) 235
- [11] T. Frederico, B.V. Carlson, R.A. Rego, and M.S. Hussein, *J. Phys. G: Nucl. Part. Phys.* 15 (1989) 297
- [12] S. Fleck, W. Bentz, K. Shimizu, and K. Yazaki, *Nucl. Phys. A* 510 (1990) 731
- [13] K. Saito and A.W. Thomas, *Phys. Lett. B* 327 (1994) 9
- [14] M.K. Banerjee, *Phys. Rev. C* 45 (1992) 1359
- [15] E. Naar and M. Birse, *J. Phys. G: Nucl. Part. Phys.* 19 (1993) 555
- [16] V.K. Mishra, G. Fai, P.C. Tandy, and M.R. Frank, *Phys. Rev. C* 46 (1992) 1143
- [17] B.D. Serot and J.D. Walecka, *Adv. Nucl. Phys.* 16 (1986) 1
- [18] K. Saito and A.W. Thomas, *Phys. Lett. B* 335 (1994) 17
- [19] K. Saito, K. Tsushima, and A.W. Thomas, *Phys. Rev. C* 55 (1997) 2637
- [20] K. Saito and A.W. Thomas, *Phys. Rev. C* 52 (1995) 2789
- [21] A. Manohar and H. Georgi, *Nucl. Phys. B* 234 (1984) 189
- [22] K. Saito, K. Tsushima, and A.W. Thomas, *Phys. Lett. B* 406 (1997) 287
- [23] H. Muller and B.K. Jennings, *Nucl. Phys. A* 640 (1998) 55
- [24] K. Saito, *Prog. Theor. Phys.* 108 (2002) 609
- [25] B.R. Serot and J.D. Walecka, *Int. J. Mod. Phys. E* 6 (1997) 515
- [26] QNP 2002, *Eur. Phys. J. A* 18 (2003) 135
- [27] K. Suzuki *et al.*, *Phys. Rev. Lett.* 92 (2004) 072302
- [28] J. Delorme, M. Ericson, P.A.M. Guichon, and A.W. Thomas, *Phys. Rev. C* 61 (2000) 025202;  
G. Chanfray, M. Ericson, and P.A.M. Guichon, *Phys. Rev. C* 63 (2001) 055202;  
K. Saito, H. Kouno, K. Tsushima, and A.W. Thomas, *nucl-th/0503022*
- [29] P.A.M. Guichon and A.W. Thomas, *Phys. Rev. Lett.* 93 (2004) 132502
- [30] P.A.M. Guichon, K. Saito, E. Rodionov, and A.W. Thomas, *Nucl. Phys. A* 601 (1996) 349
- [31] P.G. Blunden and G.A. Miller, *Phys. Rev. C* 54 (1996) 359
- [32] A. Bodek, H. Budd, and J. Arrington, *hep-ex/0309024*
- [33] F.M. Steffens, K. Tsushima, A.W. Thomas, K. Saito, *Phys. Lett. B* 447 (1999) 233;  
F.M. Steffens, A.W. Thomas, K. Tsushima, *Phys. Lett. B* 595 (2004) 237
- [34] E.D. Bloom and F.J. Gilman, *Phys. Rev. Lett.* 16 (1970) 1140; *Phys. Rev. D* 4 (1971) 2902

- [35] G.A. Miller, B.M.K. Nefkens, and I. Slaus, *Phys. Rep.* 194 (1990) 1;  
G.A. Miller and W.T.H. Van Oers, *Symmetries and Fundamental Interactions in Nuclei* (World Scientific Singapore, 1995)
- [36] P.G. Blunden and M.J. Iqbal, *Phys. Lett. B* 198 (1987) 14;  
T. Suzuki, H. Sagawa, and A. Arima, *Nucl. Phys. A* 536 (1992) 141;  
G. Krein, D.P. Menezes, and M. Nielsen, *Phys. Lett. B* 294 (1992) 7
- [37] H.B. O'Connell, B.C. Pearce, A.W. Thomas, and A.G. Williams, *Phys. Lett. B* 366 (1994) 1;  
G. Krein, A.W. Thomas, and A.G. Williams, *Phys. Lett. B* 317 (1993) 293;  
T. Goldman, J.A. Henderson, and A.W. Thomas, *Few Body Syst.* 12 (1992) 123
- [38] Y. Mori and K. Saito, *Phys. Lett. B* 552 (2003) 21
- [39] K. Tsushima, K. Saito, and A.W. Thomas, *Phys. Lett. B* 465 (1999) 36;  
K. Saito, *Symmetries in Subatomic Physics* (AIP conference proceedings vol.539, 2000)
- [40] J.C. Hardy and I.S. Towner, *nucl-th/0412056*
- [41] K. Saito and A.W. Thomas, *Phys. Lett. B* 363 (1995) 157
- [42] G.M. Huber *et al.* (TAGX Collaboration), *Phys. Rev. C* 68 (2003) 065202;  
G.J. Lolos *et al.* (TAGX Collaboration), *Phys. Rev. Lett.* 80 (1998) 241
- [43] K. Saito, K. Tsushima, and A.W. Thomas, *Phys. Rev. C* 56 (1997) 566
- [44] D. Trnka *et al.*, *Phys. Rev. Lett.* 94 (2005) 192303
- [45] M. Naruki *et al.*, *nucl-ex/0504016*
- [46] R. Vogt, *Phys. Rep.* 310 (1999) 197
- [47] A. Sibirtsev, K. Tsushima, K. Saito, A.W. Thomas, *Phys. Lett. B* 484 (2000) 23
- [48] A. Chodos, R.L. Jaffe, K. Johnson, and C.B. Thorn, *Phys. Rev. D* 10 (1974) 2599
- [49] J.D. Jackson, *Classical Electrodynamics* (Wiley New York, 1967)
- [50] C. Fuchs and H. Lenske, *Phys. Rev. C* 52 (1995) 3043;  
H. Lenske and C. Fuchs, *Phys. Lett. B* 345 (1995) 355
- [51] M.E. Bracco, G. Krein, and M. Nielsen, *Phys. Lett. B* 432 (1998) 258;  
G. Krein, A.W. Thomas, and K. Tsushima, *Nucl. Phys. A* 650 (1999) 313
- [52] K. Saito, K. Tsushima, and A.W. Thomas, *Nucl. Phys. A* 609 (1996) 339
- [53] K. Saito and A.W. Thomas, *Phys. Rev. C* 51 (1995) 2757
- [54] K. Saito, K. Tsushima, and A.W. Thomas, *Mod. Phys. Lett. A* 13 (1998) 769
- [55] V. Bernard and Ulf-G. Meissner, *Nucl. Phys. A* 489 (1988) 647
- [56] T. Hatsuda and T. Kunihiro, *Phys. Rep.* 247 (1994) 221; *Phys. Rev. Lett.* 55 (1985) 158
- [57] K. Saito, T. Maruyama, and K. Soutome, *Phys. Rev. C* 40 (1989) 407;  
K. Soutome, T. Maruyama, and K. Saito, *Nucl. Phys. A* 507 (1990) 731
- [58] K. Saito, K. Tsushima, A.W. Thomas, and A.G. Williams, *Phys. Lett. B* 433 (1998) 243
- [59] M. Prakash, P.J. Ellis, and J.I. Kapusta, *Phys. Rev. C* 45 (1992) 2518;  
B.D. Serot and H.B. Tang, *Phys. Rev. C* 51 (1995) 969
- [60] D. Vautherin and D.M. Brink, *Phys. Rev. C* 5 (1972) 626
- [61] J. Friedrich and P.G. Reinhard, *Phys. Rev. C* 33 (1986) 335
- [62] J. Zimanyi and S.A. Moszkowski, *Phys. Rev. C* 42 (1990) 1416
- [63] Y. Sugahara and H. Toki, *Prog. Theor. Phys.* 92 (1994) 803;  
P.G. Reinhard, M. Rufa, J. Maruhn, W. Greiner, and J. Friedrich, *Z. Phys. A* 323 (1986) 13
- [64] X. Jin and B.K. Jennings, *Phys. Lett. B* 374 (1996) 13; *Phys. Rev. C* 54 (1996) 1427
- [65] H. Müller and B.K. Jennings, *Nucl. Phys. A* 626 (1997) 966;  
H. Müller, *Phys. Rev. C* 57 (1998) 1974;  
J.C. Caillon and J. Labarsouque, *Phys. Lett. B* 425 (1998) 13
- [66] D.H. Lu, K. Tsushima, A.W. Thomas, A.G. Williams, and K. Saito, *Nucl. Phys. A* 634 (1998) 443

- [67] S. Hama, B.C. Clark, E.D. Cooper, H.S. Sherif, and R.L. Mercer, *Phys. Rev. C* 41 (1990) 2737; S.J. Wallece, *Ann. Rev. Nucl. Part. Sci.* 37 (1987) 267
- [68] I. Sick, *Comments Nucl. Part. Phys.* 18 (1988) 109; *Phys. Lett. B* 157 (1985) 13
- [69] J. Jourdan, *Phys. Lett. B* 353 (1995) 189
- [70] H. Toki, U. Meyer, A. Faessler, and R. Brockmann, *Phys. Rev. C* 58 (1998) 3749; H. Shen and H. Toki, *Phys. Rev. C* 61 (2000) 045205
- [71] Y.H. Tan, H. Shen, and P.Z. Ning, *Phys. Rev. C* 63 (2001) 055203
- [72] H. Shen and H. Toki, *Nucl. Phys. A* 707 (2002) 469
- [73] H. Shen and H. Toki, *nucl-th/0410072*
- [74] P. Wang, Z.Y. Zhang, Y.W. Yu, R.K. Su, and Q. Song, *Nucl. Phys. A* 688 (2001) 791; P. Wang, H. Guo, Z.Y. Zhang, Y.W. Yu, R.K. Su, and Q. Song, *Nucl. Phys. A* 705 (2002) 455; P. Wang, V.E. Lyubovitskij, Th. Gutshe, and A. Faessler, *Phys. Rev. C* 67 (2003) 015210; P. Wang, D.B. Leinweber, A.W. Thomas, and A.G. Williams, *Nucl. Phys. A* 744 (2004) 273; P. Wang, D.B. Leinweber, A.W. Thomas, and A.G. Williams, *Nucl. Phys. A* 748 (2005) 226; P. Wang, S. Lawley, D.B. Leinweber, A.W. Thomas, and A.G. Williams, *nucl-th/0506014*
- [75] W. Bentz and A.W. Thomas, *Nucl. Phys. A* 696 (2001) 138
- [76] H. Mineo, W. Bentz, N. Ishii, A.W. Thomas, and K. Yazaki, *Nucl. Phys. A* 735 (2004) 482A735 (2004); T. Horikawa and W. Bentz, *nucl-th/0506021*
- [77] I.C. Cloet, W. Bentz, and A.W. Thomas, *nucl-th/0504019*, to appear in *Phys. Rev. Lett.*
- [78] C.J. Horowitz and B.D. Serot, *Nucl. Phys. A* 368 (1981) 503
- [79] X.R. Zhou, G.F. Burgio, U. Lombardo, H.-J. Schulze, and W. Zuo, *Phys. Rev. C* 69 (2004) 018801
- [80] A. Akmal, V.R. Pandharipande, and D.G. Ravenhall, *Phys. Rev. C* 58 (1998) 1804
- [81] E.N.E. van Dalen, C. Fuchs, and A. Faessler, *Nucl. Phys. A* 744 (2004) 227
- [82] F. de Jong and H. Lenske, *Phys. Rev. C* 58 (1998) 890
- [83] M.A. Shifman, A.I. Vainshtein, and V.I. Zakharov, *Nucl. Phys. B* 147 (1979) 358; *Nucl. Phys. B* 147 (1979) 448
- [84] L.J. Reinders, H.R. Rubinstein, and S. Yazaki, *Phys. Rep.* 127 (1985) 1
- [85] E.G. Drukarev and E.M. Levin, *Nucl. Phys. A* 511 (1990) 679; *Nucl. Phys. A* 516 (1990) 715(E)
- [86] M. Baldo, P. Castorina, D. Zappalà, *Nucl. Phys. A* 743 (2004) 3
- [87] T.D. Cohen, R.J. Furnstahl, and D.K. Griegel, *Phys. Rev. C* 45 (1992) 1881
- [88] M. Lutz, S. Klimt, and W. Weise, *Nucl. Phys. A* 542 (1992) 521
- [89] J. Gasser, H. Leutwyler, and M. Sainio, *Phys. Lett. B* 253 (1991) 252
- [90] K. Tsushima, T. Maruyama, and A. Faessler, *Nucl. Phys. A* 535 (1991) 497; T. Maruyama, K. Tsushima, and A. Faessler, *Nucl. Phys. A* 537 (1992) 303
- [91] R.L. Jaffe, *Phys. Rev. D* 21 (1980) 3215; *Nucl. Phys. A* 478 (1988) 3c
- [92] M.C. Birse and J.A. McGovern, *Phys. Lett. B* 309 (1993) 231; M.C. Birse, *Phys. Rev. C* 49 (1994) 2212; *Phys. Rev. C* 53 (1996) R2048
- [93] V. Bernard, N. Kaiser, and Ulf-G. Meissner, *Int. J. Mod. Phys. E* 4 (1995) 193
- [94] H.Q. Song and R.K. Su, *Phys. Lett. B* 358 (1995) 179
- [95] P.K. Panda, A. Mishra, J.M. Eisenberg, and W. Greiner, *Phys. Rev. C* 56 (1997) 3134
- [96] R.J. Furnstahl and B.R. Serot, *Phys. Rev. C* 41 (1990) 262
- [97] P.K. Panda, R. Sahu, and C. Das, *Phys. Rev. C* 60 (1999) 038801
- [98] P.K. Panda, D.P. Menezes, and C. Providência, *Phys. Rev. C* 69 (2004) 025207; *Phys. Rev. C* 69 (2004) 058801
- [99] D.P. Menezes, P.K. Panda, and C. Providência, *astro-ph/0506196*
- [100] I. Zakout and H.R. Jaqaman, *Phys. Rev. C* 59 (1999) 962; *Phys. Rev. C* 59 (1999) 968



- [101] I. Zakout, H.R. Jaqaman, S. Pal, H. Stöcker, and W. Greiner, *Phys. Rev. C* 61 (2000) 055208
- [102] S. Pal, M. Hanauske, I. Zakout, H. Stöcker, and W. Greiner, *Phys. Rev. C* 60 (1999) 015802
- [103] I. Zakout, W. Greiner, and H.R. Jaqaman, *nucl-th/0411028*
- [104] C.J. Horowitz, D.P. Murdoch, and B.D. Serot, *Computational Nuclear Physics 1* (Springer Berlin, 1991)
- [105] B.B.P. Sinha *et al.*, *Phys. Lett. B* 53 (1971) 217
- [106] R. Machleidt, *Adv. Nucl. Phys.* 19 (1989) 189
- [107] I. Sick *et al.*, *Phys. Lett. B* 88 (1979) 245
- [108] B. Frois *et al.*, *Phys. Rev. Lett.* 38 (1977) 152
- [109] J.L. Friar and J.W. Negele, *Adv. Nucl. Phys.* 8 (1975) 219
- [110] I. Sick and J.S. McCarthy, *Nucl. Phys. A* 150 (1970) 631
- [111] L.A. Fajardo *et al.*, *Phys. Lett. B* 37 (1971) 363
- [112] B. Frois, *Lecture Notes in Physics* 108 (1979) 52
- [113] L. Ray, *Phys. Rev. C* 19 (1979) 1855;  
L. Ray and P.E. Hodgson, *Phys. Rev. C* 20 (1979) 2403
- [114] T. Nikšić, D. Vretenar, and P. Ring, *Phys. Rev. C* 66 (2002) 064302
- [115] M.K. Banerjee and J.A. Tjon, *Phys. Rev. C* 56 (1997) 497
- [116] C.Y. Ryu, C.H. Hyun, J.Y. Lee, S.W. Hong, *nucl-th/0506052*
- [117] X. Jin and M. Nielsen, *Phys. Rev. C* 51 (1995) 347
- [118] F. Klingl, N. Kaiser, W. Weise, *Nucl. Phys. A* 624 (1997) 527
- [119] F.S. Navarra, M. Nielsen, K. Tsushima, *Phys. Lett. B* 606 (2005) 335
- [120] A. Hayashigaki, *Prog. Theor. Phys.* 101 (1999) 923
- [121] F. Klingl, S. Kim, S.H. Lee, P. Morath, W. Weise, *Phys. Rev. Lett.* 82 (1999) 3396
- [122] S. Kim, S.H. Lee, *Nucl. Phys. A* 679 (2001) 517
- [123] A. Hayashigaki, *Phys. Lett. B* 487 (2000) 96
- [124] K. Tsushima, K. Saito, J. Haidenbauer, A.W. Thomas, *Nucl. Phys. A* 630 (1998) 691;  
K. Tsushima, K. Saito, A.W. Thomas, *Phys. Lett. B* 411 (1997) 9; (E)*Phys. Lett. B* 421 (1998) 413
- [125] K. Tsushima, F.C. Khanna, *Phys. Lett. B* 552 (2003) 138
- [126] K. Tsushima, F.C. Khanna, *J. Phys. G* 30 (2004) 1765; *Phys. Rev. C* 67 (2003) 015211; *Prog. Theor. Phys. Suppl.* 149 (2003) 160
- [127] R.J. Furnstahl and B.D. Serot, *Nucl. Phys. A* 468 (1987) 539
- [128] J. Cohen, *Phys. Rev. C* 48 (1993) 1346
- [129] J. Cohen, and R.J. Furnstahl, *Phys. Rev. C* 35 (1987) 2231
- [130] K. Tsushima, K. Saito, A.W. Thomas, S.V. Wright, *Phys. Lett. B* 429 (1998) 239; (E)*Phys. Lett. B* 436 (1998) 453
- [131] K. Tsushima, D.H. Lu, A.W. Thomas, K. Saito, R.H. Landau, *Phys. Rev. C* 59 (1999) 2824
- [132] R.M. Barnett *et al.*, *Phys. Rev. D* 54 (1996) 1
- [133] D.E. Groom *et al.*, *Eur. Phys. J. C* 15 (2000) 1
- [134] C. Caso *et al.*, *Eur. Phys. J. C* 3 (1998) 1
- [135] K. Hagiwara *et al.*, *Phys. Rev. D* 66 (2002) 010001
- [136] T.M. Ito, R.S. Hayano, S.N. Nakamura, and T.P. Terada, *Phys. Rev. C* 58 (1998) 2366;  
M. Iwasaki, *Nucl. Phys. A* 670 (2000) 190c
- [137] S. Hirenzaki, Y. Okumura, H. Toki, E. Oset, and A. Ramos, *Phys. Rev. C* 61 (2000) 055205
- [138] J. Mareš and J. Žofka, *Z. Phys. A* 333 (1989) 209
- [139] M. Rufa, H. Stöcker, P-G Reinhard, J. Maruhn, and W. Greiner, *J. Phys. G* 13 (1987) L143
- [140] E.D. Cooper, B.K. Jennings, and J. Mareš, *Nucl. Phys. A* 580 (1994) 419;  
J. Mareš and B.K. Jennings, *Phys. Rev. C* 49 (1994) 2472

- [141] B.K. Jennings, *Phys. Lett. B* 246 (1990) 325;  
M. Chiapparini, A.O. Gattone, B.K. Jennings, *Nucl. Phys. A* 529 (1991) 589
- [142] J. Cohen and H.J. Weber, *Phys. Rev. C* 44 (1991) 1181
- [143] C.B. Dover and A. Gal, *Prog. Part. Nucl. Phys.* 12 (1985) 171
- [144] A. Bouyssy and J. Hüfner, *Phys. Lett. B* 64 (1976) 276
- [145] R. Brockmann and W. Weise, *Phys. Lett. B* 69 (1977) 167; *Nucl. Phys. A* 355 (1981) 365
- [146] W. Brückner *et al.*, *Phys. Lett. B* 79 (1978) 157
- [147] S. Ajimura *et al.*, *Nucl. Phys. A* 585 (1995) 173c
- [148] J. Johnston and A.W. Thomas, *J. Phys. G* 8 (1982) L105; *Nucl. Phys. A* 392 (1983) 409
- [149] C.B. Dover and A. Gal, *Ann. Phys. (N.Y.)* 146 (1983) 309; *Prog. Part. Nucl. Phys.* 12 (1984) 171;  
C.B. Dover, D.J. Millener and A. Gal, *Phys. Rep.* 184 (1989) 1
- [150] P.M.M. Maessen, T.A. Rijken, and J.J. de Swart, *Phys. Rev. C* 40 (1989) 2226
- [151] A. Reuber, K. Holinde, and J. Speth, *Nucl. Phys. A* 570 (1994) 543
- [152] I.R. Afnan and B.F. Gibson, *Phys. Rev. C* 67 (2003) 017001;  
S.B. Carr, I.R. Afnan and B.F. Gibson, *Nucl. Phys. A* 625 (1997) 143
- [153] R.E. Chrien *Nucl. Phys. A* 478 (1988) 705c
- [154] O. Hashimoto, H. Tamura, to appear in *Prog. Part. Nucl. Phys.*
- [155] R.I. Sawafra for the E887 and E905 Collaborations, *Nucl. Phys. A* 639 (1998) 103c;  
S. Bart *et al.*, *Phys. Rev. Lett.* 83 (1999) 5238
- [156] P.K. Saha *et al.*, *Phys. Rev. C* 70 (2004) 044613
- [157] T. Harada, *Phys. Rev. Lett.* 81 (1998) 5287
- [158] T. Yamazaki *et al.*, *Phys. Rev. Lett.* 54 (1985) 102; *Phys. Lett. B* 207 (1998) 393;  
R.S. Hayano *et al.*, *Phys. Lett. B* 231 (1989) 355; *Nuovo Cimento A* 102 (1989) 437
- [159] J. Mareš *et al.*, *Nucl. Phys. A* 594 (1995) 311
- [160] A.A. Tyapkin, *Sov. J. Nucl. Phys.* 22 (1976) 89
- [161] C.B. Dover and S.H. Kahana, *Phys. Rev. Lett.* 39 (1977) 1506
- [162] B.F. Gibson, C.B. Dover, G. Bhamati, and D.R. Lehman, *Phys. Rev. C* 27 (1982) 2085
- [163] H. Bando, and M. Bando, *Phys. Lett. B* 109 (1982) 164;  
H. Bando, and S. Nagata, *Prog. Theor. Phys.* 69 (1983) 557
- [164] T. Bressani, F. Iazzi, *Nuovo Cimento A* 102 (1989) 597;  
S.A. Buyatov, V.V. Lyukov, N.I. Strakov and V.A. Tsarev, *Nuovo Cimento A* 10413611991
- [165] K. Tsushima, D.H. Lu, A.W. Thomas and K. Saito, *Phys. Lett. B* 443 (1998) 26;  
K. Tsushima, *Proceedings, ISHEPP 98*, Vol. 1. 2000. pp. 120, *nucl-th/9811063*
- [166] K. Tsushima, *Nucl. Phys. A* 670 (2000) 198c
- [167] Q. Haider, L.C. Liu, *Phys. Lett. B* 172 (1986) 257;  
L.C. Liu, Q. Haider *Phys. Rev. C* 34 (1986) 1845
- [168] H.C. Chiang, E. Oset, L.C. Liu, *Phys. Rev. C* 44 (1991) 738
- [169] S.A. Rakityansky *et al.*, *Phys. Rev. C* 53 (1996) R2043
- [170] R.S. Hayano, S. Hirenzaki, A. Gillitzer, *Eur. Phys. J. A* 6 (1999) 99
- [171] F. Klingl, T. Waas, W. Weise, *Nucl. Phys. A* 650 (1999) 299
- [172] S. Hirenzaki *et al.*, *Nucl. Phys. A* 663 (2000) 553;  
D. Jido, H. Nagahiro, S. Hirenzaki, *Phys. Rev. C* 66 (2002) 045202;  
S. Hirenzaki, H. Nagahiro, T. Hatsuda, T. Kunihiro, *Nucl. Phys. A* 710 (2002) 131;  
D. Jido, H. Nagahiro, S. Hirenzaki, *Nucl. Phys. A* 721 (2003) 665;  
S. Hirenzaki, *Nucl. Phys. A* 738 (2004) 377
- [173] H. Nagahiro, S. Hirenzaki, *hep-ph/0412072*

- [174] C. García-Recio, T. Inoue, J. Nieves, E. Oset, *Phys. Lett. B* 550 (2002) 47
- [175] T. Waas, W. Weise, *Nucl. Phys. A* 625 (1997) 287
- [176] T. Inoue, E. Oset, *Nucl. Phys. A* 710 (2002) 354
- [177] X.H. Zhong, G.X. Peng, P.Z. Ning, *nucl-th/0506020*
- [178] T. Hatsuda, S.H. Lee, *Phys. Rev. C* 46 (1992) R34
- [179] K. Tsushima, *hep-ph/0206069*, *Proceedings, Physics at the Japan Hadron Facility (JHF)*, pp.303 (World Scientific, 2002).
- [180] T. Waas, R. Brockmann and W. Weise, *Phys. Lett. B* 405 (1997) 215;  
T. Yamazaki *et al.*, *Phys. Lett. B* 418 (1998) 246
- [181] D.H. Lu and R.H. Landau, *Phys. Rev. C* 49 (1994) 878;  
Y.R. Kwon and F. Tabakin, *Phys. Rev. C* 18 (1978) 932 R.H. Landau, *Quantum Mechanics II* (John Wiley & Sons, New York, 1990)
- [182] K. Saito, K. Tsushima, D.H. Lu, and A.W. Thomas, *Phys. Rev. C* 59 (1999) 1203
- [183] R.S. Hayano, private communication
- [184] D. H. Lu, A. W. Thomas, and A. G. Williams, *Phys. Rev. C* 57 (1998) 2628; *Phys. Rev. C* 55 (1997) 3108
- [185] R. E. Peierls and D. J. Thouless, *Nucl. Phys. A* 38 (1962) 154
- [186] A. L. Licht and A. Pagnamenta, *Phys. Rev. D* 2 (1970) 1150; *Phys. Rev. D* 2 (1970) 1156
- [187] D.H. Lu, A.W. Thomas, K. Tsushima, A.G. Williams, K. Saito, *Phys. Lett. B* 417 (1998) 217
- [188] A.W. Thomas, *Adv. in Nucl. Phys.* 13 (1984) 1  
G.A. Miller, *Int. Rev. Nucl. Phys.* 2 (1984) 190
- [189] S. Th  berge, G. A. Miller, and A. W. Thomas, *Can. J. Phys.* 60 (1982) 59;  
S. Th  berge and A.W. Thomas, *Nucl. Phys. A* 393 (1983) 252
- [190] I. Sick, in *Proc. Int. Conf. on Weak and Electromagnetic Interactions in Nuclei*, ed. H. Klapdor (Springer-Verlag, Berlin, 1986) p.415
- [191] D.H. Lu, K. Tsushima, A.W. Thomas, A.G. Williams, K. Saito, *Phys. Rev. C* 60 (1999) 068201
- [192] J.J. Kelly, private communication
- [193] D.H. Lu, A.W. Thomas, K. Tsushima, A.G. Williams and K. Saito, *Phys. Lett. B* 441 (1998) 27
- [194] T. De Forest, Jr., *Nucl. Phys. A* 392 (1983) 232;  
H.W.L. Naus and J.H. Koch, *Phys. Rev. C* 36 (1987) 2459;  
H.W.L. Naus, S.J. Pollock, J.H. Koch and U. Oelfke, *Nucl. Phys. A* 509 (1990) 717
- [195] W.M. Alberico, T.W. Donnelly, and A. Molinari, *Nucl. Phys. A* 512 (1990) 541;  
D.O. Riska, *Phys. Rep.* 181 (1989) 207;  
W. M. Alberico, M. Ericson, and A. Molinari, *Ann. Phys. (N.Y.)* 154 (1984) 356;  
J. W. Van Orden and T. W. Donnelly, *Ann. Phys. (N.Y.)* 131 (1981) 451;  
J.L. Friar, and S. Fallieros, *Phys. Rev. C* 13 (1976) 2571
- [196] K. Tsushima, D.O. Riska, P.G. Blunden, *Nucl. Phys. A* 559 (1993) 543
- [197] D.V. Bugg, *The  $\pi N$  newsletter* 8 (1993) 1
- [198] J.D. Walecka, *Theoretical nuclear and subnuclear physics* (Oxford, 1995)
- [199] H. Kurasawa and T. Suzuki, *Phys. Lett. B* 165 (1985) 234
- [200] J.-M. Laget, *Nucl. Phys. A* 579 (1994) 333
- [201] J.M. Udias *et al.*, *Phys. Rev. Lett.* 83 (1999) 5451;  
J.A. Caballero *et al.*, *Nucl. Phys. A* 632 (1998) 323;  
J.M. Udias, J.R. Vignote, *Phys. Rev. C* 62 (2000) 034302
- [202] J.J. Kelly, *Phys. Rev. C* 60 (1999) 044609;
- [203] Z.E. Meziani *et al.*, *Phys. Rev. Lett.* 52 (1984) 2130;  
W.M. Alberico, P. Czerski, M. Ericson, and A. Molinari, *Nucl. Phys. A* 462 (1987) 269

- [204] For example, H. Kurasawa and T. Suzuki, *Nucl. Phys. A* 445 (1985) 685;  
C.J. Horowitz, *Phys. Lett. B* 208 (1988) 8
- [205] K. Saito, K. Tsushima, and A.W. Thomas, *Phys. Lett. B* 465 (1999) 27;  
K. Saito, *Nucl. Phys. A* 680 (2001) 246c
- [206] J. Morgenstern and Z.E. Meziani, *Phys. Lett. B* 515 (2001) 269
- [207] D.H. Lu, A.W. Thomas, and K. Tsushima, *nucl-th/0112001*
- [208] A. Arima *et al.*, *Adv. Nucl. Phys.* 18 (1987) 1;  
I.S. Towner, *Phys. Rep.* 155 (1987) 263;  
F. Osterfeld, *Rev. Mod. Phys.* 64 (1992) 491
- [209] K. Tsushima, D.O. Riska, *Nucl. Phys. A* 549 (1992) 313
- [210] K. Tsushima, Hungchong Kim, and K. Saito, *Phys. Rev. C* 70 (2004) 038501
- [211] L.B. Auerbach *et al.*, *Phys. Rev. C* 66 (2002) 015501
- [212] C. Athanassopoulos *et al.*, *Phys. Rev. C* 56 (1997) 2806
- [213] M. Albert *et al.*, *Phys. Rev. C* 51 (1995) R1065
- [214] E. Kolbe, K. Langanke, P. Vogel, *Nucl. Phys. A* 652 (1999) 91;  
C. Volpe *et al.*, *Phys. Rev. C* 62 (2000) 015501;  
A.C. Hayes, I.S. Towner, *Phys. Rev. C* 61 (2000) 044603;  
S.K. Singh *et al.*, *Phys. Rev. C* 57 (1998) 2687;  
F. Krmpotić, A. Mariano, A. Samana, *Phys. Lett. B* 541 (2002) 298;  
Y. Umino, J.M. Udias, *Phys. Rev. C* 52 (1995) 3399;  
C. Maieron *et al.*, *Phys. Rev. C* 68 (2003) 048501
- [215] Hungchong Kim, J. Piekarewicz, C.J. Horowitz, *Phys. Rev. C* 51 (1995) 2739; *nucl-th/9502041*
- [216] C.J. Horowitz, Hungchong Kim, J. Piekarewicz, *Phys. Rev. C* 48 (1993) 3078
- [217] Hungchong Kim, S. Schramm, C.J. Horowitz, *Phys. Rev. C* 53 (1996) 3131
- [218] M.J. Musolf, T.W. Donnelly, *Nucl. Phys. A* 546 (1992) 509
- [219] T. Kitagaki *et al.*, *Phys. Rev. D* 28 (1983) 436
- [220] K.A. Brueckner, *Phys. Rev.* 110 (1958) 587;  
N.M. Hugenholtz, L. Van Hove, *Physica* 24 (1958) 363
- [221] See, for example, A. Hotta *et al.*, *Phys. Rev. C* 30 (1984) 87
- [222] T. Kuramoto *et al.*, *Nucl. Phys. A* 512 (1990) 711
- [223] K. Saito and K. Tsushima, *Phys. Lett. B* 575 (2003) 4
- [224] J. Aubert *et al.*, *Phys. Lett. B* 123 (1982) 275;  
A. Bodek *et al.*, *Phys. Rev. Lett.* 51 (1983) 534;  
R.G. Arnold *et al.*, *Phys. Rev. Lett.* 52 (1984) 727
- [225] O. Benhar, A. Fabrocini, and S. Fantoni, *Nucl. Phys. A* 505 (1989) 267
- [226] H. Mütter and A. Polls, *Prog. Part. Nucl. Phys.* 45 (2000) 243
- [227] S. Boffi, C. Giusti, F.D. Pacati, and M. Radici, *Electromagnetic Response of Atomic Nuclei* (Clarendon Press Oxford, 1996)
- [228] G.A. Miller, *Phys. Rev. C* 56 (1997) 8; *Phys. Rev. C* 56 (1997) 2789; *Prog. Part. Nucl. Phys.* 45 (2000) 83
- [229] M.C. Birse, *Phys. Lett. B* 299 (1993) 186
- [230] D.M. Alde *et al.*, *Phys. Rev. Lett.* 64 (1990) 2479
- [231] K. Saito, A. Michels, and A.W. Thomas, *Phys. Rev. C* 46 (1992) R2149;  
A.W. Thomas, K. Saito, and A. Michels, *Aust. J. Phys.* 46 (1993) 3
- [232] K. Saito and A.W. Thomas, *Nucl. Phys. A* 574 (1994) 659
- [233] A.I. Signal and A.W. Thomas, *Phys. Rev. D* 40 (1989) 2832;  
A.W. Schreiber, A.I. Signal, and A.W. Thomas, *Phys. Rev. D* 44 (1991) 2653

- [234] S.D. Drell and T.-M. Yan, *Phys. Rev. Lett.* 24 (1970) 181
- [235] G.B. West, *Phys. Rev. Lett.* 24 (1970) 1206; *Phys. Rev. D* 14 (1976) 732
- [236] I. Niculescu *et al.*, *Phys. Rev. Lett.* 85 (2000) 1182;  
C.S. Armstrong *et al.*, *Phys. Rev. D* 63 (2001) 094008
- [237] R. Ent, C.E. Keppel and I. Niculescu, *Phys. Rev. D* 62 (2000) 073008
- [238] W. Melnitchouk, R. Ent, C.E. Keppel, *Phys. Rep.* 406 (2005) 127
- [239] A. de Rújula, H. Georgi and H.D. Politzer, *Ann. Phys. (N.Y.)* 103 (1975) 315
- [240] X. Ji and P. Unrau, *Phys. Rev. D* 52 (1995) 72; *Phys. Lett. B* 333 (1994) 228;  
X. Ji and W. Melnitchouk, *Phys. Rev. D* 56 (1997) 1
- [241] C.E. Carlson and N.C. Mukhopadhyay, *Phys. Rev. D* 41 (1989) 2343;  
*Phys. Rev. Lett.* 74 (1995) 1228; *Phys. Rev. D* 58 (1998) 094029
- [242] W. Melnitchouk, *Phys. Rev. Lett.* 86 (2001) 35; (E)*Phys. Rev. Lett.* 93 (2004) 199901
- [243] W. Melnitchouk, *Nucl. Phys. A* 680 (2001) 52
- [244] S. Simula, *Phys. Rev. D* 64 (2001) 038301
- [245] R. Ent, C.E. Keppel and I. Niculescu, *Phys. Rev. D* 64 (2001) 038302
- [246] W. Melnitchouk and A.W. Thomas, *Phys. Lett. B* 377 (1996) 11
- [247] W. Melnitchouk, K. Tsushima, A.W. Thomas, *Eur. Phys. J. A* 14 (2002) 105
- [248] L.L. Frankfurt and M.I. Strikman, *Nucl. Phys. B* 250 (1985) 1585; *Phys. Rep.* 160 (1988) 235;  
M. Sargsian, L.L. Frankfurt and M.I. Strikman, *Z. Phys. A* 335 (1990) 431
- [249] W. Melnitchouk, M. Sargsian and M.I. Strikman, *Z. Phys. A* 359 (1997) 99
- [250] M.M. Sargsian, S. Simula and M.I. Strikman, *Phys. Rev. C* 66 (2002) 024001
- [251] I.R. Afnan, F. Bissey, J. Gomez, A.T. Katramatou, W. Melnitchouk, G.G. Petratos and A.W. Thomas,  
*Phys. Lett. B* 493 (2000) 36
- [252] E. Pace, G. Salme, S. Scopetta and A. Kievsky, *Phys. Rev. C* 64 (2001) 055203
- [253] K. Tsushima, K. Saito, F.M. Steffens, *Phys. Lett. B* 612 (2005) 5
- [254] F.M. Steffens, K. Tsushima, *Phys. Rev. D* 70 (2004) 094040
- [255] A. De Rújula, H. Georgi, H.D. Politzer, *Ann. Phys. (N.Y.)* 103 (1997) 315; *Phys. Rev. D* 15 (1977) 2495
- [256] G.P. Zeller *et al.*, *Phys. Rev. Lett.* 88 (2002) 091802
- [257] J.T. Londergan, A.W. Thomas, *hep-ph/0407247*
- [258] D.B. Kaplan and A.E. Nelson, *Phys. Lett. B* 175 (1986) 57; (E)*Phys. Lett. B* 179 (1986) 409
- [259] C.M. Ko, Z.G. Wu, L.H. Xia and G.E. Brown, *Phys. Rev. Lett.* 66 (1991) 2577; *Phys. Rev. Lett.* 67 (1991) 1811
- [260] C.H. Lee, G.E. Brown, D.P. Min, M. Rho, *Nucl. Phys. A* 585 (1995) 401
- [261] T. Maruyama, T. Muto, T. Tatsumi, K. Tsushima, and A.W. Thomas, *nucl-th/0502079*, to appear in  
*Nucl. Phys. A*
- [262] T. Waas, M. Rho and W. Weise, *Nucl. Phys. A* 617 (1997) 449
- [263] T. Waas, N. Kaiser and W. Weise, *Phys. Lett. B* 365 (1996) 12; *Phys. Lett. B* 379 (1996) 34
- [264] A. Sibirtsev and W. Cassing, *Nucl. Phys. A* 641 (1998) 476
- [265] E. Friedman, A. Gal and C.J. Batty, *Phys. Lett. B* 308 (1993) 6; *Nucl. Phys. A* 579 (1993) 518;  
E. Friedman, A. Gal and J. Mares *Phys. Rev. C* 60 (1999) 024314
- [266] G.Q. Li, C.M. Ko and X.S. Fang, *Phys. Lett. B* 329 (1994) 149
- [267] W. Cassing, E.L. Bratkovskaya, U. Mosel, S. Teis, and A. Sibirtsev, *Nucl. Phys. A* 614 (1997) 415
- [268] G.Q. Li, C.H. Lee and G.E. Brown, *Nucl. Phys. A* 625 (1997) 372
- [269] E.L. Bratkovskaya, W. Cassing and U. Mosel, *Nucl. Phys. A* 622 (1997) 593
- [270] W. Cassing and E.L. Bratkovskaya, *Phys. Rep.* 308 (1999) 65
- [271] A. Schroter *et al.*, *Z. Phys. A* 350 (1994) 101

- [272] P. Senger *et al.*, *Acta Phys. Polon. B* 27 (1996) 2993
- [273] R. Barth *et al.*, *Phys. Rev. Lett.* 78 (1997) 4007
- [274] F. Laue *et al.*, *Phys. Rev. Lett.* 82 (1999) 1640
- [275] P. Senger and H. Strobele, *J. Phys. G* 25 (1999) R59
- [276] P. Senger *et al.*, *Prog. Part. Nucl. Phys.* 42 (1999) 209
- [277] G.Q. Li, C.M. Ko and W.S. Chung, *Phys. Rev. C* 57 (1998) 403
- [278] C. Fuchs, Amand Faessler, E. Zabrodin *Phys. Rev. Lett.* 86 (2001) 1974
- [279] C. Hartnack, J. Aichelin *J. Phys. G* 28 (2002) 1649
- [280] Lie-Wen Chen, Che Ming Ko, Yiharn Tzeng *Phys. Lett. B* 584 (2004) 269
- [281] Yu-Ming Zheng *et al.*, *Phys. Rev. C* 69 (2004) 034907
- [282] A. Mishra *et al.*, *Phys. Rev. C* 70 (2004) 044904
- [283] K. Tsushima, A. Sibirtsev, and A.W. Thomas *Phys. Rev. C* 62 (2000) 064904
- [284] K. Tsushima, S.W. Huang and A. Faessler, *Phys. Lett. B* 337 (1994) 245; *J. Phys. G* 21 (1995) 33; *Austral. J. Phys.* 50 (1997) 35;  
K. Tsushima, A. Sibirtsev and A.W. Thomas, *Phys. Lett. B* 29 (1997) 390;  
K. Tsushima, A. Sibirtsev, A.W. Thomas and G.Q. Li, *Phys. Rev. C* 59 (1999) 369; (E)*Phys. Rev. C* 61 (2000) 029903
- [285] A. Sibirtsev, K. Tsushima and A.W. Thomas, *Phys. Lett. B* 421 (1998) 59;  
A. Sibirtsev, K. Tsushima, W. Cassing and A.W. Thomas, *Nucl. Phys. A* 646 (1999) 427
- [286] G.Q. Li, *nucl-th/9710008*, Sec. III B;  
G.Q. Li, C.-H. Lee, and G. E. Brown, *Phys. Rev. Lett.* 79 (1997) 5214
- [287] G.Q. Li, and C.M. Ko, *Nucl. Phys. A* 594 (1995) 439; *Phys. Rev. C* 54 (1996) 1987;  
Bao-An Li and Che Ming Ko, *Phys. Rev. C* 52 (1995) 2037;  
Y. Nara *et al.*, *Nucl. Phys. A* 614 (1997) 4337;  
C. Fuchs *et al.*, *Phys. Rev. C* 56 (1997) 606; *Phys. Lett. B* 434 (1998) 245;  
W.S. Chung, G.Q. Li and C.M. Ko, *Nucl. Phys. A* 625 (1997) 347;  
W.S. Chung, C.M. Ko and G.Q. Li, *Phys. Rev. C* 641 (1998) 347;  
Z.S. Wang *et al.*, *Nucl. Phys. A* 628 (1998) 151; *Nucl. Phys. A* 645 (1999) 177; (E)*Nucl. Phys. A* 648 (1999) 281
- [288] T.M. Knasel *et al.*, *Phys. Rev. D* 11 (1975) 1
- [289] R.D. Baker *et al.*, *Nucl. Phys. B* 141 (1978) 29
- [290] V. Pandharipande and S.C. Pieper, *Phys. Rev. C* 45 (1992) 791
- [291] A. Baldini, V. Flaminio, W.G. Moorhead, Douglas R.O. Morrison, *Landolt-Börnstein, Numerical Data and Functional Relationships in Science and Technology* Ed. H. Schopper, Vol. 12 (1988) (Springer-Verlag)
- [292] A. Hombach, W. Cassing, S. Teis, U. Mosel, *Eur. Phys. J. A* 5 (1999) 77
- [293] W. Cassing, E.L. Bratkovskaya and S. Juchem, *Nucl. Phys. A* 674 (2000) 249
- [294] A.E. Nelson, D.B. Kaplan, *Phys. Lett. B* 192 (1987) 193
- [295] G.E. Brown, K. Kubodera, M. Rho, *Phys. Lett. B* 192 (1987) 273
- [296] M. Lutz, A. Steiner, W. Weise, *Nucl. Phys. A* 574 (1994) 755
- [297] G.Q. Li, C.M. Ko, G.E. Brown, *Phys. Lett. B* 381 (1996) 17
- [298] J.L. Ritman *et al.*, *Z. Phys. A* 352 (1995) 355
- [299] Y. Shin *et al.*, *Phys. Rev. Lett.* 81 (1998) 1576
- [300] D.E. Kharzeev, *Sov. J. Nucl. Phys.* 51 (1990) 185; *Nucl. Phys. A* 558 (1993) 331c; *Sov. J. Nucl. Phys.* 55 (1993) 746
- [301] A. Sibirtsev, K. Tsushima, A.W. Thomas *Eur. Phys. J. A* 6 (1999) 351

- [302] A. Sibirtsev, *Sov. J. Nucl. Phys.* 54 (1991) 426;  
A. Sibirtsev *et al.*, *Z. Phys. A* 347 (1994) 277;  
M. Buescher, A. Sibirtsev, K. Sistemich, *Z. Phys. A* 350 (1994) 161;  
A. Sibirtsev, *Acta Phys. Polon. B* 24 (1994) 1849; *Z. Phys. A* 345 (1993) 59; *Sov. J. Nucl. Phys.* 55 (1992) 729
- [303] R.M. Barnett *et al.*, *Phys. Rev. D* 54 (1994) 1
- [304] A.B. Kaidalov, P.E. Volkovitsky, *Phys. Rev. C* 63 (1994) 517
- [305] A. Sibirtsev, *Phys. Lett. B* 359 (1995) 29
- [306] M. Debowski *et al.*, *Z. Phys. A* 356 (1996) 313
- [307] A. Sibirtsev, W. Cassing, U. Mosel, *Z. Phys. A* 358 (1997) 357
- [308] I. Sick, S. Fantoni, A. Fabrocini, *Phys. Lett. B* 323 (1994) 267
- [309] C. Ciofi degli Atti, S. Simula, *Phys. Rev. C* 53 (1996) 1689
- [310] A. Badala *et al.*, *Phys. Rev. Lett.* 80 (1998) 4863
- [311] *Quark Matter '97*, *Nucl. Phys. A* (1998) 638;  
M.C. Abreu *et al.* (NA50 Collaboration), *Phys. Lett. B* 410 (1997) 337; *Phys. Lett. B* 450 (1999) 456;  
B. Alessandro *et al.*, *Eur. Phys. J. C* 39 (2005) 335
- [312] M.C. Abreu *et al.* (NA50 Collaboration), *Phys. Lett. B* 477 (2000) 28
- [313] J. Adams *et al.* (STAR Collaboration), *nucl-ex/0501009*
- [314] P. Jacobs and X.N. Wang, *hep-ph/0405125*
- [315] T. Waas and W. Weise, *Nucl. Phys. A* 625 (1997) 287
- [316] S.J. Brodsky and A.H. Mueller, *Phys. Lett. B* 206 (1988) 685;  
S. Gavin, M. Gyulassy and A. Jackson, *Phys. Lett. B* 207 (1988) 257;  
R. Vogt, M. Prakash, P. Koch and T.H. Hansson, *Phys. Lett. B* 207 (1988) 264;  
J.-P. Blaizot and J.-Y. Ollitrault, *Phys. Rev. D* 39 (1989) 232;  
C.-Y. Wong, E.S. Swanson and T. Barnes, *Phys. Rev. C* 62 (2000) 045201
- [317] N. Armesto and A. Capella, *J. Phys. G* 23 (1997) 1969; *Phys. Lett. B* 430 (1998) 23;  
N. Armesto, A. Capella and E.G. Ferreira, *Phys. Rev. C* 59 (1999) 395
- [318] D. Kharzeev and H. Satz, *Phys. Lett. B* 334 (1994) 155;  
K. Martins, D. Blaschke and E. Quack, *Phys. Rev. C* 51 (1995) 2723;  
D. Kharzeev, H. Satz, A. Syamtomov and G. Zinovev, *Phys. Lett. B* 389 (1996) 595
- [319] S.G. Matinyan and B. Müller, *Phys. Rev. C* 58 (1998) 2994;  
B. Müller, *Nucl. Phys. A* 661 (1999) 272
- [320] A. Capella, E.G. Ferreira and A.B. Kaidalov, *Phys. Rev. Lett.* 85 (2000) 2080
- [321] T. Matsui and H. Satz, *Phys. Lett. B* 178 (1986) 416
- [322] S. Gavin and R. Vogt, *Nucl. Phys. B* 345 (1990) 104;  
S. Gavin, H. Satz, R.L. Thews and R. Vogt, *Z. Phys. C* 61 (1994) 351
- [323] V.A. Miransky, *Dynamical Symmetry Breaking in Quantum Field Theories*, (World Scientific Publishing Co., 1993)
- [324] Yu.L. Kalinovsky, and C. Weiss, *Z. Phys. C* 63 (1994) 275
- [325] D. Blaschke, and C.D. Roberts, *Nucl. Phys. A* 642 (1998) 197
- [326] K. Kataja and P.V. Ruuskanen, *Phys. Lett. B* 243 (1990) 181
- [327] A.W. Thomas, P.A.M. Guichon, D.B. Leinweber, and R.D. Young, *Prog. Theor. Phys. Suppl.* 156 (2004) 124
- [328] H. Feldmeier, *Nucl. Phys. A* 515 (1990) 147
- [329] Y. Kanada-En'yo and H. Horiuchi, *Prog. Theor. Phys. Suppl.* 142 (2001) 205